TECHNISCHE UNIVERSITÄT MÜNCHEN

Joint gravimetric and geometric survey of geophysical signals - Feasibility study for the TERENO alpine and prealpine Ammer observatory

S. Tuttas

IAPG / FESG No. 31
Institut für Astronomische und Physikalische Geodäsie
Forschungseinrichtung Satellitengeodäsie

München 2011

Joint gravimetric and geometric survey of geophysical signals - Feasibility study for the TERENO alpine and prealpine Ammer observatory

S. Tuttas

IAPG / FESG No. 31

München 2011

ISSN 1437-8280
ISBN-13: 978-3-934205-30-7

Hinweis: Eine PDF-Version dieser Arbeit mit farbigen Abbildungen ist erhältlich unter
http://www.iapg.bv.tum.de/Schriftenreihe/

Adressen:
Institut für Astronomische und Physikalische Geodäsie
Technische Universität München
Arcisstrasse 21
D-80290 München
Germany
Telefon: +49-89-289-23190
Telefax: +49-89-289-23178
http://www.iapg.bv.tum.de/

Forschungseinrichtung Satellitengeodäsie
Technische Universität München
Arcisstrasse 21
D-80290 München
Germany
Telefon: +49-89-289-23191
Telefax: +49-89-289-23178
http://www.iapg.bv.tum.de/

Institut für Astronomische
und Physikalische Geodäsie

Institut für Methodik der Fernerkundung
SAR-Signalverarbeitung

Joint gravimetric and geometric survey of geophysical signals - Feasibility study for the TERENO alpine and prealpine Ammer observatory

Master's Thesis

by

Sebastian Tuttas

Supervisors: Univ.-Prof. Dr.techn. Mag.rer.nat. Roland Pail (IAPG)
Dr.-Ing. Thomas Gruber (IAPG)
Dr.rer.nat. Michael Eineder (IMF)

November 2010

Abstract

This master's thesis deals with a feasibility study for a joint gravimetric and geometric survey of geophysical signals. As test area the TERENO alpine and prealpine Ammer observatory is chosen since this initiative is associated with the installation of instruments for measuring meteorological and hydrological quantities. Gravimetric and geometric signals, which occur in the TERENO area, are estimated from available measured data.

At the beginning the theory of signals from solid Earth tide, ocean loading, pole tides, atmosphere and hydrology is outlined. The magnitudes of the expected signals are compared. It is distinguished between direct effects due to Newtonian attraction and indirect effects due to mass loading variations. Therefore the basics of mass loading calculations using Green's functions are described. Hydrologic and atmospheric signals shall be measured with different measurement techniques; the other mentioned effects can be reduced by models.

As gravimetric measurement techniques different gravimeter types and the GRACE mission are introduced. For measuring geometric signals spaceborne SAR (TerraSAR-X and TanDEM-X) and GNSS are presented.

The Scintrex CG-3M gravimeter, owned by the IAPG, was used for test measurements. First it was utilized as stationary instrument to investigate the influence of air pressure and drift. A field campaign was performed as a second experiment. It was measured above a storm water basin to simulate a groundwater change.

A further test measurement was performed to validate ranges and azimuths measured in SAR-images against ranges and azimuths derived from corner reflector coordinates, determined by GPS measurements. This method is used to evaluate the accuracy level of absolute SAR measurements.

Starting from the estimated signals and the experiences from the test measurements, different approaches are introduced for measuring atmospheric and hydrological signals using gravimetric and geometric techniques. For every approach the measurement configuration and the required instrumentation is described.

Kurzfassung

Die vorliegende Arbeit beschäftigt sich mit der Messung geophysikalischer Signale, die sowohl gravimetrisch als auch geometrisch erfasst werden sollen. Als Testgebiet ist das „TERENO alpine and prealpine Ammer observatory“ ausgewählt worden. Das TERENO Projekt umfasst die Bereitstellung einer umfangreichen Anzahl von Instrumenten zur Erfassung meteorologischer und hydrologischer Parameter. Anhand verfügbarer Messdaten erfolgt eine Abschätzung, welche gravimetrischen und geometrischen Signale im Testgebiet vorkommen und welche Größenordnung sie haben.

Zu Beginn der Arbeit werden die Effekte von festen Erdgezeiten, ozeanischen Auflasteffekten, Polgezeiten, Atmosphäre und Hydrologie unter theoretischen Gesichtspunkten vorgestellt und ihre Größenordungen verglichen. Es wird zwischen direkten Effekten aufgrund der Massenanziehung und indirekten Effekten aufgrund von Auflasteffekten unterschieden. Deshalb werden die Grundlagen der Berechnung von Auflasteffekten dargestellt.

Die Arbeit zielt darauf ab, die hydrologischen und atmosphärischen Signale unter Verwendung verschiedener Messtechniken zu erfassen. Die anderen genannten Effekte sollen mit Hilfe von Modellen in den Messdaten reduziert werden.

Als gravimetrische Messsysteme werden unterschiedliche Gravimetertypen sowie die Satellitenmission GRACE vorgestellt. Satellitengestütztes SAR (TerraSAR-X, TanDEM-X) sowie Satellitennavigationssysteme sind die verwendeten geometrischen Mess-verfahren.

Für praktische Testmessungen ist das Scintrex CG-3M Gravimeter des IAPG verwendet worden. In einem ersten Versuch wurden in einer stationären Messung die Auswirkungen von Luftdruck-Variationen und des Instrumentendrifts untersucht. Der zweite Versuch war eine Feldkampagne, bei der oberhalb eines Regenüberlaufbeckens gemessen wurde, um Grundwasserschwankungen zu simulieren.

In einer dritten Messkampagne wurden Koordinaten von Corner Reflektoren mit GPS bestimmt, um damit theoretische SAR Ranges und Azimute zu berechnen. Diese werden zur Bewertung der Genauigkeit von in SAR-Bildern gemessenen Ranges und Azimuten verwendet.

Ausgehend von den abgeschätzten Signalen und den Erfahrungen aus den Testmessungen werden unterschiedliche Verfahren für die Erfassung von atmosphärischen und hydrologischen Signalen mit gravimetrischen und geometrischen Messverfahren vorgeschlagen. Dazu werden die jeweilige Messkonfigurationen und die benötigten Instrumente beschrieben.

Table of contents

1 Introduction

1.1 Test site for joint gravimetric and geometric surveys

The shape of the Earth is changing with time. Geophysical fluids (hydrology, oceans, atmosphere) as well as Sun and Moon interact with the solid Earth, leading to geometric and physical changes of the shape. Variations in mass distributions cause variations of gravitational attraction. Because the Earth is not rigid but elastic, these variations in mass load cause deformations and hence both geometric and gravimetric changes. The attraction of Sun and Moon changes directly the gravitational acceleration, but it also leads to deformations, inducing changes in the physical and geometrical shape.
The atmosphere plays also an important role because measurements from satellites, going through the atmosphere, are always influenced by its conditions.

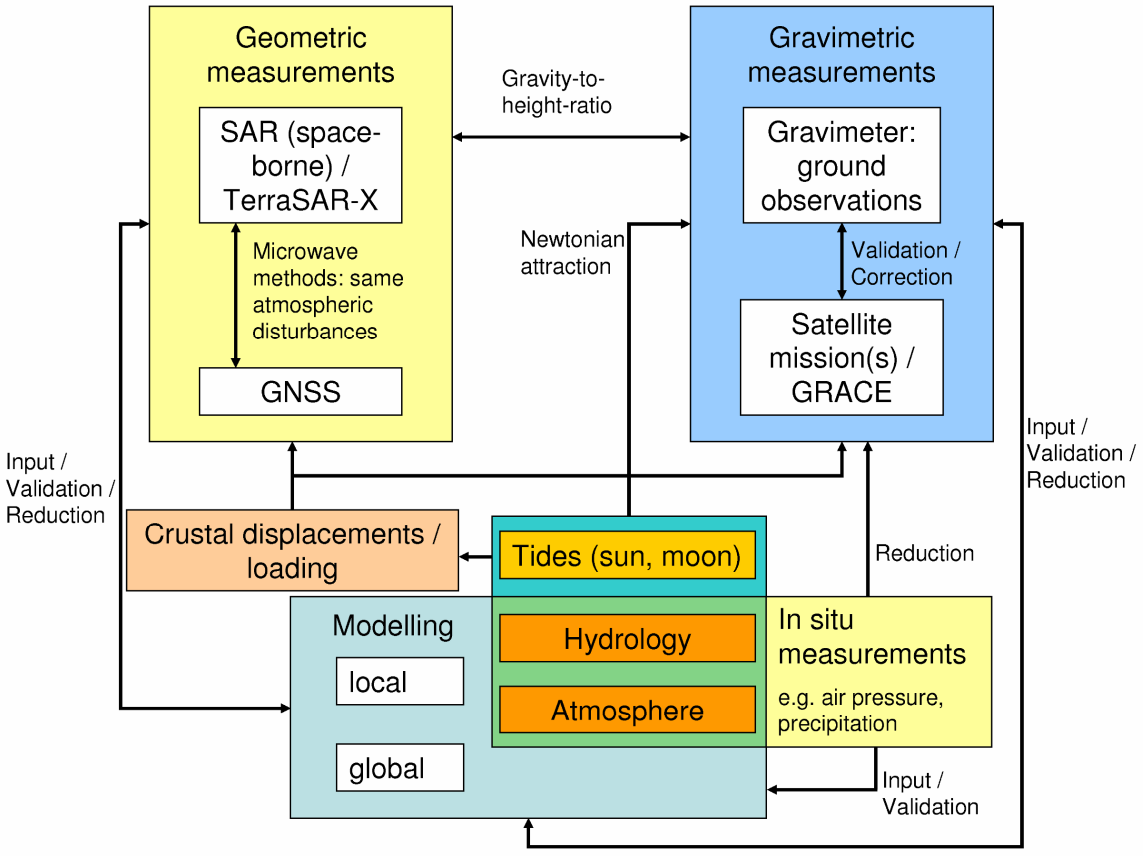

Fig. 1.1: Overview of involved measurement systems and signals and their relations

A lot of different measurement systems and modelling efforts in Earth's science can detect the same geophysical signals or have to cope with the same disturbing effects while observing a certain signal. Thus different techniques can be used to evaluate each other or to provide input data for each other. The relationships between the four blocks geometric measurements, gravimetric measurements, modelling and in situ measurements are depicted in Figure 1.1.

This work shall investigate possible approaches how to consider the interactions shown in Figure 1.1 with jointly surveying in a test site. The following two objectives, encouraging the idea of such a test site, initiated this work:

- The establishment of an interdisciplinary test site for Earth observation called TERENO (= Terrestrial Environmental Observatories) in the Ammer catchment.
- New approaches reaching higher accuracy levels in absolute SAR-ranging.

The motivating character of these two points is explained in the following:

- In case of the TERENO observatory the idea is to use synergy effects because the installation of this test site includes large investments in instrumentation. Furthermore the TERENO project shall initiate further research in different disciplines using the existing infrastructure. An important point, making the TERENO test site attractive for installing also a geodetic test site, is that this test site is designed as a long term project, which guarantees consistent data acquisition over at least the next decade.

Thus, it is desirable to enlarge the measurable quantities with additional (geodetic) instrumentation. This gives the possibility for starting studies on several interdisciplinary research topics based on a broad data basis generated from institutes with their particular expertise.

- Spaceborne SAR ranges become more and more accurate because of increasing quality in orbit determination and the technical feasibilities of TerraSAR-X (TSX) and TanDEM-X (TDX) satellites. The enhancement from 1 m to 1-10 cm level makes Earth tide displacements detectable, and the atmospheric water vapour a non-negligible influence. So it is obvious to look for connections between the related disciplines to correct the measurements of SAR-ranges for these effects.

Based on these considerations the general aim of this work is to show type and magnitude of geometric and gravimetric signals in the TERENO area, to present possible measurement systems which can be combined in a test site, and to develop measurement concepts for integrating the different systems so that they can benefit from each other.

1.2 Benefits

In Section 1.1 it was shown that there is a connection between the four blocks mentioned in the context of Figure 1.1. Now it is outlined why the interdisciplinary consideration and combination of different measurement systems can improve our knowledge of processes in the Earth system.

In Figure 1.1 the gravimetric and geometric measurements are connected by the gravity-to-height ratio. The common observation with gravimetric (e.g. terrestrial gravimetry) and geometric (e.g. GNSS) measurement methods can be used to determine this ratio, which describes the relation between the impacts of both quantities (gravity change and radial height change). A gravimeter senses the direct mass effects and their impacts due to loading, while a geometric measurement system can only detect the latter. The gravimeter is much more sensitive on changes with small wavelength than the geometric measurements. Thus this parameter can provide useful information about the physics of the acting processes and enables separations of various contributions. Simultaneous measurements of gravity variations and surface vertical displacement are often performed in studies dealing with post-glacial rebound, tectonic motions, coseismic deformations, volcanic activity or surface loading processes. [de Linage et al. 2009]
This work is mainly focused on loading effects since the other mentioned processes do not play a considerably role in the chosen test area. Coseismic deformations and volcanic activity can not be found there. The European plate moves with approximately 2 cm per year to the northeast, what can be measured by a global GNSS network, but in a small area like here every point moves, in terms of plate tectonics, in the same direction and with the same velocity.
Post-glacial rebound plays an important role only in areas which are or have been covered by very large ice-shields like Fennoscandia, the Antarctic (Laurentide ice-sheet) or Canada. But since this is a very large-scale process it may have small influences in central Europe. The loading effects of hydrology and atmosphere remain as the major parameters which affect the gravity-to-height ratio in the test area.
An accurate monitoring of geodetic height and gravimetric changes allows the investigation of geophysical processes and the validation and improvement of loading models.
Loading models are needed because the magnitude of the loading effects is so large that it has to be corrected for them in several approaches, for example GNSS positioning for monitoring tectonic movements, gravity measurements for detecting variations caused by vertical crust movement using absolute gravimeters, measurements by superconducting gravimeters or geopotential variation measurements provided by GRACE [Guo et al. 2004].

The modelling of hydrology and atmosphere is presented as the counterpart of the three other measurement blocks in Figure 1.1. The activities around the TERENO test site include intensive activities on hydrological and atmospheric modelling. These models concentrate on the test site and thus can provide a much better spatial resolution than global models like atmosphere models from the European Centre for Medium-Range Weather Forecasts (ECMWF) or the hydrology model WaterGAP Global Hydrology Model (WGHM). Concerning the connections between measurement and models following categories can be distinguished:

- using outputs from the models for the reduction of measurements to look for other signals
- calibration of the models / using measurements as input parameters to drive the model
- validation of model results

Furthermore, results of existing models can be used for estimating expected measurement values, for example to find an adequate location for the installation of an instrument.
If a right place can be found, the instrument can account for enlarging the data basis on a certain topic, for example the hydrology. According to Leirião et al. [2009] "…the characterization and understanding of the hydrological cycle over a range of scales is becoming increasingly important due to the challenges posed by the growth of human water demand and the associated impacts. Global warming and the depletion of water resources require the development of more accurate and powerful monitoring techniques." Gravimetric measurements have a great potential being one of these techniques. For large-scale hydrology most notably the GRACE mission is to be mentioned, for hydrology in small catchments, like here, ground based gravity measurements are the right mean.

For model calibration, one of the points listed above, observed data is required, which is sometimes difficult to obtain due to insufficient ground instrumentation or inappropriate scale of the data collected on the ground. Leirião et al. [2009] also points out the capability of gravity measurements in this context: "Time-lapse gravity monitoring allows calibration of hydrological models using temporal gravity change measurements instead of, or in addition to traditional hydrological data (e.g. groundwater level data, stream discharge data)."

So far the linkage between model and ground measurement has been shown, up next the linkage between ground and satellite measurements shall be described as a further topic showing the possible benefit of the test site. The main objective is the evaluation of satellite gravity missions, especially GRACE. At first glance this is only related to the gravimetric measurements, how it is depicted in the Figure 1.1, but because of the characteristic of the measurement systems more information, especially from hydrological modelling, is required. The necessary tasks are the separation of hydrology from other effects (tides, atmosphere) and the distinction between local and large-scale effects, since

no local gravity effects can be sensed anymore in the height of the GRACE orbit. Additionally the gravity fields are smoothed by filters of several hundred km. A local hydrological model can provide the information for reducing hydrological effects, which can not be resolved by GRACE, so that ground gravity measurement data can be used for evaluation. Thus it will be important to investigate if the local effect can be removed, that a continental scale seasonal signal, which is expected to be seen by GRACE, can appear.

A possible link between SAR and the TERENO activities is the determination of snow cover and soil moisture. If SAR acquisitions are taken in regular intervals, the images can be used as an additional data input. There shall be no investigations on these topics in this work; they are only mentioned for further motivation.

Two further aspects concerning the instrumentation, namely the availability and the complementarity, shall be mentioned.
A lot of studies concerning the investigation of the influence of geophysical processes on geodetic measurements suffer because of the lack of sufficient in situ environmental parameters. This interdisciplinary test site is targeted on the attenuation of this problem (availability). Time dependent displacements of stations usually have magnitudes close to the accuracy of each individual technique and it still remains a challenge to separate the true geophysical motion from possible artefacts inherent to each measurement system. Therefore comparison of different techniques is required to detect any systematic effect induced by an individual technique and extract reliably the true geophysical signal (complementarity). [Nicolas et al. 2006]
This explains why such a multi-parameter test site has a large potential. The differences in the characteristics of the several measurement systems can complement or compensate each other:

- Resolution (temporal and spatial): Different measurement techniques provide data with different temporal and spatial resolutions due to their specific characteristic or configuration. The acquisition of data with high resolution can be restricted by economic reasons, if the benefit of an increased resolution bears no relationship to the additional costs or amount of work.
- Point or spatially information: Ground measurements (GPS, Gravimetry, rain gauge, …) normally provide only measured values for a certain location, satellite data instead delivers information over the whole acquisition area.
  Ground measurements have to be interpolated for reaching a spatial coverage. The more instruments are available (i.e. the denser the network), the better such an interpolation can be carried out.
- Integral effect or only a certain parameter: Some instruments measuring the overall effect of a certain process (gravimeter → mass change) other only a single parameter (e.g. groundwater observation well → groundwater level).

- Disturbing influences: Different measurement systems are influenced by different spurious effects, what can help to correct one quantity by means of another.
- Degree of disturbance on the measured quantity: It is an advantage of the gravimeter that its measurements do not influence the measured quantities in any way (non-invasive, non-desctructive); for example sensors which are implemented in the ground can not be installed without impacts on the soil.

1.3 TERENO (Terrestrial Environmental Observatories)

The TERENO alpine and prealpine Ammer observatory was chosen as the test site for this study. Now the general aim of the TERENO observatories is outlined.
The TERENO concept is based on the cooperation of several research institutes: FZJ (Forschungszentrum Jülich), DLR (Deutsches Zentrum für Luft- und Raumfahrt), KIT (Karlsruher Institut für Technologie), HMGU (Helmholtz-Zentrum München - Deutsches Forschungszentrum für Gesundheit und Umwelt), UFZ (Helmholtz-Zentrum für Umweltforschung) and GFZ (Helmholtz-Zentrum Potsdam - Deutsches GeoForschungs-Zentrum).
The TERENO activities comprise the installation of common measurement platforms for the generation of long-term environmental data and the combination of environmental monitoring and experiments on specific tasks. The main research objective is the investigation of interactions and couplings between atmosphere, hydrosphere, pedosphere (soil) and biosphere. An important task is to overcome the discrepancy between models and measurements. Also space- and airborne techniques shall support the ground measurements.
There are four TERENO observatories in Germany, representing different climate and landscape types, one of them is the TERENO alpine and prealpine Ammer observatory. All test sites are equipped with the same instrumentation for allowing a consistent comparison between the different regions. The observatories are in the beginning of their life-time, not all instrumentation is installed yet. The duration of this project is scheduled for at least 10 years.[1]

Alpine and prealpine Ammer observatory

The area of this observatory includes the entire catchment of the Ammer (cf. Figure 1.2), except from a small part in the north of Weilheim (dashed line in Figure 1.2). It covers an area of around 30 x 50 km^2.

[1] from TERENO Website: https://teodoor.icg.kfa-juelich.de/, last access: 20.10.2010

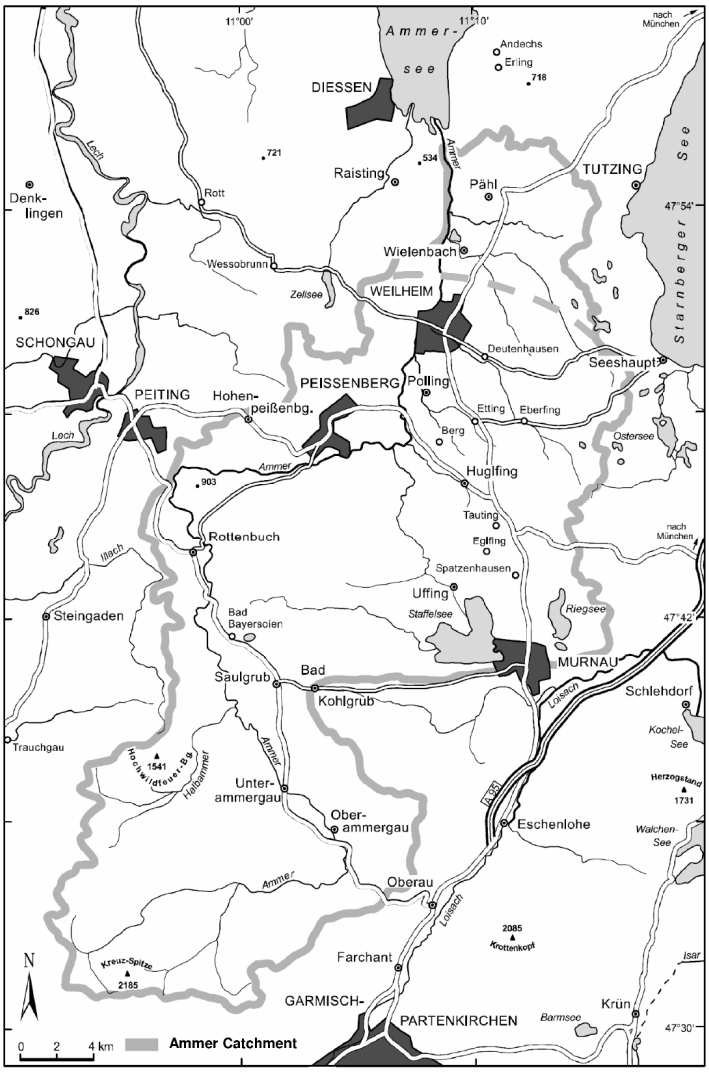

Fig: 1.2: Ammer catchment, from [Ludwig et al. 2003], the dashed line indicates the boundary of the TERENO Alpine and Prealpine Ammer Observatory area

Four main sites exist in this observatory or will soon be installed. On one site an X-Band precipitation radar has been mounted, the other sites have lysimeters and so called EC (eddy covariance) towers which are equipped with several different instruments, for measuring wind, precipitation, pressure, temperature, humidity, soil water content, radiation, surface temperature, snow height and further parameters. These parameters will be recorded in a high temporal resolution and will be made available online. More to the instruments can be found in Chapter 4.

1.4 Structure of the work

Chapter 2 comprises the theoretical description of the influences of solid Earth tides, pole tide, ocean loading, hydrology and atmosphere on the solid Earth. For all of these aspects the gravimetric as well as the geometric signals are delineated and their magnitude compared. Also the influences of the atmosphere on electromagnetic waves are shown. Additionally different routines and programs, which can be used for reducing solid Earth tides, pole tide and ocean loading are tested and compared.
Furthermore some approaches are presented which deal with atmospheric and hydrologic signals.

In Chapter 3 the study area, the Ammer catchment, which was shortly introduced in the previous section, is described in more detail. This comprises investigations which atmospheric and hydrologic signals can be expected and in what range of magnitude. In this context some important terms concerning hydrology are explained and main principles of a hydrological model are described. For hydrology as well as for atmosphere local measurements are compared to large-scale modelling efforts.

In Chapter 4 necessary measurement systems for the establishment of the test site are described. This includes in situ measurement systems for hydrological and meteorological parameters, gravimeter, GNSS (Global Navigation Satellite Systems), GRACE and spaceborne SAR (Synthetic Aperture Radar).

In Chapter 5 three test measurements are described in detail. Two experiments are performed to check the potential of the Scintrex CG-3M gravimeter, which is owned by the IAPG (Institut für Astronomische und Physikalische Geodäsie). In the first test measurement the gravimeter is used for stationary measurements, in the second for a field campaign.
The third experiment is a test campaign where GNSS is used for independent validation of absolute SAR measurements.

In Chapter 6 some measurement campaigns are proposed for detecting atmospheric and hydrological signals. It is shown how one can make benefit from the combination of different measurement systems and modelling approaches. Additionally a possible approach for the improvement of the SAR experiment is outlined.

The conclusions can be found in Chapter 7, which shall induce further actions on this test site, based on the investigations and proposition of this work.

2 Gravimetric and geometric signals

In the following chapter the gravimetric and geometric effects on the solid Earth from solid Earth tides (2.2) and smaller effects (2.3), namely ocean tides (ocean loading), non-tidal ocean loading and polar motion, are delineated. Subsequently, existing models for computing these signals are introduced (2.4). Finally the effects of hydrology and atmosphere are described (2.5).
It has to be distinguished between direct mass effects (Newtonian attraction) and indirect effects due to deformations of the solid Earth, because of its elasticity. The deformations can be induced by Sun and Moon or by changing mass loads and lead to geometric (crustal displacements) and gravimetric signals on the Earth's surface. Generally, gravity ground measurements are more sensitive to short wavelengths than vertical displacements because the Newtonian attraction is mainly affected by mass changes below and above the gravimeter, the indirect (loading) effects instead are mainly influenced by mass effects of large extent.
The elasticity of the Earth is expressed by Love numbers. Loading effects can be calculated using Green's functions, which use these Love numbers. These aspects are explained at the beginning of this chapter (2.1).

The influences of troposphere and ionosphere on satellite measurement are also discussed in the part regarding the atmosphere. This is important especially for microwave systems like GPS and SAR, because troposphere and ionosphere cause delays in the ray paths. It has to be corrected for these delays to detect a signal on the ground correctly.

2.1 Theoretical background of loading effects

The study of the loading effects is considerably more complicated than study of the body tide (= solid Earth tide). The most important difference is the characteristic of the driving forces. While the effects of the body tide can be calculated very accurately from well known ephemerides from Sun and Moon, this is much more complicated for the oceans, the atmosphere or the hydrology. Another reason is that the behaviour of the body tides is mostly dependent on the overall properties of the Earth, whereas the loading effects have a dependency on locally variable properties of crust and mantle. [Farrel 1972]

2.1.1 Elastic Earth and Love numbers

The reaction of an elastic sphere, described with the help of spherical harmonics, is usually discussed in terms of dimensionless Love (and Shida) numbers *h*, *l* and *k* [Farrel 1972]. Because they are used for spherical harmonic developments the numbers are different for each degree *n* (normally a symmetrical Earth model is used, hence they do not depend on the order *m* [de Linage et al. 2009]).

A certain meaning can be allocated to the three types of Love numbers:
- *k* Love numbers: gravitational elastic Love numbers, are related to the effect of mass redistribution
- *h* Love numbers: vertical elastic Love numbers, are related to the vertical displacement (free-air-gradient)
- *l* Love numbers: horizontal elastic Love numbers (also called Shida numbers), are related to the horizontal displacement

Since the body tides depend more on the overall properties of the Earth, as said above, they can be described using only degree 2, and for more accuracy degree 3, Love numbers. For the calculation of loading effects Love numbers up to degree 10 000 are needed.

2.1.2 Green's functions for point surface loads

Green's functions can be used to describe the reaction of the Earth's surface due to loads acting on it. They describe the response of the Earth to a point-source surface load of unit mass that has a delta-function time dependence (= point masses) [Han and Wahr 1995].
The classical approach to describe the deformation of the Earth by surface loads was formulated by Farrel [1972]. The loading masses are represented by point masses on a thin layer.

The Green's functions depend on the spherical distance ψ (solid angle) from the point mass load along a great circle to the point where the respective effect shall be calculated. According to Farrel [1972] the equations are

$$u(\psi) = \frac{a}{M_E} \sum_{n=0}^{\infty} h_n P_n(\cos\psi) \qquad (1)$$

for the vertical displacement,

$$v(\psi) = \frac{a}{M_E} \sum_{n=1}^{\infty} l_n \frac{\partial}{\partial \psi} P_n(\cos\psi) \qquad (2)$$

for the horizontal displacement, and

$$g(\psi) = \frac{g_0}{M_E} \sum_{n=0}^{\infty} \left[n + 2h_n - (n+1) k_n \right] \cdot P_n(\cos\psi) = \frac{g_0}{M_E} \sum_{n=0}^{\infty} \xi_n \cdot n \cdot P_n(\cos\psi) \quad (3)$$

for the gravimetric effect (acceleration is defined positive upwards!), with the loading gravimetric factor of degree *n* [Boy et al. 1998]:

$$\xi_n = 1 + \left(\frac{2h_n}{n} \right) - \left(\frac{n+1}{n} k_n \right) \quad (4)$$

As can be seen, the loading Love numbers h_n, l_n, k_n are needed to formulate the Green's functions. These Love numbers are calculated from a spherically symmetric, non-rotating, elastic and isotropic (SNREI) Earth model, e.g. PREM (Preliminary Earth Model), up to a high degree (around 10 000). The relations between the Earth model and the Love numbers are formulated with differential equations. Boundary conditions should be applied at all internal boundaries of the Earth model and at the surface of the Earth. With solving the differential equations the load numbers can be calculated. For high degrees the Love numbers become constant, i.e. they converge when *n* tends to infinity. [Guo et al. 2004]

The gravimetric Green's function (Equation 3) is composed of a term for the Newtonian attraction and a term for the elastic reaction of the Earth. The term due to the elasticity can be separated from the term due to the direct Newtonian attraction with subtracting the latter one from the complete equation:

$$g^E(\psi) = g(\psi) - g^N(\psi) \quad (5)$$

The term for the Newtonian attraction is [Boy et al. 2002]:

$$g^N(\psi) = \frac{g_0}{M_E} \sum_{n=0}^{\infty} n \cdot P_n(\cos\psi) = \frac{g_0}{M_E} \left[2\pi a^2 \delta(\psi) - \frac{1}{4\sin(\psi/2)} \right] \quad (6)$$

The term $2\pi a^2 \delta(\psi)$, where $\delta(\psi)$ is the delta function, can not be found in Farrell's definition (and thus has not to be subtracted). This term accounts for a mass directly above or below (with opposite sign) the observation point, in this case formulated as a Bouguer plate. This was not needed for the calculation of ocean loading, what Farell's aim was, but for atmospheric loading. [Spratt 1982], [Boy et al. 2002]

The term for the elastic part of the gravimetric loading effect is then:

$$g^E(\psi) = \frac{g_0}{M_E} \sum_{n=0}^{\infty} \left[2h_n - (n+1) k_n \right] \cdot P_n(\cos\psi) \quad (7)$$

g_0 mean surface gravity
M_E mass of the Earth
a semi-major axis of the Earth
P_n Legendre Polynom of degree *n*

The change of the observables *u*, *v*, *g* can be obtained by convolving the Green's functions with a global mass-field. How such a convolving integral looks can be found in the following example for atmosphere data.

Convolving Green's functions with an atmospheric pressure field

This section shows how it looks to convolve a mass field with Green's functions. This is done for an atmospheric pressure field as it is done in Boy et al. [2002] and Petrov and Boy [2004].
For a thin layer model the surface pressure P is linked to the surface density σ_A as follows [Boy et al. 2002]:

$$P(\theta_{load}, \lambda_{load}, t) = \sigma_A(\theta_{load}, \lambda_{load}, t) \cdot g_0 \qquad (8)$$

If a pressure field is used the Green's functions have to be divided by g_0, what leads to following convolving integral for the gravity change:

$$\Delta g(\theta, \lambda, t) = \iint_{surface} \frac{g(\psi)}{g_0} \Delta P(\theta_{load}, \lambda_{load}, t) \cdot ds \qquad (9)$$

$$\text{with} \quad ds = a^2 \sin\theta_{load}\, d\lambda_{load}\, d\theta_{load}$$

For the vertical or the horizontal displacement the Green's functions have only to be replaced by the respective term. For the horizontal term a unit vector q originating from the station, tangential to the Earth's surface, which lies in the plane determined by the radius vectors to the station and to the pressure source (in other words it shows the direction from the station to the load), has to be added [Petrov and Boy 2004]:

$$\Delta u(\theta, \lambda, t) = \iint_{surface} \frac{u(\psi)}{g_0} \Delta P(\theta_{load}, \lambda_{load}, t) \cdot ds \qquad (10)$$

$$\Delta v(\theta, \lambda, t) = \iint_{surface} q(\theta_{load}, \lambda_{load}, \theta, \lambda) \frac{-v(\psi)}{g_0} \Delta P(\theta_{load}, \lambda_{load}, t) \cdot ds \qquad (11)$$

θ_{load}, λ_{load} colatitude and longitude of the loading mass
θ, λ colatitude and longitude of the calculation point
The solid angle ψ is defined as follows [Boy et al. 2002]:

$$\cos\psi = \cos\theta \cos\theta_{load} + \sin\theta \sin\theta_{load} \cos(\lambda - \lambda_{load}) \qquad (12)$$

An algorithm to solve these integrals can be found in Petrov and Boy [2004]. The Earth's deformation of degree 0 has not to be taken in account, if the mean pressure field is subtracted from the surface pressure data [Boy et al. 2002].

Additional remarks

The approach using a thin layer as an approximation is used for ocean loading models, e.g. Farrel [1972]. A modification, where the loading is formulated accounting for the layer thickness is used for atmospheric loading, e.g. Guo et al. [2004], Merriam [1992]. Other approaches, e.g. Spratt [1982] and Boy et al. [1998], use also the thin layer model for atmospheric loading.

Farrel's Green's functions can also be used to calculate the loading effects due to continental water [van Dam et al. 2001]. In case of gravity there is the difference, compared to the atmospheric loading, that the masses are assumed to be below the gravimeter, what leads to a different sign in Equation 6.

For all loading signals, the effects in the horizontal are approximately one-third the amplitude of those in the vertical. [van Dam et al. 2003]

Calculating the loading effect with mass-field in a harmonic expansion

In the example above the mass-field (pressure-field) was given as a global distribution of pressure values in the time domain. Another possibility, described by deLinage et al. [2009] and deLinage et al. [2006], is the expression of the mass-field in a harmonic expansion. This means the field is given in the frequency domain.
Then the variation T of a geodetic observable at the location (θ, λ) induced by a variation of a 2D mass distribution $\sigma(\theta, \lambda)$ at the Earth's surface can be written as:

$$\begin{aligned} T(\theta,\lambda) &= \sum_{n=0}^{\infty} \tau_n \sum_{m=0}^{n} P_n^m(\cos\theta)\left(\sigma_n^{m,c}\cos(m\lambda) + \sigma_n^{m,s}\sin(m\lambda)\right) \\ &= \sum_{n=0}^{\infty} \tau_n \sum_{m=-n}^{n} \sigma_n^m Y_n^m(\theta,\lambda) = \sum_{n=0}^{\infty} \tau_n \sigma_n(\theta,\lambda) \end{aligned} \qquad (13)$$

T can be gravity variation (Δg), vertical (Δu) or horizontal (Δv) displacement. τ_n is the transfer function of degree n for the observable T.
$\sigma_n(\theta, \lambda)$ is the load distribution on the Earth's surface, expanded into a series of spherical harmonics, expressed as mass unit per unit area (surface density), e.g. [kg/m^2].
The transfer function τ does not depend on the order m, because a spherical symmetrical model for the Earth is used. The transfer function can be obtained by dividing the degree n term of the corresponding Green's function by σ_n [de Linage et al. 2009]:

$$\sigma_n = \frac{2n+1}{4\pi a^2} \qquad (14)$$

This term represents a point-mass located at the pole of a sphere with radius a, what corresponds to a delta function.

The transfer function for the vertical displacement is:

$$u_n = \frac{3}{\bar{\rho}_E}\frac{1}{2n+1}h_n \qquad (15)$$

For the gravity terms now holds, in contrast to Equations 3, 6 and 7, that acceleration is positive downwards!
The transfer function for elastic term of the gravity variation is:

$$g_n^E = -\frac{3g_0}{a\bar{\rho}_E}\frac{2h_n-(n+1)k_n}{2n+1} \qquad (16)$$

The transfer function for the Newtonian attraction of the mass loads is:

$$g_n^N = -\frac{3g_0}{a\bar{\rho}_E}\frac{n}{2n+1} \qquad (17)$$

if the local masses are above the measurement point, and

$$g_n^N = \frac{3g_0}{a\bar{\rho}_E}\frac{n+1}{2n+1} \qquad (18)$$

if the local masses are below the measurement point.

$\bar{\rho}_E$ mean density of the Earth

For Love numbers calculated from a realistic Earth model, it can be seen (Figure 2.1), that g^E is most sensitive to the lowest degrees and becomes insignificant as n tends to infinity.

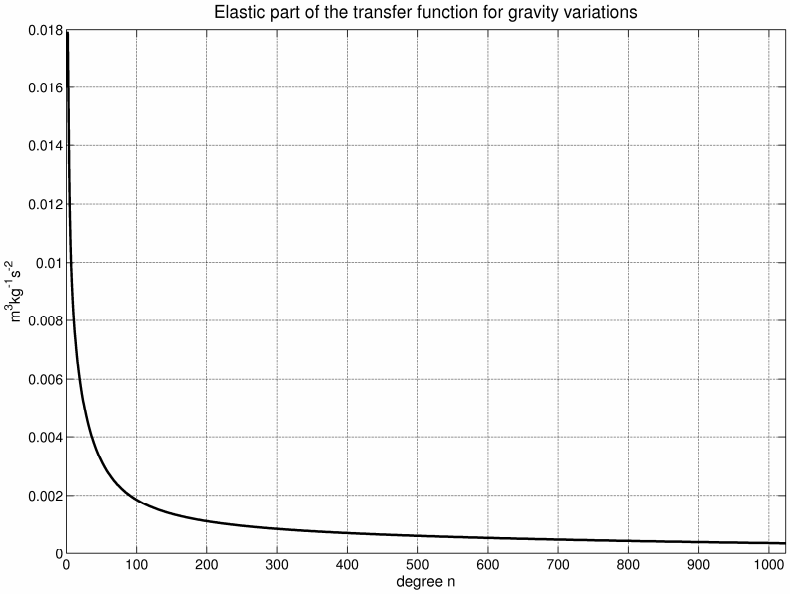

Fig. 2.1: Elastic part (g^E) of the transfer function for gravity variations

That means that the elastic term is mainly sensitive on mass signals with long wavelengths, and thus negligible for very local loads. The same holds for the displacement terms. This

seems to be clear as a small load at a certain place can not deform the Earth, but loads acting on the Earth over a large area have the power to change the Earth's shape.
The term for direct Newtonian attraction becomes -2πG (mass above) and 2πG (mass below), respectively, when *n* tends to infinity, corresponding to the gravity effect of a Bouguer plate.
The load Love numbers used for the computation in Figure 2.1 are in the coordinate system with the centre of mass of the total Earth (Earth and Atmosphere) and gained from the atmospheric pressure loading service[2].

2.1.3 Gravity-to-height ratio

Now theoretical values for the gravity-to-height ratio shall be derived from the transfer functions shown above. If the ratio is calculated for both gravimetric parts (elastic and Newtonian) and masses below the gravimeter, the ratio

$$\frac{\left(g_n^E + g_n^N\right)}{u_n} = -\frac{g_0}{a}\left(2 - \frac{(n+1)(k_n+1)}{h_n}\right) \qquad (19)$$

is dominated by the Newtonian effect (as can be seen in Figure 2.2), especially for higher degrees, since the vertical displacement tends to zero for very local loads. Because of this it is also interesting to look at the ratio, which is only calculated with the elastic part of the gravity effect, since the geometric vertical displacements are induced by the loading effect, which is not related to the direct (local) attraction.
The elastic term of the gravity effect is composed of two components. The first component is the gradient for vertical displacement in the unperturbed gravity field, the effect of free air motion. Divided by the vertical displacement one get the "classical" free-air gradient, which accounts for the vertical movement but not for the mass movements due to the deformations [de Linage 2009]:

$$\frac{g_n^{E,\,free-air}}{u_n} = -\frac{2g_0}{a} = -0.3076\ \mu\text{Gal/mm} \qquad (20)$$

with $g_0 = 9.81\ \text{m/s}^2$ and $a = 6378\ \text{km}$

If the second term, which accounts for the effects due to the mass redistributions, is added one gets the following equation for the elastic gravity-to-height ratio [de Linage 2006]:

$$\frac{g_n^E}{u_n} = -\frac{g_0}{a}\frac{2h_n - (n+1)k_n}{h_n} = -\frac{2g_0}{a} + \frac{g_0}{a}\frac{(n+1)k_n}{h_n} \qquad (21)$$

De Linage [2009] also calculated a ratio with an additional global Newtonian attraction term, for which the attraction at the observation point is zero, i.e. this case is valid for a station outside the loaded area:

[2] http://gemini.gsfc.nasa.gov/aplo/Load_Love2_CM.dat; last access: 20.10.2010

$$\frac{g_n^{N,global} + g_n^E}{u_n} = \frac{g_0}{a}\left(\frac{1}{2h_n} - 2 + \frac{(n+1)k_n}{h_n}\right) \qquad (22)$$

This corresponds for example to the ocean loading case or an ice cap change, where no masses are below or above the station. For that case a representative value for the ratio, irrespective of its spectrum, is the mean value for degree 1 to 50 with -0.26 µGal/mm. The average value of the elastic ratio is -0.22 µGal/mm. These values are representative, since the values converge for high degrees. This is not the case for the total ratio, which is dominated by the local Newtonian effect (see Figure 2.2).

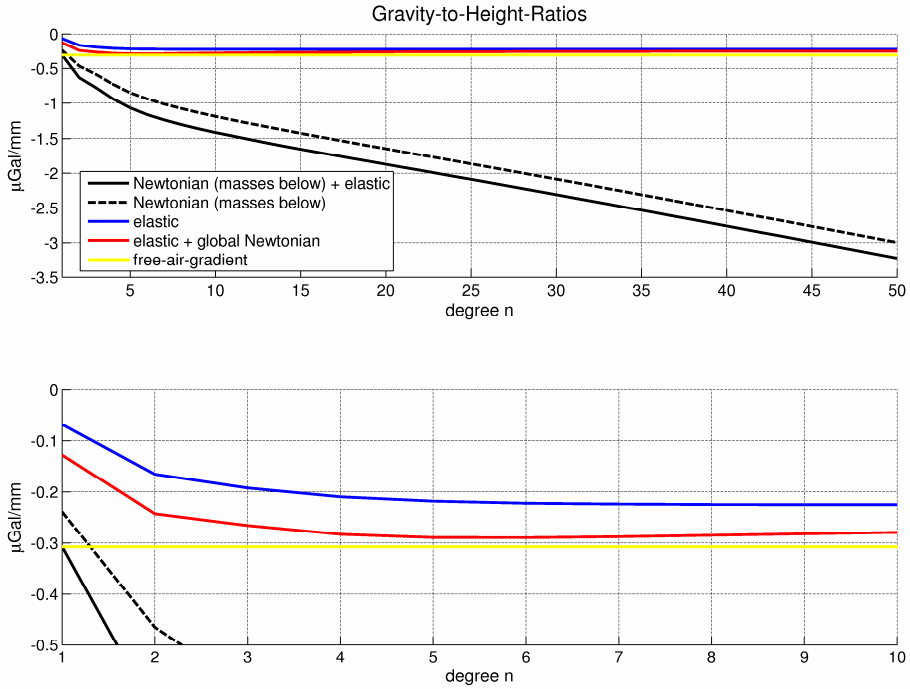

Fig. 2.2: Comparison of different gravity-to-height ratios for degree 1-50 (above) and 1-10 (below)

For analysis, the theoretical values can be compared either with model derived ratios or with measured values. Therefore it has to be considered carefully how the attraction of local masses is handled. To convert measured vertical displacements to gravity changes, which shall only represent the loading effect, only lower degrees of the theoretical gravity-to-height ratio may be considered, since mass variations with extents of a few [m] to [km] (for example a local water level) do not contribute to the loading effect.
If a gravity-to-height ratio is measured the ratio reflects how strong local gravity variations are influenced by local mass variations, since the modulus of the ratio becomes much larger when there are large local gravity variations above or below the instrument.

2.1.4 Connections between mass fields and gravity coefficients

In the following equations are given which relate changes of a mass field, expressed in surface density, to changes of the gravity field, expressed in spherical harmonics. The mass field can also be regarded as equivalent water heights (EWH) or surface pressure. The relation between these quantities is shown first.

Conversions surface density - EWH - pressure

- The relation between surface density and pressure was already used in Equation 8:

$P = \sigma_A \cdot g$ (23)

- The relation between pressure and equivalent water height is as follows:

$P = (Volume/Area) \cdot \rho \cdot g$ (24)

$P = EWH \cdot \rho_w \cdot g$ (25)

$\Rightarrow$ 1 cm EWH complies approximately with 1 mbar

- For conversion from surface density change $\Delta\sigma_A$ to EWH the following equation holds:

$$EWH = \frac{\Delta\sigma_A(\theta,\lambda)}{10} \text{ [cm]} \qquad (26)$$

1 cm water/m^2 = 10 kg/m^2 $\approx$ 10 l/m^2

P pressure [Pa = kg s^{-2}m^{-1}]

ρ density of the mass [kg/m^3]; for computations with EWH, the density of water ($\approx$ 1000 kg/m^3) has to be used

g gravity ($\approx$ 9.81 m/s^2)

σ_A surface density [kg/m^2]

Conversion gravity field variations $\rightarrow$ mass distribution

Gravity changes, e.g. derived with GRACE, can be transferred to surface density. The calculation of the global mass distribution out of gravity field changes (expressed in ΔC_{nm} and ΔS_{nm}) using the assumption, that density changes are limited to a thin layer on the Earth's surface, is [Wahr et al. 1998]:

$$\Delta\sigma_A(\theta,\lambda) = \frac{R \cdot \bar{\rho}_E}{3} \sum_{n=0}^{\infty} \sum_{m=0}^{n} \left[\frac{2n+1}{1+k_n} \right] \cdot \bar{P}_{nm}(\cos\theta) \left[\Delta\bar{C}_{nm} \cos(m\lambda) + \Delta\bar{S}_{nm} \sin(m\lambda) \right] \qquad (27)$$

This equation comprises the effect of the direct mass attraction and the indirect loading effect, since the term $1+k_n$ accounts for the direct attraction (1) and the deformation (mass redistribution) of the underlying Earth (k_n).

To get surface pressure instead of mass density Equation 27 has to be multiplied with the factor g_0 (cf. Equation 23).

$\Delta\bar{C}_{nm}\ \Delta\bar{S}_{nm}$ normalized spherical harmonic coefficients
$\bar{\rho}_E = 5517\ kg/m^3$ constant mean density of the Earth
k_n loading Love number
R mean Earth's radius
$\bar{P}_{nm}$ normalized Legendre function
θ , λ colatitude and latitude
$\Delta\sigma_A$ surface density change or mass density change [kg/m^2]

Since the geometric height change due to loading is dependent on the surface density change also vertical displacements can be derived from gravity field changes (ΔC_{nm} and ΔS_{nm} have to be used in such way, that they represent surface mass). A equation for this can be found in Tesmer et al. [2010]:

$$\Delta h(\lambda,\varphi) = R\sum_{n=1}^{N}\frac{h_n^{'}}{1+k_n^{'}}\sum_{m=0}^{n}\bar{P}_{nm}(\sin\varphi)\left[\Delta\bar{C}_{nm}\cos(m\lambda)+\Delta\bar{S}_{nm}\sin(m\lambda)\right] \qquad (28)$$

Conversion mass distribution → gravity field variations

The following equations show how gravity field changes can be computed out of surface density change or surface pressure. They also regard direct and loading effects of the masses.
The equation for using surface pressure is [Gruber et al. 2008]:

$$C_{nm} = \frac{a^2(1+k_n)}{(2n+1)Mg_0}\iint_{Earth}\left(P_S-\tilde{P}_S\right)\bar{P}_{nm}(\cos\theta)\cos(m\lambda)dS \qquad (29)$$

$$S_{nm} = \frac{a^2(1+k_n)}{(2n+1)Mg_0}\iint_{Earth}\left(P_S-\tilde{P}_S\right)\bar{P}_{nm}(\cos\theta)\sin(m\lambda)dS \qquad (30)$$

P_S surface pressure
$\tilde{P}_S$ mean surface pressure
a semi-major axis of the reference ellipsoid
dS surface element $\sin\theta d\lambda d\theta$

To get the equation for the surface density, the factor g_0 has to be removed and $\left(P_S-\tilde{P}_S\right)$ has to be replaced by $\Delta\sigma_A$.

2.2 Solid Earth tides

The solid Earth tides are responsible for the largest gravity variations and for the largest deformations the Earth's surface experiences.
For tides generally only the effects of Moon and Sun are considered, the contribution of the planets is negligible. The Moon is responsible for around 2/3 and the Sun for 1/3 of the total effect. There are different so called tidal waves with different periods, which are composed to describe the solid Earth tide signal. The most important waves have ter-diurnal, semi-diurnal, diurnal, semi-monthly, monthly and semi-annual periods. Additionally there are stationary tides, which lead to a permanent gravity change and deformation of the Earth.
For the calculation of solid Earth tides the ephemeris of Sun and Moon are needed. Because they are very well known the theoretical tides for a rigid Earth can be determined very precisely.

2.2.1 Gravimetric effect

The theoretical radial tidal acceleration da_z for a development of the tidal potential with degree two is [Rummel 2007]:

$$da_z = \frac{3}{2} GM_{M,S} \frac{r_P}{r^3_{M,S}} \left[3\left(\sin^2 \varphi_P - \frac{1}{3} \right)\left(\sin^2 \delta_{M,S} - \frac{1}{3} \right) + \right. \\ \left. + \sin 2\varphi_P \sin 2\delta_{M,S} \cos \tau_{M,S} + \cos^2 \varphi_P \cos^2 \delta_{M,S} \cos 2\tau_{M,S} \right] \qquad (31)$$

G gravitational constant
φ_P latitude of the observed point
$\delta_{M,S}$ declination of Moon (M) or Sun (S)
$\tau_{M,S}$ hour angle of Moon (M) or Sun (S)
$r_{M,S}$ distance from mass centre of the Earth to Moon (M) or Sun (S)
r_P distance from mass centre of the Earth to the observed point

As can be seen in Equation 31 the tidal effect is latitude (because of φ and δ) and height (because of r) dependent. The dependence on the longitude, i.e. the time, is included in the hour angle τ.
The term $\left(1/3 - \sin^2 \varphi_P\right)$ is responsible for the stationary (permanent) tides. They cause a permanent decrease of the equatorial gravity by -0.30 μm/s^2 = -30 μGal and an increase of the polar gravity by 0.61 μm/s^2 = 61 μGal. The handling of the permanent tides related to reference frames is outlined in Section 2.2.3.

The tidal variations reach following maximum effect (peak-to-peak) for Sun and Moon:
Moon: 1.65 μm/s^2 = 165 μGal
Sun: 0.76 μm/s^2 = 76 μGal
(Planets: less than 0.1 nm/s^2 = 0.001 μGal)
→ Sum: 2.41 μm/s^2 = 241 μGal
The variations due to higher degrees than two are small. The largest of them, the lunar harmonic term of third degree, reaches 27 nm/s^2 = 2.7 μGal. [Torge 1989]
"The ephemeris of Sun and Moon can be formulated as harmonic functions which depend on five astronomical fundamental quantities, so that a corresponding harmonic expansion can also be performed for the tides. The tidal acceleration follows as the sum of time-dependent cosine functions of constant frequency and amplitudes as well as computable phases (partial tides)." [Torge 1989].
For highest accuracy there are developments up to degree four and several hundred to thousand partial tides. The main principal tidal waves are listed in Table 2.1. The tidal wave with the greatest amplitude is the M2 lunar wave with an amplitude of 751.2 nm/s^2 at the equator and a period of 12.42 h.

symbol	**name**	**period (solar hours)**	**amplitude (φ = 45°, h = 0) [nms^{-2}]**
long-periodic-waves			
M0	constant *l* tide	-	102.9
S0	constant *s* tide	-	47.7
Ssa	declination tide to S0	182.62 d	14.8
Mm	elliptical tide to M0	27.55 d	16.8
Mf	declination tide to M0	13.66 d	31.9
diurnal-waves			
O1	main diurnal *l* tide	25.82 d	310.6
P1	main diurnal *s* tide	24.07 d	144.6
Q1	elliptical tide to O1	26.87 d	59.5
K1	main diurnal *ls* declination tide	23.93 d	436.9
semi-diurnal-waves			
M2	main *l* tide	12.42 d	375.6
S2	main *s* tide	12.00 d	174.8
N2	elliptical tide toM2	12.66 d	71.9
K2	declination tide to M2, S2	11.97 d	47.5
ter-diurnal-waves			
M3	terdiurnal *l* tide	8.28 d	5.2

Table 2.1: Principle tidal waves (*l* = lunar, *s* = solar), from [Torge 1989]

The astronomical fundamental quantities are [Tamura 1987]:

1: τ time angle in lunar days
2: s Moon's mean longitude
3: h Suns's mean longitude
4: p longitude of Moon's mean perigee
5: N′ negative longitude of Moon's mean node
6: p′ longitude of Sun's mean perigee

Above only five quantities are mentioned. This is because τ can be expressed by s and h, if aberration and the difference between dynamical and universal time are ignored.

The theoretical tides are valid for a rigid Earth, but this is not the case. Because of the elasticity of the Earth, the attraction of Sun and Moon also leads to a displacement of the Earth's surface, what changes the potential at the surface. Additionally the mass shift induced by the tides evokes an additional deformation potential, which is proportional to the tidal potential.

The reaction of a symmetric, not-rotating, oceanless Earth for a tidal development of degree two can be determined as follows [Torge 2003], [Rummel 2007]:

The tidal induced vertical displacement Δr_{el} of the Earth's surface is:

$$\Delta r_{el} = h \cdot \Delta r_t \qquad (32)$$

Δr_t is the shift of the equipotential surface:

$$\Delta r_t = \frac{V_t}{g} \qquad (33)$$

V_t is the tidal potential for the rigid Earth.

The additional deformation potential V_d is:

$$V_d = k \cdot V_t \qquad (34)$$

The gravity potential on the Earth's surface due to the tides is changed by three different parts, the potential of the direct attraction, the deformation potential and the change because of the vertical displacement:

$$V_{el} = V_t + V_d - g \cdot \Delta r_{el} = V_t \cdot (1 + k - h) \qquad (35)$$

Using a second degree development the tidal acceleration can be calculated as follows:

$$\begin{aligned} da_{z,el} &= da_z + \frac{\partial V_d}{\partial r} + \frac{\partial}{\partial r}\left(-g \cdot \Delta r_{el}\right) \\ &= \frac{2dV_t}{r} - \frac{3k}{r} dV_t + h\frac{2g}{r}\frac{dV_t}{g} \\ &= \left(1 + h - \frac{3}{2}k\right) da_z \end{aligned} \qquad (36)$$

with $\xi = \left(1 + h - \frac{3}{2}k\right) da_z$

The Love numbers of the second degree of the tidal potential are [Torge 2003]:
$h = 0.6$, $l = 0.08$, $k = 0.30$
ξ is the so called gravimetric (amplitude) factor. If the Love numbers above are used this factor is 1.15. This means as a global average the amplitudes of the tides of the rigid Earth are increased by approximately 15 %. Using this value the maximum variation due to solid Earth tides becomes 280 μGal.

For higher accuracy, describing in a better way the properties of the elastic Earth, Love numbers of higher degrees and the introduction of frequency dependent Love numbers are necessary (see also below).

2.2.2 Geometric effect

The deformations induced by the attraction of Sun and Moon change the position of a station on the Earth's surface.
The displacement due to the tidal effects can reach 30 cm in the radial and 5 cm in the horizontal direction. For 5 mm level of precision only the displacement due to degree 2 tides and a height correction term are necessary [Kouba 2009]:

$$\Delta\vec{r} = \sum_{j=2}^{3} \frac{GM_j R_E^4}{GM_E R_j^3}\left[h_2\hat{r}\left(\frac{3}{2}\left(\hat{R}_j\cdot\hat{r}\right)^2 - \frac{1}{2}\right) + 3l_2\left(\hat{R}_j\cdot\hat{r}\right)\left(\hat{R}_j - \left(\hat{R}_j\cdot\hat{r}\right)\hat{r}\right)\right] + \left[-0.025\ \mathrm{m}\cdot\sin\varphi\cdot\cos\varphi\cdot\sin(\bar{\Theta}_0 + \lambda)\right]\hat{r} \qquad (37)$$

In case of greater accuracy requirements not only the degree 2 tides of Sun and Moon (Equation 38) but also the degree 3 tides of the Moon (Equation 39) have to be considered as described in IERS Conventions 2003 [McCarthy and Petit 2004]. The nominal Love (h_2 and h_3) and Shida (l_2 and l_3) numbers (see Equation 40) are used.

$$\Delta\vec{r} = \sum_{j=2}^{3} \frac{GM_j R_E^4}{GM_E R_j^3}\left[h_2\hat{r}\left(\frac{3}{2}\left(\hat{R}_j\cdot\hat{r}\right)^2 - \frac{1}{2}\right) + 3l_2\left(\hat{R}_j\cdot\hat{r}\right)\left(\hat{R}_j - \left(\hat{R}_j\cdot\hat{r}\right)\hat{r}\right)\right] \qquad (38)$$

$$\Delta\vec{r} = \frac{GM_2 R_E^5}{GM_E R_2^4}\left[h_3\hat{r}\left(\frac{5}{2}\left(\hat{R}_j\cdot\hat{r}\right)^3 - \frac{3}{2}\left(\hat{R}_j\cdot\hat{r}\right)\right) + l_3\left(\frac{15}{2}\left(\hat{R}_j\cdot\hat{r}\right)^2 - \frac{3}{2}\right)\left(\hat{R}_j - \left(\hat{R}_j\cdot\hat{r}\right)\hat{r}\right)\right] \qquad (39)$$

$j = 2$	Moon
$j = 3$	Sun
$\hat{R}_j, R_j$	unit vector from the geocenter to Moon / Sun and its magnitude
R_E	Earth's equatorial radius
$\hat{r}, r$	unit vector from the geocenter to the station and its magnitude
φ , λ	latitude, longitude
$\bar{\Theta}_0$	Greenwich Mean Sideral Time

The nominal degree 2 (latitude dependent) and degree 3 Love and Shida numbers are [McCarthy and Petit 2004]:

$$\begin{aligned} h_2 &= 0.6078 - 0.0006\left[\frac{3\sin^2\varphi - 1}{2}\right] \\ l_2 &= 0.0847 + 0.0002\left[\frac{3\sin^2\varphi - 1}{2}\right] \\ h_3 &= 0.292 \\ l_3 &= 0.015 \end{aligned} \qquad (40)$$

For high accuracy requirements it has to be regarded, that Love and Shida numbers are latitude and frequency dependent and that the Earth does not react fully elastically (small delay of the deformation with respect to the generating potential) [Rothacher 2007] .
Thus site displacements caused by tides of spherical harmonic degree *n* and order *m* are characterized by the Love h_{nm} and Shida l_{nm} numbers, which effective values depend on station latitude and tidal frequency. The latitude-dependence is caused by the Earth's ellipticity and the Coriolis force. A frequency-dependence within the diurnal band is produced by the Nearly Diurnal Free Wobble resonance associated with the Free Core Nutation. A further frequency-dependence, mainly in the long-period tidal band, arises from mantle anelasticity. [McCarthy and Petit 2004]
This leads to further correction terms, which have to be added to the degree 2 and 3 terms (Equation 38 and 39), for the following effects [McCarthy and Petit 2004]:

- influence of the $l^{(1)}$ term (only for transverse displacement)
- out of phase contributions from the imaginary parts of $h_{2m}^{(0)}$ and $l_{2m}^{(0)}$ (radial and transverse displacement)
- correction for frequency dependence of the Love and Shida numbers

These calculations are implemented in the program *solid.exe* (cf. Section 2.4) and in *dehanttideinel.f* which is provided in the internet[3].

2.2.3 Handling of the permanent tides

As the definition of the reference geopotential or reference system is important for the right appliance of the correction terms for the solid Earth tides, the handling of the permanent or stationary tides is described here. The permanent tides lead to a persistent, time independent change of geopotential and positions of points on the crust. It is distinguished between geopotential (gravimetric) and crust (geometric). The following definitions are a summary of the statements from Chapter 1 of the IERS Conventions 2003 [McCarthy and Petit 2004].

[3] ftp://tai.bipm.org/iers/convupdt/chapter7/; last access 22.10.10

Gravimetric

If all time dependent (periodic) parts of the tidal effects are removed, one gets the **"mean tide" potential**. The direct effect of the permanent tides and the deformations, which are originated from them, are included in the mean geopotential. When gravity field quantities are observed, the mean tide system is implicitely adopted.
If the external potential (= direct permanent tidal effect) is removed, one gets the geopotential of the deformed Earth, the **"zero tide" geopotential**. Thus the direct influence of Sun and Moon is removed, but not the potential which is induced by them in form of the permanent deformation. If the latter is also removed, the result is the **"tide free" geopotential**. This represents a system without presence of Sun and Moon.
Because the perturbing objects are always present, a "tide free" quantity is unobservable. Thus the permanent tides can only be removed via models.

Geometric

The geometric position of a station is influenced because the change of geopotential implicates a deformation and so (mainly) a change of station height.
If all time dependent (periodic) parts of the tidal effects are removed, one gets the **"mean tide" crust** or **"mean" crust**. Hence the permanent part of the deformation produced by the tidal potential is present in the mean crust
If the deformation due to the permanent tides is removed from the "mean tide" crust, the result is the **"tide free" crust**.
Thus, as it regards the crust, the term "zero tide" is equal to the term "mean tide". This is because there is no direct change of the station height due to the pure existent of Sun and Moon, but only due to the indirect deformation effect.

Geometric correction term for permanent deformation
("conventional tide free" crust → "mean tide" crust), from [McCarthy and Petit 2004]

- radial component (positive upwards):

$$\left[-0.1206 + 0.0001 \cdot P_2(\sin\varphi)\right] \cdot P_2(\sin\varphi)\ [m] \qquad (41)$$

(≈ -12cm at the poles and +6cm at the equator)

- transverse component (northwards):

$$\left[-0.0252 - 0.0001 \cdot P_2(\sin\varphi)\right] \cdot \sin(2\varphi)\ [m] \qquad (42)$$

with $P_2(\sin\varphi) = \left(3(\sin\varphi)^2 - 1\right)/2$

φ latitude

Definition for reference geopotential and reference system

The reference geopotential (e.g. EGM 96) and the International Terrestrial Reference Frame (ITRF) are obtained by removal of all tidal contributions with models, which use the nominal Love numbers, and so they are **"conventional tide free"**. The term "conventional" is added because the deformational response is actually characterized by the secular (or fluid limit) Love numbers and so the "conventional tide free", which is used for the reference quantities, differs from the true "tide free".

2.2.4 ITRF and regularized positions

The International Terrestrial Reference Frame (ITRF) is the realisation of the International Terrestrial Reference System (ITRS) (cf. Section 5.2.2). Since the beginning all stations use a conventional tide-free correction, so the ITRF is a "conventional tide free" frame. It is specified by Cartesian equatorial coordinates.
In terms of geometric measurement a coordinate is defined as regularized position if it is present in the ITRF. The regularized position of a station are related to their instantaneous position by the corrections for stations displacements, described in Chapter 7 of the IERS Conventions 2003 [McCarthy and Petit 2004]. These corrections include the solid Earth tides as described in Section 2.2.2 and the effects described in the following Section 2.3.
Because of the appliance of these corrections the regularized position is free from high-frequency time variations, so that only a linear motion of the station remains, mainly due to tectonic plate motion. Thus the station position is still time dependent ($\Rightarrow$ station velocity).

2.3 Other effects

Beside the large effect of the solid Earth tides there are some other, smaller effects which affect measurements on the Earth's surface directly or indirectly.

2.3.1 Ocean tides

Up to now it was only talked about the solid Earth tides, for the calculation of the ocean tides there are special models.
The calculation of ocean tide models is based on tide gauge measurements, satellite altimetry and analysis of satellite orbits. The models account for water depth. Some of the

models, one can access at the ocean loading provider[4] (cf. Section 2.3.2) are introduced below:
The Schwiderski model from 1980 has been the standard for many years. It is a hydrodynamic model, given on a 1 by 1 degree grid, and uses an interpolation scheme to fit the tide gauges. The tidal waves M2, S2, K2, N2, O1, P1, K1, Q1, Mf, Mm and Ssa are included.
FES2004 is a further development in the FES series. FES2004 has a 0.125 degree resolution. It assimilates TOPEX/POSEIDON altimetry into a hydrodynamic tide model. In FES2004 solutions the following tidal waves are included[5]: M2, S2, K2, N2, 2N2, O1, P1, K1, Q1, Mf, Mtm, Mm, Msqm and M4.
EOT08a is based on harmonic analysis of multi-mission altimetry (TOPEX, Jason-1, ERS1, ERS2, ENVISAT, GEOSAT Follow-On) which implies a 13 year time base. The tides are represented on a 0.125 degree grid. EOT08a consists of M2, S2, N2, K2, 2N2, K1, O1, P1, Q1 and M4 tidal constituents [Savcenko and Bosch 2008].

For measurements on land the ocean tides have a direct attraction effect on the gravimetric measurements, but only near to the coast. The changing load of the oceans, instead, can lead to observable height changes also far away from the shore.

2.3.2 (Tidal) ocean loading

The direct effect of the ocean tide does not play a role for the observations considered in this work, since the test site is far away from the coast, but the indirect effect, the ocean loading, has a clear influence on gravimetric and geometric measurements. The effect arises from the redistribution of water masses what changes the weight of the column of water above a certain point. At high tide more mass presses on the continental plate and the stations on the plain are moved, mainly in radial direction.
Since the loading effect is dependent on the tidal frequencies, the effect of the ocean loading is expressed in phases and amplitudes of the tidal waves. The contribution of 11 main tidal waves (M2, S2, N2, K2, K1, O1, P1, Q1, Mf, Mm and Ssa) for gravimetric and geometric variations are provided by the “Ocean tide loading provider” of the Onsala space observatory[6]. Different ocean models (for example the one introduced above) can be chosen. The results are given in the BLQ format. An example of a BLQ file for the displacement case can be seen in Figure 2.3.
The first three data lines in Figure 2.3 are the amplitudes with the unit [m] for the radial, east-west tangential and north-south tangential displacement. Displacement is defined

[4] http://129.16.208.24/loading/tidemodels.html; last access 22.10.2010
[5] http://www.legos.obs-mip.fr/en/share/soa/cgi/getarc/v0.0/index.pl.cgi?contexte=SOA&donnees=maree... &produit=modele_fes; last access 11.08.2010
[6] http://129.16.208.24/loading/; last access 22.10.2010

positive upwards, in south and in west direction. The second three lines are the respective phases with the unit decimal degrees. The order of the tidal waves is in the same sequence how they are mentioned above.
For the gravity effect the amplitudes can be obtained in [μm/s^2] or in [mGal]. The gravitational acceleration is defined positive upwards.

```
  PPM1
$$ Complete EOT08a
$$ Computed by OLFG, H.-G. Scherneck, Onsala Space Observatory 2010-Sep-15
$$ PPM1,                       RADI TANG lon/lat:   11.2775   48.0842  641.02
  .00557 .00175 .00121 .00054 .00198 .00099 .00074 .00007 .00049 .00027 .00023
  .00217 .00053 .00050 .00015 .00035 .00026 .00010 .00005 .00005 .00003 .00003
  .00046 .00020 .00008 .00006 .00033 .00006 .00011 .00002 .00001 .00001 .00000
   -71.8  -43.2  -90.2  -44.0  -63.2  -96.2  -59.0 -143.2    8.1    5.8    1.1
    80.5  105.0   59.7  110.1  103.5   33.3  101.6  -21.0 -174.2 -168.8 -177.5
   -40.6  -16.7  -41.7  -15.4   44.0   -8.9   47.2  159.8 -155.9  174.1 -156.4
```

Fig. 2.3: Example for BLQ file

The crustal displacement and the gravity variations, respectively, can then be calculated with the following equation, if only the 11 tidal waves, provided by the BLQ files, and corrections for the modulating effect of the lunar node are considered [McCarthy and Petit 2004]:

$$\Delta c = \sum_{j=1}^{11} f_j A_{cj} \cos\left(\omega_j t + \chi_j + u_j - \Phi_{cj}\right) \qquad (43)$$

Δc change of the observable
A_{cj} amplitude of tidal wave *j*
Φ_{cj} phase shift of tidal wave *j*
ω_j tidal angular velocity of tidal wave *j*
χ_j astronomical argument at $t = 0$ of tidal wave *j*
f_j and u_j depend on the longitude of the lunar node

The correction due to ocean loading displacement does not exceed 5 cm in the radial and 2 cm in the horizontal direction [Kouba 2009]. In the case of gravity a maximum effect of 0.2 μm/s^2 = 20 μGal is possible. Typical values are in the range from 1 to 10 μGal [Torge 1989]. The magnitude of the ocean loading corrections for concrete calculations can be seen in Section 2.4, where the Earth tide models are described.

In case of gravimetry it has to be considered that the tidal correction terms determined through a tidal analysis also include the effect of ocean loading in the specified frequency domain. [Zerbini et al. 2001]
The tidal analysis is the analysis of measurements for gravimetric Earth tides. Amplitude and phase changes of tidal waves are determined. The observed tide effect is composed of

the body tide effects of the deformable body, the attraction and loading effect of the oceans (mainly in the half diurnal waves) and atmospheric effects (which have to been reduced with regression models) [Torge 1989]. Thus, assuming that the Earth's body tide is well defined through the Earth's model, it is possible to estimate the tidal ocean loading from the tidal observations.

2.3.3 Non-tidal ocean loading

The non-tidal ocean loading is a very small effect. It is caused by sea surface height variability or pressure changes in the water column, e.g. because of changes in currents. This changes the oceanic bottom pressure, which in turn changes the geoid and the nearby crust. Measurable effects can only be observed at stations near to the coast (within a few tens of [km]). Displacement of a few [mm] with maximums up to 10 mm can be expected. The induced gravity changes are in the order of 2-3 μGal. [van Dam and Wahr 1998], [van Dam et al. 1997]
Zerbini et al. [2001] computed non-tidal-annual loading for vertical station displacements and gravity at the station in Medicina (Po Plain, Italy). These annual waves have got an amplitude of 1.4 mm and 0.4 μGal, respectively.

2.3.4 Pole tide

The pole tide is the reaction of the elastic Earth on changes of the Earth's axis position because of the polar motion. The gravimetric and geometric variations have the same periods as the polar motion, i.e. a seasonal and the Chandler period.

Gravimetric effect

The gravity variations can reach 82 nms^{-2} = 8.2 μGal as a maximum at a latitude of 45° [Torge 1989]. Because this is a very long-periodic effect it has not to be considered for relative gravimetric campaigns. Corrections have to be applied for long-term stationary (superconducting gravimeter) relative measurements and for absolute gravimetry.
The equation for the gravimetric polar motion reduction (pole tide correction) is [Torge 1989]:

$$\delta g_{Pol} = \delta_{Pol}\,\omega_E^2 R_E \sin(2\varphi)\left(x\cos\lambda - y\sin\lambda\right) \qquad (44)$$

φ , λ latitude, longitude of the station
x, y instantaneous pole coordinates (in radians)
δ_{Pol} tidal amplitude factor (values 1.0 or 1.2 can be introduced)

R_E Earth's radius
ω_E angular velocity of the Earth

In Figure 2.4 the reduction is plotted for the first 238 days of the year 2010 using a tidal factor of 1 at latitude 48.15° and longitude 11.57°. For the calculation the pole coordinates from the Earth orientation data set "EOP C04_05 series for 1962-2010 (IAU2000)" provided by the IERS[7] are used.

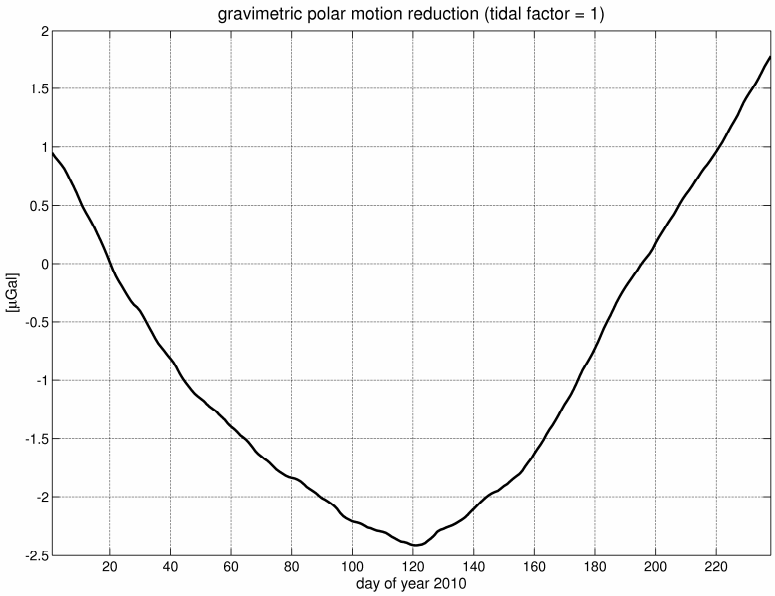

Fig. 2.4: Gravimetric pole tide correction

Geometric effect

The maximum pole tide displacements can reach 25 mm in the height and about 7 mm in the horizontal direction [Kouba 2009]. The equation for the computation of the pole tide correction can be found in [McCarthy and Petit 2004] and [Kouba 2009]:

- Correction to height (positive upwards):

$$\Delta h = -33\sin(2\varphi)\left(\left(x-\bar{x}_P\right)\cos\lambda-\left(y-\bar{y}_P\right)\sin\lambda\right) \text{ [mm]} \quad (45)$$

- Correction to latitude (positive northwards):

$$\Delta\varphi = -9\cos(2\varphi)\left(\left(x-\bar{x}_P\right)\cos\lambda-\left(y-\bar{y}_P\right)\sin\lambda\right) \text{ [mm]} \quad (46)$$

- Correction to longitude (positive eastwards):

$$\Delta\lambda = 9\cos\varphi\left(\left(x-\bar{x}_P\right)\sin\lambda+\left(y-\bar{y}_P\right)\cos\lambda\right) \text{ [mm]} \quad (47)$$

[7] http://www.iers.org/nn_11252/SharedDocs/MetaDaten/ … 11221_EOP_C04_05_62_NOW_IAU2000A.html; last access 25.10.2010

x, y instantaneous pole coordinates (in arc seconds)
$\bar{x}_P, \bar{y}_P$ mean poles (in arc seconds)

The mean poles can be calculated as follows [McCarthy and Petit 2004]:

$$\bar{x}_P = 0.054 + t_{rel} \cdot 0.00083$$
$$\bar{y}_P = 0.357 + t_{rel} \cdot 0.00395 \qquad (48)$$
$$\text{with } t_{rel} = \frac{(MJD - 51544)}{365.25}$$

MJD Modified Julian Date

2.4 Tide models

To evaluate a gravimetric or geometric signal the effects described above have to be removed from the measurements, especially since these effects are partly much larger than the signals, which are of interest. If the tidal effects are not removed correctly the observations would be interpreted incorrectly.
All models which are used or tested in this thesis are introduced in the following:

- ETGTAB version 3.0 from H.G. Wenzel

This program allows the computation of tidal potential, vertical tidal acceleration, horizontal tidal acceleration and some other quantities. Different tidal potential developments can be chosen. Here, the newest available one from Tamura [1987] with 1200 waves is taken. Pursuant to Schmeer [2006] the tidal series developed with the Tamura model (or the other models) provides the tidal effects of the solid Earth and additional synthetic tidal parameters, which are interpolated on a 1° grid. These parameters account for the elastic behaviour of the Earth. The values which are used to create the grid are generated with [Schmeer 2006]:

- Wahr-Dehant model for body tides on an elliptical, rotating, elastic and oceanless Earth
- Ocean tides and loading derived from a 1° grid ocean tide model

- Internal Earth tide correction (ETC) of the Scintrex gravimeter

The Scintrex gravimeter (used in the test measurements described in Section 5.1) uses an internal program to compensate for the Earth tides. It uses the equation from Longman. The accelerations caused by elastic deformations are taken into account by the gravimetric factor 1.16 in the Longman equation (16 % increase over the amplitude of gravimetric tides of the rigid Earth). Ocean loading and the latitude dependence of the gravimetric factor are neglected. [Scintrex 1995]

- routine hardisp

The Fortran routine *hardisp.f* can be used to calculate displacements due to ocean loading. It can be freely obtained from the internet[8].
This program reads in a file of station displacements in the BLQ format (cf. 2.3.2) for ocean loading, and outputs a time series of computed tidal displacements, using an expanded set of tidal constituents, whose amplitudes and phases are found by spline interpolation of the tidal admittance. A total of 342 constituent tides are included, which gives a precision of about 0.1 % pursuant to the annotations of the program.
Also the usage of BLQ-format files which provide phase and amplitude for gravity changes should be possible. This is not explicitly stated in the annotations, so the results are compared to that one from the routine ARG, which is presented next.

- routine ARG

The Fortran routine *ARG.f* can be obtained from the same server[8] as hardisp. It computes the angular argument which depends on time for 11-tidal-argument-calculations. These are the 11 tidal modes M2, S2, N2, K2, K1, O1, P1, Q1, Mf, Mm and Ssa, for which the ocean loading provider delivers phase and amplitude.
For the calculation of the ocean loading displacement, the following equation [McCarthy and Petit 2004] is used (see also Section 2.3.2 and Equation 43):

$$\Delta c = \sum_{j=1}^{11} f_j A_{cj} \cos\left(\omega_j t + \chi_j + u_j - \Phi_{cj}\right) \qquad (49)$$

The output of ARG corresponds to the term $\omega_j t + \chi_j$. A_{cj} and Φ_{cj} are given by the BLQ-File. Pursuant to Kouba [2009] f_j can be set to one and u_j can be set to zero for 1-3 mm precision.
Because there is no further unit-dependent term beside the amplitude, the usage of the gravimetric BLQ files is possible.

- Bernese GPS Software (Version 5.1)

There are internal routines in the Bernese GPS Software for the calculation of the correction for solid Earth tides, pole tide and ocean loading. The calculations follow the equations from the IERS conventions 2003. For comparison with the other programs, these corrections are extracted.

- solid.exe

The program *solid.exe* from Dennis Milbert can be obtained from his website[9]. Solid is based on the *dehanttideinelMJD.f* routine and implements the conventions described in

[8] ftp://tai.bipm.org/iers/convupdt/chapter7/; last access 22.10.2010
[9] http://home.comcast.net/~dmilbert/softs/solid.htm; last access 22.10.2010

Section 7.1.2 of the IERS Conventions 2003. This includes only the correction for the solid Earth tides (cyclic and permanent).[10]

Important: It holds for all cases, except for ETC (since the output of the Scintrex gravimeter gives the applied correction, cf. Section 5.1.1.1), that the corrections have to be added to come from a regularized position or gravity value (cf. Section 2.2.4) to the actual instantaneous position or gravity value. If the actual value is measured the corrections have to be subtracted to reduce the position or gravity value.
It has to be paid attention, that gravity is defined positive upwards in the ocean loading BLQ files, what means that *g* is defined negative. But in the following examples, the acceleration is defined positive, so the sign for the gravimetric ocean loading corrections is flipped for hardisp as well as for the ARG. This can also be seen in Figure 2.5, where the gravimetric and the geometric ocean loading effects are plotted using the BLQ file definition. Both effects have got the same sign, but if *g* is defined positive a rise of the crust (positive correction) corresponds to a negative correction for the gravity value.

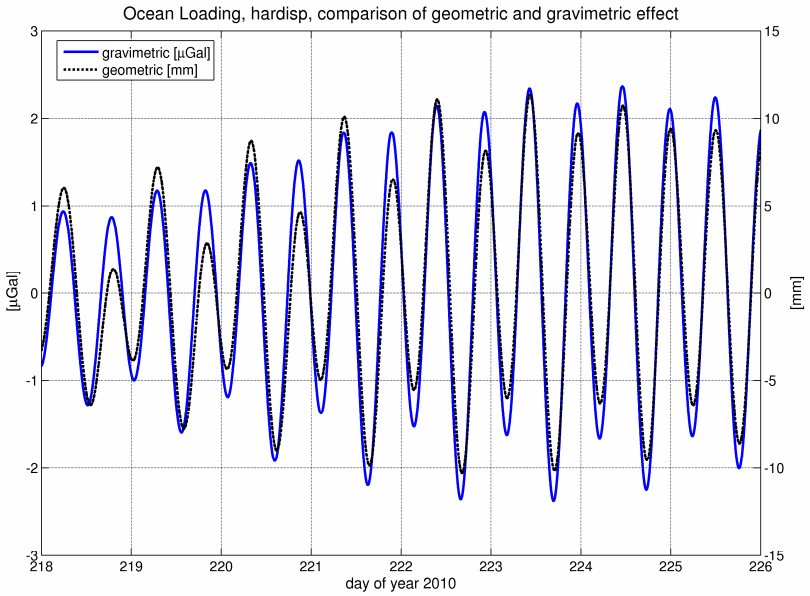

Fig. 2.5: Comparison of geometric and gravimetric ocean loading effect, computed with hardisp, using BLQ file definition for gravity effects

Gravimetric

To give an example for the gravimetric effects they are plotted for the days 218 to 226 of year 2010, which is the time interval of the third measurement session in the basement of the TU (see Section 5.1.1). All computations have been done for a latitude of 48.15° and a

[10] from webpage of *solid.exe* program: Solid Earth Tide (Milbert D), http://home.comcast.net/~dmilbert/softs/solid.htm#link0, last access: 22.10.2010

longitude of 11.75°. For the comparison the sign of ETC is defined in the same way as ETGTAB. The signs of the results from hardisp and ARG are switched, according to the definitions above.

- ***Model difference ETGTAB - ETC***

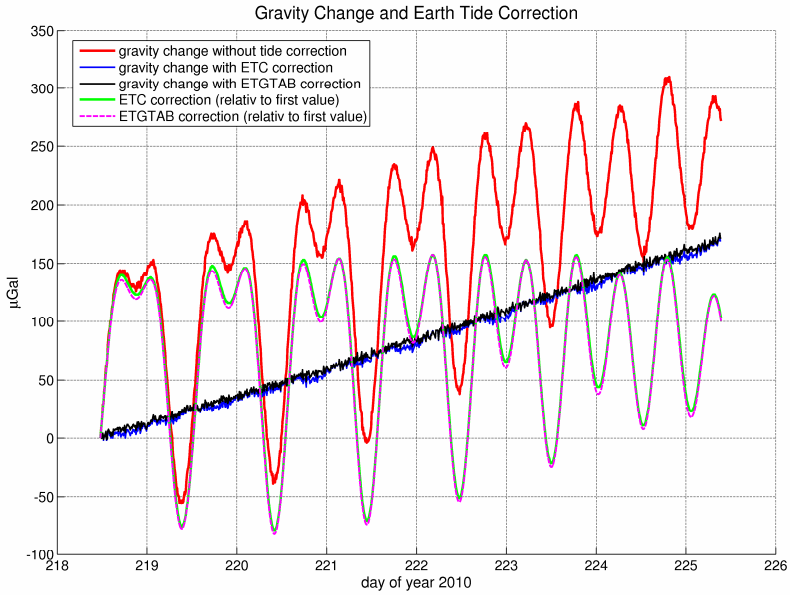

Fig. 2.6: Observed gravity changes and solid Earth tide corrections

In Figure 2.6 the measurement series from the basement experiment with the Scintrex gravimeter is shown (cf. Section 5.1.1). All values are changes relative to the first value. The gravity change with the internal applied correction (ETC) is plotted in blue; the values with the ETGTAB correction are plotted in black. The red line presents the measured gravity changes without a tide correction. As can be clearly seen, the tidal effects outrange all other influences by far. On a short time scale they are even larger than the drift. In Figure 2.6 the difference between the two correction terms (green: ETC and magenta dotted: ETGTAB) can hardly be recognized. With a closer look on it (Figure 2.7), it can be seen that the differences have a half-diurnal period. This is the same period as the main term of the missing ocean loading correction in the ETC model. For this time span the maximum deviation reaches 4 µGal. In Figure 2.9 the model differences are plotted together with the ocean loading correction from another source. If the latter is subtracted from the model differences a signal with a diurnal period and an amplitude of 2 µGal remains (see Figure 2.8).

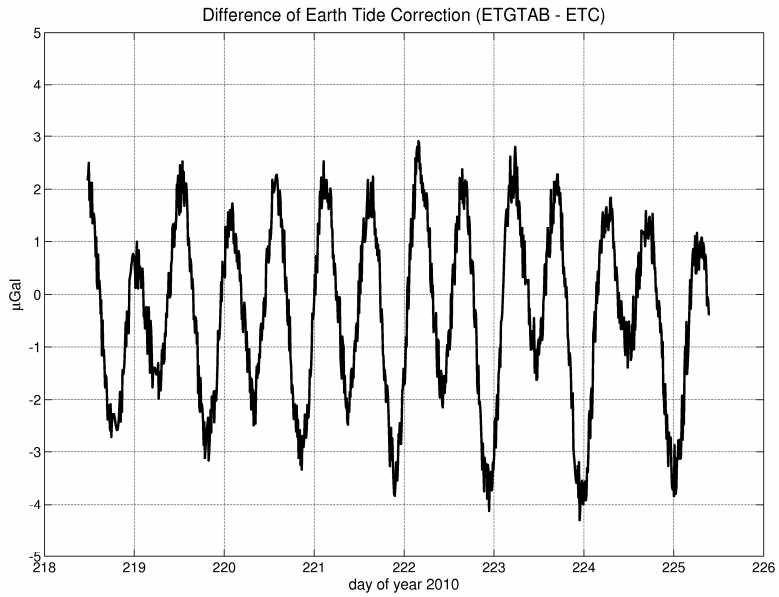

Fig. 2.7: Difference of ETGTAB and ETC correction

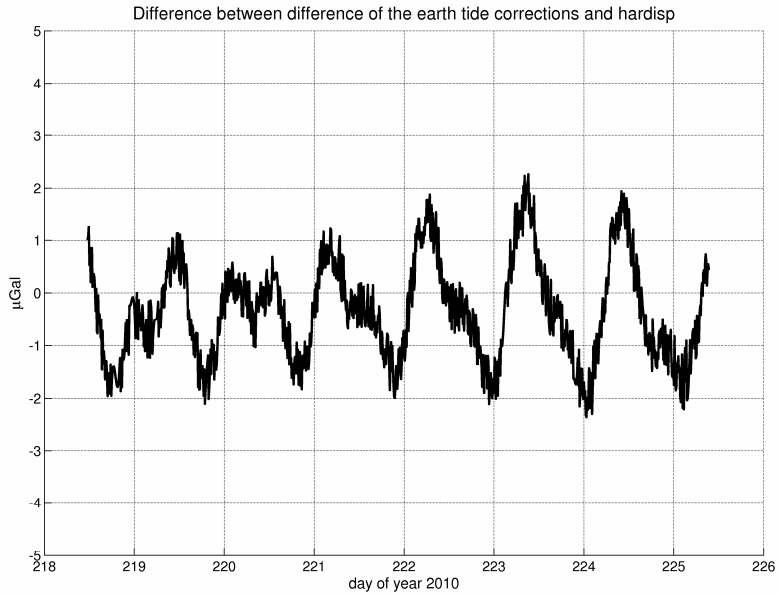

Fig. 2.8: Difference between the difference of the gravimetric solid Earth tide corrections from Figure 2.7 (ETGTAB - ETC) and the ocean loading correction calculated with hardisp.

- ***Ocean loading***

As said in the introduction of the models, it shall be tested, if the hardisp routine can be used with gravimetric BLQ files. The other question is how large is the error because of the missing lunar node information and the usage of only 11 tidal modes, when the ARG routine is used.

In the observed period the difference of the two corrections (hardisp - ARG) is very small and does not exceed 0.25 µGal, as can be seen in Figure 2.10, thus the hardisp routine seems to be appropriate for computing gravimetric corrections.

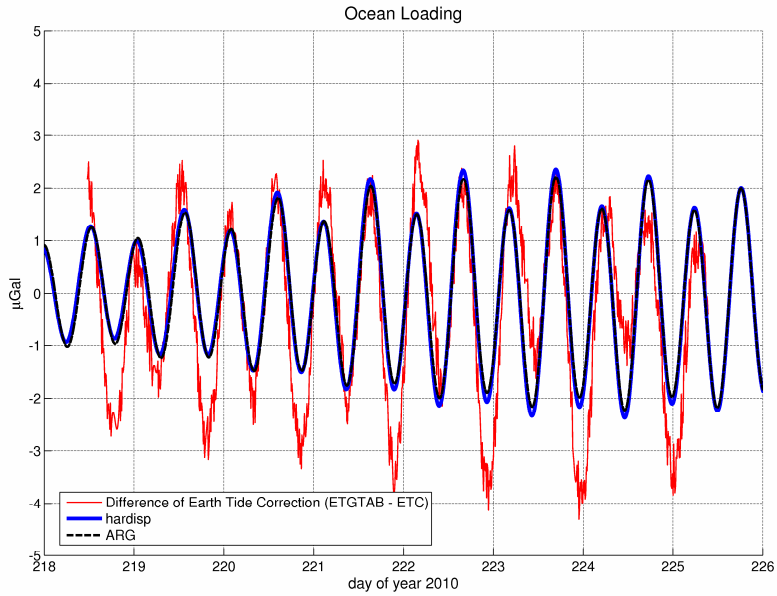

Fig. 2.9: Ocean loading correction calculated with hardisp and with ARG and difference of the Earth tide corrections from Figures 2.6 and 2.7

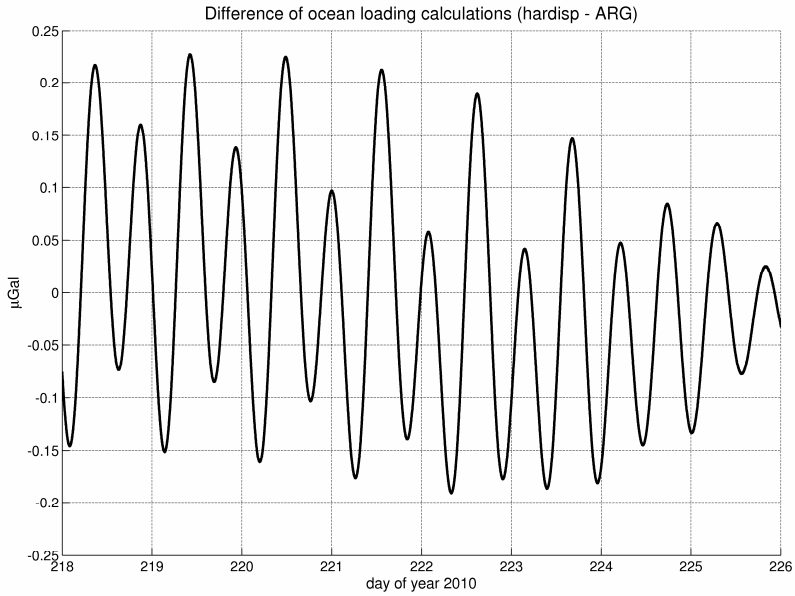

Fig. 2.10: Difference of ocean loading calculations hardisp and ARG

Geometric

In case of the geometric effects, the different effects are plotted for the day 195 of the year 2010 (14th July). This is the day of the first acquisition of a SAR image during the test campaign at DLR (see Section 5.2). The plotted corrections are computed for a latitude of 48.08° and a longitude of 11.28°. All calculations are done for the radial (up) component.

- ***Ocean loading***

Figure 2.11 shows the results for different ocean loading calculations. The Bernese software allows the calculation using the same approach as hardisp (HA) and the calculation with only 11 main tidal waves (OC), as it is done when using the ARG routine. The variation due to the ocean loading is in the range of ±10 mm. The differences between the different cases are shown in Figure 2.12. The OC-Bernese variations and the ARG variation do not differ. Between the hardisp and the Bernese HA calculations there is a difference of around 1 mm. There seems to be a systematic effect because of the constant increase of the difference within this day. It can not be assumed that the difference will increase in time linearly. The difference between the two Bernese methods varies the most, with a maximum of 1.3 mm. This shows the magnitude of the error because of the simpler calculation with ARG or OC.

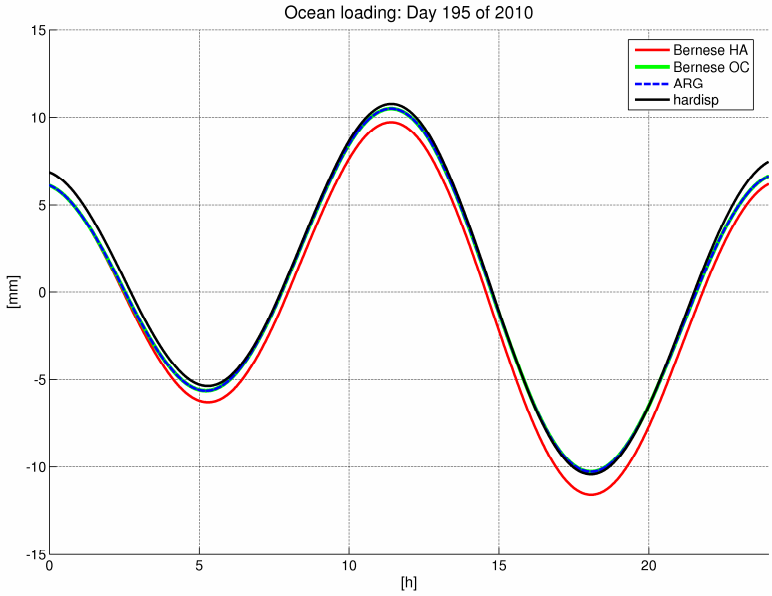

Fig. 2.11: Comparison of different geometric ocean loading corrections; computations for day 195

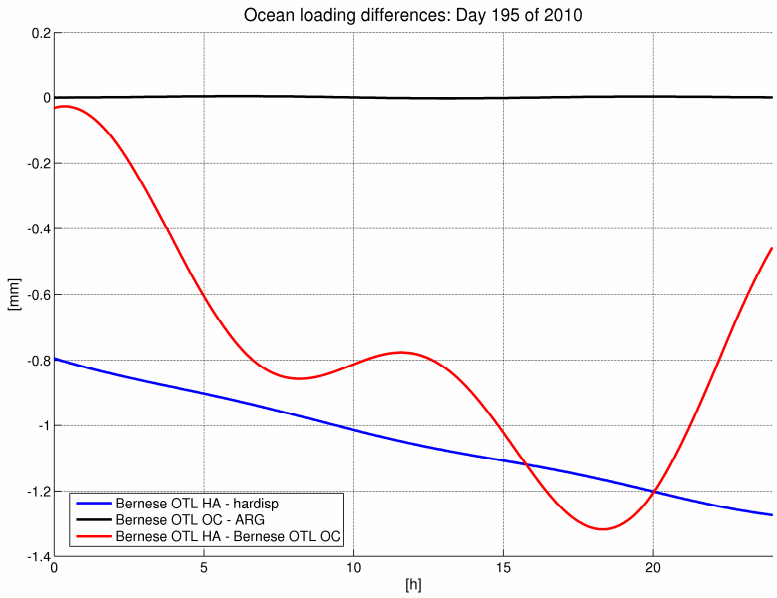

Fig. 2.12: Differences of the ocean loading computations in Figure 2.11

- ***Solid Earth tides and overall effect***

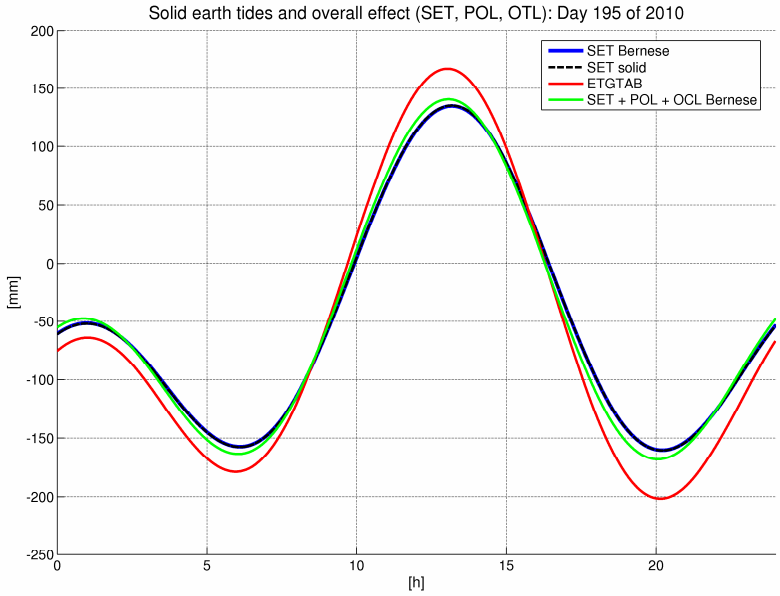

Fig. 2.13: Geometric solid Earth tide correction from Bernese (SET) and *solid.exe*, geometric ETGTAB correction and overall correction of solid Earth tide (SET), ocean loading (OTL) and pole tide (POL) from Bernese

In Figure 2.13 the geometric variation is shown only for the purely solid Earth part without any other influences. This is calculated with the Bernese software and the *solid.exe* program. The difference between them is plotted in Figure 2.14. It reaches ±0.4 mm as a maximum.

Additionally the whole tidal effect is computed with the ETGTAB software and through the combination of the three Bernese parts SET (solid Earth tides), OTL (ocean tide

loading) and POL (pole tide). This difference is plotted in Figure 2.15. As can be seen the difference is very large with up to 3.5 cm. But there should not be put so much trust in the results of the ETGTAB software as it regards the vertical displacement. The reliability of the results in that case is not guaranteed since following statement can be found in the annotation of the source code for the subroutine ETPOTA: "The routine ETPOTA computes amplitudes, phases, frequencies and body tide amplitude factors for a number of different Earth tide components using three different tidal potential developments. Attention: This routine has finally not been tested for vertical and horizontal displacements and for shear tidal strain!"

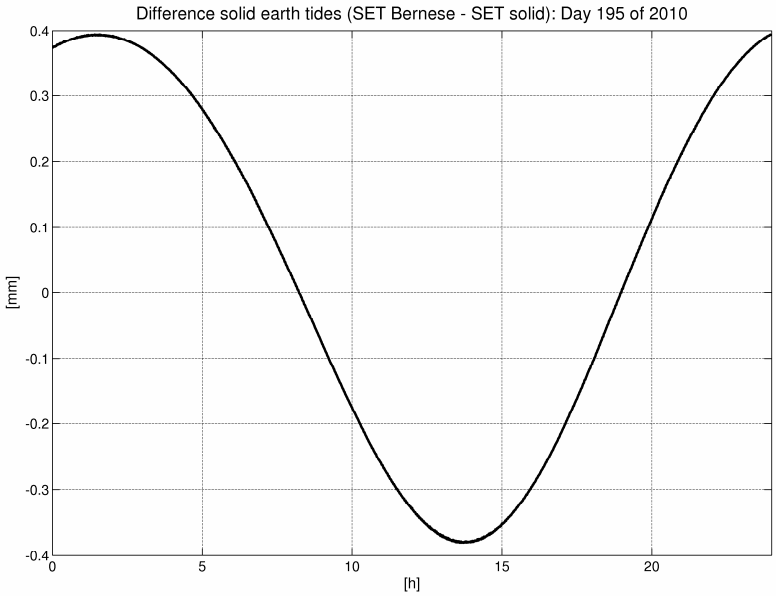

Fig. 2.14: Difference of solid Earth tide corrections from Bernese and *solid.exe*

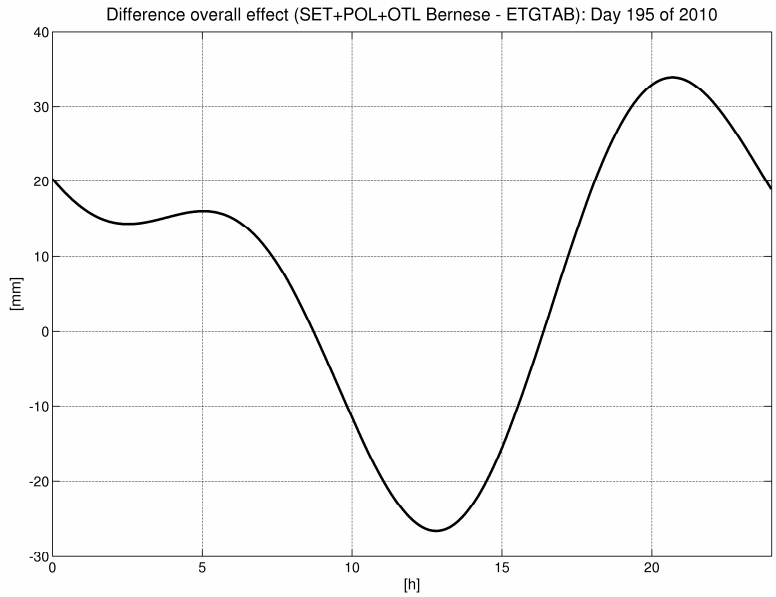

Fig. 2.15: Difference of geometric Bernese overall correction and ETGTAB correction

2.5 Atmosphere and hydrology

Equal to the solid Earth tides atmosphere and hydrology influence gravimetric measurement in two ways, directly by the gravitational effect because of mass changes below and above the gravimeter and indirectly by the deformation effect because of the reaction of the elastic Earth. Geometric measurements are only influenced by the deformation effect.

For the interpretation of measurement results in matters of hydrology or atmosphere always the question arises to which extent they were influenced by local or global changes of the respective phenomena. The origin of the signal also determines the period of the signal, which may be different for local or global changes.

In principle there are two ways of handling the influence of the loading effects. One possibility is the use of data from global weather / water models. The loading effect can then be computed by convolving Green's functions [e.g. Farrel 1972] with a global field, which describes the distribution of the loading masses, as described in Section 2.1. The other possibility is the determination of site dependent regression coefficients by fitting the geodetic observations to local variations of the respective parameter (e.g. air pressure, groundwater height) [van Dam et al. 2003]. In the case of gravity such an admittance factor includes the integrated effect of the change of direct attraction and the indirect effect because of loading, so it can not be divided between local and global (loading) parts. Of course all other disturbing effects have to be considered and removed if such an admittance factor is determined.

2.5.1 Atmosphere

The mass changes of the atmosphere can be characterized mainly by two parameters. The first one, which is much more important, is the surface pressure. This value is representative for the whole integrated mass above one point. The second parameter is the location of the mass centre of a column of air. The location of the mass centre is mainly influenced by the air temperature, since the air expands when it is warmer. Thus the mass centre is lower for lower temperatures. This only affects gravimetric measurements, since the loading effect is only dependent on the total load but the Newtonian attraction also on the distance of the masses.

The change of atmospheric pressure is induced by the passing of pressure systems. From this it can be derived that larger variations of the pressure have periods of several days,

depending on the time it takes that a high pressure (anti-cyclone) system is replaced by a low pressure (cyclone) system or the other way round.
Pursuant to van Dam et al. [2003] surface displacements due to atmospheric mass circulations are dominated by the effects of synoptic scale systems (1000 - 2000 km wavelength) with periods of approximately two weeks. The effects are larger at higher latitudes since larger pressure systems (larger in amplitude and more spatially coherent) can be found there. Annual signals are much smaller than the short term signals but also significant.
Boy et al. [2002] examined the spectral energy of a surface pressure field from the ECMWF and found that the pressure variations are dominated by harmonic degrees smaller than 10, corresponding to large-scale atmospheric structures with wavelengths larger than 4000 km.
Large pressure systems have typically peak-to-peak pressure changes of 40-50 mbar [van Dam and Wahr 1998], with maximal variation of ±60 mbar [Torge 1989]
Another important aspect is the reaction of the ocean due to the atmospheric loading variations. The inverse barometer effect attenuates the loading effect at stations near to the coast (up to 500 km distance) [van Dam et al. 2002]
Kaniuth and Vetter [2006] observed pressure changes in Europe. They computed sub-daily (six hours) anomalies as deviation of the long-time average. The maximum pressure variations within a day could be found in Fennoscandia with 40 mbar decreasing southwards to 20 mbar in the Mediterranean area. The overall pressure ranges decrease from nearly 80 mbar in the north to 40 mbar in the South.
For further information about the magnitude of pressure changes see the pressure variations for the TERENO area in Chapter 3.

2.5.1.1 Gravimetric effect

A first coarse approximation of the direct gravitational effect can always be done with a Bouguer plate:

$$\delta p = g \cdot H_{atm} \delta \rho_{atm} \qquad (50)$$

$$\delta g_{atm} = -2\pi H_{atm} \delta \rho_{atm} \qquad (51)$$

$$\delta g_{atm} = -2\pi \frac{G}{g} \delta p = -0.043 \cdot \delta p \text{ nms}^{-2} \qquad (52)$$

H_{atm} thickness of the homogenous atmospheric mass [m]
$\delta\rho_{atm}$ density change of the homogenous atmospheric mass [kg/m^3]
δp pressure change [Pa]

This means a change of 10 mbar leads to a gravity change of 4.3 μGal. Since atmospheric masses are above the gravimeter, the measured gravity becomes smaller for an increase of pressure.

In case of the atmosphere the indirect effect has the opposite sign than the Newtonian attraction. The gravitational effect dominates the atmospheric admittance factor, but is decreased by the loading effect. The combination of both leads to following equation for the approximation [Torge 1989]:

$$\delta g_{atm} = -0.03\delta p \; nms^{-2} \qquad (53)$$

This means a change of 10 mbar leads to a gravity change of 3 μGal for the overall effect.

Van Dam and Wahr [1998] present several approaches for determining an admittance factor for gravity at different stations. The resulting factors are all in the range from -0.3 to -0.4 μGal/mbar. They also mention a theoretical global admittance factor of -0.289 μGal/mbar found by [Spratt 1982].

The deformation effect is maximized when the load is coherent over large distances as happens more probably in the winter and in higher latitudes. Since the deformation effect is opposite to the mass attraction effect, the total admittance is reduced in the winter and in higher latitudes. [van Dam and Wahr 1998]

Zerbini et al. [2001] considered also vertical air mass exchanges, which can not be detected by measurement of surface pressure at the ground. They used balloon radio sounding to estimate the vertical distribution of the air mass. The changes were modelled in an annual wave with an amplitude of 0.6 μGal. An annual signal is appropriate because of the seasonal warming and cooling of the atmosphere.

Merriam [1992] presented gravity Green's functions for a column load of a model atmosphere on a spherical elastic Earth. Then he divided the atmosphere's influence into three zones (local, regional and global). He found that most of the atmospheric signal comes from the regional zone within 50 km of the gravimeter. In this zone the atmospheric pressure is essentially uniform, so that a single barometer characterizes the gravity signal from this zone very well. The admittance between gravity and local zone pressure is -0.356 μGal/mbar. The regional zone (up to 10° distance to the gravimeter) has a pressure field which usually correlates with the local pressure, but can sometimes be quite different. Thus a local fit for the admittance can often be correct, but if the regional pressure deviates, the effective admittance of local and regional zone can vary in the range from -0.27 to -0.43 μGal/mbar. For the global zone he found a gravity signal of about 1 μGal at periods of several days to seasonal.

2.5.1.2 Geometric effect

Peak-to-peak vertical displacements of 10 to 20 mm are common at mid-latitudes. Annual signals having amplitudes between 0.5 and 3 mm. [van Dam et al. 2002]

Kaniuth and Vetter [2006] developed a program for the Bernese Software, which allows estimating atmospheric loading coefficients along with all other parameters.
Because most stations used in their analyses did not provide on-site pressure measurements, they had to use a global weather model and to interpolate pressure values for the stations. They claim that the approach should be based on accurate local pressure measurement at each site for further applications.
They only use local and no large-scale pressure variations. They also did not consider the hydrology for the estimates of the regression coefficients, because they assume that these effects have other periods.
Neglecting some exceptions with special conditions (like small islands) they found regression coefficients for stations all over Europe in the range from 0.2 mm/mbar to 0.5 mm/mbar.
Very small coefficients are found for Helgoland, a small island, and Brest, which is located exposed to the Atlantic, where the inverse barometric effect seems to play a major role. In many cases, the displacements tend to decrease towards the coastline.
In Table 2.2 the results for stations, with characteristics most similar or located near to the Ammer catchment are listed with the maximum resulting surface displacement.

station	latitude	ΔP max [mbar]	*dh* [mm/mbar]	max. effect [mm]
Wettzell (WTZR)	49.1 °	52	-0.478	25
Pfänder (PFAN)	47.5 °	51	-0.315	16
Graz (GRAZ)	47.1 °	48	-0.505	24
Medicina (MEDI)	44.5 °	40	-0.284	11

Table 2.2: Atmospheric admittance factor *dh* for four stations, from Kaniuth and Vetter [2006]

Zerbini et al. [2001] also calculated the atmospheric loading effect for the station in Medicina. But they did not regard daily variations, they even smooth to reduce high frequency effects. In this case the maximum variation is 3 mm, clearly smaller than the one in Table 2.2.

Although regional anomalies would represent the characteristic of the pressure systems better, van Dam and Wahr [1998] assume that the use of local pressure as an alternative for global pressure data, for delineation of the displacement effect, is valid at many GPS sites.

2.5.2 Signal delays due to the atmosphere

Every signal which is sent to or received from a satellite has to pass the atmosphere. The propagation of these electromagnetic waves in the atmosphere has certain characteristics. In a medium like air the speed of light is reduced in comparison to the speed of light in a vacuum. This leads to light refraction and to a delayed arrival time of the signal. It has to be distinguished between group velocity (velocity of signals, i.e. different information are modulated on the carrier wave) and phase velocity (velocity of the propagation of sine or cosine waves). In a dispersive medium the propagation of the signal is frequency dependent, what also means that group and phase velocity are different.
Since the way through the atmosphere is longer when the elevation of a satellite is low, the delay in zenith direction is always smallest and increases for lower elevations. This dependency can be described by mapping functions. The simplest mapping function is the weighting with $1/\cos(z)$, what corresponds to a homogenous atmosphere with horizontal layering.
Two parts of the atmosphere play a considerably role, the troposphere and the ionosphere. Both are described in the following.

2.5.2.1 Troposphere

The troposphere is the lowermost layer of the atmosphere. It reaches a height of around 10 km. This means that signals from all satellites, independent from their orbit height, are affected the same. The propagation of the wave is independent of frequency; so, for example, a GPS signal has the same delay as an X-Band SAR-signal.
The tropospheric delay is dependent on the air pressure of the dry air, the temperature and the relative humidity (the partial pressure of the water vapour, respectively). The delay can be divided into a dry and a wet part.
The dry part accounts for around 90 % of the delay. Since it is only dependent on the air pressure it can be determined relatively well by pressure measurements on the ground. This part also changes only very slowly. The much more variable wet part is dependent on the temperature and the humidity. The determination is more difficult, because the local and temporal distribution of the water vapour is fast changing and can not be described completely by ground measurements of temperature and humidity. For a correct determination the integrated water content is needed. This quantity can be provided by water vapour radiometer.
The dry delay is around 2.3 m in zenith direction and reaches around 25 m for an elevation of 5°, the wet delay can reach 40 cm as a maximum [Rothacher 2007].
There are two different possibilities to handle the troposphere. It can be modelled and from this a delay can be determined, either with using local measurement or only with using a

standard atmosphere. The other way is the estimation of the delay directly from the measurements.
In GPS processing the dry delay is often determined by an a priori model, while the wet delay is estimated. Errors originated from the incorrectness of the dry model are then incorporated in the wet delay.
Since the water vapour content becomes zero for a height of around 10 km, but the dry air can be extended up to 40 km, often different mapping function are used for the dry and the wet part.
The total delay can be written as follows [Rothacher 2007]:

$$ZTD = ZHD + ZWD \quad (54)$$

$$TD(z) = m_h(z) \cdot ZHD + m_w(z) \cdot ZWD \quad (55)$$

ZTD	zenith total delay
ZHD	zenith hydrostatic delay (dry delay)
ZWD	zenith wet delay
TD	total delay
z	zenith distance
m_h	hydrostatic mapping function
m_w	wet mapping function

The GMF mapping function

The Global Mapping Function (GMF) mapping function is shortly described here, because it is used for estimating the ionospheric delay for the correction of SAR Ranges (see Section 5.2).
The GMF is an empirical mapping function, based on spherical harmonic developed up to degree 9, which can be determined from station latitude, longitude and height and day of the year. It was developed to have an easy to implement mapping function which is more consistent with the Vienna Mapping Function (VMF) than the often used Niell Mapping Function. The GMF is a kind of “averaged VMF”. The VMF is using raytracing through atmospheric layers which are calculated from ECMWF reanalysis data. [Boehm et al. 2006]
The Matlab-function *gmf_f_hu.m*, which computes the GMF, can be downloaded from the homepage of the Institute of Geodesy and Geophysics at the Vienna University of Technology[11].

[11] http://www.hg.tuwien.ac.at/~ecmwf1/gmf_f_hu.m; last access: 26.10.2010

2.5.2.2 Ionosphere

The Ionosphere comprises approximately the region from 50 to 1000 km height, what means that for satellites with a low orbit not the whole ionosphere has to be considered.
The delay depends on the electron density N_e, i.e. the amount of free electrons per m^3. It varies for the different layers of the ionosphere. In contrast to the troposphere the ionosphere is dispersiv. A comparison of the delay for different frequencies f is shown in Table 2.3.
The total (or integrated) electron content (TEC) is the amount of free electrons, which can be found in a column from the ground to the satellite on 1 m^2 area. The TEC is given in the unit TECU (TEC-Units): 1 TECU = 10^{16} free electrons / m^2.
For the phase and the group delay, respectively, it holds [Rothacher 2007]:

$$\delta\rho_{ion,phase} = -\alpha\frac{E}{f^2} \text{ (phase advance)} \qquad (56)$$

$$\delta\rho_{ion,group} = +\alpha\frac{E}{f^2} \text{ (group delay)} \qquad (57)$$

$$\text{with } \alpha = 40.3\cdot 10^6 \left[\frac{\text{m}}{\text{s}^2\text{TECU}^{-1}}\right]$$

E is the integrated electron content given in TECU:

$$E = \int N_e(s)\, ds \qquad (58)$$

Ionospheric disturbances are dependent on solar radiation and the activity of the Sun. Typically the largest TEC appears shortly after noon, the TEC is larger at the equator and increases and decreases synchronously to the eleven-year cycle of Sun activity [Rothacher 2007]. Typical TEC values are in the range from 0 to 50 TECU.
Frequently only the electron content in zenith direction E_V (vertical TEC = VTEC) is modelled. Thus the TEC has to be determined for the corresponding zenith distance. For that a single layer model can be used, where the total electron content is represented by a spherical layer at the mean ionospheric height. This height is assumed as H = 450 km. The point, where the line of sight to the satellite intersects this layer, is called pierce point. The zenith distance at this point is z′. Then it holds for the electron content [Seeber 2003], [Rothacher 2007]:

$$E(z) = \frac{1}{\cos(z')}\cdot E_V \qquad (59)$$

$$z' = \frac{R_E}{R_E + H}\cdot \sin(z) \qquad (60)$$

	GPS L1	X-band	GPS L1	X-band	GPS L1	X-band
z [°]	0	0	20	20	45	45
z' [°]	0	0	18.6314	18.6314	41.3384	41.3384
	delay					
TEC	[cm]	[cm]	[cm]	[cm]	[cm]	[cm]
5	81.2	2.2	85.7	2.3	108.1	2.9
10	162.4	4.3	171.4	4.6	216.3	5.8
15	243.6	6.5	257.0	6.9	324.4	8.6
20	324.7	8.7	342.7	9.1	432.5	11.5

Table 2.3: Comparison of L- and X-Band ionospheric delay for different elevations

Because of the high variability of the ionosphere modelling and prediction are difficult. An empirical model is the International Reference Ionosphere (IRI)[12]. For given location, time and date, IRI describes the electron density, electron temperature, ion temperature, ion composition and also the electron content as monthly averages in the altitude range from about 50 km to about 2000 km.
The TEC can also be estimated from GNSS network solutions. The reliability of the results is dependent on the station density. A global TEC grid is provided by the International GNSS Service (IGS).

2.5.3 Hydrology

In contrast to the atmosphere in hydrology much more parameters play a considerable role for the occurrence of gravimetric and geometric signals. The water balance, which determines the total mass gain or loss, is dependent on the complex interaction between evaporation, precipitation, soil moisture, groundwater level, surface runoff, interflow, snow cover and some more other processes. Also the topography is an important factor, since the gravity effect has the opposite sign for masses above and below the gravimeter. In case of the atmosphere, the masses, which influence the measurement values, are always above.
Because of the complexity the modelling of the hydrology on local scale has a much larger importance for measuring gravity variations than the modelling of the atmosphere. As described above the local atmospheric effects can be considered relatively well by a local admittance factor.

Because there are so many different methods how to cope with the hydrology (especially in case of gravimetry), different approaches are presented in the following. Since these investigations have been made at different test sites and with different observation scales, one can get an impression of the range of magnitude of hydrological signals.

Changes of hydrological loading and deformation can be caused by fluctuations in ground water, soil moisture, surface water and snow or ice cover. The magnitude of the

[12] http://iri.gsfc.nasa.gov/; last access: 26.10.2010

deformation signal at a certain site depends on the total surface load, averaged over a few hundred kilometres. [van Dam and Wahr 1998]
Pursuant to [Crossley et al. 2005] it is important to emphasize that the common practice of using local water table changes to derive a hydrology admittance will remove both a local effect an a continental-size effect at the same time.

2.5.3.1 Gravimetric effect

As for the atmosphere the direct gravimetric effect can be approximately described by a Bouguer plate [Torge 1989]:

- groundwater level (saturated zone):

$$\delta g_W = 2\pi G \cdot \rho_W \cdot S_y \cdot \Delta H = 4.2 \cdot S_y \cdot \Delta H \ nms^{-2} \quad (61)$$

- soil moisture (unsaturated zone):

$$\delta g_W = 2\pi G \cdot \rho_W \cdot H \cdot \Delta\eta = 4.2 \cdot H \cdot \Delta\eta \ nms^{-2} \quad (62)$$

ρ_W water density (1000 kg/m^3)
H layer thickness (in which the gravity change takes place)
S_y specific yield (cf. Section 3.2 and Formula 66)
η water-filled pore space in % / soil water content (cf. Section 3.2 and Formula 65)

Examples:

10 % free pore space (S_y)	10 % moisture change ($\Delta\eta$)
1 m ground water level rise (ΔH)	1 m soil (H)
$\Rightarrow$ 42 nm/s^2 = 4.2 μGal	$\Rightarrow$ 42 nm/s^2 = 4.2 μGal

S_y = 1 for the rise of an open water level

$\Rightarrow \delta g_W = 2\pi G \cdot \rho_W \cdot \Delta H = 4.2\delta H \ nms^{-2}$

10 cm water level rise $\Rightarrow$ 42 nm/s^2 = 4.2 μGal
50 cm snow with a density of 200 kg/m^3 leads to the same value

If the hydrologic masses are assumed to be below the gravimeter, a global loading signal would, in contrast to the atmosphere case, enlarge the effect.

Examples for gravimetric hydrology investigations

- Zerbini et al. [2001] have derived a simple admittance factor of 2.2 μGal / m (water table change) for the effect of water table variations on gravity at the SG (superconducting gravimeter) station in Medicina, Italy.

- Virtanen et al. [2006] tried to distinguish between local, regional and global hydrology effects on gravity residuals, received from a superconducting gravimeter, located at Metsähove, Finland.

The gravity residuals are strongly correlated with the local groundwater level. The regression on water level, observed by a nearby borehole, was determined in the range from 25 to 28 $nms^{-2}m^{-1}$ = 2.5 to 2.8 μGal/m. From the range of the groundwater-level change of 2.6 m follows a maximum effect (peak-to-peak) of 7 μGal for the local hydrology.

On regional scale a model of total Finnish water storage was used. The storage change was also correlated with the gravity residuals what leads to a regression coefficient of 0.058 $nms^{-2}mm^{-1}$ = 5.8 μGal/m. The range of the water storage change is 250 mm so the maximum effect (peak-to-peak) for regional hydrology is 1.5 μGal. Additionally they found gravity variations of 3 μGal, due to global loading effects, calculated with Green's functions formalism.

The maximum overall effect, considering all scales, is hence around 12 μGal, of which 2/3 are due to the local groundwater level.

- Naujoks et al. [2007] and Naujoks et al. [2010] carried out researches at the Geodynamic Observatory at Moxa, where a superconducting gravimeter is in use. Because of the topography at the Moxa observatory, water can be stored above and below the level of the gravity observations. During rain events with successive high water table and soil moisture in the gravimeter surroundings, water mass is first stored above the gravimeter level, leading to a fast gravity decrease. In the hours and days after the rain event a gradually gravity increase is observed caused by downward moving water and evaporating rainwater.

Naujoks et al. [2007] tried to detect small hydrological variations in gravity by repeated observations with relative gravimeters. They did seventeen measurement campaigns, covering a period of 26 months, in a seasonal rhythm complemented by measurements at special hydrological events. To find hydrological signals they measured gravity differences with calibrated LCR-G (and LCR-D) gravimeters between all points in a gravity network (with point distances of several ten meters). These differences should reflect the different developments in the local water balance at the single points. The gravity differences reach standard deviations between 0.9 and 1.4 μGal, what is very small for the used instruments. Gravity differences, enforced only by hydrological effects, with a maximum of 17.1 μGal between different points could be detected. The maximum difference between two successive campaigns was 13.9 μGal. They could find a connection between these differences and local soil moisture and water table measurements but no direct correlation, what they relate to the difficult hydrological situation at the observatory.

Naujoks et al. [2010] evaluate a hydrological model of the small catchment with terrestrial gravity data. They use the information of this local model to develop a reduction of local

hydrological effects in superconducting gravimeter data. For that a hydrological model based on hydrological point observations and physio-geographical information was developed. The mass variations derived from this model were converted to density changes of the subsoil bodies of a gravimetric 3D-model, which was set up for the observatory surroundings. The strategy is shown in Figure 2.16.
In repeated gravity difference measurements, described in the previous approach only local changes are observed because the large-scale variations cancel out each other.
With subtracting the local hydrological effect, obtained from the local hydrological model, from the gravity residuals of the superconducting gravimeter, a seasonal variation emerges with a maximum peak-to-peak amplitude of approximately 7 µGal. By comparing monthly means of this terrestrial data with GRACE solutions and gravity changes derived from the WGHM model a good agreement can be found. The gravity residuals without correction do not fit to the global values.

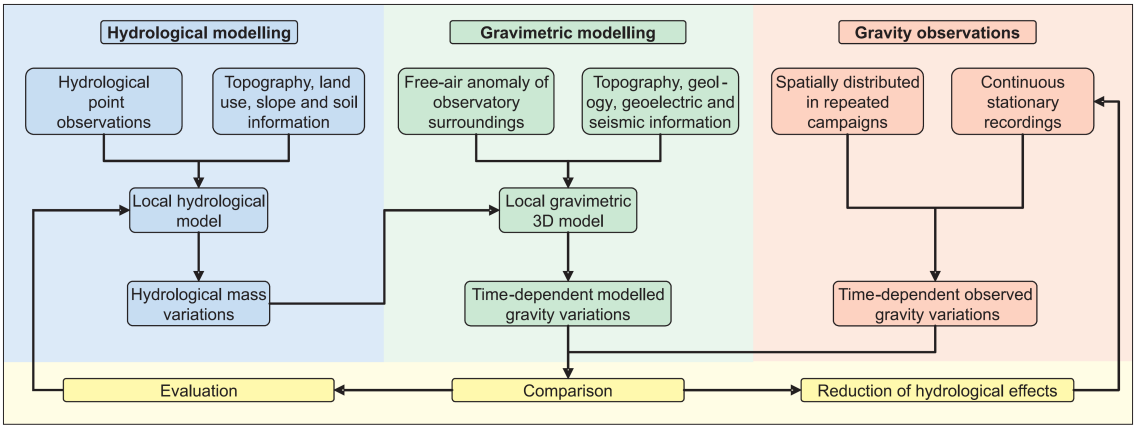

Fig. 2.16: Strategy for the interactions of hydrological modelling, gravimetric modelling and gravity observations from Naujoks [2010]

- In Creutzfeldt et al. [2010] lysimeter (explained in Section 4.1) measurements are used to estimate the hydrological influence on temporal gravimeter observations for the superconducting gravimeter (SG) at Wettzell. They define the total local water storage change (WSC) as a sum of different storage changes:

$$WSC_{local} = \Delta S_{Snow} + \Delta S_{Soil} + \Delta S_{Saprolite} + \Delta S_{Groundwater} \qquad (63)$$

The storage change from snow and soil water can be directly measured by the lysimeter because it can determine the sum of precipitation, evapotranspiration and deep drainage. The change in the saprolite (= chemically weathered rock) zone and in the groundwater is determined from the deep drainage in the lysimeter and groundwater level measurement. The gravity response of the estimated WSC was calculated from the hydrological observations and model results with a spatially nested extended point mass approach ([Leirião et al. 2009], cf. Section 3.2.3) for a 4 x 4 km^2 area around the gravimeter.
The time-series of the SG residuals and the gravity response, derived from the lysimeter estimated WSC, agree well in amplitude, phase and short-term variations. The coefficient

of correlation between both time series is 0.987. The overall seasonal peak-to-peak variation is 9.5 μGal for the SG residuals and 8.8 μGal for the gravity response.
The good agreement is remarkable since both time series have been determined completely independent. Other approaches, where this is not the case, are for example:

- Statistical approaches, where regression models for the hydrological quantities, which are used to predict the SG residuals, are estimated from the gravity data.
- Model approaches where the model is calibrated with the gravimeter data.

Large scale hydrological gravity effect was derived from global hydrological models, considering the large-scale gravity effect of Newtonian attraction (the attraction of a near zone less than 50 km around the gravimeter was excluded) and the effect of deformation due to the mass load. The resulting signal has a seasonal period with an amplitude of 2 μGal (4 μGal peak-to-peak).
The SG residuals are reduced for the local hydrological attraction effect. The remaining residuals for the lysimeter approach have a RMS of only 0.5 μGal, which means that nearly the whole signal could be removed. The remaining residuals can be assumed to be caused by large-scale hydrology. They could also reveal other geophysical gravity changes, like post-glacial rebound, processes in Earth's mantle and core or seismic and volcanic activities, but these do not play a role at Wettzell.
If approaches which try to fit the gravimetric data best (as described above) are used to determine local hydrological effects, it is not surprising if no correlation between the modelled global effect and the remaining residuals exists, since parts of or the total global signal are removed. As Creutzfeldt et al. [2010] claim this generally calls into question the benefits of these types of local hydrological reduction, when the goal is to study other geophysical processes based on SG residuals.
More astonishing is that the correlation between the remaining residuals from the (independent) lysimeter approach and the large-scale hydrology is even smaller in this study. A possible reason could be that the uncertainty of the estimation of the global effect is relatively high. Another possibility is that a local signal, eventually with seasonal amplitude, is not considered in the derivation of the gravity effect. In that case an alternative approach could be that first the global hydrology is reduced and after that the residuals from local hydrology are analysed.

2.5.3.2 Geometric effect

Van Dam et al. [2001] calculated vertical displacements up to 30 mm for the effects of long-wavelength (>100 km) variability of hydrology. Over the most continental areas the effect ranges between 9 and 15 mm. For that a model of global water-storage variation and a model of how the Earth deforms in response of surface loads are used to perform the

convolution of the surface loads with the Green's functions from Farrel [1972]. The resulting signals have a strong annual character.

Zerbini et al. [2001] computed a transfer function between the water table depth and a GPS height series at Medicina, Italy. For dry periods they get a factor of -2 mm/m (water table change), for wet periods the factor was higher with -6 mm/m (water table change). The different factors are necessary because of the changing properties of the soil with its water content. As an additional effect soil consolidation has to be considered. A water table decrease of 2 - 3 m leads to a soil settlement of a few mm. In a site specific regression coefficient this effect is already included.

Changes in station height due to local hydrology are no mass effects but are induced by changes due to the physical properties of the soil or the bedrock, e.g. soil settlements. Thus, if an admittance factor is determined, it has to be paid attention that it is a combination of completely different processes what leads to the factor. Because of this it can be impossible to determine such a factor since these processes can have different periods, what means that an admittance factor would change permanently.

2.6 Overview

In Table 2.4 all aspects considered in this chapter are listed. For every gravimetric and geometric signal (radial direction) a typical (not maximal) range for its variation (peak-to-peak) is given. The signals of the solid Earth tides are dominating. All other effects are clearly smaller in the range of one to a few [μGal] or a few [mm] to 2 cm, respectively. The direct attraction of local hydrology can be a comparatively large gravimetric signal, dependent on the local conditions.
The signal variation, which can be observed during a certain time interval, depends also strongly on the periodicity of the signal.

	gravimetric	**geometric**	**periodicity**
solid Earth tides	100 - 200 [μGal]	10 - 20 [cm]	short-periodic
ocean loading	2 - 4 [μGal]	1 - 2 [cm]	short-periodic
pole tides	2 - 8 [μGal]	1 - 2 [cm]	long-periodic
atmosphere	3 - 12 [μGal]	1 - 2 [cm]	various
local hydrology	1 - 15 [μGal]	-	various
global hydrology	2 - 4 [μGal]	1 [cm]	long-periodic
non-tidal ocean loading	< 2 [μGal] (only at coastal sites)	< 5 [mm] (only at coastal sites)	long-periodic

Table 2.4: Overview of typical range of magnitude of gravimetric and geometric signals

3 TERENO Ammer observatory - signals and hydrological modelling

In this chapter the TERENO Ammer observatory shall be presented in more detail. First the topographic, geologic and meteorological conditions are delineated (3.1). Then a hydrological model, used for the modelling of the Ammer catchment, is introduced. In this context some basic hydrological terms are explained (3.2). Finally atmospheric and hydrologic signals derived from real data are shown (3.3).

3.1 The Ammer catchment

The landscape of the catchment area is characterised by high spatial geological and pedological (= concerning soil) differentiation, a complex orography and corresponding climatological conditions.
The catchment can be divided into two landscape units: the prealpine hill country and moorland and the Swabian Upper Bavarian foothills of the Alps. The main geological units are the lime-alpine zone in the southern part, the flysch zone bordering in the north, the folded molasses and the unfolded molasses in the northern part of the catchment. Due to the relief the climate variables show typical gradients within the catchment. The precipitation is approximately 500 mm higher and the temperature 2.5° lower in the southern mountainous part (cf. Figure 3.1). Maximum precipitation is in June in the prealpine region and in July in the alpine region. The total precipitation is about 1000 mm in the northern and 1500 mm in the southern part. In the catchment there are averagely 130 days per year with snow cover larger than 10 cm. [Kunstmann et al. 2004]
From the differences of the total precipitation in combination with the different soil types one can expect very different gravimetric signals due to the hydrology. Especially in the Linder valley in the south the groundwater modelling is very difficult, because of the complicated geological situation, and has not lead to satisfying results yet [Mayr 2004]. A gravimetric campaign could show its potential for detecting (integral) groundwater variations at this location.
Further topics for investigations regarding the characteristics of the test site could be:

- Is there an influence of the atmospheric admittance factor due to higher topographic variability?
- Is it possible to detect the same large-scale hydrological signal at locations with clearly different hydrological situations?
- How does the gravimetric signal react on a rainfall event in a mountainous and in an area with less topographic variability?

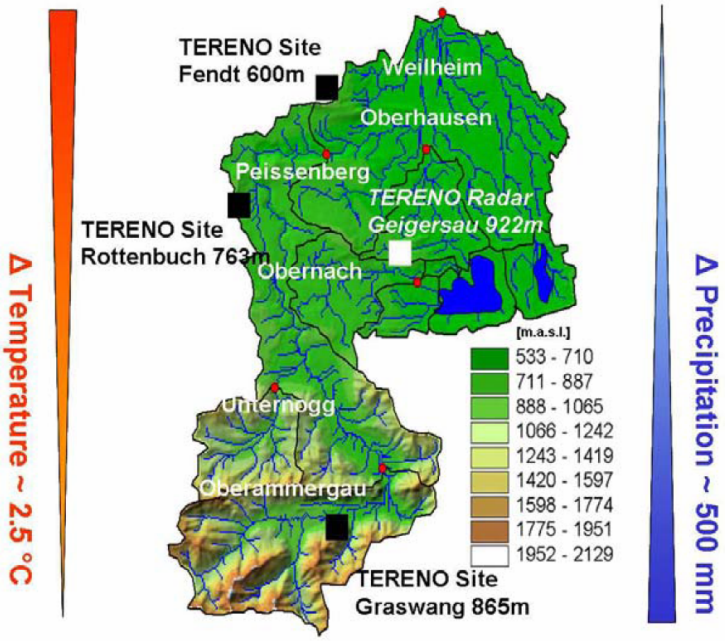

Fig. 3.1: Ammer catchment, from Kunstmann [2010]

3.2 Hydrology: basics and modelling

3.2.1 Basic terms and relations

The hydrological cycle for a catchment can be represented in form of the **water balance equation**:

$$P - Q - E - \Delta S = 0 \qquad (64)$$

P Precipitation

Q Runoff

E Evaporation

ΔS storage change (the storage change can be positive or negative since water can be released from storage or absorbed into storage)

Precipitation represents the main input of water to the catchment. It can be in the form of rainfall, snowfall or hail. Evaporation includes that from open water bodies, the soil surface, and vegetation. The storage term is explained in detail in the following.

The water balance equation contains the storage term ΔS. Within the hydrological cycle there are several areas where water can be stored, most notably soil, groundwater, snow, ice, and lakes. Since the gravimetric hydrological effect as well as the loading effect is mainly induced by changes in the water storage the following section shall give an

understanding of the water beneath (and on) the Earth's surface and explain some important terms. Some more terms are explained during the description of the hydrological model.

Water beneath the Earth's surface can be divided into the saturated and unsaturated zone. Water in the **saturated zone** is referred to as groundwater and occurs beneath a water table. This is also referred to as water in the **phreatic zone**. Water in the **unsaturated zone** is referred to as soil water and occurs above the water table. This is also called the **vadose zone**. There is movement of water through vertical infiltration and horizontal flow. This occurs in both the unsaturated and the saturated zone, although at a slower rate in the unsaturated one. [Davie 2008]

The **infiltration rate** indicates how much water enters a soil during a certain time interval. This rate is dependent on the current water content of the soil and the ability of a soil to transmit water.
The **soil water content** is normally expressed as a volumetric soil moisture content or soil moisture fraction η [Davie 2008]:

$$\eta = V_w / V_t \qquad (65)$$

V_w is the volume of water in a soil sample and V_t is the total volume of the soil sample (soil volume + water volume + air space).
Saturated water content is the maximum amount of water that the soil can hold. Soil water content as a percentage of saturated soil is a useful method to describe how wet the soil actually is. **Porosity** ε is another important soil water property. It is the fraction of pore space in the total (bulk) volume of soil. Theoretically water can fill all of the pores in a soil. [Davie 2008]
The **bulk volume** V_b is the volume per unit mass of a dry material plus the volume of the air between its particles. The **soil bulk density** is the mass of dry soil per unit bulk volume.

Once water has infiltrated through the unsaturated zone it reaches the water table and becomes groundwater. An **aquifer** is a layer of unconsolidated or consolidated (rock which is packed together more tightly than unconsolidated rock because of stress) rock that is able to transmit and store enough water for extraction. A **confined** aquifer has restricted flow above and below it while an **unconfined** aquifer has no upper limit. Water within a confined aquifer is normally under pressure. In an unconfined aquifer the water table is free to rise and fall dependent on the amount of water contained in the aquifer. [Davie 2008]

Specific yield, also known as the drainable porosity or effective porosity, is the ratio of the volume of water V_w that will drain by gravity from a rock or soil that was initially saturated

(because of surface tension and molecular effects not all water in the pore space of an aquifer drains) to the bulk volume V_b [Price 1985]:

$$S_y = V_w / V_b \quad (66)$$

The specific yield is 1 for open water bodies and typically 0.01 to 0.3 for unconfined aquifers, dependent on the soil material.

The **specific storage** S_S is the volume of water released from storage per unit volume of aquifer per unit decline in pressure head; the concept of specific storage is almost exclusively used in confined aquifer analysis; the unit is [m^{-1}] [McWhorter and Sunada et al. 1977].

The **hydraulic head** is a measure of the energy that causes groundwater to flow; it is composed of pressure head and elevation head. Head is a concept that relates the energy in an incompressible fluid to the height of an equivalent static column of that fluid and is thus expressed in [m].

In the following the different types of flow which occur in a hydrologic system are explained:

- Surface runoff: Part of the total runoff (the river flow leaving the area) which results from overland flow (water flowing across the ground surface). [Price 1985]
- Interflow: Interflow (intermediate between overland flow and true groundwater flow) is lateral movement of water through the unsaturated zone until it enters a stream or river channel without having occurred first as surface runoff. [Price 1985]
- Baseflow: For a river to flow throughout the year, even during dry periods, it must have a source of water other than surface runoff and interflow. This water is termed baseflow. It can be provided by groundwater discharge from an aquifer, from surface-water storage (e.g. lake), or from the melting of glacier ice or of snow. The first of these sources is the most common, and often the terms baseflow and groundwater discharge are used as though they were synonymous. [Price 1985]
- Groundwater flow: Water which moves down a hydraulic gradient in the saturated zone. [Davie 2008]
- Streamflow: Water flowing within a stream channel. Often referred as discharge. [Davie 2008]

The relations between all the described processes and parameters (and many more) have to be considered in a hydrological model. How such a model can be configured, is shown in the following as an example.

3.2.2 Hydrological modelling (example WaSiM-ETH)

The WaSiM-ETH (Water balance Simulation Model ETH) is a model for the simulation of the water balance. Therefore the processes of transport, storage and state change of water are described on the basis of simplified physical relations. It is a deterministic and spatially distributed working model.
In a model the processes can, because of their complexity, only be described in a simplified way. Hence, the relevant processes have to be selected and described by physical and mathematical equations. In case of the WaSiM-ETH the following components are used [Mayr 2004], [Schulla and Jasper 2007]:

- Evaporation (potential and real)

The potential evaporation is the maximum amount of water per time unit, which can evaporate directly and/or from the vegetation into the atmosphere with respect to the actual plant physiological and meteorological conditions. It is assumed that the availability of water on the ground is unlimited. The potential evaporation is computed using the approach after *Penman-Monteith*[13].
The real evaporation is derived from the potential evaporation, considering the actual soil conditions and hence the availability of water which can evaporate.

- Snow accumulation and melt

The fraction of snow on the total precipitation is computed using air temperature. For the snow melt several approaches are provided. There is for example a temperature-wind-index-method which uses air temperature and wind velocity to derive the melting rate.

- Interception

Interception is the fraction of precipitation that does not reach the soil, but is instead intercepted by the leaves and branches of plants. In WaSiM-ETH a simple bucket approach is used with a capacity depending on the leaf area index, the vegetation coverage degree and the maximum height of water on the leafs. If the interception storage is filled, further precipitation or snow melt falls directly to the soil surface. This amount is the input for the infiltration and soil model.

- Infiltration

Infiltration is the process by which water on the ground surface enters the soil. As long as the infiltration capacity (the maximum rate at which water can enter a soil) is larger than the precipitation intensity, water infiltrates into the soil. The exceeding amount (the not infiltrated water) is surface runoff. The infiltration model is an integrated part of the soil

[13] MONTEITH J L (1975): *Vegetation and the atmosphere, Vol.1: Principles*. London: Academic Press.
BRUTSAERT W (1982): *Evaporation into the atmosphere*. Dordrecht: Kluwer Academic Publishers.

model, since there is a strong interaction. The approaches for the calculations are based on the works of *Peschke*[14].

- Soil model (unsaturated zone model)

The soil model describes the fluxes in the unsaturated soil zone. Therefore the *Richards*-equation for the unsaturated zone[15], in a former version of the model the TOPMODEL approach, is used. The water content is the sum of inflow and discharge of one grid cell. The *Richards*-equation relates the water content to soil parameters to determine the fluxes. Soil parameters are hydraulic conductivity (unit [m/s]) and hydraulic head, which are expressed by further parameters. WaSiM-ETH calculates the *Richards*-equation in the spatially and temporally discretized form for each grid cell. The used soil parameters have a constant value for the whole grid cell, although the soil properties are normally inhomogeneous. Only vertical water movements between several soil layers are considered. Thus adjacent grid cells in horizontal direction do not communicate with each other.

- Groundwater flow and transport

The groundwater model describes the flow in the saturated zone. Lateral fluxes are computed as result of the distribution of the hydraulic head. The unsaturated zone module calculates the flux between the unsaturated zone and the groundwater. This flux is given to the groundwater module as upper boundary condition (known flux boundary).
The groundwater module uses a multi-layer model. Each layer is modelled 2-dimensional in horizontal direction in a regularly spaced grid. For the coupling between the layers leakage factors are used. The connection to surface water is done by leakage approaches within the unsaturated zone model. It allows to calculate infiltration from rivers as well as exfiltration into the rivers (baseflow). If the groundwater reaches the surface of the soil, surface runoff is generated.
The flux equation is a differential equation which describes the balance of water pouring in and out of a certain volume. It is a combination of the continuity equation and the *Darcy*-equation[16], which relates the discharge to hydraulic gradient and hydraulic conductivity.

- Discharge routing

This part of the model computes the water flows in the channels. WaSiM-ETH does the routing based on a hydraulic calculation of the flow velocities. This requires channel characteristics like flow profile or roughness of the stream bed. The discharge routing is

[14] PESCHKE G (1977): *Ein zweistufiges Model der Infiltration von Regen in geschichtete Böden*. Acta hydrophysica, 22 (1): 120-145.
PESCHKE G (1987): *Soil Moisture and Runoff Components from a Physically Founded Approach*. Acta hydrophysica, 31 (3/4): 191-205.
[15] RICHARDS L (1931) *Capillary Conduction of liquids through porous medium*. Physics (1): 318-333.
[16] DARCY H (1856) *Les fontaines publiques de la ville de Dijon*. Paris: V. Dalmont.

based on a cinematic wave approach using different flow velocities for different water levels in the channel. The total discharge is composed of surface runoff, baseflow, interflow and retention.

The model structure is shown in Figure 3.2:

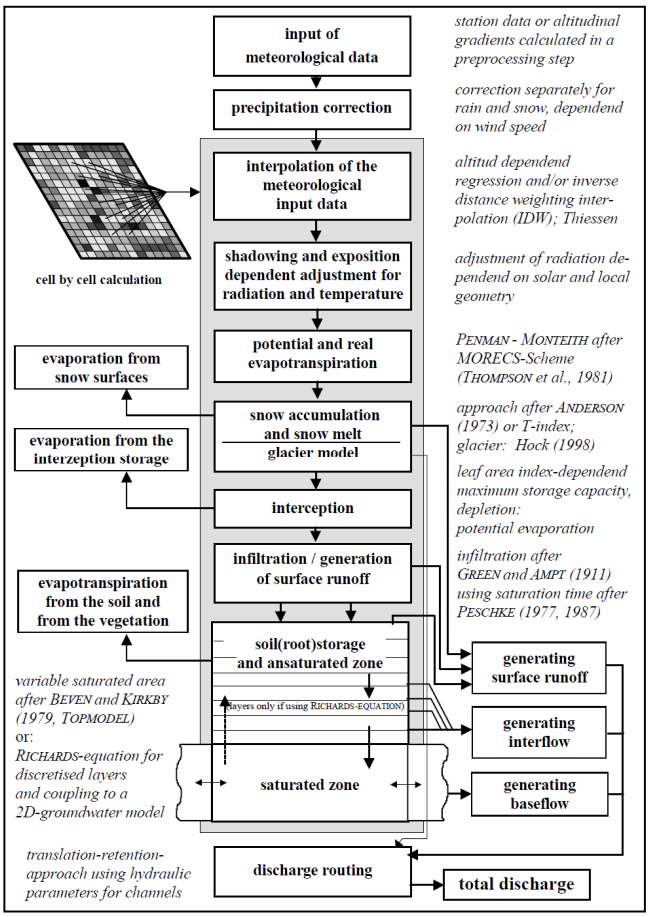

Fig. 3.2: Model structure of WaSiM-ETH, from Schulla and Jasper [2007]

Typical resolutions used for the modelling of a catchment with the size of the Ammer are:

- 90 m grid size in horizontal direction
- 15 vertical layers down to 10 m depth in the soil model

Input data:

The described model structure needs several input data. It can be distinguished between three types of data:

- geographical data
  - DEM (digital elevation model)
  - soil data (conductivity, soil type, specific capacity, soil type, thickness of soils, rock densities).
  - land use classification and characteristics

- meteorological data
  - temperature
  - precipitation
  - relative humidity
  - wind speed
  - global radiation or sunshine duration
- hydrological data.
  - discharge from gauges
  - groundwater level
  - thickness of acquifers

The main output parameters are, as can be seen in Figure 3.2, evapotranspiration, baseflow, interflow and surface runoff. Further parameters, which can be derived, are e.g. infiltration, soil moisture or groundwater recharge.

The most important input parameter is precipitation, due to the strong dependency between the amount of water which comes into the catchment and all other quantities and relations, which arise during the modelling.
For a spatially distributed model like the WaSiM-ETH the input data has to be interpolated on a grid, as far as it is not available. Land use data derived from classification of satellite images are available over the whole area but precipitation and all other meteorological data usually have to be interpolated from the recordings of measuring stations.
Measured data is necessary for the model calibration, i.e. the adjustment of model parameters, as well as for the validation of the model.
For both cases often gauge measurements are used, but in principle all quantities which can be measured and converted into an output quantity of the model can be used.

3.2.3 Converting modelling results to gravity changes

The next step is the geophysical forward problem which consists of the calculation of gravity variations from the output of a hydrological model. This task has to be performed if gravity measurements shall be reduced with modelling results. If a certain hydrological parameter shall be derived from gravity measurements the task is even more complex, since the gravity measurement integrates over all changes.
Since the gravimeter is mainly influenced by the near surrounding, a model with a relatively high resolution is needed in the area around the gravimeter. The modelling approaches in the TERENO site use a grid size of ≈ 90 m. Thus the model has to be refined for the grid cell, the gravimeter is located in.

Leirião et al. [2009] present a method which can be used to calculate hydrological-induced temporal variations in gravity from any hydrological model, provided Earth curvature effects can be neglected. The method is consisting of three equations. The water storage change in hydrological model cells is modelled as prismatic mass storage change. The hydrological density changes $\Delta\rho$ depend on the hydrological state variables, provided by the hydrological model. Three different cases for the computation of $\Delta\rho$ are distinguished:

saturated zone: $$\Delta\rho = \rho_w \cdot S_y \cdot \Delta h \qquad (67)$$

vadose zone: $$\Delta\rho = \rho_w \cdot \Delta\eta \qquad (68)$$

overland water bodies: $$\Delta\rho = \rho_w \cdot S_f \qquad (69)$$

ρ_w water density
S_y specific yield
Δh hydraulic head change
$\Delta\eta$ soil water content change
S_f flooding state (1 if flooded, 0 else)

For the density change of unconfined aquifers and overland water bodies $\Delta\rho$ is constant between the initial and final water table and zero elsewhere. Then it holds for the density change at a position x, y, z (z positive downwards):

$$\Delta\rho(x,y,z) = \rho_w \cdot S_y(x,y,z) \cdot f(x,y,z) \qquad (70)$$

$$\text{with } f(x,y,z) = \begin{Bmatrix} 1 \text{ for } z_i(x,y) < z < z_f(x,y) \text{ if } z_i < z_f \text{ (water table falls)} \\ 1 \text{ for } z_i(x,y) > z > z_f(x,y) \text{ if } z_i > z_f \text{ (water table rises)} \\ 0 \text{ else} \end{Bmatrix}$$

S_y specific yield
z_i depth of initial water table [m]
z_f depth of final water table [m]

This can also be used for the snow coverage. For that S_y has to be replaced by the percentage of the snow density with respect to the water density.

Three equations are developed for computing the incremental gravity change due to groundwater level or overland water level change for one time step. The first equation (71) holds for the assumption that all mass of one grid cell is concentrated in the centre of the cell (point mass equation). The second equation (72) holds for the case that it is integrated over the whole mass element in one cell (prism equation, cf. also [Torge 1989, Equation 4.26]). The third equation (73) is an approximation for the prism equation, derived by

MacMillan (MacMillan formula), since the prism equation becomes numerically unstable for larger distances between the instrument and the cell.

Equation 1:
$$\Delta g = G\rho_w S_y \Delta h \frac{-\bar{h}}{\left(x^2 + y^2 + \bar{h}^2\right)^{3/2}} \Delta x \Delta y \qquad (71)$$

Equation 1 can only be used in that way, if S_y is constant over the whole height, where the water level change takes place. Otherwise the equation has to be solved for several layers.

Equation 2:
$$\Delta g = G\rho_w S_y \left[x \ln\left(y+d\right) + y \ln\left(x+d\right) - z \arctan \frac{xy}{zd} \Big|_{x_{p,2}}^{x_{p,1}} \Big|_{y_{p,2}}^{y_{p,1}} \Big|_{z_{p,2}}^{z_{p,1}} \right] \qquad (72)$$

Equation 3:
$$\Delta g = G\rho_w S_y \Delta x \Delta y \Delta z \left(-\frac{z}{d^3} - \frac{5}{24} \frac{\left(ax^2 + by^2 + cz^2\right) z}{d^7} + \frac{1}{12} \frac{cz}{d^5} \right) \qquad (73)$$

with
$$a = +2\Delta x^2 - \Delta y^2 - \Delta z^2$$
$$b = -\Delta x^2 + 2\Delta y^2 - \Delta z^2$$
$$c = -\Delta x^2 - \Delta y^2 + 2\Delta z^2$$

and
$$d = \sqrt{x^2 + y^2 + z^2}$$

The instrument is located at $x = 0$, $y = 0$, $z = 0$; z is defined positive downwards!

$\bar{h}$	average depth of the water level in one time interval
$\Delta h = z_f - z_i$	difference in water level between two time steps [m]
Δx , Δy , Δz	cell size [m]
$x_{p,i}$, $y_{p,i}$, $z_{p,i}$,	corner coordinates of a resolution cell
x, y, z	centre coordinates of a resolution cell

For the decision which of the three equations is applied, following criterion is used by Leirião et al. [2009]:

$$\chi^2 = \frac{r^2}{dr^2} = \frac{x^2 + y^2 + z^2}{\Delta x^2 + \Delta y^2 + \Delta z^2} \qquad (74)$$

→ for $\chi^2 < 4$ prism equation is used
→ for $\chi^2 < 81$ MacMillan formula is used
→ else point mass equation is used

For the unsaturated (vadose) zone the density change has to be determined for every horizontal layer. The term for $\Delta\rho$ is now only valid for a layer with height Δz_l and the point mass equation (71) is replaced by the sum of the gravity change for each layer:

$$\Delta g = \sum_{i=1}^{layers} G\rho_w(\eta_f - \eta_i)\Delta z_{l,i} \frac{\overline{z}_i}{\left(x^2 + y^2 + \overline{z}^2\right)^{3/2}} \Delta x \Delta y \qquad (75)$$

$\overline{z}$ depth of the cell centre (mean cell depth)
η_f final water content
η_i initial water content

In the other two Equations 73 and 74 $\rho_w \cdot S_y$ has to be replaced by $\rho_w(\eta_f - \eta_i)$ for the unsaturated zone.

3.3 Signals in the Ammer catchment

3.3.1 Atmosphere

Pressure variations in the TERENO area from ECMWF data

ECMWF data (Class: Operational archive, Stream: Atmospheric model, Type: Analysis, Parameter: Surface pressure, Grid: 0.25° x 0.25°)[17] for the years 2007 and 2008 for surface pressure with a temporal resolution of 6 hours and a spatial resolution of 0.25° is used to asses how large atmospheric variations are in the TERENO area. For this three grid cells with the centres at 47.5° latitude 11° longitude, 47.75° latitude 11° longitude and 47.5° latitude 11.25° longitude, which cover the whole TERENO are taken, and the mean of them is computed. To check if there are some signals with longer periods, also weekly and monthly means are calculated. To estimate the influence of these variations on gravity, the pressure variations are multiplied with the admittance factor of -0.3 µGal/mbar. Because there is also the coarse approximation of -0.3 mm/mbar for the geometric loading effect, the scale on the y-axis of the Figures 3.4, 3.6 and 3.8 is also valid for [mm].

[17] obtained from http://www.ecmwf.int/products/data/archive/finder.html; last access 25.11.2010

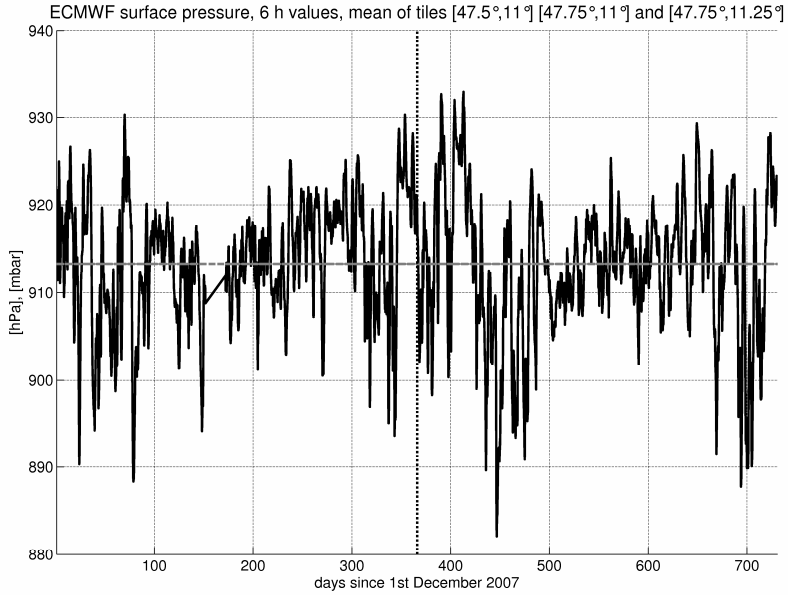

Fig. 3.3: 6 hour surface pressure values for the years 2007 and 2008 from ECMWF for tiles with the centres 47.5° lat. 11° lon., 47.75° lat. 11° lon. and 47.5° lat. 11.25° lon.; the horizontal line is mean pressure over the whole period

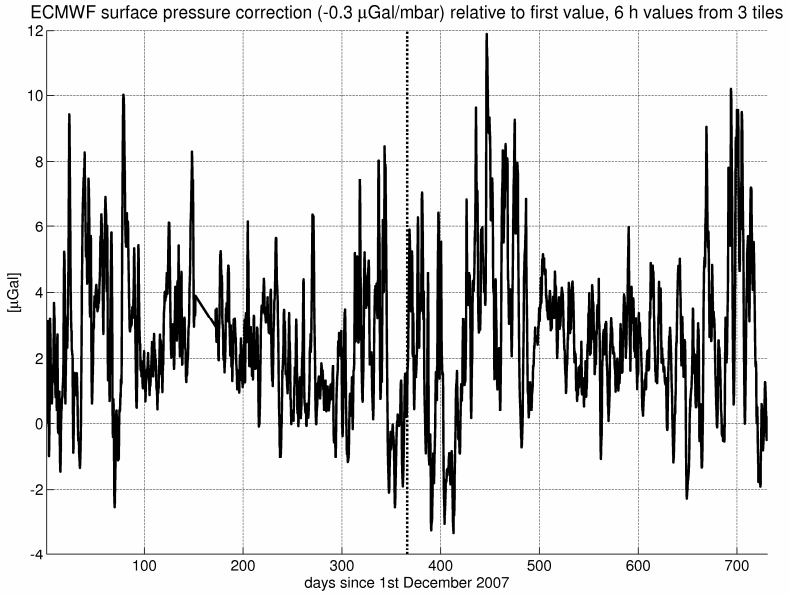

Fig. 3.4: Surface pressure correction relative to first value from 6 hour surface pressure values (cf. Figure 3.3), computed with admittance factor -0.3 µGal/mbar

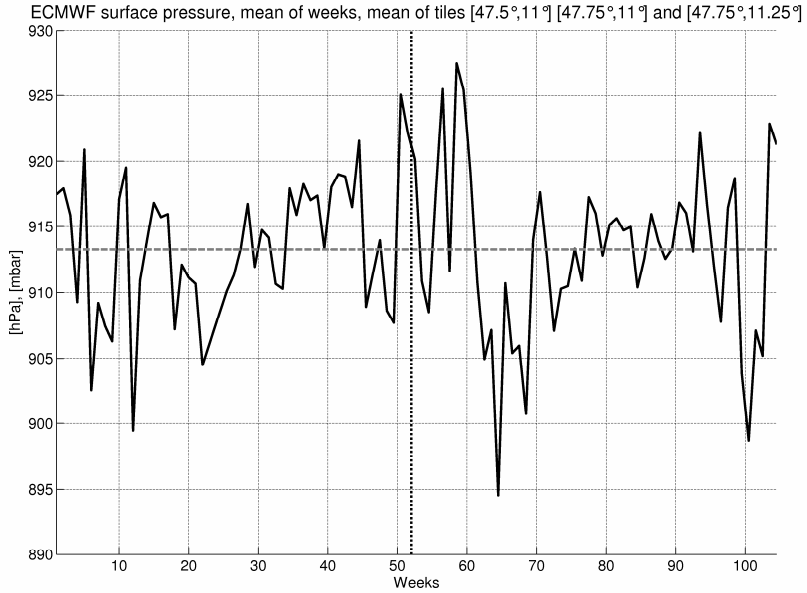

Fig. 3.5: Weekly surface pressure values for the years 2007 and 2008 from ECMWF for tiles with the centres 47.5° lat. 11° lon., 47.75° lat. 11° lon. and 47.5° lat. 11.25° lon.

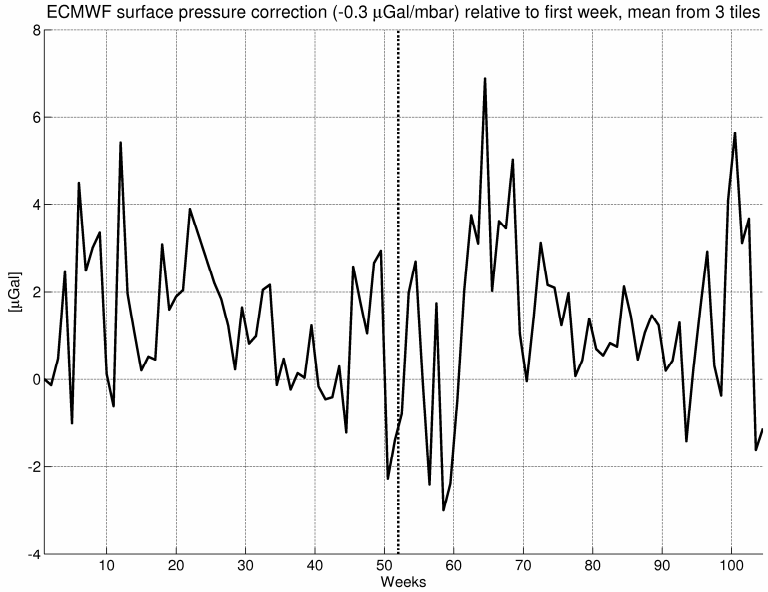

Fig. 3.6: Surface pressure correction relative to first value from weekly surface pressure values (cf. Figure 3.5), computed with admittance factor -0.3 µGal/mbar

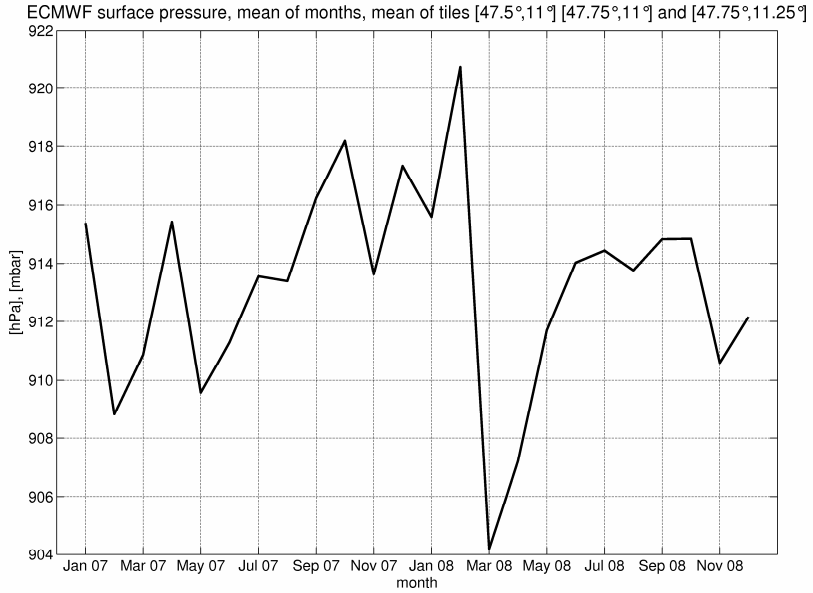

Fig. 3.7: Monthly surface pressure values for the years 2007 and 2008 from ECMWF for tiles with the centres 47.5° lat. 11° lon., 47.75° lat. 11° lon. and 47.5° lat. 11.25° lon.

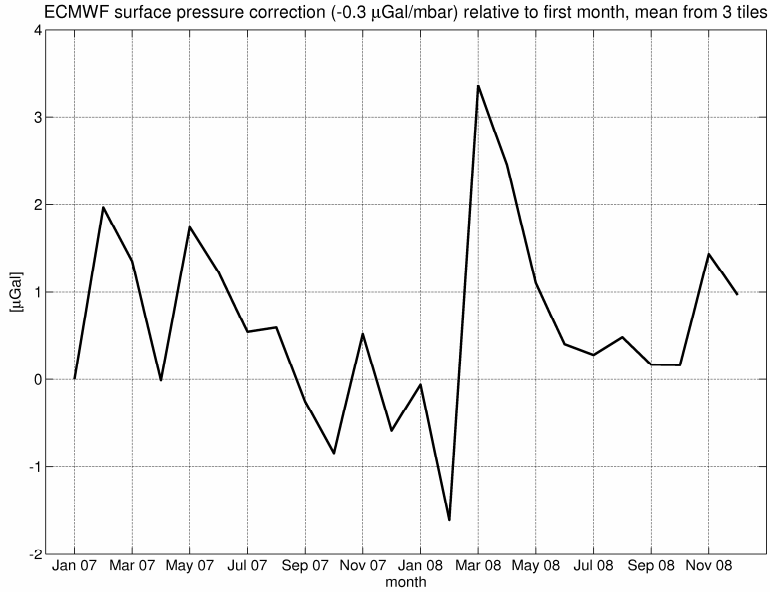

Fig. 3.8: Surface pressure correction relative to first value from monthly surface pressure values (cf. Figure 3.7), computed with admittance factor -0.3 µGal/mbar

In Tables 3.1 and 3.2 the minimum and maximum values and variations are given in [mbar] and in [μGal], respectively. They are given for the 6 hour, the weekly and the monthly values, which are shown in the Figures 3.4 to 3.8, and additionally for daily values.

	variations within two years (relative to first value)			**variations relative to previous measurement**	
	min [mbar]	max [mbar]	max var. between two values [mbar]	max change [mbar]	mean change [mbar]
6 h	-39.66	11.13	**50.79**	11.42	1.34
day	-32.19	13.67	45.86	19.90	3.34
week	-22.92	10.01	32.93	**20.07**	**4.97**
month	-11.17	5.37	16.54	16.53	3.36

Table 3.1: Pressure variations in the TERENO area

	variations within two years (relative to first value)			**variations relative to previous measurement**	
	min [μGal] ([mm])	max [μGal] ([mm])	max var. between two values [μGal] ([mm])	max change [μGal] ([mm])	mean change [μGal] ([mm])
6 h	-3.34	11.90	**15.24**	3.42	0.40
day	-4.10	9.66	13.76	5.97	1.00
week	-3.00	6.88	9.88	**6.02**	**1.49**
month	-1.61	3.35	4.96	4.96	1.01

Table 3.2: Resulting gravity and height variations from the pressure variations

It can be seen that the overall maximum deviation of two values is largest for the 6 hour values. This is understandable because the data is smoothed during the averaging for a certain time span. From the 6 hour values the maximum pressure variation of 50 mbar for the TERENO area can be derived, which corresponds to a gravity change of about 15 μGal. The changes relative to the previous time step are an indicator for the periodicity of the atmospheric signal. The largest changes occur between adjacent weeks with an average of 5 mbar. For daily and weekly data a maximum change between two time steps of 20 mbar is found, for monthly values the maximum is only 16.5 mbar. Remarkable is that there is even a pressure change of over 10 mbar in between 6 hours, but the mean change for the 6 hour values is clearly smaller than for the other time spans.

These results confirm that the main period for changes in the atmosphere are several days as described in Chapter 2. A seasonal signal, which was also claimed in Chapter 2, can not be found in this data. In Figure 3.7 no real dependency between pressure and the season can be seen. But it can be recognized in the plots with the 6 hour and weekly values (Figures 3.3 to 3.6) that the short- to medium-term variability of the pressure is larger in the winter than in the summer period.

The analysis also indicates that there are no distinct recurring periods in the atmospheric signal.
Evaluating these results with respect to geometric displacements it has also to be considered that the Earth does not react to very short-term changes, but mainly to large pressure systems of certain extent, as described in Chapter 2. Hence there should not be placed so much confidence in the estimations with the unit [mm] in Table 3.2, especially for the 6 hour and daily values.

Comparison in of situ data from Hohenpeißenberg and ECMWF data

Now the consistency of the ECMWF data is validated with measurement data from a station on Hohenpeißenberg. For that daily means have been calculated from both, the ECMWF 6 hour values and the Hohenpeißenberg hourly values. Figure 3.9 shows both data series.
The mean offset between the two data series is 22.5 mbar. This relatively high value is related to the fact, that Hohenpeißenberg is a station on a pre-alps peak and because of this the mean height of the ECMWF grid cell may be clearly smaller. But, as can be seen in Figure 3.10, the pressure changes, relative to the first day of the data, show the same behaviour. The difference of both series shows only a variation of ±2 mbar after subtracting the mean offset (Figure 3.11). From that it can be concluded that the error if ECMWF data is used, instead of local pressure, is (in this case) smaller than 1 μGal.

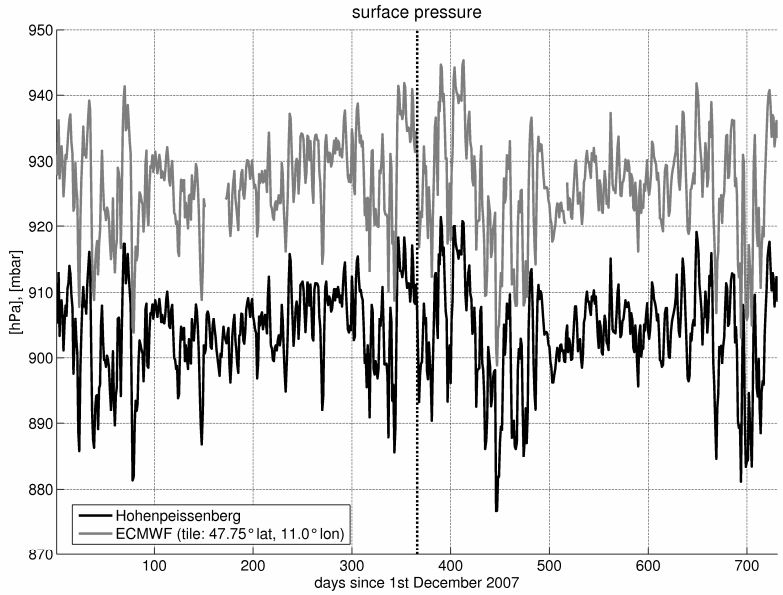

Fig. 3.9: Comparison of daily surface pressure values for the years 2007 and 2008 from observation station Hohenpeißenberg and ECMWF tile with centre 47.75° lat. 11° lon.

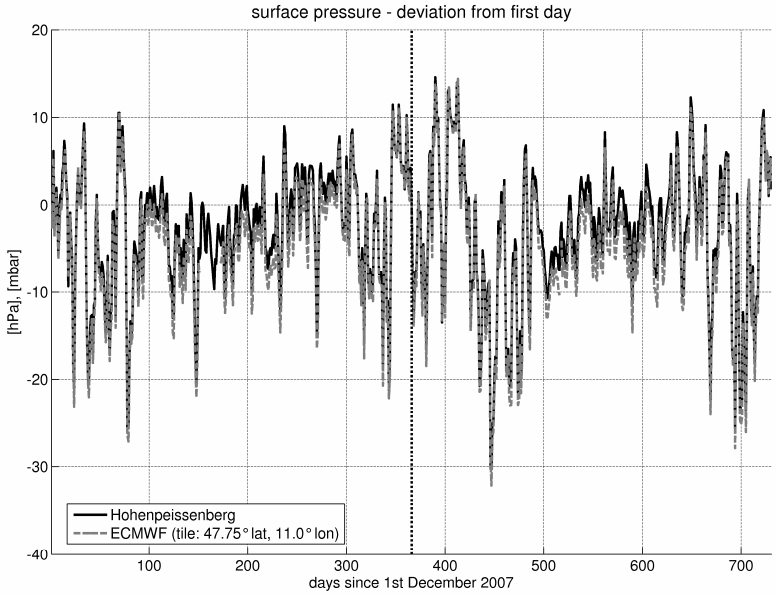

Fig. 3.10: Daily surface pressure deviations from first day, for values from Figure 3.9

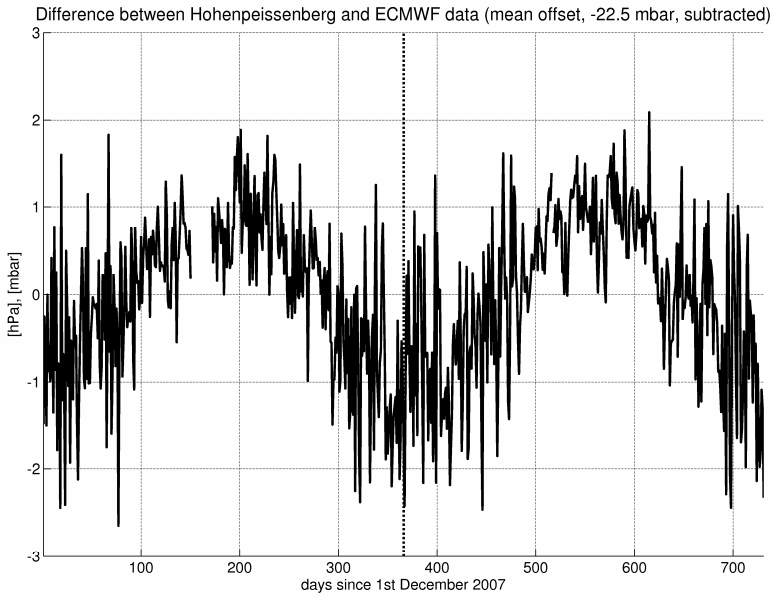

Fig. 3.11: Difference between the Hohenpeißenberg and ECWMF surface pressure data from Figure 3.9, a mean offset of -22.5 mbar is subtracted

Two characteristics of the pressure difference can be derived from the plot (Figure 3.11):

- The deviation is smaller in the summer (the largest positive values are the one with the smallest deviation because of the subtracted negative offset).
- The variability in the deviations is larger in the winter (probably because the pressure values themselves show a greater variability).

The variations in gravity are derived from the Hohenpeißenberg data in the same way as it was done for the ECMWF data (cf. Table 3.2). This delivers -4.39 µGal as minimum, 9.07 µGal as maximum and a maximum variation of 13.46 µGal, what is nearly the same as for the mean of the three ECMWF-tiles.

3.3.2 Hydrology

Precipitation

Figure 3.12 shows daily precipitations sums for the year 2008, Figure 3.13 shows monthly precipitation sums for the years 2007 to 2009, both for the stations in Ettal (Linderhof) in the south and Hohenpeißenberg in the northwest. It can be seen that the precipitation is larger in the summer period. As told in the beginning of the chapter the precipitation is larger in the southern mountainous region, what can be seen at the mean (2007 - 2009) yearly precipitation sums of the two stations:

Ettal-Linderhof: 1605 mm
Hohenpeißenberg 1118 mm

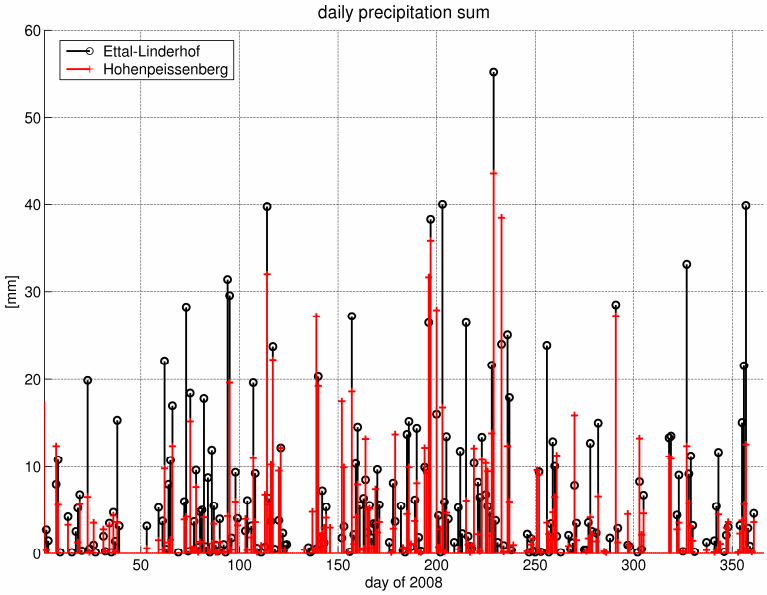

Fig. 3.12: Daily precipitation sum for the stations Ettal-Linderhof and Hohenpeißenberg for the year 2008

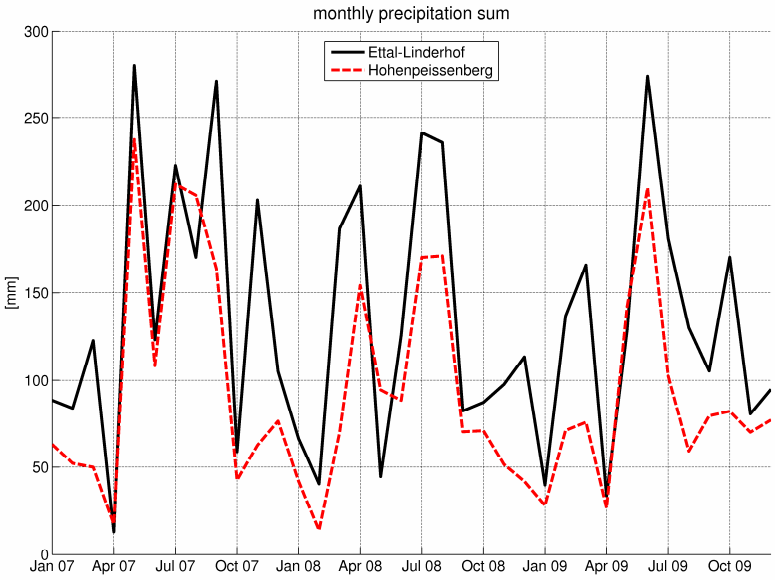

Fig. 3.13: Monthly precipitation sum for the stations Ettal-Linderhof and Hohenpeißenberg for the years 2007 to 2009

From the monthly precipitation sums the change of the water storage is estimated using the following assumptions.

The proportion of the stored water, which is not lost due to evaporation and surface runoff, is one third. Then the storage for one month is estimated using the following equation:

$$sto_i = \sum_{month=i-1}^{i-3} prec(month) + \sum_{month=i-4}^{i-6} prec(month)/2 \qquad (76)$$

This equation is also used by Demoulin et al. [2007]. It is a kind of smoothing filter for the precipitation.

Since there is no start value available, one can only estimate the storage change. Here the deviation from the mean value of the three years is calculated for both stations (Figure 3.14). An annual signal arises from these estimates, with a maximum storage in the end of summer / autumn and a minimum in spring. Snow storage, which is not considered in the approximation, may attenuate this minimum but will not change the annual characteristic of the signal. This estimation clearly differs from the signal from global models (see below).

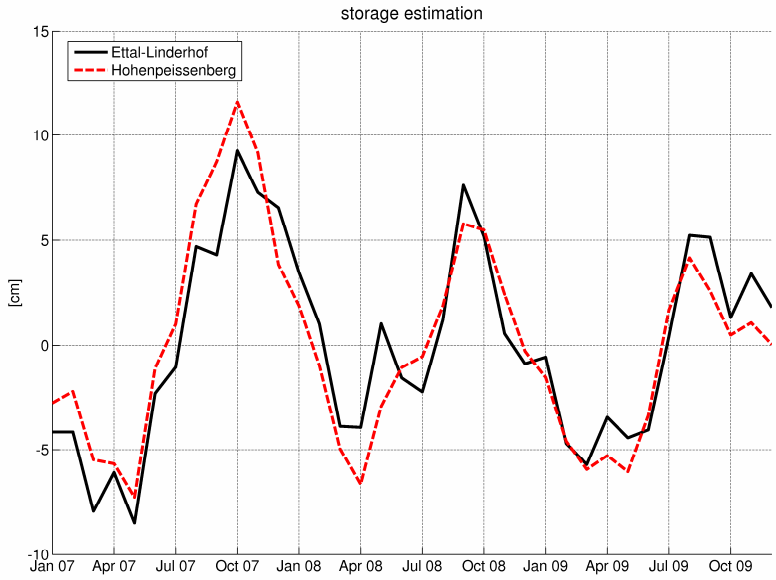

Fig. 3.14: Simple water storage variation estimation using Equation 76 for the years 2007 to 2009 with precipitation data from the stations Ettal-Linderhof and Hohenpeißenberg

Groundwater level

Groundwater level time series are available for the period from 1.11.99 to 31.10.01 [Mayr 2004]. In Figure 3.15 the groundwater level variations for the stations Ettal and Graswang in the south of the TERENO area are shown. In Figure 3.16 the groundwater variations for the stations Weindorf, Deutenhausen, St. Andrae and Kronau, all in the northeast of the TERENO area, are shown.
It can be seen that for most stations high water levels are reached in the summer period and low water levels in winter or spring. This fits relatively well to the storage estimation in Figure 3.14. It has to be regarded that the observation wells can only depict the variation of one groundwater layer and that there can be more layers above or below with different behaviour.

In Figure 3.17 gravity variations are calculated from the groundwater levels as approximation, assuming a cylinder with radius 200 m in which the groundwater change takes place. The specific yield of the saturated soil is set to 0.1. The fictive gravimeter is located at the centre of the cylinder. Except of Graswang the maximum variations for all stations are in a range of 3 to 5 µGal. Graswang shows a very high signal with a maximum variation of about 60 µGal.

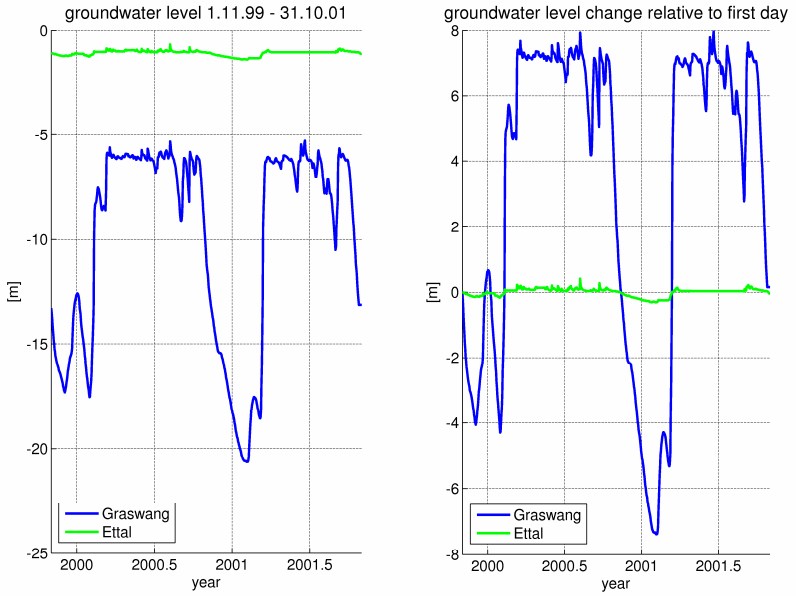

Fig. 3.15: Groundwater level (left) and groundwater level variations (right) for stations Graswang and Ettal for the period from 1.11.99 to 31.10.01

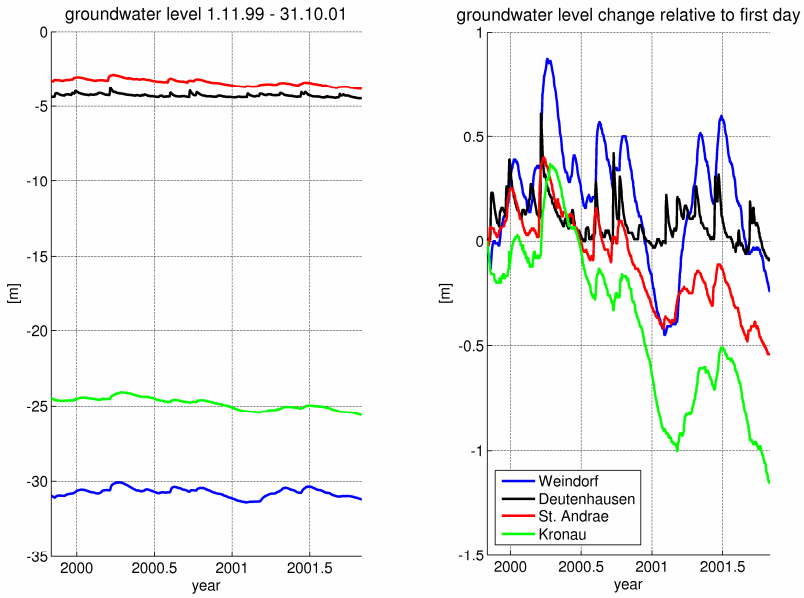

Fig. 3.16: Groundwater level (left) and groundwater level variations (right) for stations Weindorf, Deutenhausen, St. Andrae and Kronau for the period from 1.11.99 to 31.10.01

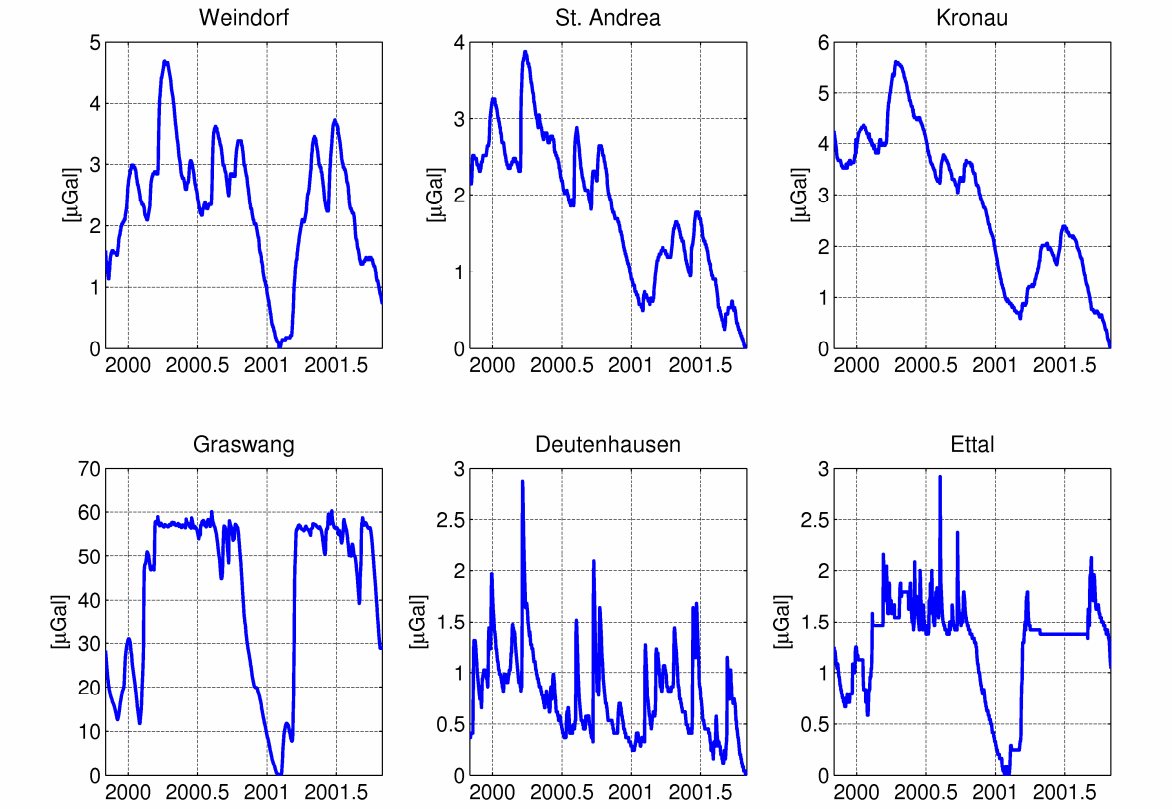

Fig. 3.17: Gravity variations due to groundwater variations shown in Figure 3.15 and 3.16, using a cylinder with 200 m radius and a specific yield of 0.1 for the approximation

Estimates of annual signals

Figures 3.19 and 3.20 show measures for signals with a mainly annual period from following sources:

- Equivalent water heights (EWH) from GRACE

Equivalent water heights are derived from monthly GRACE fields of the years 2007 to 2009. GSM-2 fields from GFZ Potsdam, developed up to degree 120, are used. The deviation of the coefficients from the mean coefficients of these three years is converted to EWH with Equation 27 given in Chapter 2. The coefficients are processed with a Gaussian filter of radius 500 km. This implicates that the EWH are representing a regional signal. The plotted EWH are the mean of two one degree cells with the following centre coordinates: φ = 47.5°, λ = 10.5° and φ = 47.5°, λ = 11.5°.
Additionally gravity anomaly variations are directly derived from the filtered deviations of the coefficients (see Figure 3.21).

- Water storage from WGHM

The WGHM (Watergap Global Hydrological Model[18]) is a conceptual global model that simulates the continental water cycles with 0.5° resolution. Modelled water storages include interception, soil water, snow, groundwater and surface water. The model is forced by climate data from the ECMWF and precipitation data from GPCC (Global Precipitation Climatology Centre). [Werth et al. 2009]

The signal in Figure 3.20 is the deviation from the mean water storage of the time interval Jan. 2007 to May 2009 for the mean of the grid cells with following centre coordinates: φ = 47.75°, λ = 10.75° and φ = 47.75°, λ = 11.25°.

- Annual deformation signals from homogeneously reprocessed VLBI and GPS height time series

Tesmer et al. [2010] calculated long term height series for VLBI and GPS stations. From these series mean annual signals were formed. This is possible because signals of annually repeating nature appear after an appropriate smoothing. Clusters of stations with similar mean signals are built and a common signal is calculated (weighted means of the mean annual signals of each clusters' stations = regional average mean annual signals). The mean annual signal in Figure 3.19 is calculated from the height series of the stations Kootwijk, Potsdam, Toulouse, Wettzell and Zimmerwald. These stations represent regional geophysical deformation effects in Central Europe (see Figure 3.18, left). A good geophysical interpretability of the data as integral vertical deformation is assumed by the authors. The good agreement of the different stations indicates that it is a real signal and no local or technical artefact. The mean annual signals for all clusters can be obtained from the IAPG homepage[19].

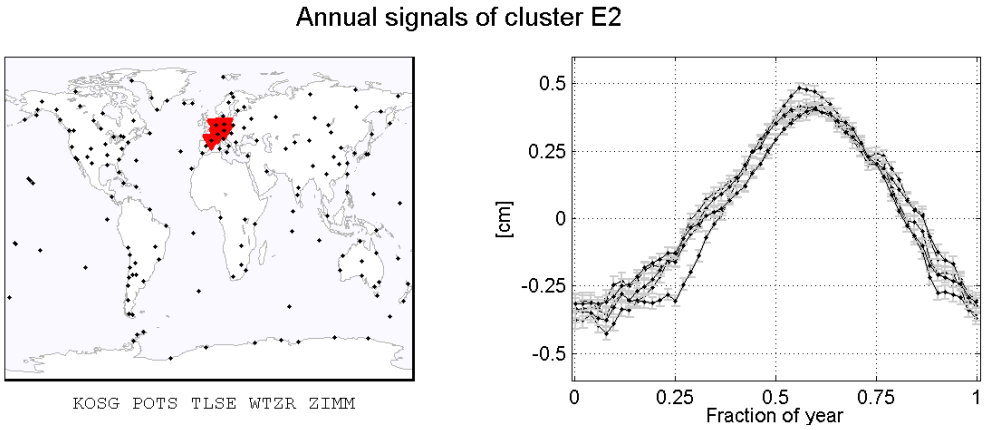

Fig. 3.18: Annual deformation signals from homogeneously reprocessed VLBI and GPS height time series [Tesmer et al. 2010]: Cluster E2 (left) and mean annual signal for all E2-stations (right), figure from IAPG homepage[19].

[18] DÖLL P, KASPAR F, LEHNER B (2003) *A global hydrological model for deriving water availability indicators: model tuning and validation*. Journal of Hydrology, 270 (1-2): 105-134.

[19] http://www.iapg.bv.tum.de/mean-annuals/; last access: 28.11.2010

The EWH should only represent the changes in water storage, while the E2 signal includes also atmospheric loading or other geophysical effects, but the hydrology is a main part of the signal, since the short term atmospheric effects should be removed because of the smoothing.
EWH and E2 are plotted in Figure 3.19. For the EWH one can detect an annual signal in the data, maxima can be found in the spring (or winter), minima in the autumn. The E2 annual signal has its maximum in August and its minimum in January. This corresponds to the EWH signal since a larger loading mass leads to a decrease in station height. There can also be seen a small phase shift between the signals, i.e. the subsidence or the rise of the station comes too early. This can have several reasons due to the different origins of the signals:

- other effects than hydrology, which may be included in the E2 signals
- signals represent not fully the same area (filter radius from GRACE ↔ area covered by E2 stations)
- area means (GRACE) vs. point data (E2)

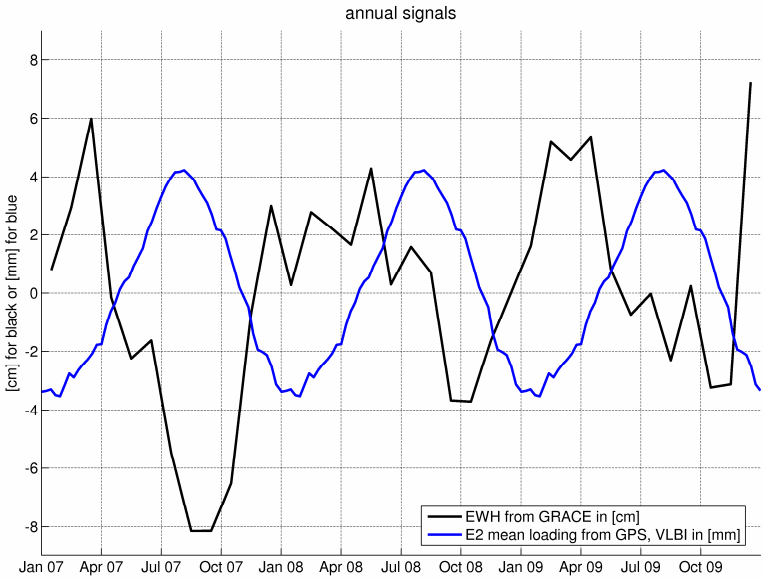

Fig. 3.19: Comparison of GRACE derived equivalent water heights and surface displacements from E2-stations (see Figure 3.18)

The geometric E2 loading signal can be taken as a reference value for the magnitude, which can be expected for the (annual) loading signal in the TERENO area:

min E2	- 3.5 mm
max E2	4.2 mm
peak to peak	7.7 mm

The peak-to-peak variation is smaller than 1 cm. If this signal shall be derived, signals with shorter wavelength, mainly the ocean loading and the short-term atmospheric pressure changes, have to be reduced accurately.

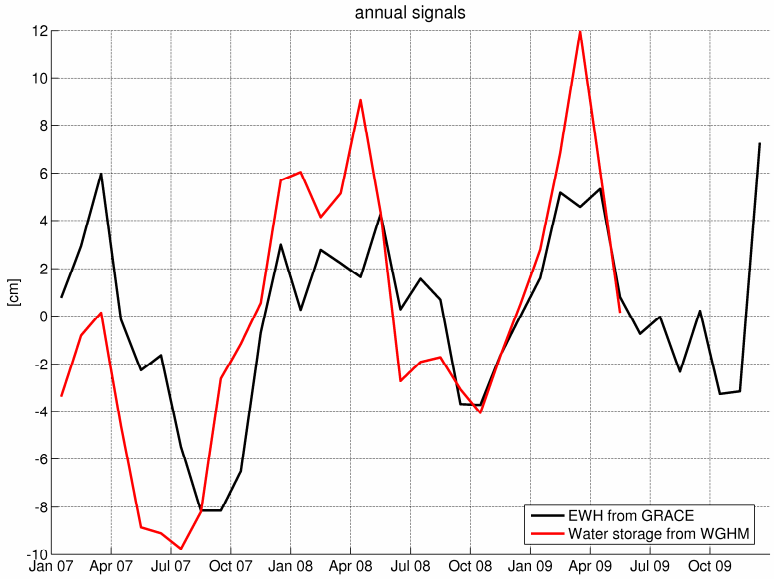

Fig. 3.20: Comparison of water storage change with EWH from GRACE and data from WGHM

In Figure 3.20 a comparison of the water storage change from GRACE and from WGHM is shown. It can be seen that the signals show a similar behaviour but the amplitudes of the WGHM data are larger. Differences arise for example from the fact that the WGHM data represents a smaller area. There also may be a shift due to the fact that the WGHM data is only available for a shorter time span. The results are shown in Table 3.3.

deviation from the mean	**EWH**		**WGHM water storage**
min	-81 mm	≙ -81 kg/m^2	-98 mm
max	73 mm	≙ 73 kg/m^2	119 mm
peak-to-peak variation	154 mm	≙ 154 kg/m^2	217 mm

Table 3.3: Comparison of the signals shown in Figure 3.20

It is remarkable that that the period with the most precipitation is the summer, what leads to the estimation of maximum storage in summer/autumn (see Figure 3.14), but the maximum of the water storage from GRACE as well as from WGHM is in spring (or winter). That indicates that the local effects may be totally decoupled from the regional or global effects.

The variations of the EWH can be approximately converted to annual gravity variations in a simple way with applying the factor $2\pi G = 0.042$ µGal m^2 kg^{-1} for the direct attraction of a Bouguer plate. This approximation for an annual gravity signal leads to a peak-to-peak variation of 6.5 µGal. It is plotted in black in Figure 3.21 and compared to gravity anomaly variations which are directly derived from the GRACE coefficient differences. As it should be this leads to a very similar signal but with smaller amplitude, the peak-to-peak variation is only 4.4 µGal.

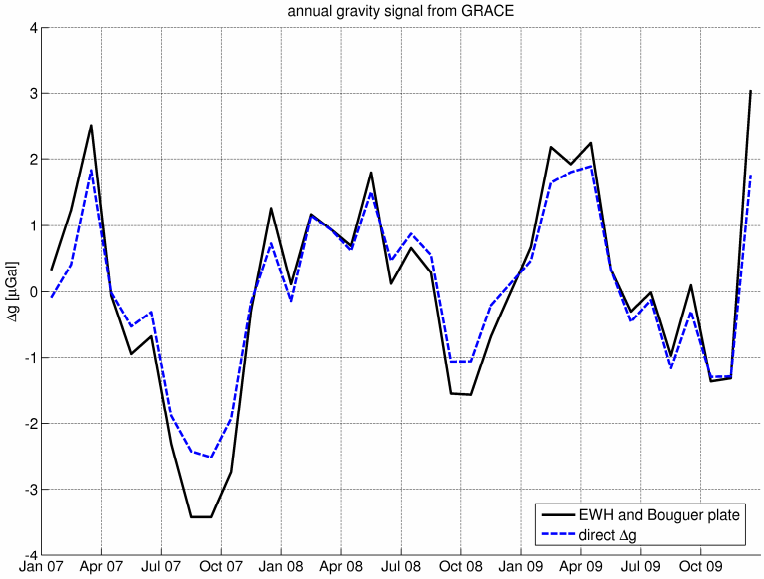

Fig. 3.21: Estimation of gravity change derived from GRACE monthly coefficients; comparison of direct computation of gravity anomaly change and computation using EWH and Bouguer plate approximation

4 Measurement techniques

In Chapter 1 the motivation for the multi-sensor test site was addressed. In the present chapter all candidate measurement techniques and instruments shall be introduced and discussed. A lot of instruments and capacities are available or (in case of the TERENO instruments) will soon be installed:

- meteorological and hydrological in situ measurement instrumentation from the TERENO alpine and prealpine Ammer observatory (full stage of extension is not reached yet)
- meteorological and hydrological in situ measurement instrumentation of other institutions like Deutscher Wetterdienst (DWD) and Wasserwirtschaftsamt (WWA) Weilheim
- relative-spring gravimeter for field observations from IAPG
- GPS receiver for measurement campaigns
- GNSS permanent stations in the TERENO area or in its vicinity from different organisations
- SAR system: TerraSAR-X and TanDEM-X; limitations with respect to the availability of images, since there may be acquisitions with higher priority
- monthly GRACE fields

Further instrumentation would be an asset for the test site:

- gravimeter with larger potential for detecting small gravity variations
- further permanent GPS stations

4.1 Meteorological / hydrological measurement stations

Beside the modelling efforts coming with the TERENO test site, several instruments, which can provide in situ data, are installed. The data from all TERENO instruments will be provided in real time on a web server in future. At all sites, hosting instruments, an internet connection is available, and all are connected to the power supply system.
Additionally to the TERENO instrumentation a list of measurement stations of other organisations is given.

TERENO Instrumentation

- *EC tower / climate stations*

In the TERENO test site two EC (= eddy covariance) towers are installed at Graswang (see Figure 4.1) and Fendt, a third one will be installed at Rottenbuch. "The eddy covariance (EC) method is a well-developed method for measuring the fluxes of momentum, sensible and latent heat (water vapour), and CO^2 between terrestrial ecosystems and the atmosphere."[20] On and around these EC-Towers several different instruments are mounted; those which are of interest are listed below:

- several water content reflectometers measuring soil water content in 6 depth levels from 2 to 50 cm
- meteorological station measuring wind velocity, wind direction, air temperature, relative humidity, air pressure, duration of rainfall, rainfall intensity, quantity of rainfall (calculated) and dew point (calculated); such an instrument is also mounted at the rain radar site in Geigersau (see below)
- acoustic distance sensor for measuring snow height

Fig. 4.1: EC tower at Graswang

Three more standard climate stations measuring wind, precipitation, pressure, temperature and humidity shall be installed in the TERENO area.

[20] from: http://imk-ifu.fzk.de/395.php; last access 01.11.2010

- *X-Band precipitation radar*

At Geigersau (Kirnberg, 949 m) an X-Band precipitation radar with a 50 km scan radius is installed. This means the whole Ammer observatory and even a larger area around can be covered using this instrument.
Evaluation of rainfall data of different time periods is performed by combining precipitation data of 40 stations within the scanned area to the *Z*/*R*-relationship [Wehrhahn et al.]. *Z* stands for the radar reflectivity factor, *R* for the rainfall rate. Because of the variability of this relationship, depending on the rain properties, its determination is an actual topic of research.

- *Lysimeter*

A lysimeter is used to measure evaporation and runoff. It is a cylinder which is embedded in the ground and filled with a soil monolith. This soil monolith shall be as conform as possible to soil and vegetation of the lysimeter's surrounding to simulate an undisturbed situation. A weighing lysimeter has a weighing device underneath (e.g. using a hydraulic pressure gauge), that allows to monitor any change in the overall water storage. Additionally the runoff through percolation (= movement of fluids through porous material) *Q* is measured at the ground of the lysimeter.
With help of the water balance-equation (cf. Formula 64) the actual evaporation *E* can be determined:

$$E = \Delta S - P - Q \qquad (77)$$

The water storage change ΔS is obtained from the weight change of the soil monolith. *P* is precipitation which has also to be measured simultaneously and closely to the lysimeter. It is also assumed that the runoff through percolation at the ground is the only runoff in Equation 77. Then the evaporation can be calculated by subtracting precipitation and runoff from the storage change. But this also means that every error in the measurement of the quantities and every non-considered effect are interpreted as evaporation. [Davie 2008]

Lysimeters are installed at the TERENO sites in Graswang (6 lysimeters) and in Fendt (18 lysimeters), and will be installed at the site in Rottenbuch (12 lysimeters). The main aim of this lysimeter network is to simulate the climate change, by bringing soil monoliths from the higher sites to the lower sites. Since the sites are at different height levels, they are at different temperature levels (cf. Figure 3.1), what simulates the warming.

The used lysimeters, shown in Figure 4.2, have the following characteristics:
- surface area: 1 m^2
- depth: 1.2 - 1.5 m
- resolution: 10 g (equivalent to 0.01 mm precipitation / water height)

Fig. 4.2: Lysimeter in Fendt

Measurement stations in the TERENO area

Further measurement stations, provided by different organisations, mainly for hydrological data, are listed in Table 4.1. Some of the data can be retrieved from the stated webpages.

Type	Location	Waters	Carrier	Source	Comments
gauge / runoff	Oberammergau	Ammer	WWA Weilheim	[1]	data online available
gauge / runoff	Obernach	Ach	WWA Weilheim	[1]	data online available
gauge / runoff	Unternogg	Halbammer	WWA Weilheim	[1]	data online available
gauge / runoff	Peißenberg	Ammer	WWA Weilheim	[1]	data online available
gauge / runoff	Weilheim	Ammer	WWA Weilheim	[1]	data online available
gauge / runoff	Obernhausen	Ach	WWA Weilheim	[1]	data online available
gauge	Seehausen	Staffelsee	WWA Weilheim	[1]	data online available
precipitation	Ettal-Linderhof	-	LfU	[2]	
precipitation	Wielenbach (Demollstr.)	-	DWD	[2]	see also meteorological station
precipitation	Oberammergau	-	DWD	[2]	
precipitation	Bad Kohlgrub	-	DWD	[2]	see also meteorological station
groundwater level	Weindorf (Murnau)	-	WWA Weilheim	[3]	
groundwater level	Wielenbach	-	WWA Weilheim	[3]	
groundwater level	Graswang	-	WWA Weilheim	[3]	
groundwater level	Deutenhausen (Weilheim)	-	WWA Weilheim	[3]	data online available
groundwater level	Kronau	-	WWA Weilheim	[3]	data online available
groundwater level	Ettal	-	WWA Weilheim	[3]	
meteorological station	Hohenpeißenberg, ID: 2290	-	DWD	[4]	data online available
meteorological station	Wielenbach (Demollstr.), ID: 5538	-	DWD	[4]	
meteorological station	Bad Kohlgrub (Rosshof), ID: 2708	-	DWD	[4]	

[1] **http://gisportal-umwelt.bayern.de/...**
website/lfw/mapservice/gkd/gkd_default.htm?appID=gkd_wstand_abfluss; last access 29.09.10

[2] **http://www.lfu.bayern.de/...**
wasser/daten/index.htm; last access 29.09.10

[3] **http://www.lfu.bayern.de/...**
wasser/fachinformationen/grundwasserstand/messstellen/index.htm; last access 29.09.10
online data from:
http://www.nid.bayern.de/grundwasser/index.php?thema=niedrigwasser&days=0&wert=grundwasser; last access 19.10.10

[4] **http://www.dwd.de/...**
bvbw/appmanager/bvbw/dwdwwwDesktop?_nfpb=true&_pageLabel=_dwdwww_menu2_leistungen_a-z_daten...
&T20411256401155013127273gsbDocumentPath=Navigation...
%2FOeffentlichkeit%2FWir__ueber__uns%2FMessnetz__node.html%3F__nnn%3Dtrue; last access 29.09.10

Table 4.1: Hydrological and meteorological measurement stations in the TERENO area

4.2 Gravimeter

There are two types of gravimeters, relative and absolute. Relative gravimeter types include superconducting gravimeters and relative-spring gravimeters. Every type is introduced in the following by examples.

4.2.1 Relative gravimeter

Relative gravimeters can measure gravity differences. In principle there are two possible measurement configurations. With a stationary gravimeter the gravity change on a single station over a long time can be recorded, with a field gravimeter gravity differences between different stations can be surveyed.
Important characteristics of relative gravimeters are:

- Calibration function / factor

A calibration function is needed to convert the measured units (counter reading) into gravity units. Because of the several parameters influencing this function it can only be modelled. The model parameters are derived from measurements of lines or profiles with known gravity differences. Generally the calibration function can be divided into a long wave (linear and non-linear) and a periodic component with frequencies depending on the instrument's design. [Torge 1989]
A calibration factor is a simpler version of the calibration function. A single factor is sufficient if the units can be transferred directly into gravity units without considering the counter reading interval.

- Drift behaviour

Relative gravimeters show a temporal variation in the display of the zero position, which is denoted as gravimeter drift. The drift can mainly be decomposed in two parts, the stationary drift due to spring aging or long-wave temperature changes and a transport drift due to shocks and the like, which additionally appears during field observations. [Torge 1989]

4.2.1.1 Relative-spring gravimeter

Gravimeters, which can be used for field measurements are normally relative-spring gravimeters. The essential part of a spring gravimeter is the spring-mass-system which functions as the gravity sensor. The properties of the counterspring which generates the equilibrium in the gravity field are decisive for its quality. A pick-off system is used to measure the change of the equilibrium position due to gravity changes.

Spring gravimeters show large drift rates. The drift is caused by fading of spring tension and by uncompensated disturbing effects. Type and magnitude of the gravimeter drift are a function of [Torge 1989]:

- type and characteristics of the specific instrument
- age and usage of the instrument
- vibrations and shocks acting on the measurement system
- uncompensated changes of the voltage of the power supply

For gravimeters, which use a metal spring (ZLS (= Zero Length Spring) technology, used for example for LCR (LaCoste-Romberg) gravimeters), the aging of the spring reduces the drift rates with time from several tens of [μGal] per day to nearly zero after several years. For quartz springs, as used for example for Scintrex gravimeters, the drift rate remains high in the order of 100 μGal to 1 mGal per day [Torge 1989].

In the following values for the accuracy of the instruments are given, but this is only a benchmark, since the accuracy which can finally be reached for a measurement is dependent on many influences like

- quality of calibration, calibration errors,
- transportation time, method of transportation (shocks),
- magnitude of total gravity difference,
- usage of a electronic feedback system (for LCR-G)
- temperature fluctuations.

Inventory

The relative-spring gravimeters listed in Table 4.2 are available, their characteristics are described in detail below.

Institution	Type	Comments
IAPG	Scintrex CG-3M	
IAPG	LaCoste & Romberg Modell G	functionality has to be proven
IAPG	LaCoste & Romberg Modell G	functionality has to be proven; with electronic feedback system
BEK	LaCoste & Romberg Modell G	

Table 4.2: Available relative-spring gravimeters

- **Scintrex CG-3M**

With the Scintrex CG-3M gravimeter gravity values can be recorded with a resolution of 1 μGal. The specification [Scintrex 1995] quotes for the typical repeatability a standard deviation of 50 μGal, which seems to be quite large, in particular as for the cheaper model a standard deviation for the typical repeatability of 10 μGal is given. The experiment in the basement (cf. Section 5.1.1) shall help to evaluate the gravimeter in terms of the measurement accuracy.

A description of the measurement principle of this instrument and its handling can be found in Schmeer [2006]. He claims an accuracy of 2 to 10 μGal for the measurement of gravity differences. Timmen and Gitlein [2004] get estimates for the accuracy (standard deviation) of single gravity differences for their Scintrex CG-3M in the order of 4 to 10 μGal on different calibration lines. On an experiment with less disturbing influences they get a standard deviation of 3.7 μGal. They also examined the drift and found a clearly linear behaviour for the (stationary) long term drift (no transportation). For the drift during field surveys the assumption of a linear behaviour does not hold anymore. Because of the enormously varying drift in that case (-0.49 to 5.92 $\mu ms^{-2}/d$, mean: 3.27 $\mu ms^{-2}/d$), they recommend to use the step measuring method (cf. [Torge 1989]) with at least three occupations of each station and by considering drift in the postprocessing procedure.
For the Scintrex gravimeter a calibration can be done with observing some gravity differences between reliable gravity stations to determine a simple calibration factor [Timmen and Gitlein 2004]. For the IAPG Scintrex gravimeter this was carried out with larger effort in the gravimetric calibration system Garmisch-Zugspitze in 2006 [Schmeer 2006].

- **LCR-G**

The functional details of the LCR-G instruments can be found in Torge [1989]. Dependent on the effort and circumstances of a measurement, accuracies of 2 to 20 μGal can be reached.
In contrast to the Scintrex gravimeter a much more extensive calibration procedure is necessary for LCR gravimeters. It is needed to improve the calibrations tables provided by the manufactures. This is because LCR gravimeters suffer from periodic errors from measurement screw and transmission, which do not exist for the CG-3 system. Thus a modelling of periodical calibration terms and of a higher order polynomial calibration function is required for the LCR-G gravimeter.
The functionality of the IAPG LCR-G gravimeter has to be tested. A first campaign was performed on 11th June 2010 with both instruments and the LCR-G gravimeter from the BEK (Bayerische Kommission für die Internationale Erdmessung). In the following a calibration campaign has to be performed for making these gravimeters ready for operation.

Optional new instruments

There are newer models on the market, which are based on the technology of the above mentioned gravimeters. These instruments provide a larger accuracy and some new features like a port for connecting a GPS receiver (CG-5) and easier ways for data logging and reading.

The **gPhone Gravity Meter** of Micro-g LaCoste is based on the LCR-G technology. The specification for this instrument[21] reports a reading resolution of 0.1 µGal, a precision of 1 µGal and a drift rate of 1.5 mGal/month ≈ 50 µGal/day. This instrument is suitable for monitoring tasks but it is not appropriate for field campaigns. The accuracy level is between the field gravimeter and the superconducting gravimeter (cf. Section 4.2.1.2).
The **Burris Gravity Meter** is based on the same technology, but can be used for field campaigns. Its specification[22] reports a data repeatability of 5 to 7 µGal and a drift of approximately 1.0 mgal/month when it is new and less than 0.3 mgal/month when it is mature.
The **Scintrex CG-5** gravimeter is the successor model of the Scintrex CG-3. Its specification[23] reports a reading resolution of 1 µGal, a standard field repeatability of less than 5 µGal and a long-term drift of less than 20 µGal/day (static).
An overview of all mentioned instruments can be found in Table 4.3.

4.2.1.2 Superconducting gravimeter

"In superconducting gravimeters (SG), the force of gravity acting on a proof mass is compensated for by a magnetic counterforce. A high long-term stability is achieved by the superconducting state of the proof masses and the current-filled coils generating the magnetic field." [Torge 1989] With this construction a non-mechanical spring is created.
The SGs are far superior to spring gravimeters with their extremely low drift rates, low noise and constant calibration factors. Because of this, SG provide a precise and continuous record of gravity variations that occur over periods of days, months, years or even decades with high stability and precision. The accuracy of 1/10 to 1/100 µGal allows the measuring of very small signals. They are the only instruments which have the feasibility to measure annual gravity signals with small amplitudes (µGal, 1/10 µGal).
SG gravimeters are very expensive (several 100 000 €) and complicated to run, especially the stationary GWR Observatory Superconducting Gravimeter (OSG) with its complex construction. SGs are used in the Global Geodynamics Project (GGP), an association of observatories with SGs, which is introduced above.

The **OSG** is a stationary instrument. The specifications for this gravimeter report a precision of 0.012 to 0.040 µGal for a one-minute averaging time and 0.002 to 0.005 µGal for a one-hour averaging time. The drift is typically less than 6 µGal / year, which is 0.016 µGal / day, after a 6 to 12 month stabilization period. [GWR Instruments 2007]
The **iGrav SG Meter** is designed to be portable, easy to use and much less expensive (≈ half of the costs) than the GWR Observatory SGs (OSG). The specifications for this

[21] http://www.lacosteromberg.com/pdf/Brochure-gPhone.pdf; last access 01.11.2010
[22] http://www.zlscorp.com/prod01.htm; last access 01.11.2010
[23] http://www.scintrexltd.com/documents/CG-5BrochureRev1.pdf; last access 01.11.2010

gravimeter[24] report a precision of 0.05 µGal for 1 minute averaging and a drift of less than 6 µGal / year. The movement of this gravimeter should not affect its calibration factor or its drift rate. Even though it is a portable instrument, it needs more effort to transport it than a LCR or Scintrex gravimeter, since it is bigger and the components have to be remounted at every station. Thus this gravimeter is not appropriate for a field campaign, but it can be used more flexible than the OSG.
The superconducting gravimeters are built by GWR-Instruments Inc., San Diego.

Global Geodynamics Project (GGP)

SGs are used in the GGP. The following statements about this project and Figure 4.3 with the European GGP stations are extracted from the GGP homepage[25]:
"The purpose of GGP is twofold. Its main objective is to record the Earth's gravity field with high accuracy at a number of worldwide stations using superconducting gravimeters. Each site is visited at least twice per year with an absolute gravimeter to co-determine secular changes and check calibration. […] The data is used in an extensive set of studies of the Earth, ranging from global motions of the whole Earth such as the Chandler wobble to the surficial gravity effects of atmospheric pressure and groundwater. The SG stations are run independently by national groups of scientists who send data each month to the GGP Data Centre […] The second objective of GGP is to maintain standards for the deployment of all GWR SGs, including site, instrument, data acquisition, and processing guidelines for SG instruments […]"

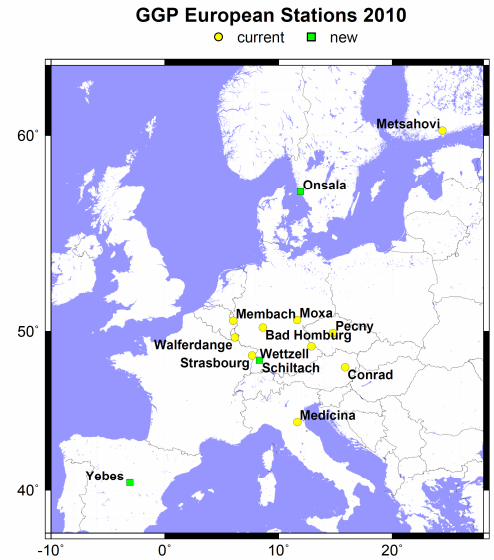

Fig. 4.3: European stations of the Global Geodynamics Project (GGP), image from GGP homepage[25]

[24] http://www.gwrinstruments.com/photos/iGrav/iGrav_091211.pdf; last access 01.11.2010
[25] http://www.eas.slu.edu/GGP/ggphome.html; last access 22.09.2010

4.2.2 Absolute gravimeter

The absolute gravimetry is based on the measurement of the acceleration quantities distance and time. Therefore the free movement of a sensor in the gravity field is observed. Nowadays only the free-fall method is used, while formerly also the pendulum method was used.
For absolute gravimeters much more efforts than for relative (-spring) gravimeters have to be made. To reach high accuracy a very stable time reference is needed and the free-fall drop has to be executed in a vacuum chamber. If a relative accuracy of $1 \cdot 10^{-9}$ shall be yielded, falling distance and time have to be determined on 1/10 [nm] level and 1/10 [ns] level, respectively [Torge 1989]. Because of the changing gravity along the falling distance the local gravity gradient has to be known exactly.

A stationary absolute gravimeter is the **FG-5** made by Micro-g LaCoste. Its specification[26] report an accuracy of 2 μGal (observed agreement between different FG-5 instruments), a repeatability of 1 μGal and a precision of 1 μGal in 3.75 minutes and 0.1 μGal in 6.25 hours.

A portable absolute gravimeter, designed for outdoor operations, is the **A-10** gravimeter, also made by Micro-g LaCoste. Its specifications[27] report an accuracy of 10 μGal, a repeatability of 10 μGal and a precision of 10 μGal in 10 minutes at a quiet site.

Absolute gravimeters are needed to provide the absolute scale for relative measurement. Because of this they can support the determination of the drift of superconducting gravimeters.

4.2.3 Overview

Table 4.3 shows all mentioned types of gravimeters and shall help to find the appropriate instrument for the particular purpose. The accuracy class is related to a single measurement, i.e. better results can be achieved with appropriate measuring configurations or longer observation duration.

[26] http://www.lacosteromberg.com/fg5specs.htm; last access 01.11.2010
[27] http://www.lacosteromberg.com/a10specs.htm; last access 01.11.2010

class			name	accuracy class	drift	price class (estimated)	comments
relative	spring	field, outdoor	LCR-G	10 µGal	30 mGal/day (new), <10 mGal/day (mature)	several 10 000 €	metal spring: zero-length-spring principle
			Scintrex CG-3M	10 µGal	hundreds of mGal/day		quartz spring
			Scintrex CG5	5 µGal	20 mGal/day		quartz spring
			Burris Gravity Meter	5 µGal	30 mGal/day (new), 10 mGal/day (mature)		metal spring: zero-length-spring principle
		portable	gPhone	1 µGal	20 mGal/day		metal spring: zero-length-spring principle
	superconducting	portable	iGrav	1/10 µGal	0.015 mGal / day	several 100 000 €	
		stationary	OSG	1/10 µGal	0.015 mGal / day		
absolute		field, outdoor	A-10	10 µGal	-	-	
		stationary (limited portable)	FG-5 / FGL	2 / 10 µGal	-	~ 200 000 € (FG-5)	FGL is a simplified version of FG-5

Table 4.3: Overview of gravimeter types

4.3 GNSS

The principles of GNSS (Global Navigation Satellite Systems) are described in many textbooks, e.g. Seeber [2003] or Hofmann-Wellenhof et al. [2008], in detail and are not presented here, only the following facts shall be mentioned:

- Main principle: Measuring of signal runtime from different satellites with known positions (orbits) to the receiver.
- Passive self-locating method: everybody who can receive the signals can use them for positioning.
- Global availability
- Microwave method: satellites send out signals in the L-band (1 - 2 GHz)
- Orbit altitude of the satellites: around 20 000 km (GPS: 20 230 km; GLONASS: 19 130 km)
- Operational systems are NAVSTAR-GPS (Navigation system with time and ranging - Global Positioning System) and GLONASS (Globalnaja Nawigazionnaja Sputnikowaja Sistema); a Chinese (COMPASS) and a European (GALILEO) system are planned, first (test) satellites are already working.

GNSS can not only be used for navigation and positioning but also for measuring geophysical signals by interpretation of changes of station coordinates or of relative coordinate changes between different stations.

For detecting signals in the [mm] range geodetic dual (at least) frequency receivers are necessary. Another important requirement is the stability of the position of the GPS antenna. That means the antenna has to be mounted on a fundament or directly on the bedrock so that no local soil settlements lead to height changes. It has always to be paid attention that there are no objects in the surrounding, which cause multi-path effects. Also snow or ice on the antenna can lead to spurious height changes.

Apart from that the observation and processing strategy is crucial for the quality of a geometric signal derived from GPS observations. Depending on that, coordinates or

coordinate changes can be detected with periods from [s] to [years] and, also dependent on these, in the [dm] to [mm] range. An important criterion is the observation duration.
Also the geodetic datum of the station coordinates has to be regarded. Dependent on the reference frame (cf. Section 5.2.2) the stations have for example different velocities (due to plate tectonics).

In Table 4.4 available GPS receivers and permanent stations for possible use are listed.

institute	type		comments
receiver (inventory)			
		number of items	
IAPG	Trimble 4000	3	old
IAPG	Ashtech	3	two of the receivers are not fit for use
IAPG	Javad	?	at least one of these receivers shall be purchased
BEK		2	can be borrowed for measurement campaign, not usable for permanent station
IMF	Leica 1200	1	
DGFI		4	can be borrowed for measurement campaign, not usable for permanent station
permanent stations			
		location	
LVG	SAPOS-Station	Garmisch-Partenkirchen (Wank)	not in TERENO area
LVG	SAPOS-Station	Weilheim	
IMK-IFU (KIT)	permanent station	Garmisch-Partenkirchen	IFU1; not in TERENO area
IMK-IFU (KIT)	permanent station	Zugspitze, permanent	ZUGS; not in TERENO area
BEK	permanent station	Wank, permanent station	not in TERENO area

Table 4.4: Available GPS receivers and permanent stations

4.4 GRACE

The GRACE (Gravity Recovery and Climate Experiment) mission is composed of two satellites, which follow each other in the same orbit with a distance of around 220 km. The main principle is the measurement of orbit perturbations due to gravity. This is done by Low-Low-SST (satellite-to-satellite tracking). This means the two satellites permanently determine their relative distance with [μm]-accuracy. From this gravity field information is derived. Non-gravitational disturbing accelerations are detected with 3D-accelerometers.
The measurements of GRACE are combined for monthly solutions of the gravity field. Various known time-variable gravity effects are already reduced from GRACE data in the course of the adjustment process. If all these effects, including oceans and atmosphere, are removed, the variations of the monthly GRACE gravity fields represent the variations of global hydrology.
These variations are normally expressed in equivalent water heights (EWH) (cf. Section 2.1.4).

4.5 SAR (TerraSAR-X, TanDEM-X)

Since the capacities of the German radar satellites TerraSAR-X (TSX) and TanDEM-X (TDX) shall be used for the measurement of geometrical signals in this work, the properties of Synthetic Aperture Radar (SAR) are shown in the context of these satellites. The advantage of SAR measurements is that they provide information over a whole scene and not only point observations.
All following explanations are extracted from Eineder and Bamler [2008], if no other is quoted.

4.5.1 Radar imaging geometry

Radar transmits microwave pulses and receives echo at the rate of the pulse repetition frequency (PRF). This means in range direction one is scanning at speed of light (radar principle), and in azimuth direction (flight direction) one is scanning at flight velocity. The radar images have complex-valued pixels, which contain amplitude (brightness) and phase information.
The radar geometry can be seen in Figure 4.4. Important for the geometry are the terms range and azimuth. The following definitions are adopted from "ESA (European Space Agency) Earthnet Online" Webpage[28]:

- *(slant) range, ground range*

"Range is the line of sight distance between the radar and each illuminated scatterer (target). In SAR usage, the term is applied to the dimension of an image perpendicular to the line of flight of the radar. Slant range is the distance from the radar, towards each target and measured perpendicular to the line of flight. Ground range is the same distance, projected using a geometrical transformation onto a reference surface such as a map. Radar data are collected in the slant range domain, but usually are projected onto the ground range plane when these data are processed into an image. The resolution of the image in the range direction is dependent on the bandwidth of the emitted pulse."[28]
If the term range is used the one-way distance between the satellite and the ground is meant, it is expressed in [m]. If the term delay is used the two-way running time of the signal is meant, it is expressed in [s].

- *azimuth*

"The term azimuth is used to indicate linear distance or image scale in the direction parallel to the radar flight path. In an image, azimuth is also known as along-track direction, since it is the relative along-track position of an object within the antenna's field of view following the radar's line of flight. Azimuth is predominately used in radar

[28] http://envisat.esa.int/handbooks/asar/CNTR5-5.htm#eph.asar.gloss.geo: GEOMETRY; last access 02.11.2010

terminology. The azimuth direction is perpendicular to the range direction. The resolution of an image in the azimuth directions for a SAR image is constant and is independent of the range."[28]

The length of the radar antenna defines the achievable resolution in azimuth direction, since a longer antenna leads to a smaller beam width on the ground. As an antenna length of several kilometres would be needed for a high resolution, the formation of the so called synthetic aperture is used. Therefore several beams along the satellite track are summed up to get a synthetic long antenna.

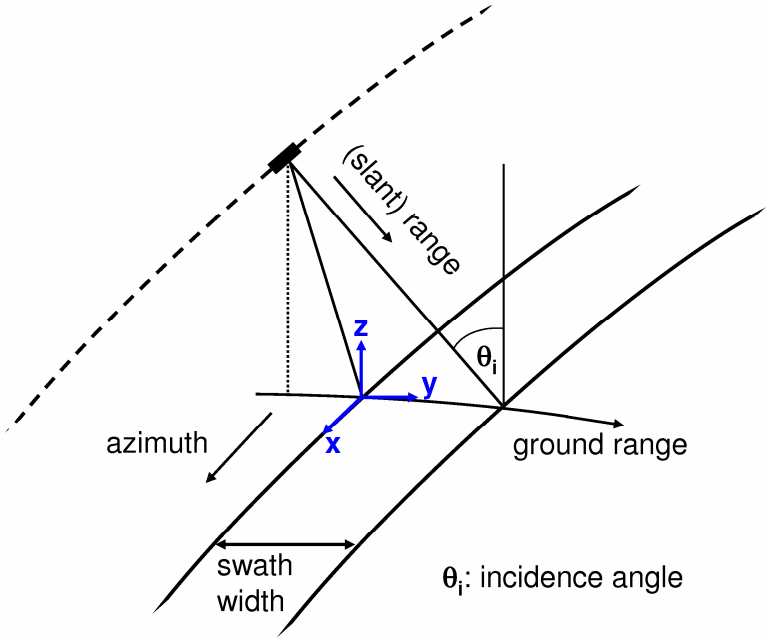

Fig. 4.4: Radar geometry

TerraSAR-X and TanDEM-X use microwaves in the X-Band. TSX uses a frequency of 9.65 GHz. The nominal orbit altitude of TSX is 514 km. There are different imaging modes for TSX with different swath width and different resolution. They are listed in Table 4.5.

mode	swath width / scene extension	azimuth resolution	ground range resolution (dependent on incidence angle)
Stripmap	30 km	3.3 m	1.70 - 3.49 m
Spotlight	10 km (azimuth) x 10 km (ground range)	1.7 m	1.48 - 3.49 m
High Resolution Spotlight	5 km (azimuth) x 10 km (ground range)	1.1 m	1.48 - 3.49 m

Table 4.5: Resolutions for TerraSAR-X imaging products for single polarisation, from [Fritz and Eineder 2009]

4.5.2 Interferometric and differential interferometric SAR

Because of the coherent waves (stable wave length), SAR can be used for interferometry. SAR interferometry (InSAR) combines one or more complex-valued SAR images to derive geometric information about the imaged objects by exploiting phase difference.

Calculation of the interferogram from two complex SAR images u_1 and u_2:

$$\nu = u_1 \cdot u_2^* \quad (78)$$

* = complex conjugated

The interferometric phase is calculated as follows:

$$\phi_\nu = \phi_1 - \phi_2 \quad (79)$$

(As an alternative the phase can be calculated directly from the interferogram.)

The different types of interferograms for different applications are shown in Table 4.6. They are all explained in detail below.

baseline type		**name**	**applications, measurement of..**
spatial	$\Delta\theta_i$	across-track	topography, DEM
temporal	Δt = [ms] to [s]	along-track	fast moving targets, moving object detection, ocean currents
	Δt = [days] to [years]	differential	glacier/ice fields/lava flows, **hydrology**, **subsidence**, seismic events, **crustal displacements**

Table 4.6: Interferometric baseline types, from [Eineder and Bamler 2008]

Across-track interferometry

For across-track interferometry the acquisition of two SAR-images from different positions is needed. Due to the different acquisition locations a baseline B is created. This baseline is the distance between the two satellites (or orbits) in the plane perpendicular to the orbits. Orbit inaccuracies can be used to derive the interferogram from images of two consecutive orbits (repeat-pass, see below).

For across-track interferometry there are the following relations:

phase of SAR image 1 $$\phi_1 = -\frac{4\pi}{\lambda_{SAR}} rg + \phi_{scatt,1} \quad (80)$$

phase of SAR image 2 $$\phi_2 = -\frac{4\pi}{\lambda_{SAR}}(rg + \Delta rg) + \phi_{scatt,2} \quad (81)$$

rg range [m]

Range difference Δrg is dependent on the length of the baseline B.

The interferometric phase is:

$$\phi_v = \phi_1 - \phi_2 = \frac{4\pi}{\lambda_{SAR}} \Delta rg \quad (82)$$

if $\phi_{scatt,1} = \phi_{scatt,2}$

This applies only if the incidence angle is the same for both images, so that the reflection properties are the same. This is approximately true only if the baseline is not too long.

The obtained interferogram (example in Figure 4.5) is used to generate a DEM; that means the topography is derived. Therefore the phases have to be unwrapped. Unwrapping refers to converting the measured phase to the absolute phase. The appropriate number of cycles has to be added to the measured phase. In other words, phase unwrapping is the counting of the fringes (fringe = one phase cycle from zero to 2π in the image).

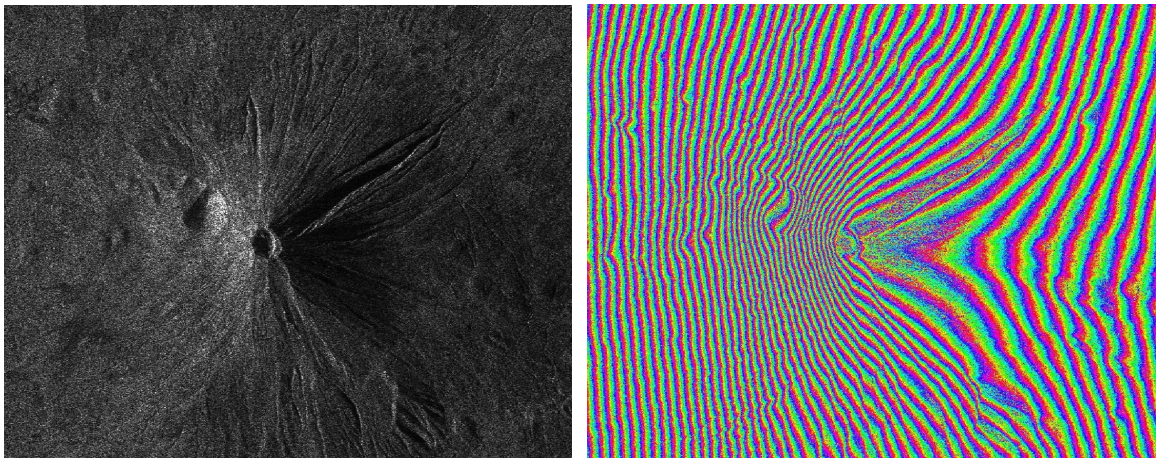

Fig. 4.5: SAR-scene: Amplitude image (left) and interferogram (right)

The phase change $\delta\phi$ due to a certain height change can be calculated as follows (rg is assumed to be constant):

$$\frac{\partial\phi}{\partial z} = \frac{4\pi}{\lambda_{SAR}} \frac{B_\perp}{rg \sin\theta_i} \quad (83)$$

θ_i incidence angle

δz change of elevation

$B_\perp$ perpendicular baseline: projection of the baseline B perpendicular to the slant range

λ_{SAR} wave length

- Interferometric sensibility in dependence of the wavelength

The shorter the wavelength the better resolved is the interferogram, i.e. one fringe stands for a smaller height difference. But this also means that the fringes lie closer together, what makes the phase unwrapping more difficult. If the wavelength is increased the distance between the fringes is increased and it is easier to count them.

- Interferometric sensibility in dependence of the baseline length

The longer the baseline the better resolved is the interferogram, but if the baseline becomes too long the assumption that the phase of the scatterers is the same for both images does not hold anymore. If the baseline is longer than the critical baseline a loss of correlation between the images occurs.

Dual-pass / single-pass interferometry

- single-pass

Both receivers receive the reflected signal of the same pulse. This ensures a high and constant quality of the DGM. This method was used for the Shuttle Radar Topography Mission (SRTM) and is used for the TanDEM-X-mission (see below). It holds for single-pass interferometry that the effective baseline is half of the length of the physical baseline.

- repeat-pass

For repeat-pass interferometry there is temporal offset between both acquisitions. Due to different atmospheric conditions and decorrelations of the backscattering, resulting from changes on the ground during the time interval, one gets a DGM with reduced and variable quality.

TanDEM-X

The TanDEM-X-mission is a satellite, constructed in the same way as TerraSAR-X. Both satellites circuit themselves on a helix-like path. Depending on the current orbit situation there is a vertical or horizontal baseline.

The advantages of the TanDEM-X-mission in comparison to other radar missions are:

- no temporal decorrelation,
- free choice of the baseline: it is possible to create along-track as well as across-track baseline.

The considerable increase of accuracy for the DGM determination will be facilitated by using two satellites realizing a long baseline with no time shift in acquisition time. Because of this several disturbing influences, like atmospheric water vapour, will cancel out.

Along-track interferometry and differential interferometry

With along-track interferometry and differential interferometry displacements on the ground in a temporal series of images shall be detected. Therefore the interferometric phase has to be separated, to distinguish between the phase due to the topography ϕ_{topo} and the differential phase ϕ_{diff} due to changes which have occurred between the two acquisitions. The interferometric phase is:

$$\phi = \phi_{topo}(z, B) + \phi_{diff} \quad (84)$$

$$\phi_{diff} = \frac{4\pi}{\lambda_{SAR}} \Delta rg_{diff} \quad (85)$$

Δrg_{diff} change of the length of *rg* because of displacements on the ground

The topography has to be compensated to receive the differential phase only. This can be achieved using a DGM, from which ϕ_{topo} can be simulated, or using at least three SAR-images.

With this technique only displacements in range direction, which is composed of the *y*- and *z*-direction, but not in azimuth direction (*x*-direction) can be detected. The largest sensitivity for displacements can be found in range (or LoS = Line of Sight) direction. The sensitivity in *y* and *z* direction is dependent on the incidence angle. The equations for the displacement monitoring sensitivity are:

$$\delta\phi_{LoS} = \frac{4\pi}{\lambda_{SAR}} d \quad (86)$$

$$\delta\phi_{y} = \frac{4\pi}{\lambda_{SAR} \cdot \sin\theta_i} d \quad (87)$$

$$\delta\phi_{z} = \frac{4\pi}{\lambda_{SAR} \cdot \cos\theta_i} d \quad (88)$$

d displacement
$\delta\phi$ phase change

For λ_{SAR} = 3.1 cm (TSX) and $\delta\phi_{LoS} = 2\pi$ (one cycle) one gets a fringe frequency of 1.55 cm / cycle, i.e. one fringe stands for a height change of 1.55 cm.

The strong limitation of differential InSAR is the missing opportunity to distinguish between influences of atmosphere, displacement and orbital errors, what makes it very difficult to detect geometric signals in the range of only a few [mm] to [cm], especially when the change of the position develops over a longer time period.

Permanent Scatterer Interferometry

Interferometric SAR with permanent scatterers can detect displacements of few [mm] per year, particularly in urban areas since there are many permanent scatterers. Permanent scatterers can be metallic fences, slanted roofs or double bounces (for example two reflections at ground and house wall), which reflect the radar signal. They have the advantage that they are scattering with a constant phase, so that decorrelations due to changes on the ground are avoided.
The phases of a single SAR-image are composed of the contributions from distance, atmosphere, scatterer and noise. An interferogram is composed of the contributions from topography, atmosphere, surface displacements, orbital errors and noise. The permanent scatterer interferometry aims at the separation of the different contributions, so that for example the surface displacements can be extracted.
For this a lot of interferograms covering a large time span (several years) are necessary. The scenes have to contain several stable and long time coherent scatterers. All possible interferograms between one master and all other slave images are formed. For removing the topography the dependence of the InSAR-phase on the baseline is used. The long time span is required to be able to separate the effects.
The limitations of this technique for the measuring of geometric signals are the need of many permanent scatterers and of a long time series of images.

4.5.3 New approach: absolute SAR measurements

In the methods above interferometric methods are necessary to derive changes on the Earth's surface. Now position changes of points on the ground or the delays in the atmosphere shall be derived from absolute measurements of the range. The main objectives, which make this possible, are the precise orbits (cm-range) for the TerraSAR-X satellite (cf. 5.2.3) and the technical feasibility of the satellite to provide high pixel localization accuracy. A [m]-accuracy for the pixel localization has been reached with implementing simple ionospheric and tropospheric models in the SAR processor to correct for their delays. [Eineder et al. 2010]
The two parameters which influence the range to a certain point on the ground most are tropospheric variations and the solid Earth tides, both with amplitudes in [dm]-range. The ionosphere is a smaller error source for X-Band-SAR (see Section 2.5.2.2 and Table 2.3).
Further influences with smaller impact, which have to be considered to increase accuracy, are:

- ocean loading, pole tide
- internal clocks / oscillators (drift, synchronisation)
- electronic delays

- surface displacements
- orbit determination

The accuracy of the azimuth measurements is influenced by the orbit determination, electronic delays and the internal clocks.
In Section 5.2.3 it is pointed out that the TSX-orbits are shifted to the phase centre of the SAR antenna what opens the opportunity for further improvements, since. If the vector from centre of mass to phase centre is not determined accurately, there will be a systematic error in the orbit and therefore in range and azimuth measurements.

If all errors would be eliminated perfectly, the coordinates of an unambiguous detectable point on the ground in different images would only differ within the orbit inaccuracies.
These possibilities motivate for following new approaches:

- Measuring surface displacements, without the typical problems of interferometry (phase unwrapping, phase ambiguity, need of reference points), since there is now an absolute difference in the location of a point on the surface between two time steps.
- Derivation of water vapour maps by definition of a standard atmosphere for which a deviation can be determined from “range anomalies”. All surface displacements have to be reduced by models before.
- Detection of orbit errors. The measured range includes all disturbing influences but not the orbit error. A range calculated from SAR orbits and a GPS position on the ground includes only the geometric distance and the orbit error in range direction (cf. Section 5.2.6). If the disturbing influences are completely removed from the measured range, the difference of measured and computed range is the orbit error.

In Section 5.2 a test campaign for evaluating measured SAR ranges, using ranges derived from GPS coordinates, is presented. This will reveal the possibility of measuring small geometric signals with TSX or TDX.

5 Test measurements

In this chapter three test campaigns are presented. Two of them are performed with the Scintrex CG-3M gravimeter (5.1). It is used as a stationary instrument in the basement of the TU München (5.1.1) and in a field campaign, measuring above a storm water basin with changing water level (5.1.2).
The third campaign is about geometric signals (5.2). The coordinates of a corner reflector are determined with GPS. They are used to compute the theoretical range and azimuth for the TSX satellite, which are subsequently compared to the measured ranges and azimuths of two TSX images.

5.1 Gravimetric campaigns

5.1.1 Basement

The gravimeter Scintrex CG-3M has been tested in the basement of the TU München. The main objectives of this test are the analysis of the drift behaviour and the influence of atmospheric pressure. It is also tested if a local admittance factor for the atmosphere can be estimated significantly or if the atmospheric signal can be detected in the gravity residuals.
For the location of the gravimeter a pillar, which is physically decoupled from the building, has been chosen. There have been four measurement sessions with durations of approximately one week. A measurement was carried out every 10 minutes, persisting of 60 one-second-samples. An overview of the sessions is given in Table 5.1. The measurements had to be interrupted for reading out the data, because of the limited size of the memory in the gravimeter.

session	start date (doy)	end day (doy)	comments
1	20.07.2010 (201)	29.07.2010 (210)	varying drift behaviour because of disturbing seismic waves
2	29.07.2010 (210)	06.08.2010 (218)	
3	06.08.2010 (218)	13.08.2010 (225)	
4	13.08.2010 (225) / 15.08.2010 (227)	20.08.2010 (232)	irregularities during the first two days (only data from 15th Aug. is used)

Table 5.1: Measurement sessions

5.1.1.1 Data

The Scintrex output file (Figure 5.1) provides following quantities:

Station	point number
Grav	corrected gravity value
SD	standard deviation
Tilt	tilt of the instrument in [arcsec]
Temp	deviation from the nominal temperature
E.T.C.	internal Earth tide correction
Dur	Duration of the cycle in [s] = number of one-second-samples
# Rej.	number of rejected measurements
Time	start time of the cycle

Important information in the header of the output file (Figure 5.1) is:

Cycle Time	interval of measurements in [s]
GMT Difference	difference between GMT and internal clock (for E.T.C.)
Drift const.	drift correction in [mGal/day], which is applied internally

```
--------------------------------------------------------------------------------
SCINTREX V4.1       AUTOGRAV / Cycling Mode          R5.31
Cycle Time:     600                                          Ser No:    310218.
Line:      1.  Grid:   9090.   Job:     11.  Date: 10/07/30  Operator:   40903.

GREF.:                      0. mGals          Tilt x sensit.:          265.4
GCAL.1:                5793.849               Tilt y sensit.:          271.0
GCAL.2:                     0.                Deg.Latitude:             48.15
TEMPCO.:               -0.1265 mGal/mK        Deg.Longitude:           -11.57
Drift const.:            0.1900               GMT Difference:            0.hr
Drift Correction Start  Time: 13:39:43        Cal.after x samples:         10
                        Date: 09/12/01        On-Line Tilt Corrected = "*"
--------------------------------------------------------------------------------
Station  Grav.     SD.   Tilt x  Tilt y    Temp.    E.T.C.  Dur  # Rej     Time
  1000. 5451.564  0.017      1.      0.    0.19   -0.015     60     0  00:01:05
  1000. 5451.567  0.017      1.      0.    0.20   -0.012     60     0  00:11:05
  1000. 5451.562  0.023      1.      0.    0.19   -0.010     60     0  00:21:05
  1000. 5451.561  0.025      1.      0.    0.19   -0.008     60     0  00:31:05
  1000. 5451.564  0.022      1.      0.    0.20   -0.007     60     0  00:41:05
  1000. 5451.565  0.021      1.      0.    0.19   -0.005     60     0  00:51:05
```

Fig. 5.1: Scintrex output file (header and first values)

The gravity value (Grav.) is already corrected for several influences:

- tilt
- temperature
- linear drift with a preset value in [mGal/day] (Drift const. in header)
- tides (ETC)

Preprocessing of the gravity data

The tidal model of the ETGTAB software is more accurate than the internal one (cf. Section 2.4). Hence the tidal correction from the internal model are removed and replaced by the ETGTAB correction.
The SD values are divided by the root of the amount of measurements in one cycle, here 60, to get the error for one cycle. This error gets into the variance-covariance-matrix of the observations Q_{bb} (the inverse of this matrix is the P_{bb} matrix in Equation 92).

Pressure Data

Pressure measurements are received from the meteo-station belonging to the GREF (Integriertes Geodätisches Referenznetz Deutschlands) station of the Bundesamt für Kartographie und Geodäsie (BKG). It is placed on the roof of the TU München. The data can be downloaded from the BKG-server[29] and is provided as RINEX (Receiver Independent Exchange Format) meteo file with a temporal resolution of 10 s.
The measured pressure values are reduced to the height of the basement by applying the gradient of a standard atmosphere. The accuracy of this step is not crucial since the important information is the pressure change. A bias in the pressure values leads to a small change in the offset, which determination is not the aim here. Finally the deviation from the standard pressure ΔP at the height of the gravimeter is calculated for the analysis. The magnitude of the pressure correction can be seen in Figure 5.2. The correction is calculated with respect to the first measurement and the standard admittance factor of -0.3 µGal/mbar.

Equation for the standard pressure [Torge 1989]:

$$P_n = 1013.25\left(1 - \frac{0.0065 \cdot H}{288.15}\right)^{5.2559} \qquad (89)$$

Deviation from standard pressure (Table 5.2) at TUM basement, calculated with the pressure values P from the GREF station:

$$\Delta P = P - P_{n,basement} + P_{diff,GREF} = P - 953\ \text{mbar} + 4\ \text{mbar} \qquad (90)$$

	height	standard pressure
GREF station	548.10 m	949.115 mbar
pillar TUM basement	511.84 m	953.254 mbar

Table 5.2: Standard pressure values

[29] ftp://igs.bkg.bund.de/GREF/obs/; last access 02.11.2010

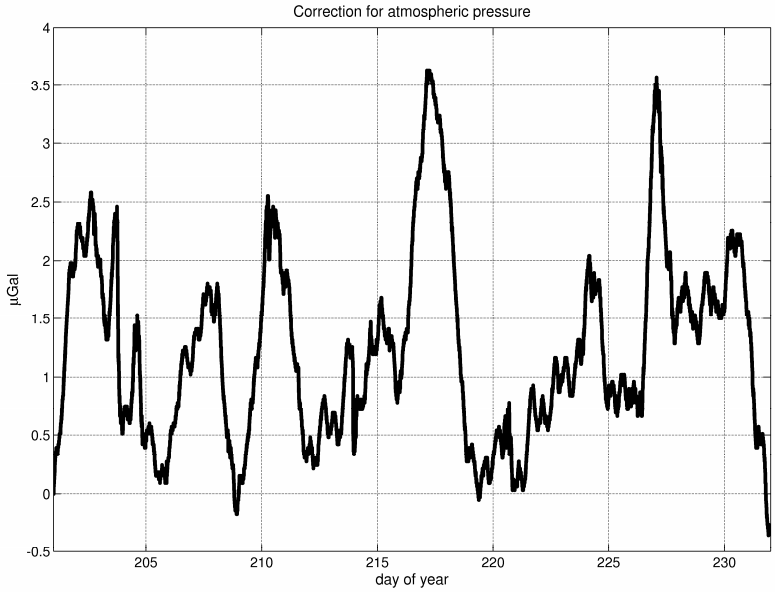

Fig. 5.2: Atmospheric correction with standard admittance factor (0.3 µGal/mbar)

5.1.1.2 Comparison of pressure data

For the time span of the test measurements the in situ measurements from the GREF station are compared to ECMWF data (Class: Operational archive, Stream: Atmospheric model, Type: Analysis, Parameter: Surface pressure, Grid: 0.25° x 0.25°)[30]. From ECMWF data the mean of two 0.25° grid cells with the centre points 48.0° latitude, 11.5° longitude and 48.25° latitude, 11.5° longitude are used. The 6 hour values have been interpolated to the 10 minute resolution of the BKG data.

For comparing the data, the pressure change, relative to the respective mean, is calculated for both and plotted in Figure 5.3 together with the difference of the pressure changes. As can be seen the difference does not exceed ±2 mbar (same value as for Hohenpeißenberg in Section 3.1.1). The corresponding gravity error, derived from the admittance factor of -0.3 µGal/mbar, can be seen in Figure 5.4. This error is always smaller than 1 µGal, and hence the usage of the ECWMF data would be sufficient for this experiment.

If absolute values are needed it has to be regarded that there is an offset between ECMWF and the local pressure. Thus local pressure measurements have to be performed.

[30] obtained from http://www.ecmwf.int/products/data/archive/finder.html; last access 25.11.2010

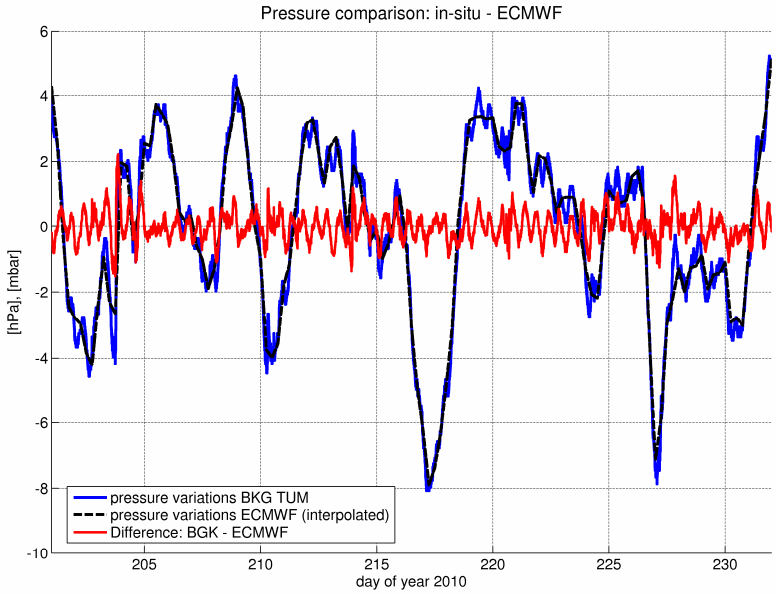

Fig. 5.3: Comparison of pressure data from day 201 to day 232 of year 2010

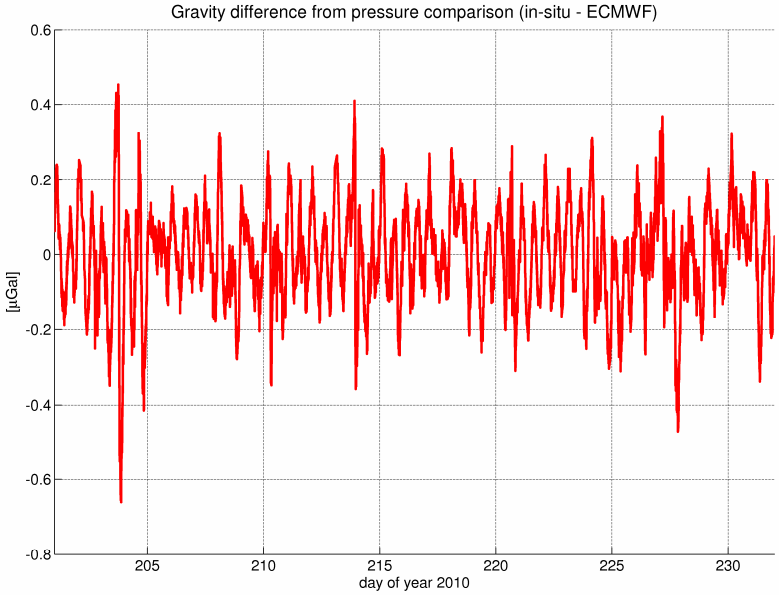

Fig. 5.4: Differences in the gravity values due to pressure variation differences between in situ and ECMWF data, computed with the admittance factor of -0.3 µGal/mbar

5.1.1.3 Analysis

For the analysis a least square adjustment (Equations 91 to 94) is performed. Because there are only linear relations, no approximate values are needed.

$$\hat{b} = f(\hat{x}) \quad (91)$$

$$\hat{x} = \left(A' P_{bb} A\right)^{-1} A' P_{bb} b \quad (92)$$

$$\hat{v} = A\Delta\hat{x} - b \quad (93)$$

$$\hat{b} = b + v \quad (94)$$

b observation vector
$f(x)$ functional model
A A-matrix
x vector of unknown parameters
v vector of increments
P_{bb} inverse of the variance-covariance-matrix of the observations
Quantities with hat (^) are adjusted values.

For characterising the drift a linear and a quadratic approach are tested. For handling the atmosphere three different ways are used:
- estimating a local admittance factor (*atmfac*)
- using an admittance factor of -0.3 μGal/mbar
- atmosphere is not taken into account

In total, there are six different observation equations (with their respective vector of unknown parameters x), so that all combinations can be studied (configuration 1-6):

① $b = grav - g_{nom} = d_1 \cdot \Delta t + d_2 \cdot \Delta t^2 + \Delta P \cdot atmfac - o \quad x = \left[d_1 \quad d_2 \quad atmfac \quad -o\right]$ (95)

② $b = grav - g_{nom} = d_1 \cdot \Delta t + \Delta P \cdot atmfac - o \quad x = \left[d_1 \quad atmfac \quad -o\right]$ (96)

③ $b = grav - g_{nom} + 0.3 \cdot \Delta P = d_1 \cdot \Delta t + d_2 \cdot \Delta t^2 - o \quad x = \left[d_1 \quad d_2 \quad -o\right]$ (97)

④ $b = grav - g_{nom} + 0.3 \cdot \Delta P = d_1 \cdot \Delta t - o \quad x = \left[d_1 \quad -o\right]$ (98)

⑤ $b = grav - g_{nom} = d_1 \cdot \Delta t + d_2 \cdot \Delta t^2 - o \quad x = \left[d_1 \quad d_2 \quad -o\right]$ (99)

⑥ $b = grav - g_{nom} = d_1 \cdot \Delta t + o \quad x = \left[d_1 \quad -o\right]$ (100)

$grav$ gravity value with applied ETGTAB correction
g_{nom} = 980725312 μGal (nominal gravity value)
Δt time since first measurement (i.e. the first value is zero, this is needed to avoid a datum defect)
ΔP deviation from standard pressure (see Equation 90)

d_1 linear drift coefficient
d_2 quadratic drift coefficient
o offset

The observation b is the measured gravity value minus the nominal gravity value g_{nom} and, for configuration 2 and 3, the atmospheric correction. The gravity residuals, which are analysed in the following, are the deviation from a constant gravity value, which should be reached if the correct configuration is chosen and all corrections are applied.

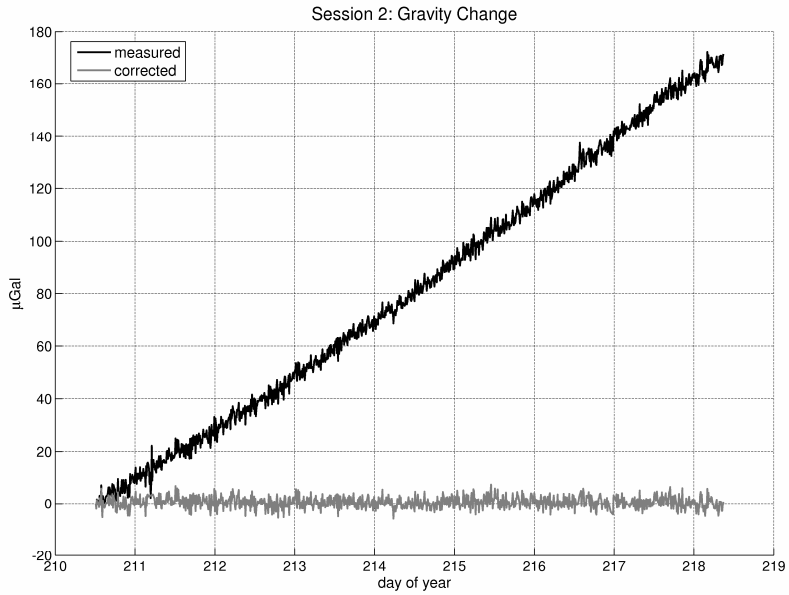

Fig. 5.5: Measured and corrected values from session 2

In Figure 5.5 the measured and Earth tide corrected gravity change from session 2 and the gravity change after applying the atmospheric correction and the estimated drift parameters for configuration 3 can be seen.

5.1.1.4 Problems encountered during the measurements

Session 1: seismic waves

At the end of day 204 very large outliers in the gravity records can be recognized (see Figure 5.6, which shows two days of measurements). This can be led back to a strong earthquake (Magnitude 7.3) at the Moro Gulf, Mindanao, Philippines at 23rd July 2010, 22:08:11 UTC[31]. The travel time of the waves is around forty-five minutes. At the same

[31] http://earthquake.usgs.gov/earthquakes/eqinthenews/2010/us2010zbbz/#details; last access 02.11.2010

time, as the outliers can be found in the gravity measurement, a strong oscillation at a nearby seismic station (Fürstenfeldbruck) was observed[32].
In Figure 5.7 the standard deviations of the measurements of the whole session 1 are shown. During the arrival of the seismic waves the values are very high. It is remarkable that it needs around three days until the standard deviations reach the low level as before the earthquake.

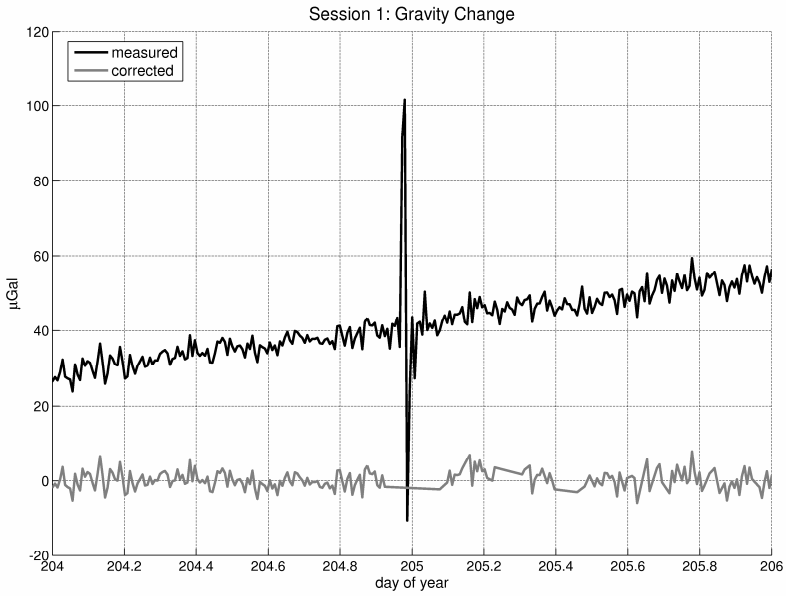

Fig. 5.6: Measured and corrected gravity values from day 204 and 205

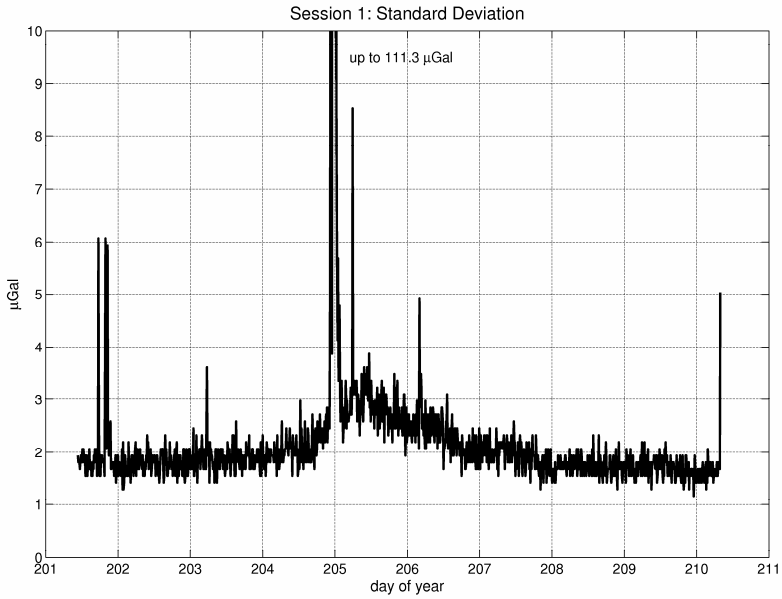

Fig. 5.7: Standard deviations of the measurements of Session 1

[32] http://www.erdbeben-in-bayern.de/daten-live/seismogramme/seismogramme; last access 02.11.2010

Also the drift behaviour has changed after the earthquake. Therefore the session 1 was split into two parts with the observations before (a) and after (b) the earthquake. Results can be seen in Table 5.5. While the residual RMS of configuration 3 and 4 (without estimating an atmospheric admittance factor) for quadratic and linear drift differ only slightly before the earthquake, the residual RMS in the estimation after the earthquake is smaller for configuration 3 (quadratic drift). It can also be seen in Table 5.5 that the quadratic factor for case (a) is very small. A comparison of the drift rates can be seen in Figure 5.12, the coefficients are taken from the estimation with configuration 3.
The sessions 1 and 1b are showing a clearly stronger quadratic behaviour than all other sessions.

It can be seen in the other sessions that such seismic events are not very seldom. None of the other events had such large impacts on the measurements, but it has always to be paid attention on seismic disturbances, especially in case of drift determination. As it is shown the drift behaviour can also change during a continuous measurement.

Session 4: jumps of gravity values at the day change

In session 4 there has been a large jump in the gravity values at the date change from the first to the second and from the second to the third day, see Figure 5.8. Because of this, only the data starting with the third day are used. Therefore, it is not possible anymore to combine this session with the other ones, which explains why the combinations with session 4 are missing in the analysis.

Station	Grav.	SD.	Tilt x	Tilt y	Temp.	E.T.C.	Dur	# Rej	Time
.									
.									
.									
1000.	5451.907	0.036	0.	-0.	0.06	-0.018	60	0	23:02:24
1000.	5451.907	0.030	0.	-0.	0.06	-0.013	60	0	23:12:24
1000.	5451.910	0.028	0.	-0.	0.06	-0.007	60	0	23:22:24
1000.	5451.910	0.025	0.	-0.	0.06	-0.002	60	0	23:32:24
1000.	5451.909	0.016	0.	-0.	0.06	0.003	60	0	23:42:24
1000.	5451.911	0.017	0.	-0.	0.05	0.008	60	0	23:52:24
start of next day									
1000.	5464.485	0.020	0.	-0.	0.06	0.012	60	0	00:02:24
1000.	5464.483	0.017	0.	-0.	0.05	0.016	60	0	00:12:24
1000.	5464.485	0.014	0.	-0.	0.05	0.021	60	0	00:22:24
1000.	5464.488	0.016	0.	-0.	0.05	0.024	60	0	00:32:24
1000.	5464.482	0.014	0.	-0.	0.06	0.028	60	0	00:42:24
1000.	5464.485	0.014	0.	-0.	0.06	0.031	60	0	00:52:24
.									
.									
.									
1000.	5464.513	0.016	-1.	-1.	0.05	-0.031	60	0	23:02:45
1000.	5464.507	0.016	-1.	-1.	0.05	-0.025	60	0	23:12:45
1000.	5464.517	0.051	-1.	-1.	0.05	-0.020	60	0	23:22:45
1000.	5464.513	0.027	-1.	-1.	0.05	-0.015	60	0	23:32:45
1000.	5464.520	0.024	-1.	-1.	0.05	-0.010	60	0	23:42:45
1000.	5464.517	0.023	-1.	-1.	0.05	-0.004	60	0	23:52:45
start of next day									
1000.	5476.260	0.110	-1.	-1.	0.05	0.001	60	0	00:02:45
1000.	5476.265	0.043	-1.	-1.	0.05	0.006	60	0	00:12:45
1000.	5476.255	0.024	-1.	-1.	0.05	0.010	60	0	00:22:45
1000.	5476.257	0.017	-1.	-1.	0.05	0.015	60	0	00:32:45
1000.	5476.261	0.017	-1.	-1.	0.05	0.019	60	0	00:42:45
1000.	5476.263	0.017	-1.	-1.	0.05	0.024	60	0	00:52:45

Fig. 5.8: Extract of the Scintrex output of session 4

5.1.1.5 Results and discussion

Residuals

Table 5.5 shows the result of the analysis for all configurations and all sessions (individual and all possible combinations). The best values are always marked in green. The smallest RMS values for the residuals of the different sessions are, except for session 1_2_3, in the range from 2.1 to 2.3 µGal.
One can see that using quadratic drift always leads to smaller residual RMS. As described above, session 1 and 1b show the strongest quadratic behaviour. Session 4 shows, apart from session 1a, the smallest difference between the residual RMS for quadratic and linear drift cases. For that session also the estimated linear coefficients are very similar for both cases.
The residuals from all sessions are, with only a few exceptions, in the range ±5 µGal for configuration 3, as can be seen in Figure 5.9. This is also shown in Table 5.3, where the percentages of the residuals, which are smaller than a certain value, are given. At least 97 % of the residuals are smaller than 5 µGal, at least 60 % are smaller than 2 µGal. This holds for all shown cases but not for the combination of session 1 to 3, what can be ascribed to the disparities in the drift behaviour between session 1 and the other sessions.

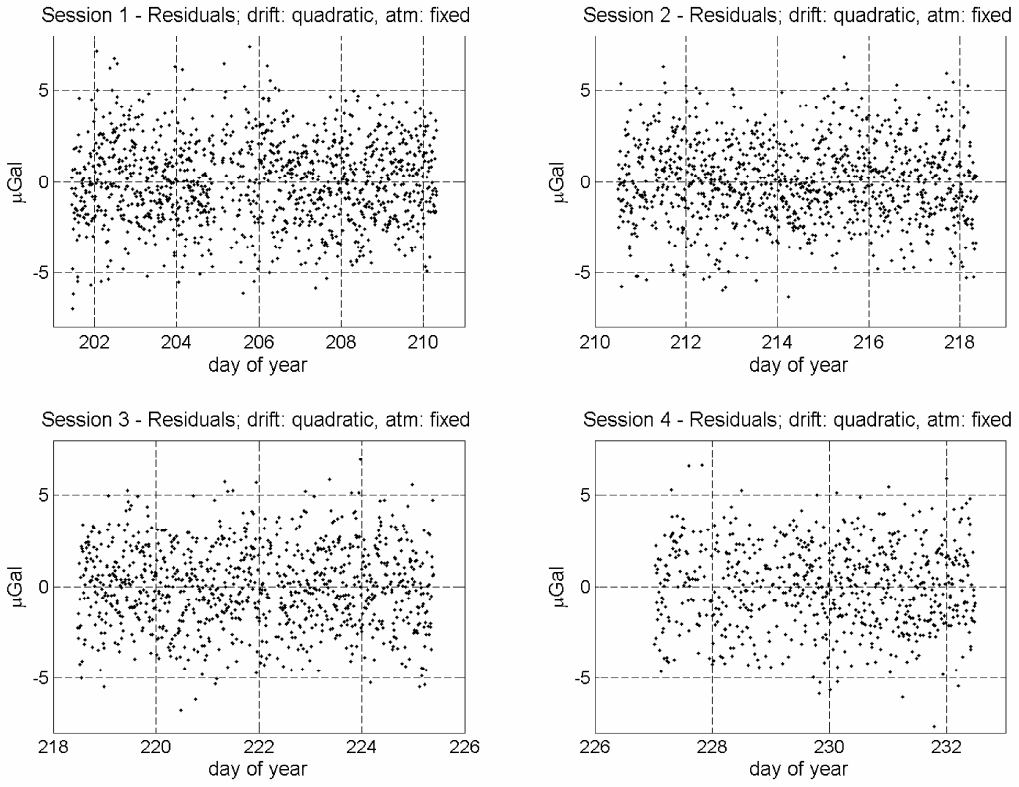

Fig. 5.9: Residuals for configuration 3 for all sessions

	< 2 µGal	< 3 µGal	< 4 µGal	< 5 µGal
session 1	62.4 %	81.4 %	92.5 %	97.3 %
session 2	65.4 %	84.4 %	93.0 %	97.5 %
session 3	60.4 %	82.3 %	93.4 %	97.9 %
session 4	60.5 %	82.3 %	93.4 %	98.0 %
session 2_3	61.9 %	81.2 %	92.5 %	97.9 %
session 1_2_3	44.1 %	61.7 %	75.4 %	85.8 %

Table 5.3: Distribution of the gravity residuals for different sessions and configuration 3

In Figure 5.10 a histogram and a quantile-quantile-plot (qq-plot) for the residuals of session 2 and configuration 3 are shown exemplarily. The results (distribution of the residuals, linear behaviour in the qq-plot) indicate a normal distribution of the residuals. Therefore it can be assumed that the used parameter model is appropriate and the residuals are real noise.

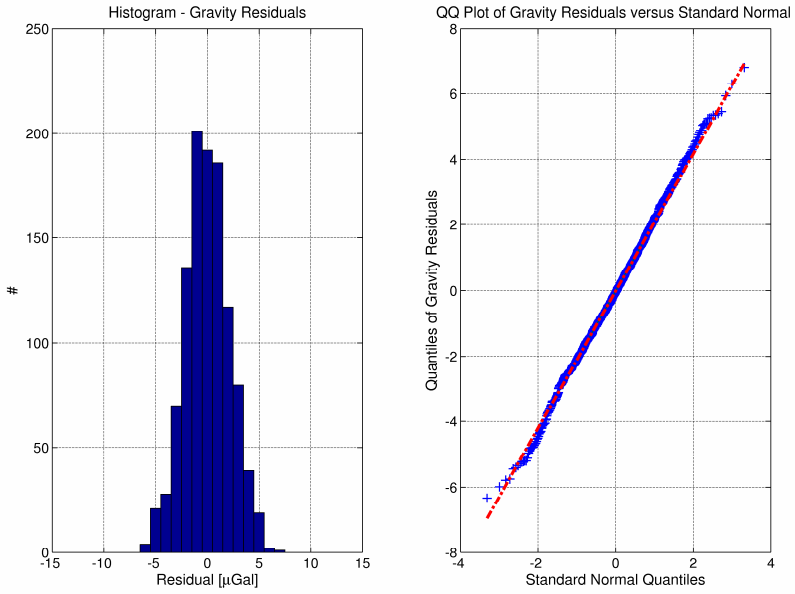

Fig. 5.10: Histogram (left) and qq-plot (right) for the residuals of session 2 with configuration 3

Drift

In Figure 5.11 the residuals for session 2 are plotted for all configurations. The quadratic characteristic of the drift can be seen here in the residuals for the linear drift without estimating the atmospheric admittance (configuration 4 and 6). The trend of the residuals has a clearly quadratic form. The estimation of the atmospheric admittance seems to compensate for the quadratic drift in some way in configuration 2, but it is impossible that this is the true estimation because the estimated atmospheric admittance factor of -0.753 µGal/mbar is far away from a realistic value.

From the estimated drift coefficients it can be derived that at least every session seems to have its own drift behaviour (see also Figure 5.12). Especially there is a large discrepancy between the drift of session 1 / combinations with session 1 and the other sessions inclusive the combination of session 2 and 3. For the latter cases an additional drift rate (since the preset drift of 7.92 µGal/h is always applied) of 1 µGal/h is a good benchmark.
In this context it has to be noted, that the instrument was not moved between the sessions. Between session 1 and 2 and between 2 and 3, the adjusting screws of the tripod were used for levelling the instrument, but only a tiny correction was applied.

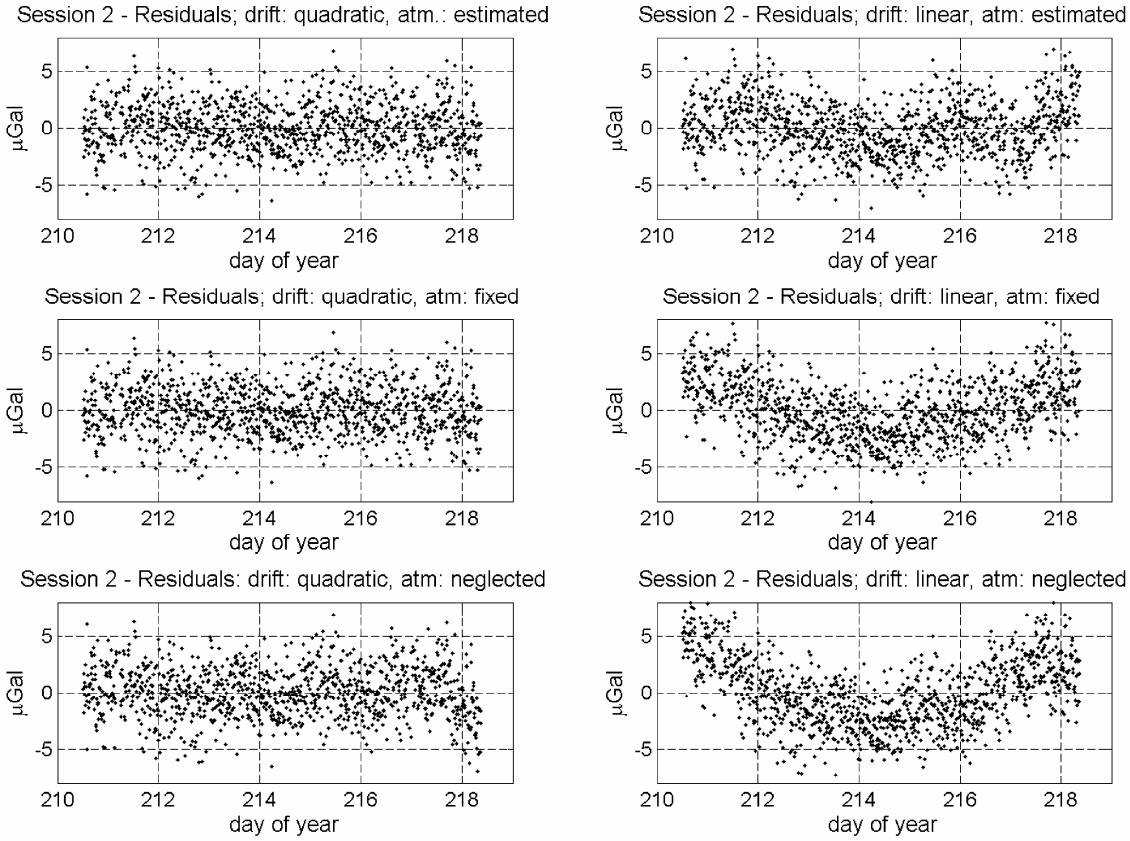

Fig. 5.11: Residuals of session 2 for all configurations

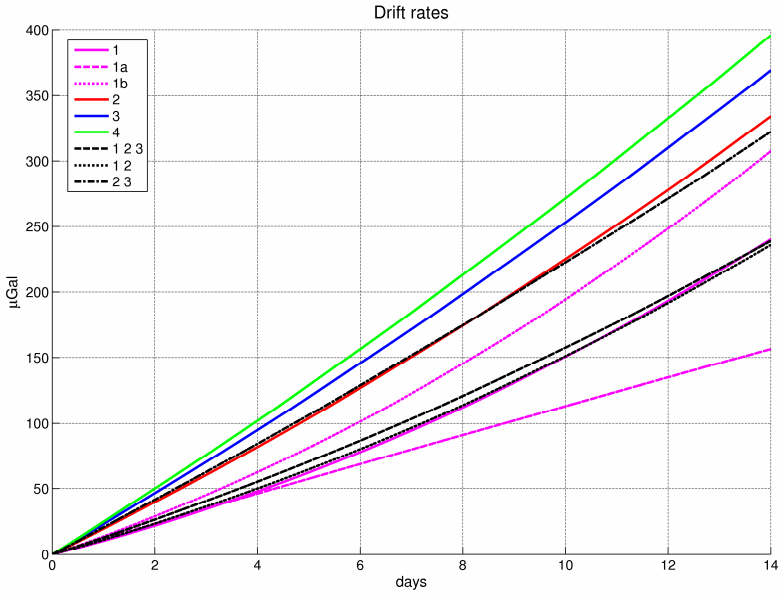

Fig. 5.12: Comparison of drift rates for all sessions

Atmosphere

Using quadratic drift estimation, admittance factors with realistic values can be estimated for all single sessions and the combination of session 2 and 3 (cf. Table 5.5). It is questionable if these values, although their variances from the adjustment are small, are more correct than the constant admittance factor, since the atmospheric correction is very small (see Figure 5.2) in comparison to the residuals, i.e. the measurement noise. Additionally the estimated factors differ more than expected from each other (max. variation 0.078 µGal/mbar) and the residual RMS from the solution with the fixed factor 0.3 µGal/mbar are slightly better or equal to the residual RMS from the solution with the estimated atmosphere admittance.

Anyhow the atmospheric correction is large enough that it should be applied, since all residual RMS from estimates without considering the atmosphere are larger. The results show also that it does not play a role, in the accuracy class of this gravimeter, if the constant or the estimated (for the cases with a realistic value) admittance factor is used.

From this the question arises if the pressure change is detectable in the gravity residuals, when no atmospheric correction is applied (configuration 5 and 6). For that the normalized residuals from configuration 3 (using fixed atmospheric admittance factor) and configuration 5 (neglecting the atmosphere) are cross-correlated with the normalized pressure change (with switched sign) and compared to each other. In Table 5.4 the cross-correlation-coefficients are shown for the different sessions and configurations. Additionally the residuals are smoothed with a mean-filter of length 9 (corresponding to 90 minutes) and the cross-correlation-coefficient is computed again. It can be seen that there is no correlation if the atmospheric correction is applied, so it has been reduced

successfully, an exception is the combination of session 1, 2 and 3, what can be probably ascribed to the drift again.

cross-correlation coefficient	configuration 3		configuration 5	
		with smoothing		with smoothing
session 1	0.014	0.031	0.219	0.457
session 2	-0.014	-0.031	0.113	0.250
session 3	0.006	0.035	0.113	0.270
session 4	0.010	0.027	0.122	0.277
session 2_3	0.035	0.074	0.380	0.667
session 1_2_3	0.195	0.246	0.397	0.481

Table 5.4: Cross-correlation coefficient between normalized residuals and normalized pressure change for configuration 3 (with applied atmospheric correction) and configuration 5 (without atmospheric correction)

The coefficients for configuration 5 have the following characteristics:
- the correlation is clearly higher than for configuration 3
- the smoothed coefficients are clearly larger than for the unsmoothed residuals (for stronger smoothing the coefficients become even larger)
- the correlation is higher for longer time series

Consequently the atmosphere can be seen in the residuals, especially if the very short-periodic noise is filtered out. This is shown in Figure 5.13, where the pressure change is plotted together with the gravity residuals of configuration 5, once smoothed with a mean filter of length 9 and once of length 51 (≈ 8 h). Then the residuals are divided by the atmospheric admittance factor to convert them to pressure values. The curves of pressure and residuals show the same behaviour, but the residuals have a clearly larger peak-to-peak variation. This can not (only) be referred to a bias in the admittance factor, since the signals fit partly very well. Further error sources which hamper the detection of the true pressure signal can be:
- short-time variation in the drift behaviour which can not be modelled with linear or quadratic drift coefficients
- disturbances which lead to small jumps in the gravity values
- short-time variations of the admittance factor.

Generally it remains the possibility that the atmospheric signal is superimposed by the drift in such a way that it can not be distinguished between both components. This holds especially for short observation intervals.

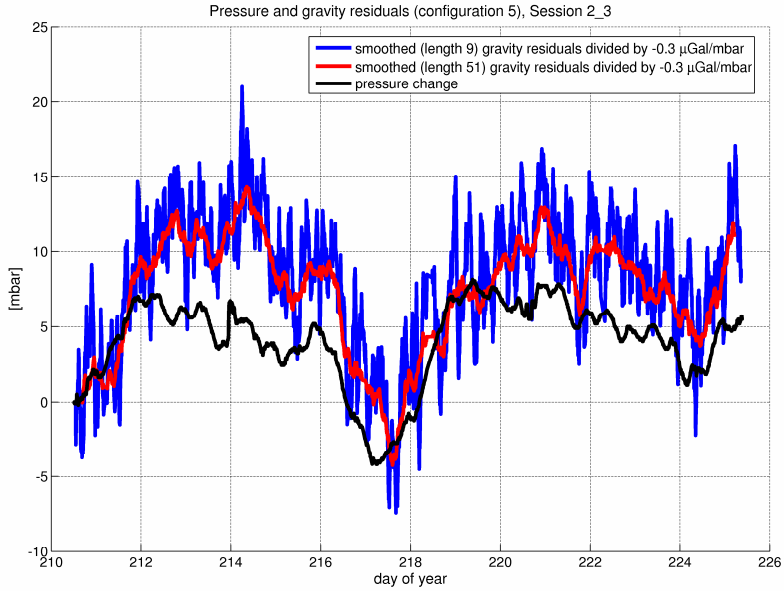

Fig. 5.13: Pressure variation and smoothed gravity residuals of configuration 5, converted into [mbar] by dividing by the admittance factor of 0.3 µGal/mbar, for session 2 and 3

Conclusions

The magnitude of the residuals with a RMS of 2-3 µGal allow a rating of the ability of the Scintrex CG-3M to measure signals of a certain magnitude.

It has to be corrected for signals in the range of magnitude of the atmospheric pressure (maximum variation here ≈ 4 µGal). The measuring of that signal is more difficult because of the magnitude of the noise (±5 µGal) and the drift. Appropriate smoothing can help to overcome the problem with the noise, since it is very short-periodic.

The drift of the instrument can not be assumed to be linear and stable. When the drift is changing during the observation, it becomes even harder to get a long term signal, but the (additional) usage of instruments with a more stable drift behaviour than the Scintrex CG-3M can attenuate this problem.

data_keller_1				Residuals RMS	sigma_0^2	mean v	d1		d2		atm		offset	
			[µGal/mbar]	[µGal]	[µGal]	[µGal]	[µGal/day]		[µGal/day^2]		[µGal/mbar]		[µGal]	
configuration	polynom	atm. est.	adm. factor					σ		σ		σ		σ
1	2	true	-	2.255	1.428	1.817	9.963	0.115	0.512	0.012	-0.364	0.033	975273887.846	0.183
2	1	true	-	3.521	3.582	2.933	14.755	0.041			-0.893	0.048	975273893.069	0.216
3	2	false	-0.3	2.254	1.431	1.816	9.858	0.102	0.521	0.011			975273887.857	0.184
4	1	false	-0.3	3.764	4.036	3.178	14.527	0.038					975273894.175	0.209
5	2	false	0	2.343	1.574	1.878	9.367	0.107	0.563	0.012			975273887.908	0.193
6	1	false	0	4.035	4.615	3.406	14.412	0.041					975273894.736	0.223

data_keller_2				Residuals RMS	sigma_0^2	mean v	d1		d2		atm		offset	
			[µGal/mbar]	[µGal]	[µGal]	[µGal]	[µGal/day]		[µGal/day^2]		[µGal/mbar]		[µGal]	
configuration	polynom	atm. est.	adm. factor					σ		σ		σ		σ
1	2	true	-	2.143	1.344	1.707	19.138	0.146	0.334	0.021	-0.313	0.039	975273755.781	0.246
2	1	true	-	2.372	1.662	1.906	21.397	0.045			-0.753	0.031	975273756.675	0.266
3	2	false	-0.3	2.143	1.343	1.707	19.111	0.122	0.339	0.015			975273755.814	0.225
4	1	false	-0.3	2.621	1.992	2.127	21.819	0.039					975273759.834	0.173
5	2	false	0	2.217	1.423	1.753	18.490	0.125	0.451	0.015			975273756.570	0.232
6	1	false	0	3.015	2.575	2.458	22.097	0.044					975273761.926	0.196

data_keller_3				Residuals RMS	sigma_0^2	mean v	d1		d2		atm		offset	
			[µGal/mbar]	[µGal]	[µGal]	[µGal]	[µGal/day]		[µGal/day^2]		[µGal/mbar]		[µGal]	
configuration	polynom	atm. est.	adm. factor					σ		σ		σ		σ
1	2	true	-	2.196	1.609	1.769	22.689	0.148	0.258	0.021	-0.360	0.061	975273581.575	0.481
2	1	true	-	2.361	1.861	1.915	24.401	0.055			-0.507	0.064	975273582.624	0.509
3	2	false	-0.3	2.196	1.609	1.771	22.698	0.147	0.262	0.020			975273581.993	0.223
4	1	false	-0.3	2.375	1.879	1.926	24.528	0.039					975273584.185	0.154
5	2	false	0	2.234	1.665	1.806	22.742	0.150	0.282	0.021			975273584.088	0.227
6	1	false	0	2.441	1.978	1.977	24.711	0.040					975273586.446	0.158

data_keller_4				Residuals RMS	sigma_0^2	mean v	d1		d2		atm		offset	
			[µGal/mbar]	[µGal]	[µGal]	[µGal]	[µGal/day]		[µGal/day^2]		[µGal/mbar]		[µGal]	
configuration	polynom	atm. est.	adm. factor					σ		σ		σ		σ
1	2	true	-	2.250	0.995	1.832	24.458	0.219	0.266	0.043	-0.286	0.047	975249051.824	0.277
2	1	true	-	2.317	1.049	1.880	25.694	0.091			-0.140	0.042	975249052.958	0.213
3	2	false	-0.3	2.250	0.994	1.831	24.447	0.215	0.272	0.037			975249051.817	0.276
4	1	false	-0.3	2.337	1.069	1.887	25.965	0.057					975249053.254	0.200
5	2	false	0	2.311	1.046	1.881	24.697	0.221	0.136	0.038			975249051.980	0.283
6	1	false	0	2.336	1.064	1.899	25.458	0.057					975249052.700	0.200

data_keller_1_2_3				Residuals RMS	sigma_0^2	mean v	d1		d2		atm		offset	
			[µGal/mbar]	[µGal]	[µGal]	[µGal]	[µGal/day]		[µGal/day^2]		[µGal/mbar]		[µGal]	
configuration	polynom	atm. est.	adm. factor					σ		σ		σ		σ
1	2	true	-	3.266	3.240	2.628	12.574	0.033	0.323	0.001	-0.529	0.023	975273892.969	0.183
2	1	true	-	14.280	63.263	12.509	20.443	0.037			-1.274	0.099	975273922.454	0.611
3	2	false	-0.3	3.336	3.339	2.700	12.514	0.033	0.325	0.001			975273893.519	0.177
4	1	false	-0.3	14.347	65.100	12.164	20.370	0.037					975273925.536	0.531
5	2	false	0	3.586	3.776	2.890	12.436	0.035	0.327	0.001			975273894.240	0.188
6	1	false	0	14.461	66.419	12.105	20.348	0.037					975273926.485	0.537

data_keller_1_2				Residuals RMS	sigma_0^2	mean v	d1		d2		atm		offset	
			[µGal/mbar]	[µGal]	[µGal]	[µGal]	[µGal/day]		[µGal/day^2]		[µGal/mbar]		[µGal]	
configuration	polynom	atm. est.	adm. factor					σ		σ		σ		σ
1	2	true	-	2.323	1.530	1.849	10.697	0.048	0.438	0.003	-0.245	0.023	975273889.275	0.141
2	1	true	-	7.618	16.892	6.034	17.857	0.033			-2.418	0.059	975273900.479	0.398
3	2	false	-0.3	2.326	1.534	1.854	10.767	0.039	0.434	0.002			975273889.258	0.141
4	1	false	-0.3	9.572	26.399	8.188	17.956	0.041					975273908.679	0.407
5	2	false	0	2.382	1.607	1.890	10.385	0.039	0.458	0.002			975273889.350	0.144
6	1	false	0	10.096	29.286	8.640	17.970	0.043					975273909.841	0.429

data_keller_2_3				Residuals RMS	sigma_0^2	mean v	d1		d2		atm		offset	
			[µGal/mbar]	[µGal]	[µGal]	[µGal]	[µGal/day]		[µGal/day^2]		[µGal/mbar]		[µGal]	
configuration	polynom	atm. est.	adm. factor					σ		σ		σ		σ
1	2	true	-	2.241	1.567	1.807	20.346	0.050	0.190	0.003	-0.326	0.019	975273757.543	0.183
2	1	true	-	3.879	4.255	3.101	23.263	0.019			-0.289	0.031	975273765.495	0.207
3	2	false	-0.3	2.242	1.567	1.808	20.347	0.050	0.190	0.003			975273757.653	0.166
4	1	false	-0.3	3.881	4.253	3.103	23.263	0.019					975273765.452	0.169
5	2	false	0	2.422	1.801	1.946	20.358	0.054	0.188	0.003			975273758.905	0.178
6	1	false	0	3.929	4.437	3.095	23.248	0.020					975273766.632	0.172

data_keller_1a				Residuals RMS	sigma_0^2	mean v	d1		d2		atm		offset	
			[µGal/mbar]	[µGal]	[µGal]	[µGal]	[µGal/day]		[µGal/day^2]		[µGal/mbar]		[µGal]	
configuration	polynom	atm. est.	adm. factor					σ		σ		σ		σ
1	2	true	-	2.230	1.524	1.744	11.431	0.456	0.086	0.146	-0.425	0.076	975273888.601	0.346
2	1	true	-	2.232	1.522	1.746	11.687	0.136			-0.402	0.065	975273888.765	0.206
3	2	false	-0.3	2.236	1.530	1.748	11.679	0.431	-0.036	0.126			975273888.860	0.309
4	1	false	-0.3	2.235	1.527	1.747	11.561	0.110					975273888.794	0.205
5	2	false	0	2.304	1.622	1.802	12.274	0.444	-0.328	0.130			975273889.481	0.319
6	1	false	0	2.312	1.640	1.807	11.191	0.114					975273888.882	0.213

data_keller_1b				Residuals RMS	sigma_0^2	mean v	d1		d2		atm		offset	
			[µGal/mbar]	[µGal]	[µGal]	[µGal]	[µGal/day]		[µGal/day^2]		[µGal/mbar]		[µGal]	
configuration	polynom	atm. est.	adm. factor					σ		σ		σ		σ
1	2	true	-	2.209	1.328	1.807	13.119	0.277	0.632	0.047	-0.301	0.038	975273842.817	0.412
2	1	true	-	2.533	1.673	2.062	16.738	0.070			-0.325	0.042	975273846.758	0.325
3	2	false	-0.3	2.209	1.326	1.807	13.119	0.276	0.632	0.047			975273842.821	0.367
4	1	false	-0.3	2.529	1.671	2.060	16.744	0.070					975273846.892	0.234
5	2	false	0	2.289	1.448	1.861	13.090	0.289	0.650	0.049			975273844.302	0.384
6	1	false	0	2.557	1.812	2.094	16.817	0.073					975273848.487	0.244

Table 5.5: Overview of the results, all results are given in [µGal], green shaded fields mark the best result of the respective case, the admittance factor has the unit [µGal/mbar]

5.1.2 Storm water basin

The Scintrex CG-3M gravimeter was used for another test campaign. In this experiment a changing groundwater level was simulated by measuring above an underground storm water basin (Regenüberlaufbecken Großlappen) operated by the "Münchner Stadtentwässerung". Reference values for the water level change are available, since it is determined using a radar instrument at the outlet of the basin. The basin is composed of three parts. During the gravity campaign only basin 1 (cf. Figure 5.14) was used, the other had been empty. Basin 1 has a length of 88 m and a width of 60 m. The maximal possible water level change is about 4 m.

The aim is to evaluate in which accuracy level the signal from the water level change can be observed with the used gravimeter. There are two different opportunities for the detection of the signal:

- measuring above the reservoir during the drain of the water
- measuring at the point above the reservoir at two different water levels and at a point with "stable" gravity; the change of the difference to that point is the measure for the water level change.

Stable means here that there is no signal, for which no correction is applied. The gravity is certainly not stable because of solid Earth tides, ocean loading and air pressure changes. For the first case also measurements on a "stable" point have to be performed before and after the survey of the water change to determine the gravimeter drift.

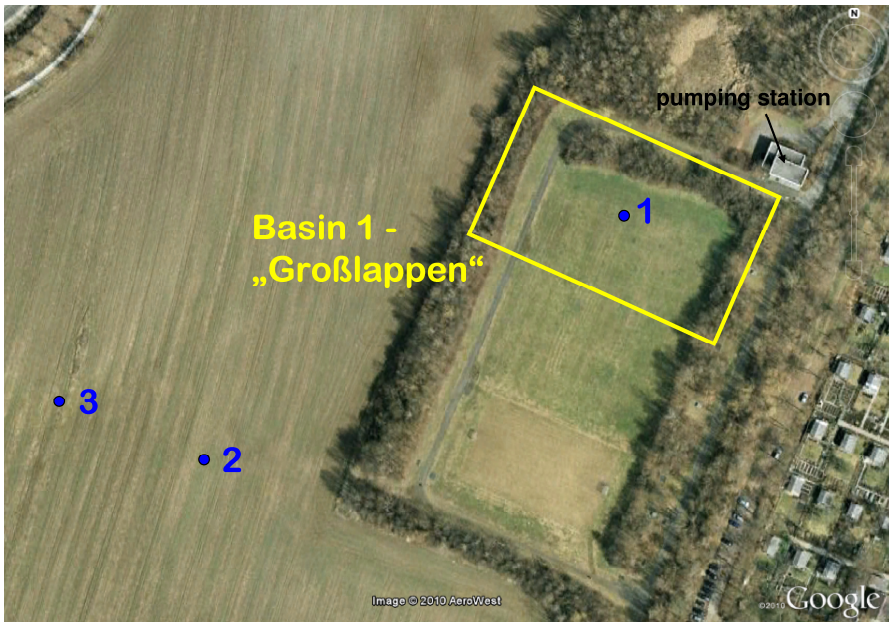

Fig. 5.14: Site of the storm water basin

5.1.2.1 Measurement configuration and data acquisition

Three measurement points have been established at the site on and around the basin (see Figure 5.14):

- point 1: point in the middle of the basin
- point 2 and 3: stable points, which are not influenced by the mass change inside the basin.

Additionally at the beginning and the end of the campaign it was measured on point 1000, the pillar in the TU basement, which was also used for the first test measurement (cf. Section 5.1.1).

A levelling has been performed for the points 1 to 3; the heights relative to point 2 are shown in Table 5.6

point	height
1	2.375 m
2	0.000 m
3	-0.272 m

Table 5.6: Results of the levelling

The measurement has been performed on 8th November. The points have been occupied in the sequence shown in Table 5.7.

step	point	status of water level	labelling (Fig. 5.16)	
1000_1	1000	-	-	-
1_1	1	high (1.59 m)	black	x
2_1	2	high (1.59 m)	blue	x
3_1	3	high (1.59 m)	red	x
1_2	1	high (1.59 m)	black	x
2_2	2	high (1.59 m)	blue	x
3_2	3	high (1.59 m)	red	x
1_3	1	high (1.59 m)	black	x
1_4	1	changing	black	o
1_5	1	low (1.21 m)	black	✳
2_3	2	low (1.21 m)	blue	x
1000_2	1000	-	-	-

Table 5.7: Measurement steps on 8th November

The water level change on this day was 38 cm. The black line in Figure 5.15 shows the water level change as it is was recorded by the control centre. The water level at the beginning is 1.59 m and falls to 1.21 m.

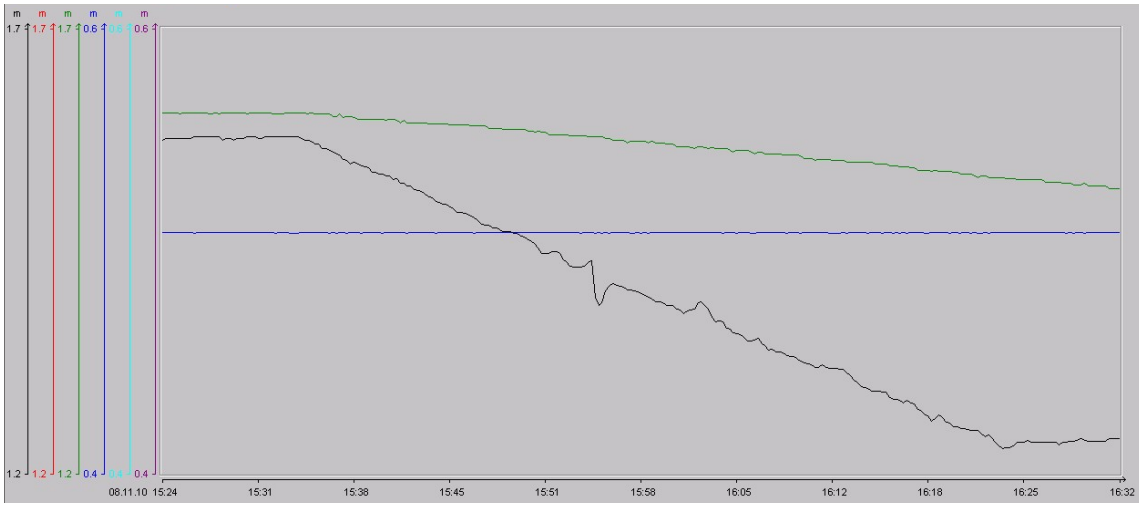

Fig. 5.15: Water level change in basin 1 (black line)

5.1.2.2 Prediction of the gravity signal

The gravity change due to this change of water level has been estimated, using the prism equation (cf. Equation 73):

$$\Delta g = G\rho_w S_y \left[\left\| x\ln(y+d) + y\ln(x+d) - z\arctan\frac{xy}{zd} \right|_{x_{p,2}}^{x_{p,1}} \right|_{y_{p,2}}^{y_{p,1}} \Bigg|_{z_{p,2}}^{z_{p,1}} \Bigg] \qquad (101)$$

The gravimeter is assumed to be placed in the middle of basin 1. The size of the basin is given above. For the density of water 1000 kg/m^3 is used. The specific yield (cf. section 3.2.1) S_y is 1. The resulting gravity change is:

- 13.5 µGal for water level change in Figure 5.15 (0.38 m)
- 55.7 µGal if the basin is completely depleted (1.59 m)

The same water level change in a soil with a specific yield of 0.1 is approximately ten times smaller than in this experiment. For the same gravity change the water level change has to be about ten times larger.

5.1.2.3 Corrections

For all gravity values the internal tide correction is replaced by the ETGTAB correction as it was done in the basement experiment (cf. 5.1.1.1, “Preprocessing of the gravity data”).

The following corrections are applied to the gravity values of point 1 to 3:

- atmospheric correction (maximum relative correction 1.4 µGal)
- instrument height, reduction with the free-air-gradient (-0.3086 µGal/mm)

- Gravity values of point 3 are reduced to the height level of point 2 with the Bouguer-reduction (*BOR*) and the free-air-gradient (*FAR*) [Rummel 2007]:

$$\Delta g_{32}^{BO} = (BOR + FAR) \cdot \Delta H_{32} = (0.1119 - 0.3086) \cdot \Delta H_{32} \qquad (102)$$

- For the reduction of the gravity values of point 1 only the free-air-gradient with the height difference of point 1 and 2 is used, since a Bouguer-reduction does not make sense because of the missing mass below the gravimeter. Mass is missing, since the basin is not completely filled with water and the density of water is smaller than the density assumed for the Bouguer-reduction.

For point 1000 only the atmospheric correction (maximum relative correction 3.0 µGal) is applied.

In Figure 5.16 all gravity values for the points 1, 2 and 3 with the applied corrections are shown. From all of them a constant value (first gravity value of point 2) is subtracted. As drift correction only the preset value of 190 µGal/day (cf. Section 5.1.1.1 and Figure 5.1) is initially applied, so a residual drift remains.

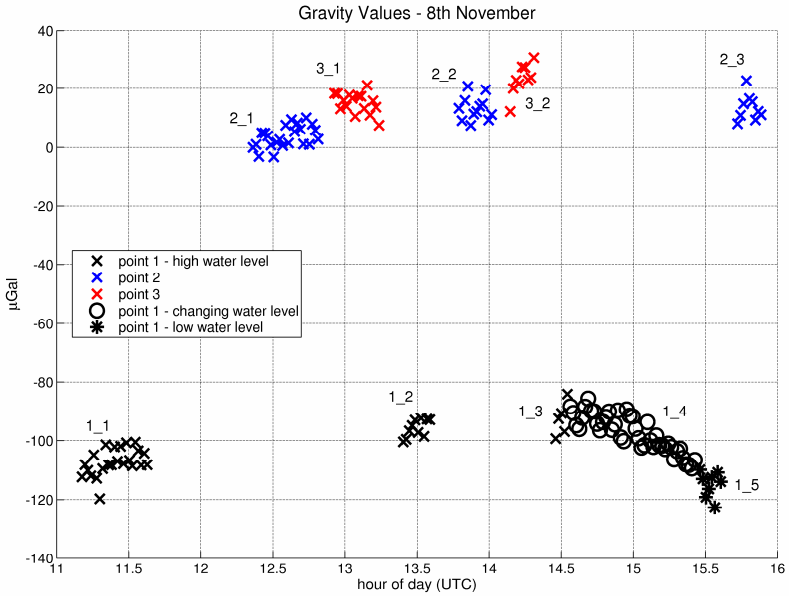

Fig. 5.16: Corrected gravity values of point 1, 2 and 3

The following can be seen in Figure 5.16:

- The gravity values of point 1 are clearly smaller than these of point 2 and 3 because of the missing mass below.
- Decrease of the gravity values during the drain of the water (black circles)
- Inconsistent drift behaviour, e.g. the gravity values clearly increase from measurement step 2_1 to 2_2, but stay stable from step 2_2 to 2_3, a similar behaviour can be seen for the measurement steps 1_1, 1_2 and 1_3 (explanation of notations see Table 5.7).

5.1.2.4 Drift analysis

For the determination of the drift the following procedure is used:
For every point a drift is determined for every pair of single measurements, which do not belong to the same step. The drift rate is the gravity change divided by the time difference of each pair. Subsequently the mean and standard deviation of all drift rates between two (or three) steps are computed. The results can be seen in Table 5.8.
The drift rates are not consistent. A good agreement can only be found for the drift from step 2_1 to 2_2 and 3_1 to 3_2. For point 1 and point 2 the drift rates are smaller for the drift from step 1_2 to 1_3 (2_2 to 2_3, respectively) than for the drift from step 1_1 to 1_2 (2_1 to 2_2, respectively). The drift from step 2_2 to 2_3 is nearly zero. Since the period of the measurements during the changing water table lies in between these steps, no further drift correction is applied for analysis of the induced gravity change. This concerns the steps 1_3, 1_4 and 1_5.

steps	drift [µGal / h]	σ
1_1 → 1_2	5.4	2.4
1_1 → 1_3	4.6	2.1
1_2 → 1_3	2.9	5.9
1_1 → 1_2, 1_3	5.1	2.3
2_1 → 2_2	7.3	4.1
2_1 → 2_3	3.1	1.7
2_2 → 2_3	0.1	3.0
2_1 → 2_2, 2_3	5.5	3.8
3_1 → 3_2	7.0	5.4

Table 5.8: Drift rates for different measurement step combinations

5.1.2.5 Determination of the gravity signal

As described in the beginning of the chapter there are two different possibilities for the determination of the gravity change:

- ***gravity differences***

Therefore the mean gravity values of the steps 1_3, 1_5, 2_2 and 2_3 are computed. Since the single measurements are repeated after the same time interval a linear drift during one step is cancelling out. The differences of the measurement steps 1_5 and 1_3 is **22.0 µGal**. This calculation is only possible for measurements in such a short time span, when the

relative gravity values can be related to each other. A more suitable method, which is also used in the gravity difference concept proposed in Section 6.1.1, is the following:
The change of the gravity difference between point 1 and 2 is determined. Since the time span between measurements 1_3 and 2_2 as well as 1_5 and 2_3 is not very large, the residual drift plays an inferior role. The results can be seen in Table 5.9.

	difference	**time difference**	**change of difference**
1_3 ↔ 2_2	838.9 µGal	36 min	- 22.2 µGal
1_5 ↔ 2_3	861.1 µGal	16 min	

Table 5.9: Results of the gravity difference approach

- ***stationary measurement during the water drain***

A linear fit is computed for the gravity values of step 1_4 (see Figure 5.17). A linear approach is appropriate, since the pump which was used to deplete the basin worked with constant power and the water level changes with nearly constant rate, what can be seen in Figure 5.15. The result of the fit is a drift rate. This rate is multiplied with the time interval within the water level change has happened.

Drift rate: -21.0 µGal / h
Duration: 0.83 h
Gravity change: **-17.4 µGal**
RMS of the fit: 3.2 µGal

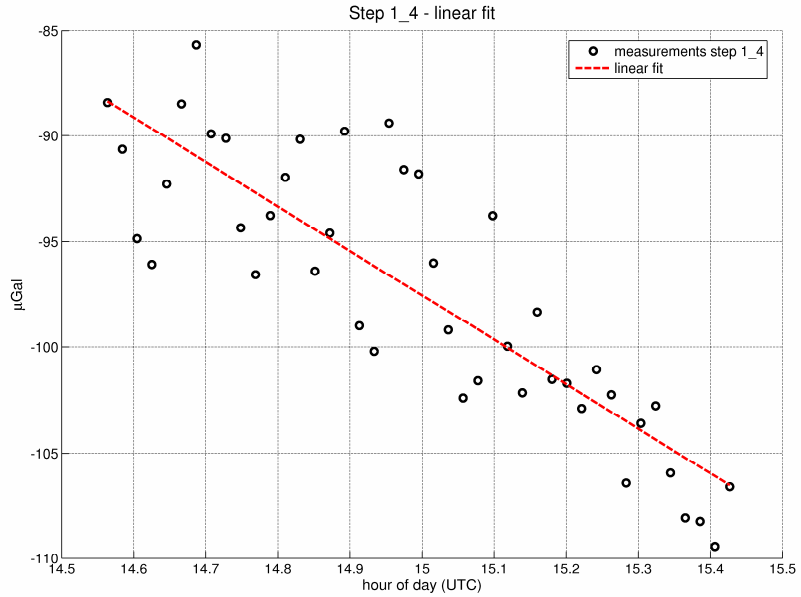

Fig. 5.17: Linear fit for the measurement step 1_4 (during the depletion of the basin)

Deviation from the estimated gravity change

The deviation from the predicted signal is
- 8.7 μGal, what corresponds to a larger water level change of 24 cm (22.2 μGal → 62 cm), for the gravity difference approach and
- 3.9 μGal, what corresponds to a larger water level change of 11 cm (17.4 μGal → 49 cm), for the linear fit approach.

This range of accuracy allows the qualitative evaluation of the water level change but not an accurate measurement of the concrete value. Better results can be achieved if the impact of the problems listed below ("Probable error sources") can be attenuated. But it has also to be regarded that the capability of the instrument for measuring such small signals is limited. The measurement in the basement has shown that the range of the measurement noise is ±5 μGal and the RMS of the gravity residuals is 2 μGal or larger, even if the instrument is not transported and the drift is easy to determine. The standard deviations of the measurements for the single steps in this campaign are in the range from 3 to 5 μGal.

Probable error sources

Following error sources probably lead to the insufficient results:
- varying drift due to transportation and / or due to deficiencies of the instrument
- spurious signal due to unstable ground (subsidence of the tripod)
- tilt meter shows irregularities due to transportation and / or the internal tilt correction is not adjusted correctly (cf. Section 5.1.2.6).

It is recommended to perform further investigations considering the drift behaviour, the behaviour of the tilt meters and the tilt correction.

5.1.2.6 Drift, tilt and transport

The measurements on point 1000 also show the problems of transport and tilt. It can be seen in Figure 5.18 that the tilt of the instrument changes at the beginning of the measurement step 1000_2. The measurement started shortly after it has been transported with a car. For analysis the step 1000_2 is divided in two parts, one with the changing (→ part 2) and one with the stable tilt (→ part 3). Part 1 is the measurement step 1000_1 at the beginning of the day. The changing of the tilt during part 2 is unexpected, since the instrument is mounted on stable ground.
For estimating the drift a linear and a quadratic fit is performed for four different cases (see Table 5.10). For every case a different combination of measurements is used. Only for the case with the measurements from part 2 and 3 the quadratic fit shows a significant smaller

RMS. In all other cases the linear fit is a sufficient assumption. The cases with part 1 and 3 and with only part 3 show nearly the same linear (residual) drift of approximately 1 µGal/h, which was also found in basement experiment (cf. Section 5.1.1.5). But there is also a large difference in comparison to the drifts estimated during the outdoor measurements.
The case with only part 2 observations results in a clearly higher drift rate, which indicates that either the tilt meter or the spring have been disturbed during the transport.

part	RMS linear	RMS quadratic	linear drift rate
1 and 3	3.6 µGal	3.6 µGal	1.1 µGal/h
3	3.6 µGal	3.5 µGal	0.9 µGal/h
2 and 3	4.4 µGal	3.5 µGal	-
2	3.4 µGal	3.4 µGal	3.9 µGal/h

Table 5.10: RMS values for linear / quadratic fits and drift rates for point 1000

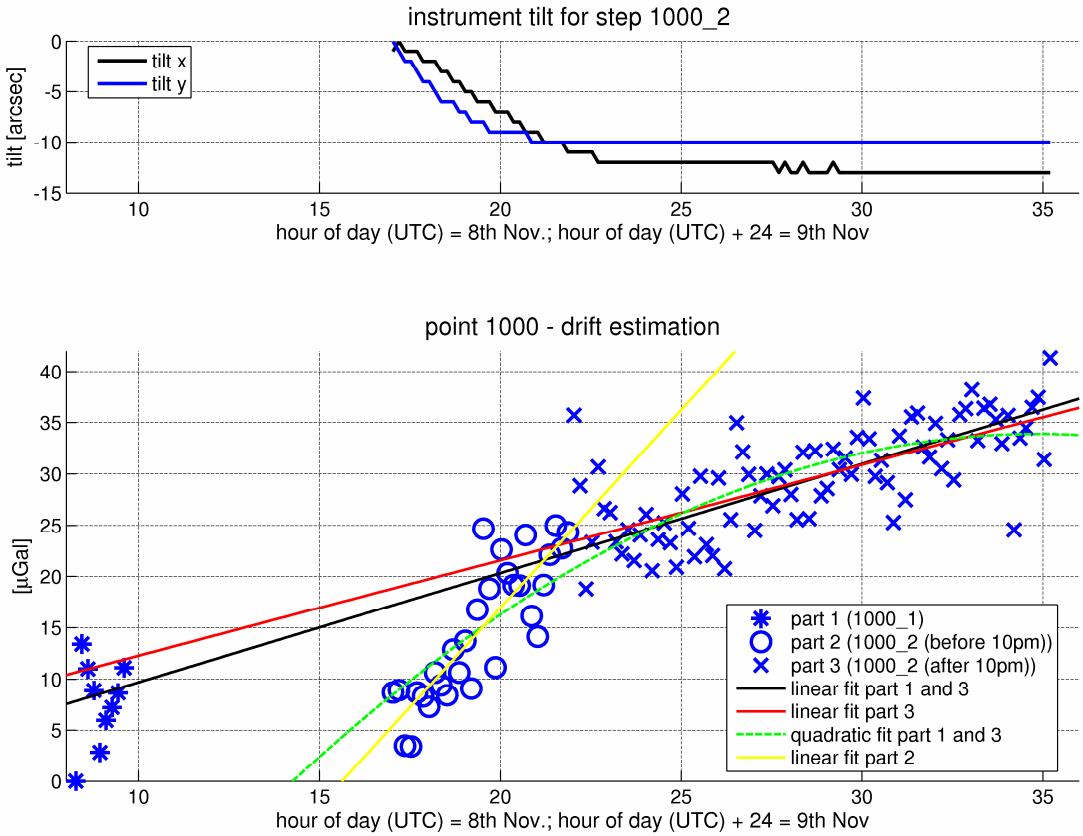

Fig. 5.18: Tilt, gravity values and fits for drift determination for point 1000

A campaign was performed under the same conditions. In that case an equal behaviour of the tilt but no variations of the drift could be detected. Because of this the situation shown in Figure 5.18 can just be an individual case.

5.2 Geometric campaign - SAR and GPS

5.2.1 Measurement configuration

The following test campaign is performed to check the quality of absolute SAR measurements. For that independent corner reflector coordinates are determined with GPS, which are used to get theoretical values for azimuth and range which can be compared to the actual SAR measurements. Additionally the influences of solid Earth tides, pole tides, ocean loading, troposphere and ionosphere on the measurement systems are depicted and approaches to remove them are shown.
The measurement configuration with the disturbing influences of solid Earth tides, troposphere and atmosphere is shown in Figure 5.19.

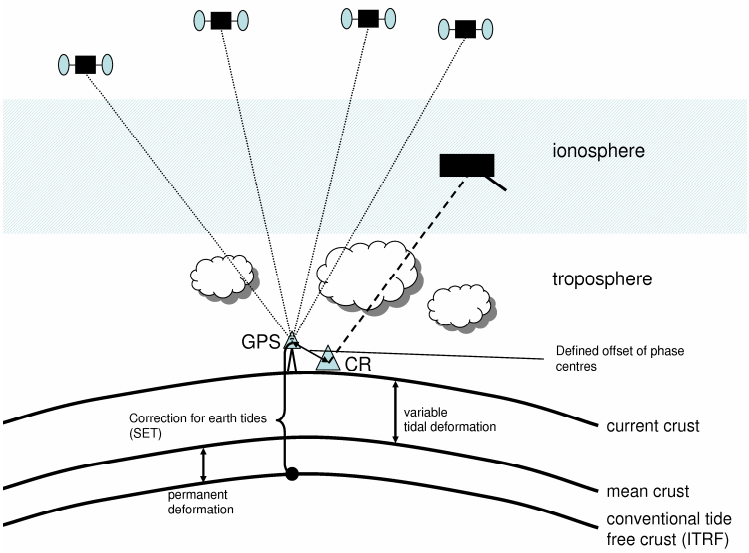

Fig. 5.19: Measurement configuration

In the course of the campaign corner reflector coordinates for two acquisitions of the TerraSAR-X satellite at the 14th and 17th July (see Table 5.11) were determined with GPS. A corner reflector (CR) was placed at the grounds of the DLR at Oberpfaffenhofen. The coordinates of the phase centre of the reflector have been determined using GPS (Leica L2 System 1200). For the two days also observations of the permanent station PPM1 operated by the Institute for Navigation and Communication, also located on the DLR grounds in Oberpfaffenhofen, are available.

image	orbit	date	doy	CR ID	UTC	incidence angle θ_i
TSX 14	ascending	14.7.2010	195	CR 14	16:51:32	20.58 °
TSX 17	descending	17.7.2010	198	CR 17	05:18:02	51.14 °

Table 5.11: SAR acquisitions

5.2.2 Reference systems (ETRS and ITRS)

The choice of the right reference system is an important task, especially if data from different sources is compared or processed together. Since the distinction between the European Terrestrial Reference System (ETRS) and International Terrestrial Reference System (ITRS) is essential, it is described in the following.
The definition of such a system is called the reference system. A reference frame, which is composed of a set of geocentric station coordinates and velocities, is the realisation of the reference system.
All ITRS stations have a station velocity, and thus temporal variable coordinates, because of the movement of the Earth's crust (plate tectonics). The ETRS is a temporally stable system since it is coupled to the stable part of the Eurasian plate. The ETRS 89 system is set equal to the ITRS at the epoch 1989.0. Since then ETRS 89 is moving away from the global reference system.
As an example the European Terrestrial Reference Frame (ETRF) coordinates from the station PPM1 are transformed to International Terrestrial Reference Frame (ITRF) 2005, epoch 2010.5. For this purpose the online service from the EUREF homepage[33] is used. The results can be seen in Table 5.12. Since the used realisation of the ETRS 89 coordinates for PPM1 could not be found, the transformation is performed for ETRF 2000 and ETRF 1989. The comparison of the results for these both cases shows a difference of a few [cm].
The differences between the ITRF and the ETRF coordinates mainly represent the movement of the station on the plate from epoch 1989 to 2010.5. The station has moved about 40 cm in North and 40 cm in East direction.

PPM1		x [m]	y [m]	z [m]	B [°]	L [°]	h [m]	vx [m/s]	vy [m/s]	vz [m/s]
	ETRF	4186741.7988	834903.5755	4723619.1394	48.0842852	11.2777587	641.0170	0.0000	0.0000	0.0000
Transformation to ITRF 2005 Epoch 2010.5	*taking coordinates as ETRF 2000*	4186741.4314	834903.9087	4723619.4130	48.0842888	11.2777640	641.0234	-0.0146	0.0178	0.0110
	Difference ITRF - ETRF	**-0.3674**	**0.3332**	**0.2736**	**3.6186E-06 = 0.4021 m**	**5.3498E-06 = 0.3971 m**	**0.0064**			
	taking coordinates as ETRF 1989	4186741.3991	834903.8937	4723619.4741	48.0842894	11.2777639	641.0458	-0.0160	0.0169	0.0139
	Difference ITRF - ETRF	-0.3997	0.3182	0.3347	4.2172E-06 = 0.4686 m	5.2371E-06 = 0.3887 m	0.0288			
	Difference between the both ITRF solutions (1989 - 2000)	-0.0323	-0.0150	0.0611	5.9864E-07 = 0.0665 m	-1.1265E-07 = -0.0125 m	0.0223	-0.0014	-0.0009	0.0029

Table 5.12: Example for ETRF - ITRF transformation

Figures 5.20 and 5.21 show maps with European and world wide IGS stations, respectively, with their horizontal velocity vector in the ITRF. The maps were generated with the "Jules Verne Voyager" web map tool[34] of the University NAVSTAR Consortium (UNAVCO).

[33] http://www.epncb.oma.be/_dataproducts/coord_trans/; last access 05.11.2010; form see appendix
[34] http://jules.unavco.org/Voyager/Earth?grd=0&pre=dxdt&gmt=52&vel=1036&opt=8; last access 05.11.2010

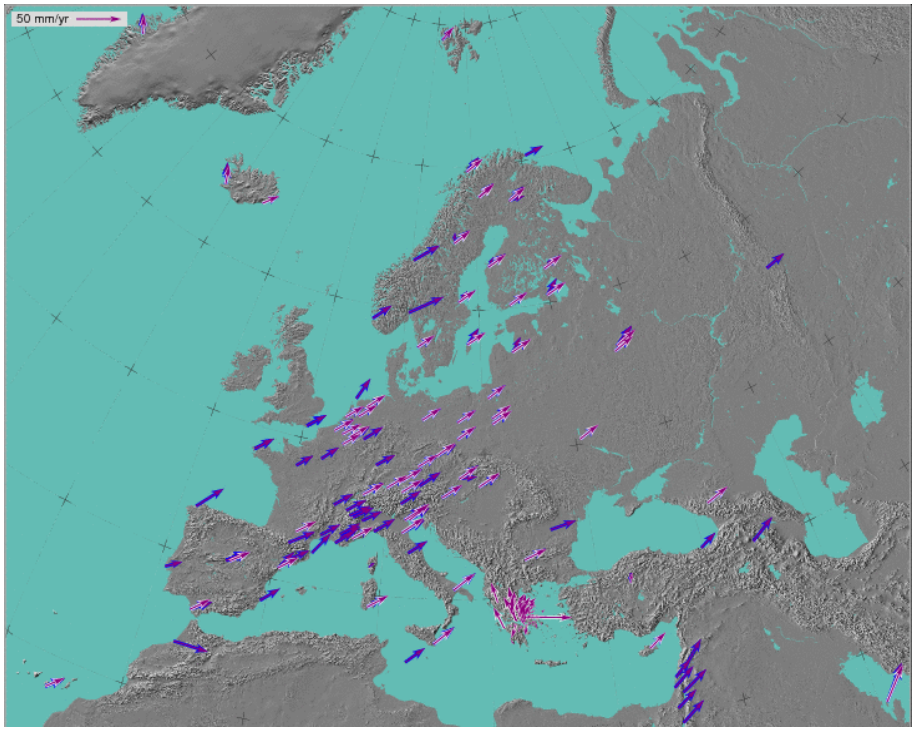

Fig. 5.20: Velocity of European IGS stations in the ITRF

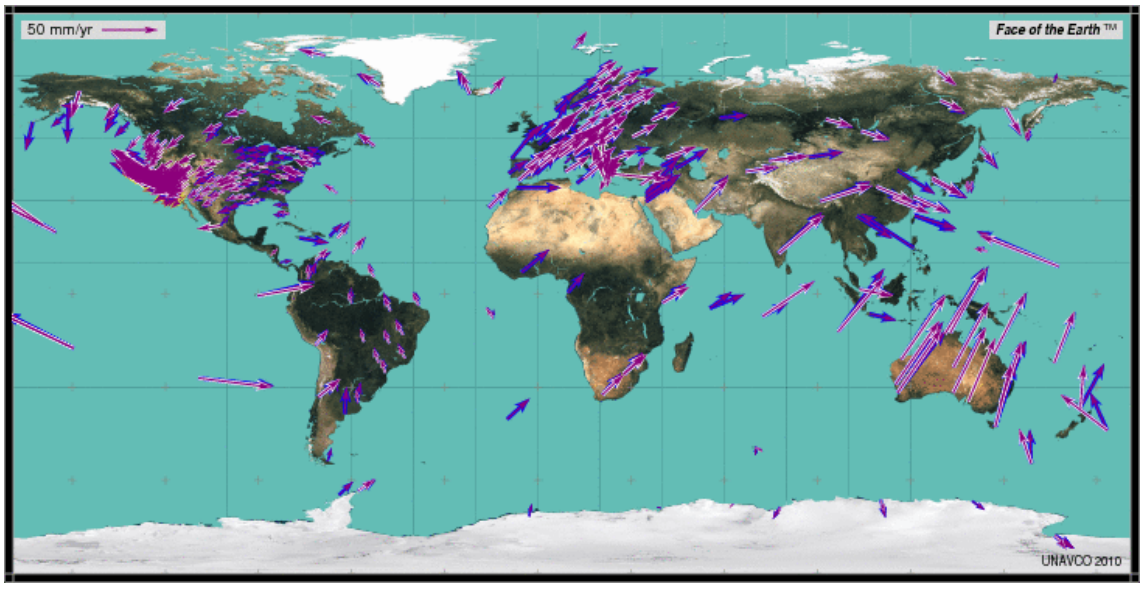

Fig. 5.21: Velocity of global IGS stations in the ITRF

5.2.3 TSX orbits

To compute range and azimuth from given coordinates, the precise SAR orbits and the acquisition direction, which can be found in the image annotation, are needed. The precise science orbits (PSO) are generated using the CODE (Center for Orbit Determination in Europe) Rapid GNSS orbits and GPS clocks (30 s temporal resolution) [Yoon et al. 2009].

Thus the TerraSAR-X orbit information is related to the reference system which is used in the CODE products. This is the IGS05, which is a GPS-only realisation of the International Terrestrial Reference Frame ITRF 2005.
The specified 3D accuracy requirement for the PSO is 20 cm [Yoon et al. 2009]. To value the real quality of the PSO, the results of two approaches for validation performed by Yoon et al. [2009] are outlined: The PSO products generated at DLR/GSOC (= German Space Operation Centre) are verified against orbit solutions provided by GFZ Potsdam. The agreement of the estimated orbit solution shows a 3D-RMS of 4.2 cm averaged over a period of ten days. An absolute orbit validation was performed using SLR measurements. A RMS of the range biases, averaged over eight stations, at 2 cm level was reached.
In the TSX-products the orbits are shifted that they represent the position of the phase centre of the SAR antenna.

5.2.4 Corner reflectors

A corner reflector is composed of three equal triangles. They are often used for geometric and radiometric calibration of SAR images, because their reflecting area and their geometric phase centre can be manufactured and determined accurately, in the order of millimetres. In SAR images corner reflectors appear as impulse response function of the SAR system. Corner Reflectors, which are oriented correctly, appear as a bright white feature in a SAR amplitude image.
A corner reflector can be located with an accuracy of

$$\sigma_{point} \approx \frac{0.55}{\sqrt{SCR}} \qquad (103)$$

in units of resolution elements, where SCR (signal-to-clutter ratio) is the signal to background clutter (including noise) power ratio. The signal power or backscatter of a corner reflector depends on its size and the wavelength, while the background clutter depends on the scattering characteristics in the surrounding of the corner reflector. [Eineder et al. 2010]

5.2.5 Installation of corner reflector and GPS-Receiver

The corner reflector has to be adjusted in such a way that the radar beam will be reflected back to the satellite with maximum power. The azimuth angle can be determined from the corner coordinates of the scene, which are provided in advance. The edge of the ground plane has to be oriented parallel to the azimuth direction.
For the tilt of the corner reflector the direction of the backscattering has to be considered. The incidence angle for a not tilted corner reflector (i.e. horizontal ground plane) is 57.74°.

To obtain the tilt of the ground plane relative to the horizontal, the incidence angle has to be subtracted from 57.74°. In Figure 5.22 the incidence angle was 20.58°, so the ground plane is tilted by 37.16°.

Fig. 5.22: GPS measurement of corner reflector coordinates at the DLR on 14th July

Since the GPS antenna can not be mounted in such a way that its phase centre corresponds to the CR phase centre, it is essential to know the exact distance from the corner reflector phase centre to the GPS antenna phase centre. Here the GPS antenna was mounted on a pole of exactly 1 m length. The peak was put in the corner reflector phase centre and the pole was fixed in a vertical position, so that the offset is 1 m in radial direction (see Figure 5.22). Additionally, phase centre offset of the GPS antenna have to be considered.

5.2.6 Procedure

In the following the general procedure for comparing range and azimuth derived from GPS coordinates (required) with range and azimuth measured in TSX or TDX images (actual) is described. First the main steps (1-8) of the procedure are outlined. Afterwards all steps are explained in detail.

During the GPS processing, correction for ionosphere and troposphere are taken into account, so that the GPS coordinates are free from these influences. The range delays derived from TSX/TDX images are influenced by these effects. Thus the delays from troposphere and ionosphere have to be added to the required range or removed from the actual range, to get comparable quantities. The GPS coordinates are given in the IGS05 (ITRF 2005) reference system, thus they have to be transferred to the instantaneous position (cf. Section 2.2.4) of the corner reflector to get the geometrical correct range and azimuth.

The main steps are:

1. Estimation of the IGS05 (ITRF 2005) coordinates of the corner reflector phase centre $\vec{p}_{ITRF,CR14}$ and $\vec{p}_{ITRF,CR17}$ for the respective epoch with differential GPS (reference station required).
→ 5.2.6.1

2. Corrections for solid Earth tides (SET), ocean loading (OTL) and pole tides (POL) extracted from Bernese 5.1. subroutines to receive the instantaneous position of the CR at SAR-image acquisition time:

$$\vec{p}(t) = \vec{p}_{ITRF} + \Delta\vec{r}_{SET}(t) + \Delta\vec{r}_{OTL}(t) + \Delta\vec{r}_{POL}(t) \quad (104)$$

→ 5.2.6.2

3. Estimation of the tropospheric zenith dry (*ZHD*) and wet (*ZWD*) delay from the reference station observations and determination of the slant delay of the troposphere in range direction (see Equation 55):

$$\Delta rg_{trp}(\theta_i,t) = m_{h,GMF}(\theta_i,t)\,ZHD + m_{w,GMF}(\theta_i,t)\,ZWD \quad (105)$$

Δrg_{trp} tropospheric delay in range direction [m]

→ 5.2.6.3

4. Estimation of the total TEC from the International Reference Ionosphere (IRI) and calculation of the slant group delay Δrg_{ion} using Equations 57, 59 and 60.

Δrg_{ion} ionospheric delay in range direction [m]

→ 5.2.6.3

5. Determination of the SAR-antenna position $\vec{S}(t')$ derived by solving the zero Doppler equation for the coordinates derived with GPS:

$$\left(\vec{S}(t') - \vec{p}(t')\right) \cdot \dot{\vec{S}}(t') = 0 \quad (106)$$

t' acquisition time

→ 5.2.6.4

6. Determination of required range and azimuth.
The geometrical distance between CR and SAR-antenna is:

$$rg_{geom} = \left|\vec{S}(t') - \vec{p}(t')\right| \text{ [m]} \quad (107)$$

Then it holds for the required range delay:

$$rg_{req} = \frac{rg_{geom}}{c} \cdot 2 \text{ [s]} \quad (108)$$

The required azimuth is the acquisition time:

$$az_{req} = t' \text{ [s]} \quad (109)$$

→ 5.2.6.4

7. Determination of actual (measured) range *rg′* and azimuth *az′* through measurement of the image coordinates of the corner reflector.

One gets the following range and azimuth pixel positions in a SAR image, if no corrections are applied:

$$rg_{pixel} = \left[\left(\frac{rg_{geom}}{c} \cdot 2 + \Delta t_{trp}(\theta_i) + \Delta t_{ion}(\theta_i) + \tau_{el} \right) - t_{rg,start} \right] \cdot RSF \text{ [Pixel]} \quad (110)$$

$$az_{pixel} = \left(t' - t_0 + \tau_{az} \right) \cdot PRF \text{ [Pixel]} \quad (111)$$

RSF	range sampling frequency
PRF	pulse repetition frequency
$t_{rg,start}$	time of the first pixel in range direction
t_0	start time of the acquisition
t'	time of the pulse, acquisition time
τ_{el}	instrument range delay or electronic delay
τ_{az}	instrument azimuth delay
$\Delta t_{trp/ion}$	tropospheric / ionospheric range delay [s]
c	speed of light

The range delay is derived from the pixel position with following equation, if no corrections for the atmospheric delays are applied:

$$rg' = \left(\frac{rg_{pixel}}{RSF} + t_{rg,start} - \tau_{el} \right) = \frac{rg_{geom}}{c} \cdot 2 + \Delta t_{trp}(\theta_i) + \Delta t_{ion}(\theta_i) \text{ [s]} \quad (112)$$

The image, from which the actual range delay *rg′* is derived, is corrected for the constant instrument range delay τ_{el}, which was determined in the calibration process.

The actual azimuth az' is

$$az' = \frac{az_{pixel}}{PRF} + t_0 \text{ [s]} \quad (113)$$

if further delays, included in τ_{az}, are not regarded. A value for τ_{az} is given in the annotations of the image.

For gaining the quantities in distance and not in time, the azimuth has to be multiplied with the flight velocity (zero Doppler velocity) and the range delay has to be multiplied with the speed of light and divided by two (by definition).

→ 5.2.6.4

8. As can be seen above the corrections for troposphere, atmosphere and azimuth delays are not regarded during the determination of actual range and azimuth. Since these influences are missing in the required range and azimuth, they have to be subtracted from measured range and azimuth. This leads to the following equations for the computation of the differences between actual and required range and actual and required azimuth:

$$\delta rg = rg' - \Delta t_{trp}(\theta_i) - \Delta t_{ion}(\theta_i) - rg_{req} \text{ [s]} \quad (114)$$

$$\delta az = az' - \tau_{az} - az_{req} \text{ [s]} \quad (115)$$

δrg, δaz residual range / azimuth error

→ 5.2.7

5.2.6.1 GPS-processing

All GPS-processing has been done using Bernese GPS Software, version 5.1, at the IAPG.

- *PPP-Solution*

For the reference station (PPM1) a PPP (Precise Point Positioning) solution, also called zero-difference-processing, was performed. That means no reference station is used. To receive accurate results with PPP at least 12 hours, preferably 24 hours of observations are needed.
For a PPP solution precise orbits and clocks from a GNSS analysis centre (here CODE) have to be used. They are needed to determine the geodetic datum.
Following Products were used for day 195 (14th July) (and for day 197 / 198, respectively):

- CODE Final GNSS orbits and GPS clocks for year-day 10-195: Middle day of a 3-day arc GPS/GLONASS solution
- CODE final GPS clock information for day 195

The a priori coordinates of the PPM1 station are given in the ETRF with no reliable information of the epoch and chosen realisation (cf. Section 5.2.2), but IGS05 coordinates are needed. Therefore the PPP solution of the day 197 has been used to determine IGS05 coordinates for the reference station (see Table 5.13).

In this solution, coordinates of the station, tropospheric parameters and the receiver clock error are estimated. The accuracy of coordinates estimated with PPP is in the range of 1-2 cm.

PPM1	X [m]	Y [m]	Z [m]
	4186741.4074	834903.9076	4723619.3881
WGS-84 ellipsoid	B	L	h [m]
	48° 5′ 3.4397″	11° 16′ 39.9506″	640.9890

Table 5.13: Coordinates of PPM1 station, determined with PPP-Solution for 16th July

- *Determination of the corner reflector coordinates*

A differential GPS approach was used to estimate the coordinates of the CR. It was turned and slightly moved between the two days with acquisitions, thus two different coordinates have to be determined. CR14 is the position at the 14th July and CR 17 is the position at the 17th July, which is equal to the position at the 16th July, since the CR has not been moved.
Because the baseline (PPM1 ↔ CR14/17) is so short, only the determination of relative tropospheric delays is possible in this approach, hence the absolute delays estimated in the PPP step are used as input.
The estimation was performed using following settings:
- using L1 only
- heavy constrains on the PPM1 coordinates (0.0001 m, 0.0001 m, 0.001 m)
- estimating ambiguities with the SIGMA method
- estimating tropospheric delays only for the reflector.

5.2.6.2 Corrections for solid Earth tides, pole tide and ocean loading

The GPS coordinates are given in the IGS05, thus they are conventional tide free. The TerraSAR-X satellite instead always observes the distance to the current Earth crust. This means the effects of solid Earth tides have to be added to the GPS coordinates again. For higher accuracy this also has to be done with the ocean loading and pole tide displacements.
The displacements of the stations for these effects are calculated with a subroutine of the Bernese software and are added to the IGS05 coordinates. These are shown in Table 5.14 and finally used as input for the calculation of the required range and azimuth. The total correction for SET, POL and OTL in radial direction is -4.0 cm for CR 14 and +2.9 cm for CR 17.
The corrections for CR 14 are shown in Figures 5.23 to 5.25, the time of acquisition is marked with the vertical dotted line, SET stands for solid Earth tides, POL for pole tide and OTL for ocean tide loading.

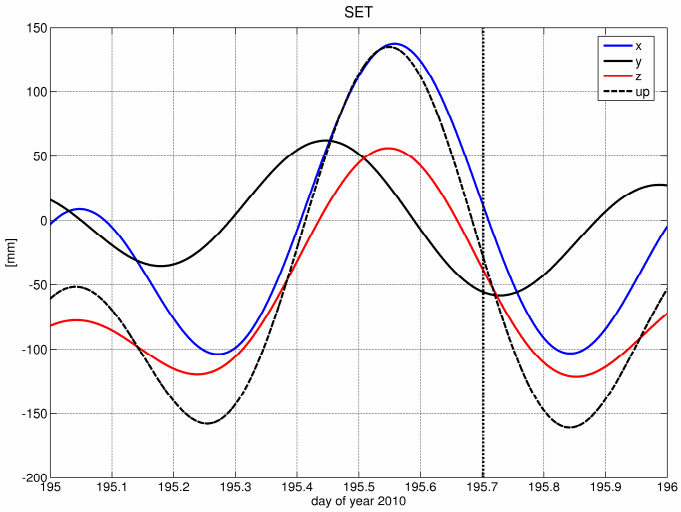

Fig. 5.23: Solid Earth tide correction for 14th July

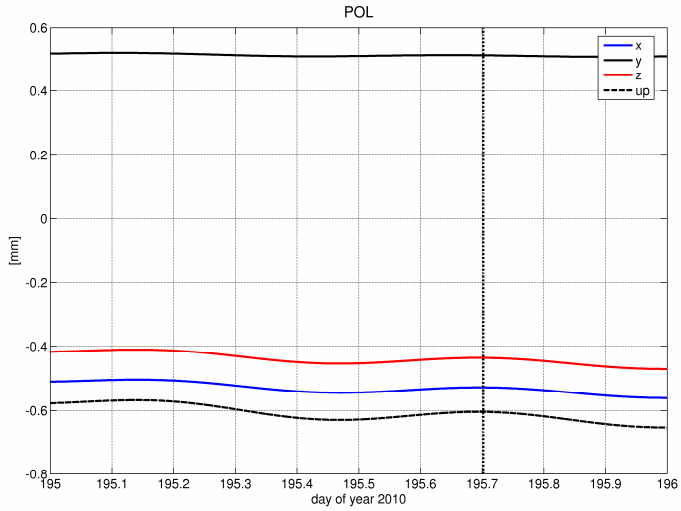

Fig. 5.24: Pole tide correction for 14th July

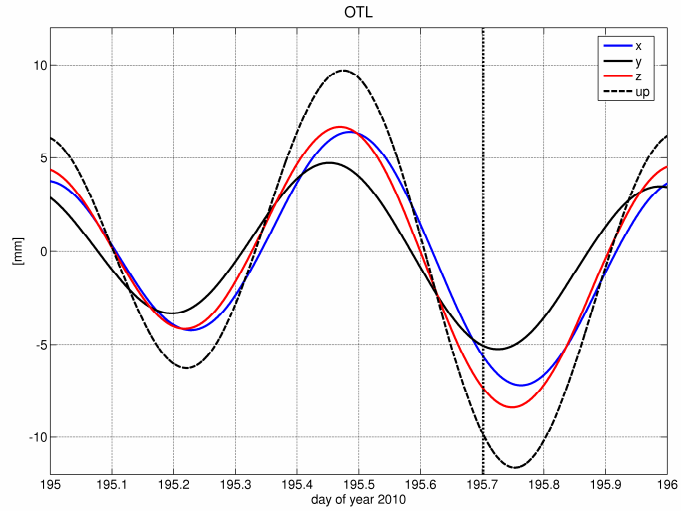

Fig. 5.25: Ocean loading correction for 14th July

CR 14	X [m]	Y [m]	Z [m]
	4186880.1721	834871.5509	4723484.7315
WGS-84 ellipsoid	B	L	h [m]
	48° 4′ 57.4017″	11° 16′ 37.1065″	627.473
CR 17	X [m]	Y [m]	Z [m]
	4186880.3041	834871.3010	4723484.7709
WGS-84 ellipsoid	B	L	h [m]
	48° 4′ 57.4006″	11°16 ′37.0934 ″	627.556

Table 5.14: Instantaneous coordinates for the corner reflectors at acquisition time

5.2.6.3 Atmospheric delays

- *Troposphere*

The tropospheric delay was estimated during the PPP solution with 2 hours resolution. For computing the a priori zenith path delay the dry Global Mapping Function (GMF) model is chosen. The wet part of the delay is estimated using the wet GMF model. The GMF is introduced in Section 2.5.2.1. The results can be seen in Figure 5.26.

STA	YYYY	MM	DD	HH	MM	SS	MOD_U	CORR_U	SIGMA_U	TOTAL_U
PPM1	**2010**	**07**	**14**	**14**	**00**	**00**	**2.1546**	**0.16558**	**0.00089**	**2.32022**
PPM1	**2010**	**07**	**14**	**16**	**00**	**00**	**2.1546**	**0.20435**	**0.00051**	**2.35898**
PPM1	2010	07	14	18	00	00	2.1546	0.21656	0.00050	2.37119
PPM1	2010	07	14	20	00	00	2.1546	0.20142	0.00049	2.35605
PPM1	2010	07	14	22	00	00	2.1546	0.21853	0.00059	2.37316
PPM1	2010	07	15	00	00	00	2.1546	0.25241	0.00086	2.40704

STA	YYYY	MM	DD	HH	MM	SS	MOD_U	CORR_U	SIGMA_U	TOTAL U
PPM1	2010	07	16	00	00	00	2.1546	0.19101	0.00072	2.34562
PPM1	2010	07	16	02	00	00	2.1546	0.17761	0.00041	2.33222
PPM1	**2010**	**07**	**16**	**04**	**00**	**00**	**2.1546**	**0.16335**	**0.00036**	**2.31796**
PPM1	**2010**	**07**	**16**	**06**	**00**	**00**	**2.1546**	**0.17986**	**0.00044**	**2.33447**
PPM1	2010	07	16	08	00	00	2.1546	0.19033	0.00037	2.34494
PPM1	2010	07	16	10	00	00	2.1546	0.20056	0.00035	2.35517
PPM1	2010	07	16	12	00	00	2.1546	0.19412	0.00043	2.34873
PPM1	2010	07	16	14	00	00	2.1546	0.20702	0.00036	2.36163
PPM1	2010	07	16	16	00	00	2.1546	0.22261	0.00041	2.37722
PPM1	2010	07	16	18	00	00	2.1546	0.24884	0.00042	2.40345
PPM1	2010	07	16	20	00	00	2.1546	0.24046	0.00042	2.39507
PPM1	2010	07	16	22	00	00	2.1546	0.24238	0.00043	2.39698
PPM1	2010	07	17	00	00	00	2.1546	0.20044	0.00070	2.35505

Fig. 5.26: Results for the estimation of the tropospheric delay (extracted from Bernese TRP files)

`MOD_U`	a priori (dry) zenith delay model [m] (= *ZHD* in Equation 54 and 55)
`CORR_U`	estimated (wet) zenith delay [m] (= *ZWD* in Equation 54 and 55)
`SIGMA_U`	formal error of `CORR_U` [m]
`TOTAL_U`	`MOD_U + CORR_U` [m]

The delay for the correct time was interpolated from the estimates before and after the acquisition (bold lines in Figure 5.26). These values are inserted into Equation 55 together with the factors provided by the GMF. The resulting delays are shown in Table 5.15.

Date	Δrg_{trp}	$\Delta rg_{trp,dry}$	$\Delta rg_{trp,wet}$
14th July	2.5302 m	2.3059 m	0.2243 m
17th July	3.7766 m	3.4425 m	0.3341 m

Table 5.15: Tropospheric delay

- *Ionosphere*

The ionospheric delay is not estimated during the GPS processing. The effects of the ionosphere are cancelling out in both approaches:
For the long term PPP observations the ionosphere free linear combination is used, which makes use of the dispersive behaviour of the ionosphere.
For the differential GPS solution with very short baseline (here ≈ 200 m) the ionosphere can assumed to be equal at both stations and so it cancels out during the creation of the double differences.

The VTEC for the correction of the range value is derived from the International Reference Ionosphere 2007 (IRI-2007). Since the effect of the ionosphere on the X-Band frequency is much smaller than that of the troposphere, the model values can be used as sufficient approximation.
The values given below are computed with the IRI online computation tool[35] (see attachment). The VTEC has been calculated for the TerraSAR-X satellite nominal height of 514 km with a resolution of 0.5 hours, the results are shown in Table 5.16. Additional input parameters are latitude, longitude and time.

date	time (UTC)	IRI VTEC	resulting slant delay: Δrg_{ion}
14th July	16:30	8.9	
	17:00	9.2	
	16:51 (interpolated)	9.1	4.2 cm
17th July	4:00	5.0	
	4:30	5.5	
	5:18 (interpolated)	5.3	3.4 cm

Table 5.16: TEC values and ionospheric delay

[35] http://omniweb.gsfc.nasa.gov/vitmo/iri_vitmo.html; last access 05.11.2010; form see appendix

With known incidence angle the delay can be calculated using the Equations 57, 59 and 60 given in Chapter 2. For SAR pulses the ionospheric delay has to be calculated for group propagation [Eineder et al. 2010]. Regarding the respective incidence angles the ionospheric delay is 4.2 cm at the 14th July and 3.4 cm at the 17th July.

5.2.6.4 Determination of range and azimuth

The GPS coordinates are used to get the SAR antenna position for the acquisition time of the CR using the DLR software for Zero-Doppler-Equation solution. From this the required range delay and azimuth for the corner reflector can be derived.
The sub-pixel position of the corner reflectors is measured in the Point Target Analysis software to receive actual range and azimuth. This software is shown in Figure 5.27. The corner reflector in the image from 14th July is marked with a yellow circle.

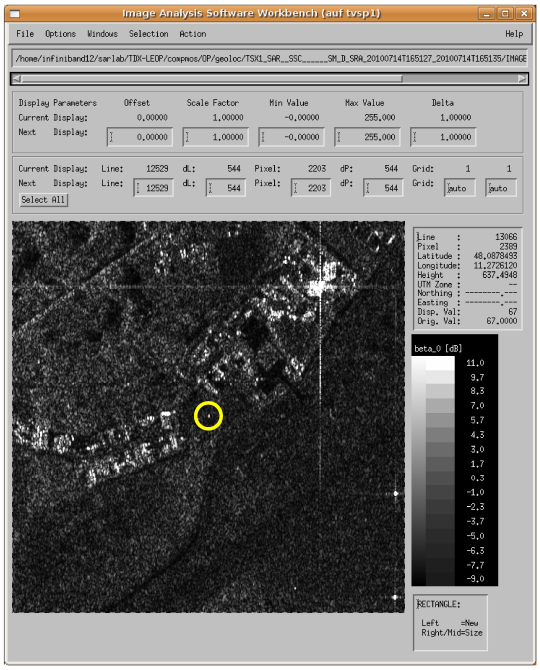

Fig. 5.27: DLR software for Point Target Analysis (position and power of the CR)

5.2.7 Results and discussion

Table 5.17 shows required range delay rg_{req} and azimuth az_{req} derived from the GPS positions (see Table 5.14) and actual range delay rg' and azimuth az' derived from the measurement of the corner reflectors in the SAR images.
Peak amplitude and peak phase are quantities in the SAR image at the position of the reflector.

corner ID	peak amplitude [dB]	peak phase [degree]	required position		actual position			
			azimuth [s of day]	range [s]	azimuth (UTC)	azimuth [s of day]	range [ms]	range [s]
CR-14	62.79	-161.54	60691.79629	0.003646	2010-07-14T16:51:31.796261507	60691.796262	3.646	0.003646
CR-17	66.07	133.45	19082.16303	0.005186	2010-07-17T05:18:02.162980022	19082.162980	5.186	0.005186

Table 5.17: Required and actual azimuth and range for CR 14 and CR 17

In Table 5.18 the differences between actual azimuth / range delay and required azimuth / range delay are given. The additional delays which have to be removed from actual azimuth and range delay are given in the columns "delay". In the two upper lines the delays from the annotation of the SAR images are used. In the lines below the delays estimated with GPS and extracted from IRI, as described above, are used. In the last two lines it is the same as in the lines before only that it is corrected for the tropospheric dry delay but not for the wet delay.
The last two columns show the remaining difference in [m], after the delays have been applied (cf. Equation 114 and 115).

corner ID	difference (act-req)		delay (annotated values)			remaining difference		remaining difference	
	azimuth [s]	range [s]	azimuth [s]	troposphere [s]	ionosphere [s]	azimuth [s]	range [s]	azimuth [m]	range [m]
CR-14	-3.1973E-05	1.6221E-08	-4.4720E-05	1.4797E-08	1.5444E-10	1.2747E-05	1.2698E-09	0.090	0.190
CR-17	-4.6803E-05	2.3904E-08	-4.4720E-05	2.2160E-08	2.3096E-10	-2.0833E-06	1.5136E-09	-0.015	0.227
					mean	5.3318E-06	1.3917E-09	0.038	0.209
					sigma	1.0486E-05	1.7237E-10	0.074	0.026

corner ID	difference (act-req)		delay (GPS for tropo., IRI for iono.)			remaining difference		remaining difference	
	azimuth [s]	range [s]	azimuth [s]	troposphere [s] wet + dry	ionosphere [s]	azimuth [s]	range [s]	azimuth [m]	range [m]
CR-14	-3.1973E-05	1.6221E-08	-4.4720E-05	1.6880E-08	2.7886E-10	1.2747E-05	-9.3729E-10	0.090	-0.140
CR-17	-4.6803E-05	2.3904E-08	-4.4720E-05	2.5195E-08	2.2349E-10	-2.0833E-06	-1.5142E-09	-0.015	-0.227
					mean	5.3318E-06	-1.2258E-09	0.038	-0.184
					sigma	1.0486E-05	4.0796E-10	0.074	0.061

corner ID	difference (act-req)		delay (GPS for tropo., IRI for iono.)			remaining difference		remaining difference	
	azimuth [s]	range [s]	azimuth [s]	troposphere [s] only dry	ionosphere [s]	azimuth [s]	range [s]	azimuth [m]	range [m]
CR-14	-3.1973E-05	1.6221E-08	-4.4720E-05	1.5383E-08	2.7886E-10	1.2747E-05	-9.3729E-10	0.090	0.084
CR-17	-4.6803E-05	2.3904E-08	-4.4720E-05	2.2966E-08	2.2349E-10	-2.0833E-06	-1.5142E-09	-0.015	0.107
					mean	5.3318E-06	-1.2258E-09	0.038	0.095
					sigma	1.0486E-05	4.0796E-10	0.074	0.016

Table 5.18: Differences of required and actual azimuth and required and actual range without and with corrections (= remaining difference); in the first case the annotated corrections are used, in the cases below the corrections derived from GPS and IRI are used; it is not corrected for the tropospheric wet delay in the last case.

For the azimuth delay τ_{az} a constant value of -0.00004472 s is taken into account. This value is also annotated in the products, but not used for correction of the images. It includes for example errors due to uncertainties in the synchronisation of the time stamps of GPS receiver, which is used for orbit determination, and SAR oscillator.

The TSX instrument range delay τ_{el} was calibrated with a static troposphere model and a static VTEC of 5 TECU. For both cases the mapping function $1/\cos\theta_i$ is used.
The annotated and IRI derived ionospheric delays are nearly the same for CR 17, since the TEC value for this day was nearly 5 TECU. For CR 14 the delay is larger for the IRI values since this acquisition was in the afternoon, when the ionospheric activity is usually stronger than in the morning.

The troposphere model uses a constant value for the vertical delay, where only the hydrostatic part of the tropospheric delay is considered. The constant value is scaled with the barometric height equation to the respective terrain height of the scene.
Hence, there are the following three error sources, which lead to a bias in τ_{el}:

- using a constant value for the tropospheric hydrostatic delay
- using a constant value for the ionospheric delay
- neglecting the tropospheric wet delay.

The neglecting of the wet delay results in a systematic underestimating of the tropospheric total delay during the calibration. Hence the estimation of the instrument range delay leads to a value, which is too large, because the tropospheric wet delay is incorporated in τ_{el}.
The tropospheric delay values from the model, which was also used for calibration, can be found in the image annotations. They are given in Table 5.18 (upper two lines). It can be seen that they are smaller than the tropospheric delays, which have been estimated during the GPS processing, what confirms that the tropospheric delay, used for calibration, is too small. The differences (for Δrg_{trp}) are

- 31 cm for acquisition TSX 14 and
- 45 cm for acquisition TSX 17.

Since τ_{el} is too large, ranges derived from image coordinates are systematically determined too small.
In Equation 114 the tropospheric wet delay is, at least partially, subtracted two times, once with the tropospheric correction Δt_{trp} and once with τ_{el}, which is included in rg'. The resulting negative values in Table 5.17

- -14.0 cm for acquisition TSX 14 and
- -22.7 cm for acquisition TSX 17

for the residual error δrg (converted to [m]) are a consequence of this. The difference between the acquisitions is 8.7 cm, what is clearly larger than the 3.7 cm from the case with annotated values. This can be ascribed to the calibration process, which was performed in such a way that the best results are achieved for the used models. The 8.7 cm difference might be too large if an orbit accuracy of 2 to 4 cm is assumed, but it is still in the range of the specified orbit accuracy of 20 cm (cf. Section 5.2.3).
If the tropospheric correction in Equation 114 is only applied for the dry delay, the residual errors (converted to [m]) have the following values:

- +8.4 cm for acquisition TSX 14 and
- +10.7 cm for acquisition TSX 17.

Now the difference between the two acquisitions is only 2.3 cm, which is in the range of the 2 to 4 cm orbit accuracy. Since τ_{el} is not dependent on the incidence angle, the difference of the wet delay should still be inherent in rg'. This does not fit to the observations here, where a better result is achieved by neglecting these differences.

The remaining absolute errors in the range of 1-2 dm can be mainly ascribed to the imperfect calibration process or more specifically to the imperfect atmospheric models used for it. Additional contributions are the orbit errors and all other small effects, for which no correction is applied yet.

5.2.8 Conclusions

It has been shown in this section that it is necessary to consider all mentioned influences, possibly with the exception of the pole tide ([mm] range) if absolute SAR measurements shall be performed. It is also pointed out that there has to be consistency concerning the reference systems. A systematic error in the azimuth could be eliminated with determining ITRF coordinates for the corner reflector, instead of the formerly used ETRF coordinates.
The results also show that further investigations, with more acquisitions and with a preferable large variety of incidence angles and tropospheric as well as ionospheric conditions, have to be made to expose all existing errors in the range and azimuth determination. The instrument range delay has to be calibrated with regarding the correction for troposphere and ionosphere, to get a higher accuracy for this term. Only under this precondition the potential of the TSX/TDX satellites can be fully exploited.
If all disturbing effects can be removed correctly, the orbit accuracy is the remaining error source for absolute SAR coordinates / ranges. If the orbit accuracy is a few [cm] as claimed above, small signals in the range of a few [mm] to a few [cm] (e.g. atmospheric loading) still are undetectable, but the variation of the wet delay due to the water vapour is large enough to be a quantity which could be derived by absolute range measurements. The larger effects of solid Earth tides, plate tectonics (over longer periods) and tropospheric dry delay shall be visible too. Since these effects are less variable and/or well predictable from models, it can be easily corrected for them.

6 Measurement concepts

In this chapter ideas shall be developed how the different measurement systems, described in Chapter 4, can be combined usefully to derive new or more precise information on hydrologic and atmospheric processes. Additionally, there is a proposal for an improved version of the SAR-GPS test measurement (cf. Section 5.2).
In Section 6.1 campaigns dealing with hydrology are proposed. Gravity differences shall be used to detect variations in the water storage change in the test site area (6.1.1). In a second campaign a stationary gravimeter shall be used to separate large-scale and local signals (6.1.2). In the latter approach a geometric measurement system (GPS permanent station) shall support the task. For both campaigns the connections to hydrological modelling and instruments are depicted.
In terms of atmosphere an approach is suggested applying a stationary gravimeter for a measurement period of several weeks for investigations about the local atmospheric admittance factor (6.2).
Finally in Section 6.3 a proposal on a measurement station for the evaluation of SAR range and azimuth accuracy and for detecting remaining errors is outlined.

6.1 Hydrology campaigns

Before starting a measurement campaign the objectives have to be clearly defined, so that an appropriate measurement strategy can be developed. Therefore, the following points, regarding the hydrology, have to be considered:

- Utilisable or spurious signal

There are two ways of looking at hydrology in terms of gravity measurements. On the one hand hydrological variations can be a signal which shall be measured, on the other hand they can be a disturbing influence on the gravity value, if gravity changes due to other sources shall be detected.

- Small or large-scale signal

Another distinction has to be made between local and large- (continental-) scale effects of hydrology. If the integrative effect of local hydrology shall be measured, the large-scale effect has to be removed. In contrast to this local effects can not be found in a large-scale hydrological model or in GRACE measurements since they are smeared out because of the coarse resolution. Thus gravity values have to be corrected for local hydrology in such a way that only the large-scale signal is preserved, if, for example, GRACE data shall be validated. The large-scale effect usually has a seasonal signal, as has been shown in Section 3.3. Generally it can be said, that the separation from local and large-scale

hydrological effects is not an easy task, since the large-scale effect is only a few [μGal] (or [mm], respectively), and other effects in the same magnitude range, such as atmosphere or ocean loading, have to be measured or modelled correctly.

- Derivation of gravity changes or of hydrological parameters

If a hydrological model shall be validated, its results can be converted to integrative gravity change and then compared to the measurements. If hydrological parameters shall be derived the gravity variations have to be converted, so that they can depict local hydrological dependencies. Since there is a large contrast between hydrological complexity and the integrative measurement of the gravimeter this can only be done empirically (see next point).

- Simple admittance factor or complex approach

If gravity measurements shall only be reduced for the hydrological effect, a local admittance factor between gravity (or height change) and a local dominating hydrological quantity, e.g. ground water level, can be determined. These quantities have to be measured close to the gravity site. After correcting for other effects the relation between the measured values can be determined. If this is not sufficient the (local) hydrological situation has to be modelled.

6.1.1 Gravity differences (profile, network)

- Objectives
  - validating hydrological models
  - evaluation of the hydrological situation
- Instrumentation
  - relative field gravimeter (possibly usage of additional gravimeter from different manufacturers)
  - GPS receiver, levelling instrument
- Requirements for the location
  - setting long-term stable reference marks to avoid spurious signals e.g. due to local settlements
  - selection of appropriate observation points considering the hydrologic conditions
- Tasks
  - measuring the marks (GPS and/or levelling)
  - regular gravimetric measuring campaigns, dependent on the period of the signal
- Measured quantity
  - change of gravity differences

Possible configurations

- *Gravity profile*

A possible approach for gravity differences could be the connection of two groundwater observation wells with a profile of gravity measurement points. From this information about the hydrological situation between both points can be derived.

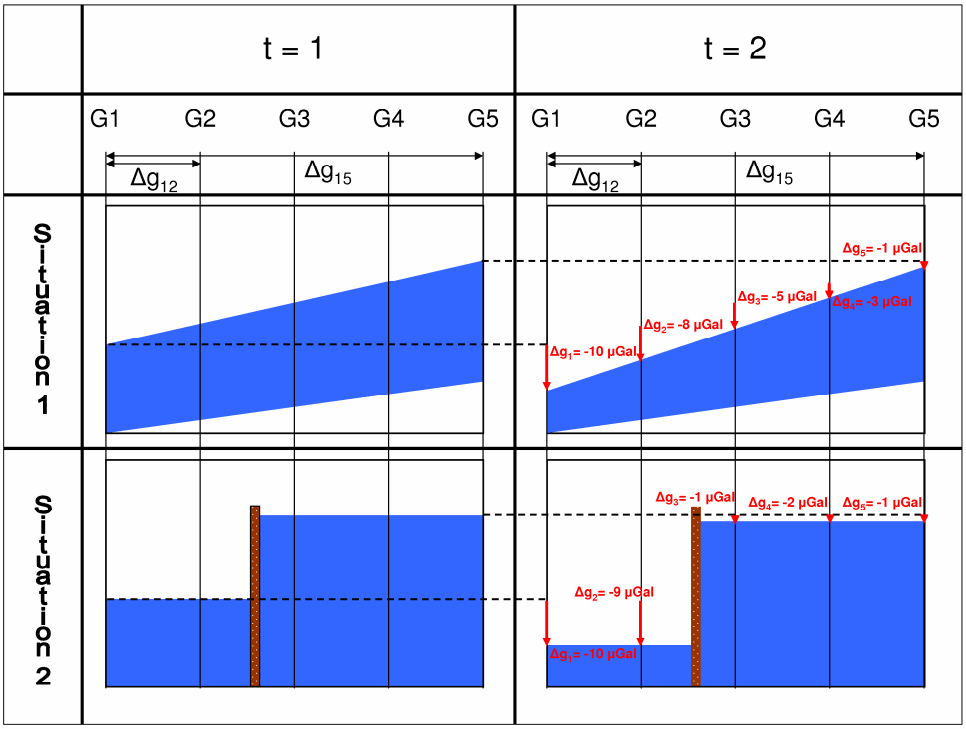

Fig. 6.1: Example for gravity profile for detection of groundwater variations; with approximation of Equation 61: 1 µGal is equal to 24 cm water level change (for a specific yield of 0.1)

The fictive situation in Figure 6.1 is generated in dependence on the situation at the observation wells in Graswang and Ettal (cf. Section 3.3.2). The figure shows two different possible situations for the groundwater (blue area) along the profile with the observation points G1 to G5:

- Situation 1: single aquifer with groundwater table, which rises from G1 to G5
- Situation 2: two aquifers, which are separated through a impermeable vertical soil layer

The water table changes from time step 1 to 2. The change at start and end point G1 and G5 shall be equal for both situations, for all other points the change is diverging due to different conditions in the ground. The fictive gravity changes are sketched in Figure 6.1 for time step 2. With the approximation of Equation 61 1 µGal is equal to 24 cm water level change, for a specific yield of 0.1.

In Figure 6.2 gravity differences (relative to G1) and gravity difference changes (between time step 1 and 2) can be seen for this simple example. The gravity differences of time step 1 are assumed to be equal and are chosen arbitrarily. The changes of the gravity differences are plotted on the right and are computed for the values given in Figure 6.1.
It can be derived how the amount of water beneath the surface changes at the different observation points relative to each other. Observation wells can provide the relation to the absolute water table change. Looking at the behaviour of the curve of the gravity changes, statements about the geological situation can be derived, for example whether the water tables are connected or not.

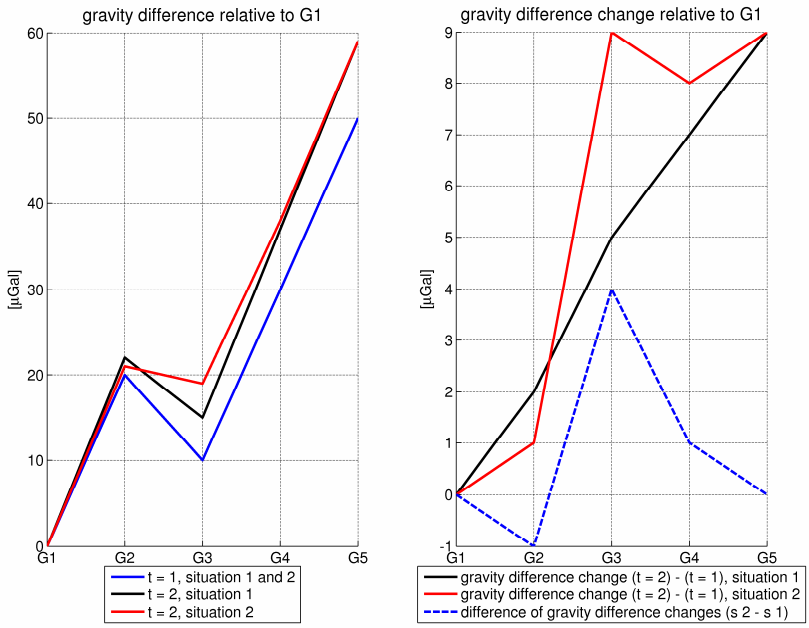

Fig. 6.2: Gravity differences (left) and gravity difference changes (right) for the situations shown in Figure 6.1

- *Gravity Network*

The aim of the network is to derive a measure for validating a hydrologic model of the type described in Section 3.2.2, with a horizontal resolution of around 100 m. Therefore a gravity network over the catchment area shall be established. The choice of the location of the measurement points shall be driven by the demands of the hydrologists. The sites have to be selected in such a way that a measurable signal can be expected. The idea is to derive differences in the water storage change by measuring the gravity difference changes between areas with strong hydrological signal and areas with small signal.
A possible measurement configuration can be seen in Figure 6.3. For every location (A, B, C) at least three measurement points within one grid cell (e.g. 90 m x 90 m) of the hydrological model are recommended. These points can be occupied two or three times

without long transport ways to determine the drift. At least the first location should be revisited to get a reliable drift estimation; in the case that the drift behaviour of the gravimeter turns out to be unstable it can be useful to revisit all positions. The test measurement at the storm water basin (cf. Section 5.1.2) has for example shown a large variability of the drift for the Scintrex gravimeter.

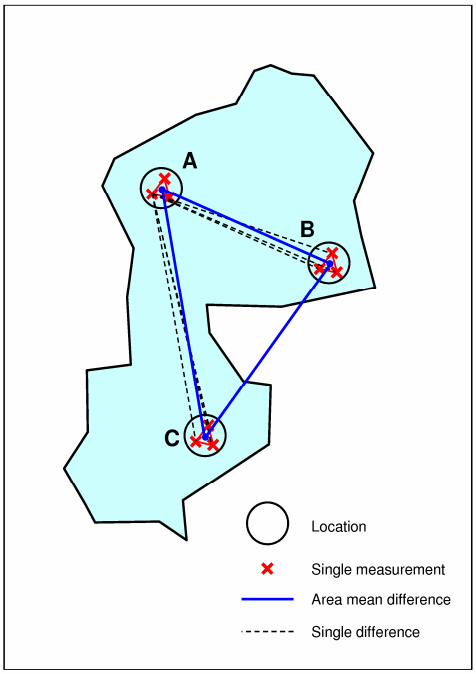

Fig. 6.3: Schematic depiction of a gravity difference network

For every location the mean of the gravity values of the single measurements can be calculated. For this it has to be corrected for instrument height to reduce the gravity value to the marker on the ground with the free-air-gradient, since the instrument can not be installed exactly the same every visit. For the height of the observation point (marker height) it has only be corrected for, if the gravity values shall be reduced to the same height level. For that the usage of the refined Bouguer topographic reduction ([Rummel 2007]) is recommended, what requires a local elevation model. Since the height differences between the markers stay stable, this correction is not obligatory.
The gravity difference changes between the mean values shall represent the differences in the water storage change of the model grid cells. For further analysis the differences between every single measurement point can be used. This can help to detect outlier in the single measurements.

To derive absolute gravity changes absolute gravity measurements have to be performed at one of the locations. Another possibility to relate gravity values of different times to each other is the installation of a stationary instrument, which records the gravity change

continuously at one of the locations. Again the drift has to be determined exactly to get the real gravity change. A possible instrument for that task could be the gPhone.

Another use of this concept could be the finding of a measure for the runoff process in the alpine zone. Therefore measurements have to be performed on several days after a strong precipitation event. The differences are calculated for a station near to a slope in the alpine part in the south of the area and for a station in the flat northern part. Different storage changes are expected, since at the alpine station water will be stored in regions above the gravimeter and will move downwards with time, while in the flatland station water will be stored instantly below the gravimeter.

Measurement frequency

How often a measurement shall be executed is dependent on the expected period of the signal, which shall be detected. Then an appropriate constant interval between the measurements can be chosen, for example every month. This can be complemented by measurements after certain events, for example a strong precipitation event.

Large-scale and long-term signals

In difference approaches the large-scale hydrological effect will mostly cancel out, since it affects measurement points with distances of maximal a few tens of [km] in the same way. Also all other long-term variations (with periods of months or longer), which show the same or at least a similar signal for all measurement points, will not play a role. This is because the gravity differences are determined within one or two days, and thus the disturbing influence changes only very slightly. The atmospheric pressure, instead, has to be considered, since there are also short-term variations.

Magnitude of signals and measurement accuracy

Whether a storage change is detectable or not, is dependent on the variety within the catchment as well as the accuracy and drift behaviour of the used instrument.
In this concept only small differences between the stations of only one to a few [μGal] are expected (see also example for gravity profile), dependent on the time interval between the measurements and the hydrological variability.
Because of this the used gravimeter has to provide an appropriate accuracy. The accuracy level of gravimeters, which are suitable for outdoor operation, is in the range of the expected signals (cf. Table 4.3). This means that following points have to be regarded to get the best possible accuracy out of the instruments:

- The instruments have to be calibrated very accurately.

- Investigations have to be made to get a precise knowledge of the drift behaviour. An appropriate strategy for drift determination has to be chosen, since every gravity change due to the drift, which is not captured by the drift correction, is interpreted as hydrological signal. (see also “Usage of more than one gravimeter” below)
- The transport of the instrument should disturb the drift behaviour to the least possible extent.
- Atmospheric correction has to be applied.

Since the drift behaviour of the Scintrex gravimeter was not easy to handle during the test measurements, the usage of (additional) LCR gravimeter or Burris Gravity Meter would be useful since the measurement method of these instruments provides a more stable drift behaviour, especially for mature springs (cf. Section 4.2.1 and Table 4.3).

Usage of more than one gravimeter

The usage of a second or more gravimeters has the following advantages:
- The campaign can be accomplished in a shorter time, because different gravity differences can be observed at the same time; for that also more staff is needed. The instruments should preferably be of the same type to get consistent observations.
- Independent determination of the gravity differences. The instruments should preferably be of different types.
- More observations are available for a better drift determination. The instruments should preferably be of different types.

6.1.2 Separation of large-scale and local hydrology

- Objectives:
  - Separating large-scale and local hydrology (Approach 1 + 2)
  - Objectives categorized for two different variants of this campaign are shown in Table 6.1.

Approach 1	***Approach 2***
- Extracting and analysing large-scale signal	- Extracting and analysing local signal
- Validation of GRACE measurements	- Evaluating local hydrological model results
- Reducing local hydrology with local model	- Reducing large-scale signal

Table 6.1: Comparison of objectives for Approach 1 and 2

- Instrumentation
  - superconducting gravimeter (iGrav) or gPhone
  - permanent GPS station
  - absolute gravimeter for drift determination (optional)
- Requirements for the location
  - TERENO site with lysimeter
  - secure building for the instruments
  - site with appropriate hydrological situation
- Tasks
  - Set up of a hydrological model which is adapted to the local conditions of the chosen site.
  - Integration of the GPS station in a GPS network to reach [mm]-accuracy for the station coordinates time series. Observations over at least one year are necessary for the detection of annual temporal variations.
  - Computation of loading effects using global models or GRACE measurements.
  - Learning the handling of the gravimetric instrument (it needs some experience to operate gravimeters, especially superconducting gravimeters, in such a way that high accuracy requirements can be fulfilled).
- Measured quantities
  - gravity residuals representing hydrology
  - station height variations representing hydrology

This campaign is the most sophisticated and requires the most effort. It comprises the installation of a stationary gravimeter and a permanent GNSS station.

Preprocessing

In the following it is described which corrections have to be applied that the measurements represent hydrology:

- Gravimetric and geometric measurement time series have to be reduced for solid Earth tides, ocean loading and pole tide.
- To correct for the atmospheric signal, direct and indirect influence of the atmosphere have to be computed using global models and the Green's functions formalism (cf. Section 2.1).
- The gravimeter measurements have to be corrected for the drift. Measurements with absolute gravimeters in certain intervals can support the drift determination.
- The gravity values have also to be analysed for spurious signals due to seismic events. The origin of such a signal can be small local events or large earthquakes far away, as it occurred during the basement experiment (cf. Section 5.1.1).
  It is also possible to have signals from seismic activity in the GNSS measurements.

The deviations from a non-constant gravity value are the gravity residuals. A constant gravity value would be the result if all variations, inclusive hydrology, are reduced perfectly. The geometric signal is the residual (vertical) movement of the station.

Description of the structure of Figure 6.6 and 6.7

Figure 6.6 and Figure 6.7 depict the procedure of the Approaches 1 and 2, respectively. The meanings of the elements in the figures are:

- red elements → gravimetric measurements
- yellow elements → geometric measurements
- blue elements → hydrologic measurements (local)
- green elements → global hydrologic models / measurements
- black rectangles → representing the hydrological signals

The points explained in "Preprocessing" are depicted by the red and yellow boxes. They represent the corrections, which have to be applied.

The hydrological signal is represented by the rectangles in the middle of the figures, one for the gravimetric and one for the geometric signal. The signal can be divided into different parts, as shown in Figure 6.4. There are six boxes, which all represent one part of the signal. Every box is filled with a grey rectangle, whose size shall illustrate the relative magnitude of the signal part. The relation may vary, partially strongly, from station to station. The expected magnitude of the total signal is given above the rectangle.

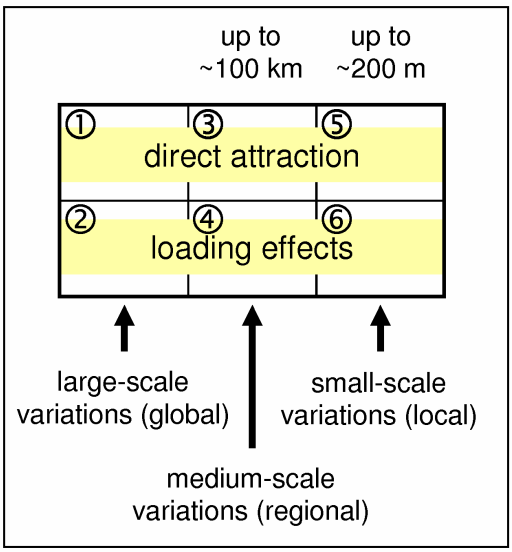

Fig. 6.4: Legend for Figures 6.6 and 6.7

The boxes 5 and 6 on the right stand for the local attraction and the loading effect due to mass changes with small extent (= mass distributions with high frequency), respectively.

The boxes 3 and 4 in the middle represent the attraction of masses which are more distant than a few hundred meter and loading masses with a spatially coherent extent up to 100 km (regional scale), respectively.
The boxes 1 and 2 on the left represent all masses which are not covered by the other boxes and loading masses with large spatial extent (global or continental scale), respectively.
The upper three boxes (1, 3 and 5) represent the direct attraction of the masses, the lower three (2, 4 and 6) the indirect loading effects. From this follows that for the geometric effect only the boxes 2, 4 and 6 are relevant, since there is no direct effect.
Vertical displacements due to further local processes like soil settlements are assigned to the local loading effects (rectangle with the stripe pattern in box 6) as spurious signal in this depiction. These displacements lead to gravity variations again, thus the striped rectangle can also be found in box 6 for the gravimetric signal.

Hydrological signals

In Figure 6.6 and 6.7 the local attraction is depicted as the largest gravimetric effect. The direct effect becomes smaller for more distant masses. For the loading case it is just the opposite. In this case the largest effect is due to the large-scale mass effects. The signal becomes smaller for mass variations of smaller wavelengths and is close to zero for very local loads (cf. Section 2.1.2 and Figure 2.1). This holds for the geometric as well as for the gravimetric signal.
Normally the (local) direct mass effect is the dominating part of the hydrologic signal and of the gravity-to-height ratio (cf. Section 2.1.3 and Figure 2.2). Because of this the rectangle in box 6 is the largest by far.

Local hydrological model

Another prerequisite for this campaign is that the local hydrological situation can be described in a high resolution. The 90 m grid from the modelling approaches, described in Section 3.2.2, is too large for the nearest surrounding of the gravimeter, so the grid cell with the gravimeter station has to be refined by additional observations. Since a lysimeter provides valuable data about the hydrological fluxes, it can support the determination of the local hydrological situation.

Benefits of the geometric measurements

Geometric measurements help to define the deformation / loading term and thus to support the determination of the real annual or large-scale signal. If the annual or large-scale signal shall be eliminated, the gravity-to-height ratio (cf. Section 2.1.3) can be used to convert the geometric measurements to gravity variations. A ratio has to be used, for which a

representative value, irrespective of the spectrum of the loading masses, exists. If only the indirect effects (boxes 2 and 4) shall be regarded the ratio for the elastic effect has to be used (cf. Equation 21). If also the direct attraction of large-scale loads (boxes 1 and 3) shall be included the ratio with the additional global Newtonian attraction (Equation 22) term can be used.

Approach 1

- *Objectives*

The aim of Approach 1 is to analyse and extract a large-scale signal. This signal can be used for the validation of GRACE data. Therefore the only possibility is the use of a superconducting gravimeter or, with restriction, the gPhone (see Section 4.2.1). As it was shown in the basement experiment (cf. Section 5.1.1) the accuracy of a gravimeter in the class of the tested Scintrex CG-3M is not sufficient and the drift behaviour is not stable enough to extract small long-periodic signals from a stationary gravity recording.

- *Location*

For this purpose a location for the gravimeter is preferable, where the hydrological and topographical situation is not too complex, since this would help to model the local hydrology correctly. Large gradients in topography, as occur in the south of the TERENO site, can make the situation more complex. For example if the gravimeter is placed below a slope the gravity can first decrease during a precipitation event because the area above the gravimeter gets more mass. If this water moves down, as surface runoff or as interflow, the gravity increases. Such effects enlarge the short time variability of local hydrology.
The TERENO station in Fendt could be a possible location. Several instruments, including a lysimeter, are mounted there (cf. Section 4.1). The station is located in the northwest of the TERENO area, where no large topographic variations occur. The local hydrological variations may also be relatively small there.

- *Procedure*

In Figure 6.6 the procedure for Approach 1 is shown. The hydrological situation has to be modelled for the surrounding of the gravimeter. This model shall lead to an estimation of the local water storage change. Therefore a 3D-grid of the soil has to be used. The necessary resolution of this grid is dependent on the variability of the soil properties and on the distance to the gravimeter. For every grid cell the change of water content has to be calculated from the hydrological model and/or in situ measurements (e.g. lysimeter). Then

this has to be converted into gravity changes, e.g. with the approach of Leirião et al. [2009] (cf. Section 3.2.3).
These local variations have to be subtracted from the gravity residuals, and then the large-scale signal should appear. This is expected to have an annual period (see estimation of the annual signal in Section 3.3).
Since the geometric and the gravimetric signal have an equal origin now, they should have a linear dependency (gravity-to-height ratio without local effects). Deviations can be ascribed to errors of the local hydrological model or in the elimination of other signals and have to be analysed. The large amount of recorded parameters at TERENO sites may help to find possible reasons for unexplained effects.

The measured loading effects can be compared to loading effects calculated from global mass fields derived from hydrology models or GRACE measurements with the help of Green's functions.
The geometric time series can directly be compared to height changes derived from GRACE coefficients (see Equation 28). The measured gravity-to-height ratio can be compared with a theoretical gravity-to-height ratio (cf. Section 2.1.3).

In all these considerations a problem emerges concerning the direct attraction at the observation point. The question arises, what are local and what are regional mass effects; and does the regional signal still exist if the local effect is subtracted? The situation is depicted in Figure 6.5. Theoretically only the hydrologic signal which is not represented by the loading mass field resolution cell, in which the gravimeter is positioned, has to be eliminated to obtain the large and regional scale signal. For example, if EWH from GRACE or water storage change from a model are calculated, a certain mass variation is derived for the area around the gravimeter, which does not have to be in accordance to the local signal (as shown in Section 3.3). The investigations during this measurement campaign shall help to clarify this.

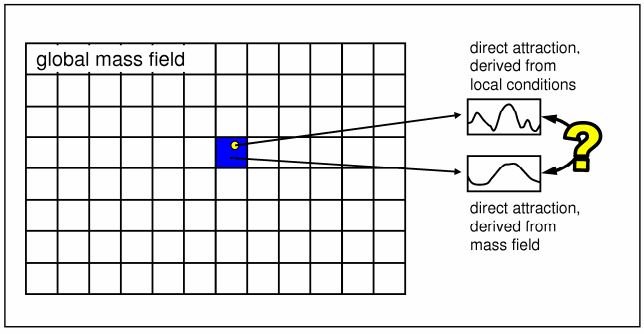

Fig. 6.5: Problem of regional and local direct gravity signals

Additionally observations of different SG stations in central Europe (see Figure 4.3) can be analysed for common signal parts, to gain a large-scale signal.

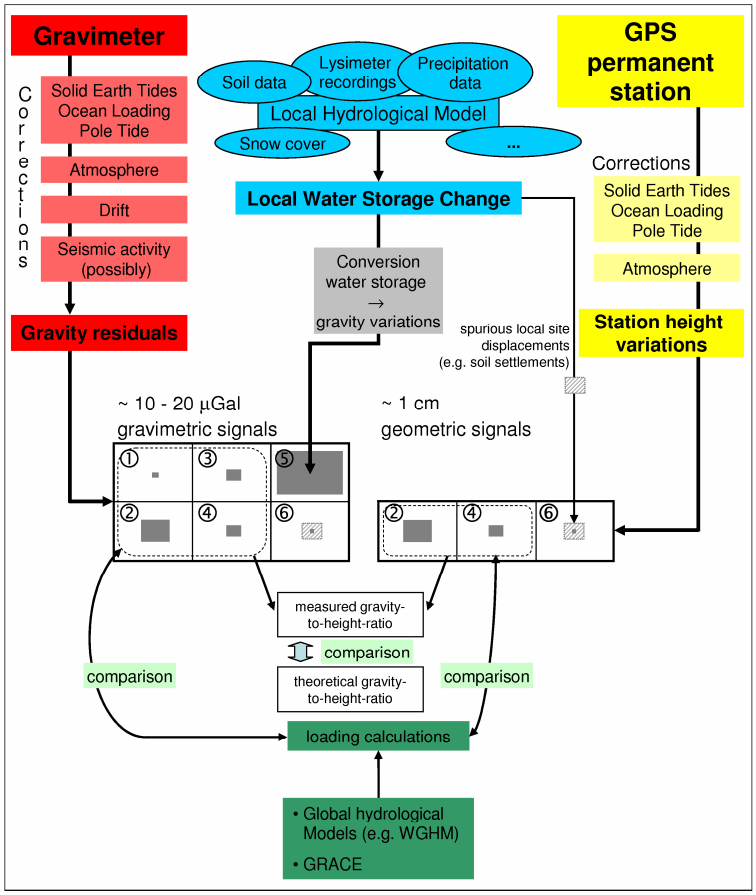

Fig. 6.6: Relationships in Approach 1

Approach 2

- *Objectives*

The objective of Approach 2 is to use the gravimetric data for evaluating local hydrological model results or gaining hydrological parameters. For this purpose the large-scale and medium-scale effects have to be reduced. For this task the knowledge from Approach 1 about the annual signal in this region can be utilized.

- *Location*

The gravimeter shall be located at a station, which is close to that from Approach 1, and which has a more complex hydrological situation. This approach shall illustrate the possibility of validating hydrological models with the signal from the gravity recordings.
Even if this works very well, it has to be remarked that such a measurement is bound up with immense effort for providing single point information. This argument becomes even more important if it is considered that the modelled area of the TERENO observatory has

an extent of several hundred [km^2]. To complement the stationary measurements, additional field campaigns with a relative-spring gravimeter can provide more information about the surrounding of the SG station.

- *Procedure*

In Figure 6.7 the procedure for Approach 2 is depicted. There are only slight differences compared to Figure 6.6. Now the loading calculation shall be used to reduce the large-scale effects, so that only the direct effect of local hydrology remains. Another possibility is that the theoretical gravity-to-height ratio or the one, found in Approach 1, are used to derive large-scale gravity variations from the geometric height changes.
The local signal can be converted to a total water storage change at the location of the gravimeter. This information can then be used to validate model results. Since only the integrative effect is available it may be the right approach for validating models with resolutions of 50 to 100 m, if there is no special situation in the nearest surrounding of the gravimeter.

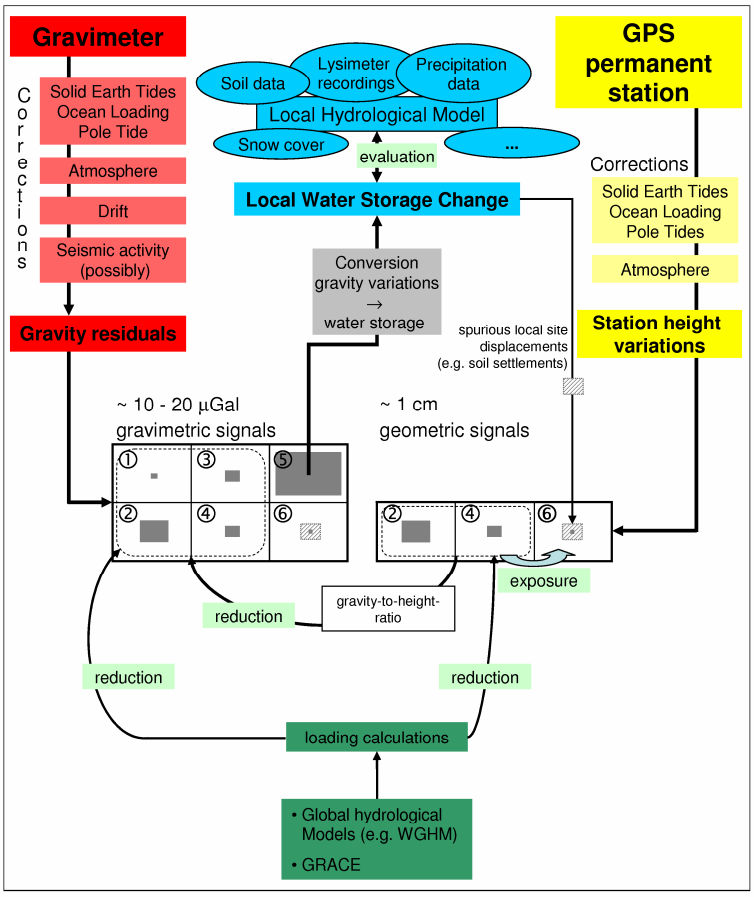

Fig. 6.7: Relationships in Approach 2

In Figure 6.7 it is also depicted that a geometric height series can help to detect spurious local signals. This signal should be the only remaining, if the loading effects have been reduced correctly from the height variation signal. Thus the geometric measurements can help to distinguish between real hydrological signals and gravity variations due to geometrical station movements.

Accuracy requirements and instrumentation

For this approach the accuracy requirements are very high since long period (annual) signals with small amplitudes (less than 1 to 2 μGal) shall be detected. This also requires very stable drift behaviour. Beside of superconducting gravimeter only the gPhone (cf. Table 4.3) is in the required accuracy class.
The station height variations have to be determined with [mm] or even sub-[mm] accuracy since the loading effects are expected to have a magnitude of only 1 cm (cf. Section 3.3.2).

Remarks

If both approaches shall be realized an iGrav would suggest itself to be used, since it can be mounted at another station and has the ability to measure also very small long term signals.

The installation of a combined SG and geometric test site in an area with many hydrological investigations will provide much experience how to reduce local and global hydrology. This knowledge can be utilized if the (portable) SG is used at other geophysical interesting locations, where for example post-glacial rebound takes place.

6.2 Atmospheric admittance factor

- Objectives
  - investigations regarding local atmospheric admittance factor; detection of its spatial and temporal variability
- Instrumentation
  - stationary relative gravimeter
  - pressure recording (TERENO site)
- Requirements for the location
  - two stations with different topographic characteristics
  - secure building for the instruments

- Tasks
  - correlating pressure values to gravity residuals
  - appropriate handling of the hydrology
- Measured quantity
  - atmospheric admittance factor (local pressure ↔ gravity residuals)

The dependence of local topography on the atmospheric admittance factor could be a further topic for the investigations in the test site. An admittance factor is determined by correlating a pressure time series to gravity residuals. Since this factor is often used for the reduction in gravimetric campaigns it is important to know, if it can be assumed to be constant over the whole area. Therefore a comparison of admittance factors derived at the southern mountainous part and in the northern flat part can be performed.
The used gravity residuals have to be corrected for other influences properly. For the investigations concerning the atmosphere observation intervals of several weeks are sufficient, since the main signal has a period of several days (cf. Section 3.3.1). Thus, a period for the observations can be chosen with small hydrologic variability. If the hydrology effect can be controlled it can also be investigated if there are different admittance factors for different seasons.
The correlation can be performed with a high temporal resolution, since the pressure data from the TERENO sites is provided continuously.

The gravimetric admittance factor is dependent on the direct effect and the loading of the atmosphere. The loading effect is very similar within the Ammer catchment because of the small distances (<50 km). The direct effect may be different in the mountainous part because of small-scale weather effects which can lead to a different distribution of air molecules in the air column above and because of the “missing air” due to the existence of the mountains. The station height has not to be considered since the admittance factor is dependent on the surface pressure change and independent of the total pressure.

The accuracy requirements of this campaign arise from the magnitude of the atmospheric admittance factor and its variations. The admittance factor is approximately 0.3 μGal/mbar and its expected variation is in the range of ±0.05 μGal/mbar. If a pressure variation of 30 mbar is assumed the maximum variation due to the uncertainty of the atmospheric admittance factor is around ±1.5 μGal. This is also again in the accuracy class of superconducting gravimeter and gPhone. Since air pressure recordings are performed simultaneously the pressure signal itself is available, what makes it possible to estimate the admittance factor with less accurate instruments, as it was done in the basement experiment (cf. Section 5.1.1). The instrument shall provide a stable drift behaviour and shall have the capability of recording gravity values over several weeks without the need of

interruption of the measurement for any reason. (In the basement experiment the measurement had to be stopped because of data dumping.)

6.3 Geometric measurement station (SAR - GNSS)

- Objectives
  - independent validation of SAR measurements with GNSS derived CR coordinates
  - systematic reduction of errors in SAR measurements
- Instrumentation
  - 2 corner reflectors (per station)
  - GNSS permanent station (per station)
  - tachymeter
  - SAR satellite(s)
- Requirements for the location
  - construction of a stable station
  - good visibility of GNSS satellites
  - no lay-over or shadowing effects in SAR images
- Tasks
  - comparison of theoretical ranges, derived from GNSS coordinates, with measured SAR ranges
  - gaining atmospheric delays from GNSS measurements or a local atmospheric model
  - integration of the GNSS station in a GNSS network to reach [mm]-accuracy for the station coordinate time series
  - implementing corrections terms for time variable geometric effects (station displacements) and atmospheric delays (ionosphere, troposphere)
- Measured quantities
  - SAR ranges and azimuth
  - troposphere parameter (GNSS)
  - GNSS coordinates

In the following an approach is introduced for realising an improved version of the test measurement in Section 5.2 to get reliable accuracy estimations for absolute SAR measurements. There shall be a systematic comparison of measured SAR ranges and azimuths to theoretical ranges and azimuths, derived from GNSS coordinates for the corner reflectors, for different incidence angles, orbits and atmospheric conditions.
The aim is to minimize the differences between the theoretical GNSS ranges and azimuths and the measured SAR ranges and azimuths. For that all possible error sources (cf. Section 4.5.3) have to be checked and potential systematic dependencies have to be analysed.

This station has not to be established in the TERENO area, but measured geometrical signals, from GNSS or SAR, could be used for further analysis in combination with gravimetric measurements.

Set-up and the requirements for the measurement station: The station consists of two SAR corner reflectors and a GNSS receiver (Figure 6.8). The components have to be installed in a geometrically stable condition, i.e.:

- the instruments have to be mounted on a stable foundation to minimize influence of soil settlements
- the instruments shall be mounted preferably on the same foundation to guarantee that the geometric relation between the phase centres remains stable
- the station has to be protected from external influences like animals

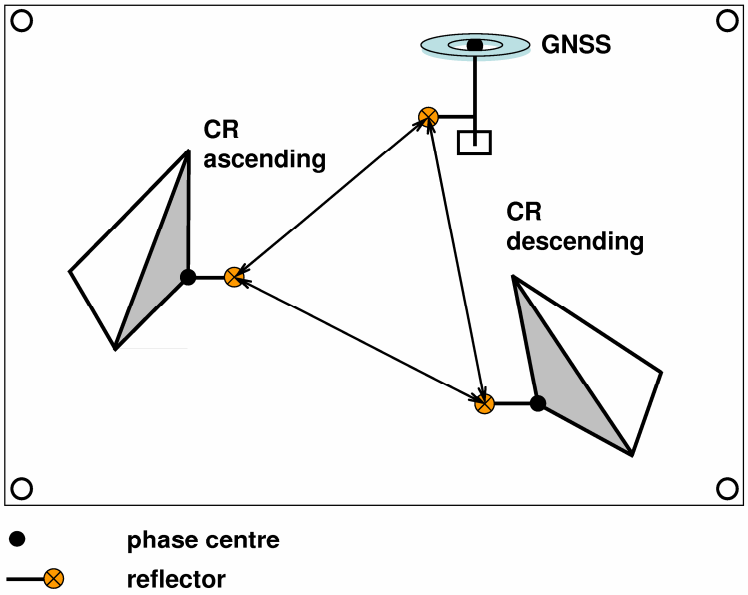

Fig. 6.8: Combined GNSS and SAR measurement station

The geometric relation between the phase centres of the reflectors and the antenna has to be determined very accurately. A possible way to realize this is to mount retro-reflectors at the corner reflectors and the GPS marker with a well-determined offset. The vectors between the phase centres can then be observed by a tachymeter.
The location of the GPS antenna has to be chosen in such a way, that disturbing reflections in the SAR images are avoided. The corner reflectors have to be mounted in such a way that no multi-path effects are caused by them.
One corner reflector is oriented for acquisitions from descending orbits, the other one for acquisitions from ascending orbits. To study different configurations one of the reflectors shall be set up for a small and the other for a large incidence angle.

If the orientation of one of the corner reflectors shall be changed, the vectors between the phase centres have to be determined again.
Control measurements to approve the geometric stability have to be carried out in a certain interval.

In a first long term measurement with the GPS-receiver, IGS05 (ITRF) coordinates for the station have to be determined. A measurement-duration of at least one year is necessary to provide annual variations of the station coordinates. To define a station velocity at least 2.5 years of observations are required. To determine coordinates with [mm]-accuracy with a differential approach, observations of one day are sufficient.

Following corrections have to be applied as a standard feature at the IGS05 coordinates at the epochs of the SAR image acquisitions, as shown in Section 5.2.6.2:
- solid Earth tides
- ocean loading
- pole tides

The accuracy requirements for the GPS-coordinates and station movements are high ([mm]), so that the coordinates can be assumed to be error free in comparison to SAR measurements and orbit accuracy. As shown in the test measurement (cf. Section 5.2) the accuracy of absolute range measurements is in the range of 1-2 dm and shall be increased to 1-2 cm.
The determination of the vectors between the phase centres has also be done with [mm]-accuracy.

With a second station also a differential approach is possible. Differential movements of two stations can be determined with higher accuracy than the absolute movement of a single station. This is because the following effects cancel out in the range difference, if the stations are in between one SAR image:
- orbit errors
- tropospheric dry delay
- tropospheric wet delay dependent on the atmospheric conditions: if the water vapour distribution within the SAR scene is variable, the difference of the delays of the stations remains in the differential vector
- solid Earth tides, ocean loading

These differential movements can also be validated independently by the GPS-measurements.

7 Conclusions

In the beginning of this thesis gravimetric and geometric signals, resulting from geophysical sources, are introduced. It is concentrated on signals, which might occur in the area of the TERENO alpine and prealpine Ammer observatory since it was chosen as test site for this study. The solid Earth tides are responsible for the largest effects; they are in the range of hundreds of [μGal] or 2-3 [dm], respectively. All other signals, namely ocean loading, pole tide, hydrology and atmosphere, are clearly smaller and in a similar range of magnitude. The signal amplitudes range from fractions of [μGal] to tens of [μGal], and from [mm] to some [cm], respectively. This implies that all signals, which shall not be observed, have to be reduced carefully.
The Earth is elastic, thus changes of mass load due to mass redistributions lead to deformations. The properties of the elastic Earth are described by Love numbers. The deformations are measurable as (geometric) height changes and gravimetric variations due to the height changes. This is called the indirect effect (loading effect). Gravimetric effects are also induced by the change of the direct Newtonian attraction due to mass variations. The loading effect is mainly a large-scale signal; the direct attraction is primarily induced by local mass changes.
The effects from solid Earth tides, ocean loading and pole tide can be reduced from measured quantities by existing models and programs; thus, the main objective of this thesis is the measuring of atmospheric and hydrological signals.

Many instruments for in situ measurements (e.g. lysimeter, meteo-stations, rain radar) are or will be available in the TERENO observatory for obtaining hydrological and atmospheric quantities. Unfortunately, the observatory is not yet fully operational, and the modelling efforts did not have the required progress yet for performing an operational campaign in this study.
Therefore, first test measurements have been performed at other locations. The experiments have been performed with a Scintrex CG-3M gravimeter. The first one in the basement of the TU München has shown its potential for stationary measurements. The accuracy level is about 5 μGal. Beside the measurement noise, the drift behaviour could be identified as limiting factor, since it turned out to be non-linear during these measurements. With the second experiment the potential for the detection of groundwater variations using gravity differences was tested. The accuracy of the gravity differences derived in this campaign did not allow the correct determination of the water table change because of the limitations of the used instrument. For this type of campaign several requirements are identified, such as stable grounding for reference points or the usage of a second gravimeter for improved drift determination. This shall be regarded for the proposed

gravity difference campaigns, which work after the same principle. Another finding of this test measurement is that the drift determination plays a major role for all campaigns with relative field gravimeters.
Both campaigns have shown that it is important to have experience with the handling of the individual gravimetric instrument to exploit the full accuracy potential.

It emerges in this work that the efforts in the TERENO observatory, especially in the case of hydrology, will justify the use of gravimeters. The results of gravimetric campaigns can be used to validate a hydrological model by comparing the measured to the computed gravity signal or to reduce gravity data for the hydrological effect, if other signals shall be measured. Furthermore it can be attempted to measure hydrological signals. This is most promising for ground water variations, which cause problems in the hydrological modelling of the Ammer catchment. In this context it has to be remarked that conventional hydrology models are not ready for the use of gravimetric data as input. The integration of gravimetric measurement capabilities for the standard use in hydrological modelling is a topic for further investigations.
It is difficult to derive hydrological quantities out of gravity values, since different effects have to be separated from the integrative gravity values. It is simpler to convert mass variations derived from hydrological measurements and modelling into gravity variations, because in that case all hydrological information has to be combined to one quantity. An approach, how this conversion can be done, is presented.

Concrete atmospheric and hydrologic signals in the Ammer catchment have been investigated.
For the atmosphere it could been shown, that in situ measurements of the air pressure and large-scale modelling results show only very small deviations in their variations because atmospheric changes are mainly large-scale effects. However, the offset can be very large resulting from the height variation in between one model grid cell. Incorporating the results from the experiment performed in the basement of the TU München, the following conclusions can be drawn for the gravimeter of the outdoor field class: It is sufficient to use the atmospheric admittance factor, which relates pressure changes to gravity changes, of 0.3 μGal/mbar and pressure variations from a large-scale model to reduce the atmospheric effect from relative gravimeter measurements. For higher accuracy, if e.g. a superconducting gravimeter is used, loading calculations for global mass fields have to be performed. Finally a campaign is proposed to specify an atmospheric admittance factor for the TERENO area.
In case of hydrology it has been shown that much more parameters than for the atmosphere are influencing its variability. During the investigation of the hydrological signals a clear difference between local measurements and large-scale water storage changes (GRACE, global hydrology model) was observed. This is also the case in other investigations,

introduced in this work, considering other areas in Germany. The large-scale signals are mainly annual, i.e. long-term, signals.
In Chapters 3 and 4, concerning the instruments and the expectable signals, respectively, it has been shown that long-term signals, in terms of gravimetry, can only be detected by superconducting gravimeters. These instruments have, in comparison to relative-spring gravimeters, very small drift rates and an accuracy which allows detecting signals in the 1/10 [µGal] range.
It is a challenge to separate between local and large-scale (hydrological) signals correctly, which motivates for a campaign applying a superconducting gravimeter for detailed analysis concerning this task. This shall, for example, provide information to evaluate GRACE measurements or for the better understanding of the relations between hydrology of a small catchment and continental wide hydrology. The instrumentation at the TERENO sites (e.g. lysimeter) will help to reduce local hydrological signals. Geometric measurements, in the form of height changes of a GNSS-permanent station, can provide additionally information, since they are only affected by large-scale effects.

A further test campaign, concerning geometric measurements, was performed at the DLR Oberpfaffenhofen. GPS derived coordinates of a corner reflector have been used to calculate theoretical SAR (TerraSAR-X) range and azimuth. These were compared to measured range and azimuth. The SAR ranges have to be corrected for signals of solid Earth tides and for tropospheric and ionospheric as well as for electronic delays. Azimuths have only to be corrected for solid Earth tides and electronic delays. Also the movement of the Earth's crust due to plate tectonics has to be regarded. It is shown that the electronic delay used for the correction of TerraSAR-X ranges is too large. The main reason is that only the dry but not the wet part of the troposphere was regarded during the calibration process.
Signals in the lower [cm] and [mm] range are too small to be detectable by absolute SAR measurements yet, but it can be seen in the experiment that there is the potential to reach at least 5 cm accuracy. If absolute SAR measurements shall move in the direction of this accuracy class, further investigations have to be done. The proposed measurement station shall help to find and eliminate the remaining errors. Possible error sources are:

- errors in the calibration constants (electronic delays)
- errors in the determination of the ionospheric and atmospheric delays
- orbit errors
- small signals on the Earth's surface (error or signal)

Overall, this work has shown that the combination of different measurement systems has the potential to provide further information about large- and small-scale geophysical signals:

- Connecting element for all kind of geometric and gravimetric measurement is that they have to be corrected for solid Earth tides, ocean loading and pole tides.
- In long-term time series geometric measurements (GNSS height changes) can help to separate hydrological large-scale and small-scale signals in gravimetric signals, since they are only affected by the large-scale variations. If the separation works properly the validation of GRACE derived gravity changes, which are also mainly affected by large-scale effects, with ground gravity observation will be possible.
- Spaceborne SAR is able to detect geophysical signals like the solid Earth tides with absolute measurements. GNSS observation are used to provide atmospheric corrections (especially for the wet tropospheric delay) and for independent validation of the absolute SAR measurements.
- With gravimetric measurements the total water storage change provided by a hydrological model can be validated. If atmospheric signals shall be measured or the drift behaviour of a gravimeter shall be investigated, the model results are used to reduce the hydrological part of the gravity signal.

The following measurement concepts are proposed, as a result of the investigations described above:

- Using gravity differences for the validation of hydrological models
- Using superconducting gravimeter, GNSS permanent station, local hydrological models and in situ data from TERENO sites for the separation of large- and small-scale hydrological signals
- Stationary gravimetric measurement for estimating variations in the atmospheric admittance factor
- Measurement station with GNSS permanent station and corner reflectors for performing an improved version of the SAR-GPS experiment.

Finally it has to be emphasised that this work does not have the intention of completeness, since this is not possible for the many different subjects which have been introduced. It shall rather give a preferably large overview of the addressed issues and motivate for further investigations, based on the proposed measurement concepts. A reader of this work shall become acquainted with the basics needed for deepened investigations.

Acknowledgements

I want to thank...

... my supervisors Prof. Roland Pail, Dr. Thomas Gruber and Dr. Michael Eineder for the continuous support throughout this work,

... Dr. Peter Steigenberger for helping me with the handling of the Bernese Software,

... Christian Ackermann, who was performing the test measurements with the Scintrex gravimeter with me,

... Dr. Bernhard Böhm and Raimund Daffner from Münchner Stadtentwässerung for making the measurement at the storm water reservoir possible,

... Dr. Ulrich Balss, Dr. Thomas Fritz and Christian Minet from DLR for the support during the SAR-GPS campaign, and

... Dr. Sven Wagner from KIT IMK-IFU for providing information about the TERENO observatory and hydrology models.

References

BOEHM J, NIELL A, SCHUH H, TESMER V, TREGONING P (2006) *Mapping functions for atmospheric delay modelling in GNSS analysis*. In: Proceeding 2006 IGS Workshop, Darmstadt.

BOY J-P, HINDERER J, GEGOUT P (1998) *Global atmospheric loading and gravity*. Physics of the Earth and Planetary Interiors, 109 (3-4): 161-177, doi: 10.1016/S0031-9201(98)00122-8.

BOY J-P, GEGOUT P, HINDERER J (2002) *Reduction of surface gravity data from global atmospheric pressure loading*. Geophysical Journal International, 149 (2): 534-545, doi: 10.1046/j.1365-246X.2002.01667.x.

CREUTZFELDT B, GÜNTNER A, WZIONTEK H, MERZ B (2010) *Reducing local hydrology from high-precision gravity measurements: a lysimeter-based approach*. Geophysical Journal International, Early View: Article first published online: 27 Aug 2010, doi: 10.1111/j.1365-246X.2010.04742.x.

CROSSLEY D, HINDERER J, LLUBES M, FLORSCH N (2003) *The potential of ground gravity measurements to validate GRACE data*. Advances in Geoscience, 1: 65-71.

CROSSLEY D, HINDERER J, BOY J-P (2005) *Time variations of the European gravity field from superconducting gravimeters*. Geophysical Journal International, 161 (2): 257-559, doi: 10.1111/j.1365-246X.2005.02586.x.

DAVIE T (2008) *Fundamentals of Hydrology, Second Edition*. London: Routledge.

DE LINAGE C, HINDERER J, BOY J-P (2006) *A search on the gravity / height ratio induced by surface loading; theoretical investigation and numerical applications*. Bulletin d'Information des Marées Terrestres, 142: 11451-11460.

DE LINAGE C, HINDERER J, BOY J-P (2009) *Variability of the Gravity-to-Height Ratio Due to Surface Loads*. Pure and Applied Geophysics, 166 (8-9): 1217-1245, doi: 10.1007/s00024-004-0506-0.

DEMOULIN A, DUCARME B, EVERAETS M (2007) *Seasonal height change influence in GPS and gravimetric campaign data*. Journal of Geodynamics, 43 (2): 308-319, doi: 10.1016/j.jog.2006.09.008.

EINEDER M, BAMLER R (2008) *Remote Sensing - Advanced Methods*. München: TUM, Lehrstuhl für Methodik der Fernerkundung, Lecture Notes.

EINEDER M, MINET C, STEIGENBERGER P, CONG X, FRTIZ T (2010) *Imaging Geodesy - Towards centimetre-level ranging accuracy with TerraSAR-X*. IEEE Transactions on geoscience and remote sensing, early access, doi: 10.1109/TGRS.2010.2060264.

FARREL W E (1972) *Deformation of the Earth by surface loads*. Reviews of Geophysics and Space Physics, 10 (3): 761-797.

FRITZ T, EINEDER M (2009) *TerraSAR-X Ground Segment: Basic Product Specification document, TX-GS-DD-3302, Issue 1.6*. CAF - Cluster Applied Remote Sensing.

GRUBER T, PETERS T, ZENNER L (2008) *The role of the Atmosphere for Satellite Gravity Field Missions*. In: Sideris M G (ed) Observing our Changing Earth, International Association of Geodesy Symposia, 133 (2): 105-112, doi: 10.1007/978-3-540-85426-5_13.

GUO J Y, LI Y B, HUANG Y, DENG H T, XU S Q, NING J S (2004) *Green's function of the deformation of the Earth as a result of atmospheric loading*. Geophysical Journal International, 159 (1): 53-68, doi: 10.1111/j.1365-246X.2004.02410.x.

GWR INSTRUMENTS (2007) *GWR Observatory Superconducting Gravimeter and Support Systems Descriptions and Specifications July 30, 2007*. San Diego (California, USA): GWR Instruments Inc., Technical Report, available at http://www.gwrinstruments.com/photos/osg/obsspecs.pdf, last access: 01.11.2010.

HAN D, WAHR J (1995) *The viscoelastic relaxation of a realistically stratified Earth, and a further analysis of postglacial rebound*. Geophysical Journal International, 120 (2): 287-311, doi: 10.1111/j.1365-246X.1995.tb01819.x.

HOFMANN-WELLENHOF B, LICHTENEGGER H, WASLE E (2008) *GNSS - Global Navigation Satellite Systems GPS, GLONASS, Galileo & more*. Wien: Springer.

KANIUTH K, VETTER S (2006) *Estimating atmospheric pressure loading regression coefficients from GPS observations*. GPS Solutions, 10 (2): 126-134, doi: 10.1007/s10291-005-0014-4.

KOUBA J (2009) *A Guide to using International GNSS Service (IGS) Products*. Available at http://acc.igs.org/UsingIGSProductsVer21.pdf, last access: 29.06.2010.

KUNSTMANN H (2010) *Hydrological Observatory Description: River Ammer, Germany*. Karlsruhe Institute of Technology, Institute of Meteorology and Climate Research (KIT/IMK-IFU), Technical Report, available at http://www.peer.eu/fileadmin.../user_upload/projects/flagship_projects/PEER_Euraqua/Ammer%20Germany.pdf, last access 26.10.2010.

KUNSTMANN H, SCHNEIDER K, FORKEL R, KNOCHE R (2004) *Impact analysis of climate change for an Alpine catchment using high resolution dynamic downscaling of ECHAM4 time slices*. Hydrology and Earth System Sciences, 8 (6): 1031-1045, doi: 10.5194/hess-8-1031-2004.

LEIRIÃO S, HE X, CHRISTIANSEN L, ANDERSEN O B, BAUER-GOTTWEIN P (2009) *Calculation of the temporal gravity variations from spatially variable water storage change in soils and aquifers*. Journal of Hydrology, 365 (3-4): 302-309, doi: 10.1016/j.jhydrol.2008.11.040.

LUDWIG R, TASCHNER S, MAUSER W (2003) *Modelling Floods in Ammer catchment Limitations and challenges with a coupled meteo-hydrological model approach*. Hydrology and Earth System Sciences, 7 (6): 833-847, doi: 10.5194/hess-7-833-2003.

MAYR S (2004) *Inverse flächendifferenzierte hydrologische Modellierung des Ammer einzugsgebietes mittels Kombination von Grund- und Oberflächenwasserdaten*. Universität Augsburg, Fakultät für angewandte Informatik, Institut für Geographie, Lehrstuhl für physische Geographie; durchgeführt am: Forschungszentrum Karlruhe, Institut für Meteorologie und Klimaforschung Atmosphärische Umweltforschung (IMK-IFU), Diplomarbeit.

MCCARTHY D D, PETIT G (2004) *IERS Conventions (2003), IERS Technical Note 32*. Frankfurt am Main: Bundesamt für Kartographie und Geodäsie.

MCWHORTER D B, SUNADA D K (1977) *Ground-water Hydrology and Hydraulics*. Fort Collins: Water Resources Publications.

MERRIAM J B (1992) *Atmospheric pressure and gravity*. Geophysical Journal International, 109 (3): 488-500, doi : 10.1111/j.1365-246X.1992.tb00112.x.

NAUJOKS M, WEISE A, KRONER C, JAHR T (2008) *Detection of small hydrological variations in gravity by repeated observations with relative gravimeters*. Journal of Geodesy, 82 (9): 543-553, doi: 10.1007/s00190-007-0202-9.

NAUJOKS M, KRONER C, WEISE A, JAHR T, KRAUSE P, EISNER S (2010) *Evaluating local hydrological modelling by temporal gravity observations and a gravimetric three-dimensional model*. Geophysical Journal International, 182 (1): 233-249, doi: 10.1111/j.1365-246X.2010.04615.x.

NICOLAS J, NOCQUET J-M, VAN CAMP M, VAN DAM T, BOY J-P, HINDERER J, GEGOUT P, CALAIS E, AMALVICT M (2006) *Seasonal effect on vertical positioning by Satellite Laser Ranging and Global Positioning System and on absolute gravity at the OCA geodetic station, Grasse, France*. Geophysical Journal International, 167 (3): 1127-1137, doi: 10.1111/j.1365-246X.2006.03205.x.

PETROV L, BOY J-P (2004) *Study of the atmospheric pressure loading signal in very long baseline interferometry observations*. Journal of Geophysical Research - Solid Earth, 109 (3): B03405, doi: 10.1029/2003JB002500.

PRICE M (1985) *Introducing groundwater*. London: Chapman & Hall.

ROTHACHER M (2007) *Satellitengeodäsie 2*. München: TUM, Institut für Astronomische und Physikalische Geodäsie, Vorlesungsskript 2007/08.

RUMMEL R (2007) *Erdmessung - Teil 3*. München: TUM, Institut für Astronomische und Physikalische Geodäsie, Vorlesungsskript.

SAVCENKO R, BOSCH W (2008) *EOT08a - empirical ocean tide model from multi-mission satellite altimetry*. München: Deutsches Geodätisches Forschungsinstitut, Technical Report: DGFI Report 81.

SCHMEER M (2006) *Zeitliche Stabilität und zeitliche Veränderungen im Gravimetereich-system Garmisch-Zugspitze*. München: TUM, Institut für Astronomische und Physikalische Geodäsie, Diplomarbeit.

SCHULLA J, JASPER K (2007) *Model Description - WaSiM-ETH*. Zürich: ETH, Technical Report, available at http://www.wasim.ch/products/wasim_description.htm, last access 01.10.2010.

SCINTREX (1995) *Scintrex: CG-3/3M AUTOGRAV - Automated gravity meter operator manual*. Concord (Ontario, Canada): Scintrex a division of LRS, User's Manual.

SEEBER G (2003) *Satellite Geodesy 2nd edition*. Berlin: de Gruyter.

SPRATT R S (1982) *Modelling the effect of atmospheric pressure variations on gravity*. Geophysical Journal of the Royal Astronomical Society, 71 (1): 173-186, doi: 10.1111/j.1365-246X.1982.tb04991.x.

TAMURA Y (1987) *A harmonic development of the tide-generating potential*. Bulletin d'Information des Marées Terrestres, 99: 6813-6855.

TESMER V, STEIGENBERGER P, ROTHACHER M, BOEHM J, MEISEL B (2009) *Annual deformation signals from homogeneously reprocessed VLBI and GPS height time series*. Journal of Geodesy, 83 (10): 973-988, doi: 10.1007/s00190-009-0316-3.

TESMER V, STEIGENBERGER P, VAN DAM T, MAYER-GÜRR T (2010) *Vertical deformations from homogeneously processed GRACE and global GPS long term series*. Journal of Geodesy, submitted.

TIMMEN L, GITLEIN O (2004) *The capacity of the Scintrex Autograv CG-3M No. 4492 gravimeter for "absolute scale" surveys*. Revista Brasileira de Cartografia 56 (2): 89-95.

TORGE W (1989) *Gravimetry*. Berlin: de Gruyter.

TORGE W (2003) *Geodäsie*. Berlin: de Gruyter.

VAN DAM T M, WAHR J (1998) *Modeling Environment Loading Effects: a Review*. Physics and Chemistry of the Earth, 23 (9-10): 1077-1087, doi: 10.1016/S0079-1946(98)00147-5.

VAN DAM T M, WAHR J, CHAO Y, LEULIETTE E (1997) *Predictions of crustal deformation and of geoid and sea-level variability caused by oceanic and atmospheric loading*. Geophysical Journal International, 129 (3): 507-517, doi: 10.1111/j.1365-246X.1997.tb04490.x.

VAN DAM T, WAHR J, MILLY P C D, SHMAKIN A B, BLEWITT G, LAVALLEE D, LARSON K M (2001) *Crustal displacements due to continental water loading*. Geophysical Research Letters, 28 (4): 651-654.

VAN DAM T, PLAG H-P, FRANCIS O, GEGOUT P (2003) *GGFC Special Bureau for Loading: Current status and Plans*. In: Richter B, Schwegmann W, Dick W R (eds) Proceedings of the IERS Workshop on Combination Research and Global Geophysical Fluids, Bavarian Academy of Sciences, Munich, Germany, 18. - 21. November 2002, IERS Tech. Note 30: 180-198.

VIRTANEN H, TERVO M, BILKER-KOIVULA M (2006) *Comparison of superconducting gravimeter observations with hydrological models of various spatial extents*. Bulletin d'Information des Marées Terrestres 142: 11361-11368.

WAHR J M, MOLENAAR M, BRYAN F (1998) *Time variability of the Earth's gravity field: Hydrological and oceanic effects and their possible detection using GRACE*. Journal of Geophysical Research - Solid Earth, 103 (B12): 30205-30229, doi: 10.1029/98JB02844.

WERHAHN J, QIU W, KUNSTMANN H *Precipitation Radar in the Ammer TERENO-Observatory*. Poster.

WERTH S, GÜNTNER A, SCHMIDT R, KUSCHE J (2009) *Evaluation of GRACE filter tools from a hydrological perspective*. Geophysical Journal International, 179 (3): 1499-1515, doi: 10.1111/j.1365-246X.2009.04355.x.

YOON Y T, EINEDER M, YAGUE-MARTINEZ N, MONTENBURCK O (2009) *TerraSAR-X precise trajectory estimation and quality assessment*. IEEE Transactions on geosicence and remote sensing, 47 (6): 1859-1868, doi: 10.1109/TGRS.2008.2006983.

ZERBINI S, RICHTER B, NEGUSINI M, ROMAGNOLI C, SIMON D, DOMENICHINI F, SCHWAHN W (2001) *Height and gravity variations by continuous GPS, gravity and environmental parameter observations in the southern Po Plain, near Bologna, Italy*. Earth and Planetary Science Letters, 192 (3): 267-279, doi: 10.1016/S0012-821X(01)00445-9.

ZERBINI S, NEGUSINI M, ROMAGNOLI C, DOMENICHINI F, RICHTER B, SIMON D (2002) *Multi-parameter continuous observations to detect ground deformation and to study environmental variability impacts*. Global and Planetary Change, 34 (1-2): 37-58, doi: 10.1016/S0921-8181(02)00105-4.

Table of figures

List of tables

Abbreviations

BEK	Bayerische Kommission für die Internationale Erdmessung
BKG	Bundesamt für Kartographie und Geodäsie
CODE	Center for Orbit Determination in Europe
CR	corner reflector
DEM	Digital Elevation Model
DLR	Deutsches Zentrum für Luft- und Raumfahrt
DWD	Deutscher Wetterdienst
EC	eddy covariance
ECMWF	European Centre for Medium-Range Weather Forecasts
ESA	European Space Agency
ETC	Earth Tide Correction (internal Program of SCINTREX gravimeter)
ETRF	European Terrestrial Reference Frame
ETRS	European Terrestrial Reference System
EWH	equivalent water height
FZJ	Forschungszentrum Jülich
GFZ	Helmholtz-Zentrum Potsdam - Deutsches GeoForschungs-Zentrum
GGP	Global Geodynamics Project
GLONASS	Globalnaja Nawigazionnaja Sputnikowaja Sistema
GMF	Global Mapping Function
GMT	Greenwich Mean Time
GNSS	Global Navigation Satellite Systems
GPCC	Global Precipitation Climatology Centre
GPS	Global Positioning System
GRACE	Gravity Recovery and Climate Experiment
GREF	Integriertes Geodätisches Referenznetz Deutschlands
GSOC	German Space Operation Centre
HMGU	Helmholtz-Zentrum München - Deutsches Forschungszentrum für Gesundheit und Umwelt
IAPG	Institut für Astronomische und Physikalische Geodäsie (TU München)
IERS	International Earth Rotation and Reference System Service
IGS	International GNSS Service
InSAR	SAR interferometry
IMF	Institut für Methodik der Fernerkundung (DLR)
IMK-IFU	Institut für Meteorologie und Klimaforschung, Bereich Atmosphärische Umweltforschung

IRI	International Reference Ionosphere
ITRF	International Terrestrial Reference Frame
ITRS	International Terrestrial Reference System
KIT	Karlsruher Institut für Technologie
LCR	LaCoste-Romberg
LfU	Bayrisches Landesamt für Umwelt
LoS	Line of Sight
LVG	Landesamt für Vermessung und Geoinformation (Bayern)
MJD	Modified Julian Date
NAVSTAR	Navigation system with time and ranging
OSG	Observatory Superconducting Gravimeter
OTL	ocean tide loading
POL	pole tide
PPP	Precise Point Positioning
PREM	Preliminary Earth Model
PRF	pulse repetion frequency
PSO	precise science orbits
RINEX	Receiver Independent Exchange Format
RMS	root mean square
RSF	range sampling frequency
SAPOS®	Satellitenpositionierungsdienst der deutschen Landesvermessung
SAR	Synthetic Aperture Radar
SET	Solid Earth Tides
SCR	signal-to-clutter ratio
SG	superconducting gravimeter
SRTM	Shuttle Radar Topography Mission
SST	satellite-to-satellite tracking
TDX	TanDEM-X
TEC	total electron content
TECU	TEC-Unit
TERENO	Terrestrial Enviromental Observatories
TSX	TerraSAR-X
UNAVCO	University NAVSTAR Consortium
UTC	Coordinated Universal Time
VMF	Vienna Mapping Function
VTEC	vertical TEC
WaSiM-ETH	Water balance Simulation Model ETH
WGHM	WaterGAP Global Hydrology Model
WSC	water storage change
WWA	Wasserwirtschaftsamt

Appendix

- Form of the ETRS89/ITRS transformation tool on the EUREF network homepage http://www.epncb.oma.be/_dataproducts/coord_trans/ (last access 05.11.2010)
  → Section 5.2.2

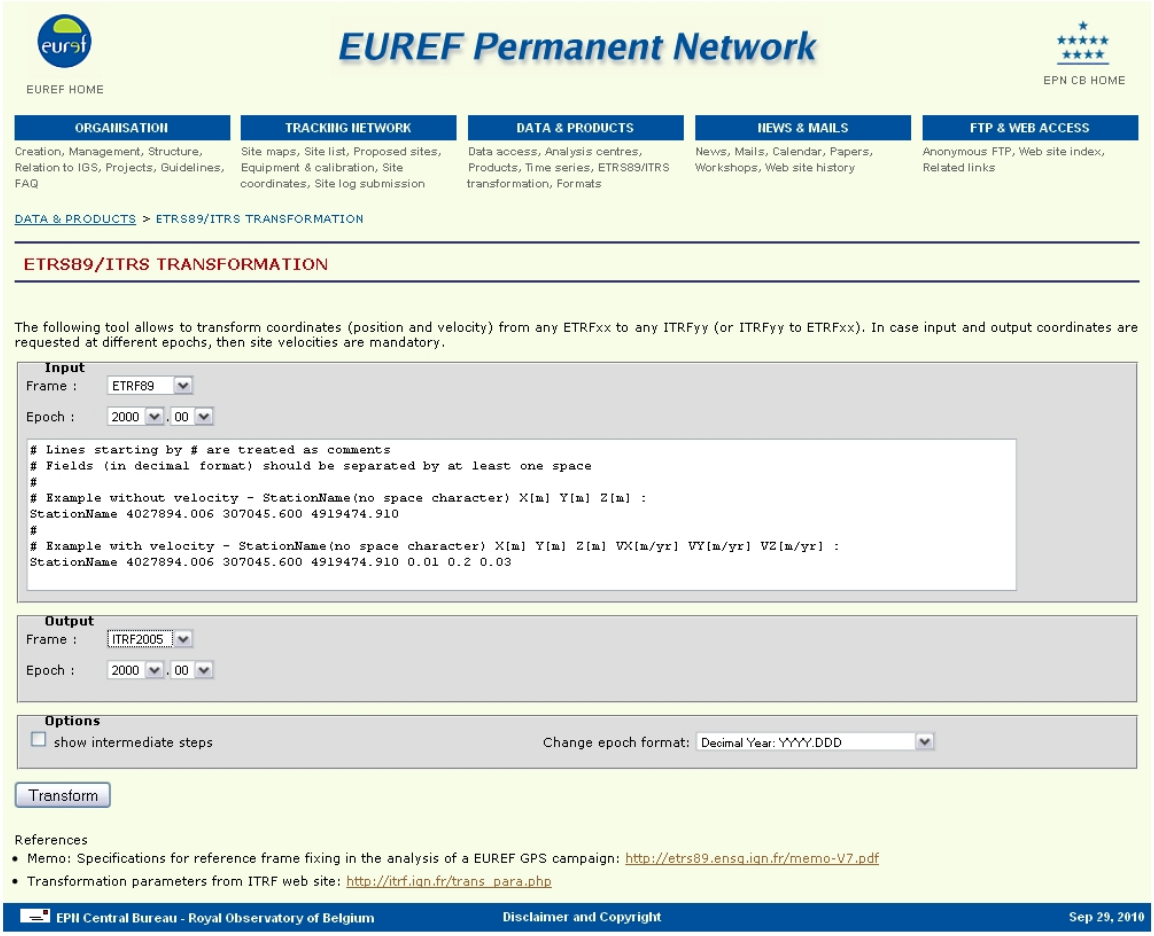

- Form of the IRI online computation tool on http://omniweb.gsfc.nasa.gov/vitmo/iri_vitmo.html (last access 05.11.2010)
  → Section 5.2.6.3

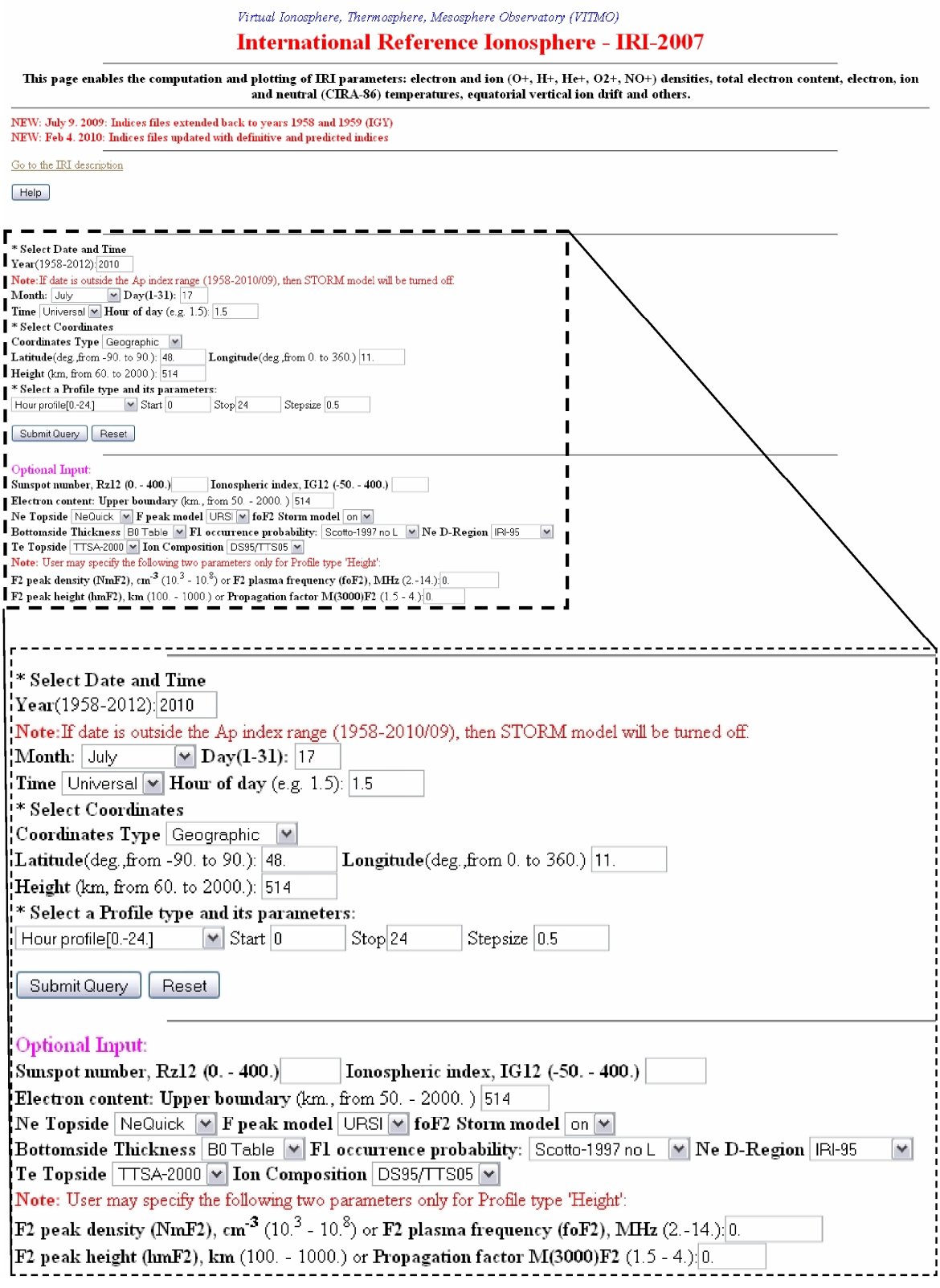

Virtual Ionosphere, Thermosphere, Mesosphere Observatory (VITMO)

International Reference Ionosphere - IRI-2007

This page enables the computation and plotting of IRI parameters: electron and ion (O+, H+, He+, O2+, NO+) densities, total electron content, electron, ion and neutral (CIRA-86) temperatures, equatorial vertical ion drift and others.

NEW: July 9, 2009: Indices files extended back to years 1958 and 1959 (IGY)
NEW: Feb 4, 2010: Indices files updated with definitive and predicted indices

Go to the IRI description

Help

* Select Date and Time
Year(1958-2012): 2010
Note: If date is outside the Ap index range (1958-2010/09), then STORM model will be turned off.
Month: July Day(1-31): 17
Time Universal Hour of day (e.g. 1.5): 1.5
* Select Coordinates
Coordinates Type Geographic
Latitude(deg.,from -90. to 90.): 48. Longitude(deg.,from 0. to 360.) 11.
Height (km, from 60. to 2000.): 514
* Select a Profile type and its parameters:
Hour profile[0.-24.] Start 0 Stop 24 Stepsize 0.5

Submit Query Reset

Optional Input:
Sunspot number, Rz12 (0. - 400.) Ionospheric index, IG12 (-50. - 400.)
Electron content: Upper boundary (km., from 50. - 2000.) 514
Ne Topside NeQuick F peak model URSI foF2 Storm model on
Bottomside Thickness B0 Table F1 occurrence probability: Scotto-1997 no L Ne D-Region IRI-95
Te Topside TTSA-2000 Ion Composition DS95/TTS05
Note: User may specify the following two parameters only for Profile type 'Height':
F2 peak density (NmF2), cm^{-3} (10^3 - 10^8) or F2 plasma frequency (foF2), MHz (2.-14.): 0.
F2 peak height (hmF2), km (100. - 1000.) or Propagation factor M(3000)F2 (1.5 - 4.): 0.

Select output form:

- (•) List model data
- ( ) Create model data file in ASCII format for downloading
- ( ) List model data in XML format
- ( ) Create model data file XML format for downloading
- ( ) Plot model data

Note 1: The first selected parameter below always will be along the X-axis, the other selections will be along Y-axis.
(e.g. if you want a Height profile, you may specify Height as the first parameter in the listing below.)
Note 2: User may get scatter plot if he specifies any two parameters below and changes the "connect type"
in the "Advanced plot selections" to "show points only"

[Submit Query] [Reset]

Select desired output parameters

Independent Variables

- [x] Year
- [x] Month
- [x] Day of month
- [ ] Day of year
- [ ] Hour of day, UT/LT (depending on user's choice above)
- [ ] Solar zenith angle, degree
- [x] Height, km
- [ ] Geographic/Geomagnetic Latitude, deg. (depending on user's choice above)
- [ ] Geographic/Geomagnetic Longitude, deg. (depending on user's choice above)
- [ ] Magnetic inclination (DIP), degree
- [ ] Modified dip latitude, degree

IRI Model Parameters

- [ ] Electron_density (Ne), m^{-3}
- [ ] Ratio of Ne and F2 peak density(Ne/NmF2)>
- [ ] Neutral Temperature Tn, K
- [ ] Ion Temperature Ti, K
- [ ] Electron Temperature, Te, K
- [x] Total Electron Content (TEC), 10^{16} m^{-2}
- [ ] TEC top, percentage
- [ ] Atomic Oxygen ions (O^+), percentage
- [ ] Atomic Hydrogen (H^+),ions, percentage
- [ ] Atomic Helium (He^+), ions, percentage
- [ ] Molecular Oxigen (O_2^+) ions, percentage
- [ ] Nitric Oxide ions (NO^+), percentage
- [ ] Cluster ions, percentage
- [ ] Atomic Nitrogen (N^+) ions, percentage

- [ ] Height of F2 peak (hmF2), km
- [ ] Height of F1 peak (hmF1), km
- [ ] Height of E peak (hmE), km
- [ ] Height of D peak (hmD), km
- [ ] Density of F2 peak (NmF2), m^{-3}
- [ ] Density of F1 peak (NmF1), m^{-3}
- [ ] Density of E peak (NmE), m^{-3}
- [ ] Density of D peak (NmD), m^{-3}
- [ ] Propagation factor M(3000)F2
- [ ] Bottomside thickness (B0), km
- [ ] Bottomside_shape (B1)
- [ ] E-valley width, km
- [ ] E-valley depth (Nmin/NmE)
- [ ] F2 plasma frequency (foF2), MHz
- [ ] F1 plasma frequency (foF1), MHz
- [ ] E plasma frequency (foE), MHz
- [ ] D plasma frequency (foD), MHz

- [ ] Equatorial vertical ion drift, m/s
- [ ] Spread F probability
- [ ] Ratio of foF2 storm to foF2 quiet
- [ ] F1 probability 1979
- [ ] F1 probability 1995 incl. L-condition
- [ ] F1 probability 1995

Indices used by the model

- [ ] 12-month running mean of sunspot number (Rz12)
- [ ] Ionospheric Index IG12
- [ ] Daily Solar Radio Flux F107D

[Submit] [Clear]

Advanced plot selections (optional)

Connect Type: [Connect data points] Character size(0.5-2.0) [ ]
Plot Symbol: [Asterisk] Symbol Size(0.1-4.0): [ ]
Y-axis Scale: [Linear] X-axis Scale: [Linear]
Image size (pixels):X: [640] Y: [480]

[Submit] [Reset]

Send questions about this model to Dr. Dieter Bilitza, E-mail: dieter.bilitza-1@nasa.gov
Send questions about WWW access to this model to Dr. Natalia Papitashvili, E-mail: Natalia.E.Papitashvili@nasa.gov,
Mail Code 672, NASA/Goddard Space Flight Center, Greenbelt, MD 20771

NASA Official: **Dr. Robert McGuire, Head of the Space Physics Data Facility**

Veröffentlichungen in der Schriftenreihe IAPG / FESG (ISSN 1437-8280):
Reports in the series IAPG / FESG (ISSN 1437-8280):

No. 1: Müller J., Oberndorfer H. (1999). *Validation of GOCE Simulation.* ISBN-10 3-934205-00-3, ISBN-13 978-3-934205-00-0.

No. 2: Nitschke M. (1999). SATLAB – *Ein Werkzeug zur Visualisierung von Satellitenbahnen.* ISBN-10 3-934205-01-1, ISBN-13 978-3-934205-01-7..

No. 3: Tsoulis D. (1999). *Spherical harmonic computations with topographic/isostatic coefficients.* ISBN-10 3-934205-02-X, ISBN-13 978-3-934205-02-4..

No. 4: Dorobantu R. (1999). *Gravitationsdrehwaage.* ISBN-10 3-934205-03-8, ISBN-13 978-3-934205-03-1.

No. 5: Schmidt R. (1999). *Numerische Integration gestörter Satellitenbahnen mit* MATLAB. ISBN-10 3-934205-04-6, ISBN-13 978-3-934205-04-8.

No. 6: Dorobantu R. (1999). *Simulation des Verhaltens einer low-cost Strapdown-IMU unter Laborbedingungen.* ISBN-10 3-934205-05-4, ISBN-13 978-3-934205-05-5.

No. 7: Bauch A., Rothacher M., Rummel R. (2000). *Bezugssysteme in Lage und Höhe. Tutorial zum Kursus INGENIEURVERMESSUNG 2000.* ISBN-10 3-934205-06-2, ISBN-13 978-3-934205-06-2.

No. 8: Rothacher M., Zebhauser B. (2000). *Einführung in GPS. Tutorial zum 3. SAPOS-Symposium 2000 in München.* ISBN-10 3-934205-07-0, ISBN-13 978-3-934205-07-9.

No. 9: Ulrich M. (2000). *Vorhersage der Erdrotationsparameter mit Hilfe Neuronaler Netze.* ISBN-10 3-934205-08-9, ISBN-13 978-3-934205-08-6.

No. 10: Seitz F. (2000). *Charakterisierung eines bistatischen Rayleigh- und Raman-Lidars zur Bestimmung von höhenaufgelösten Wasserdampfprofilen.* ISBN-10 3-934205-09-7, ISBN-13 978-3-934205-09-3.

No. 11: Meyer F. (2000). *Messung von höhenaufgelösten Wasserdampfprofilen unter Verwendung eines bistatischen Raman-Lidars.* ISBN-10 3-934205-10-0, ISBN-13 978-3-934205-10-9.

No. 12: Peters T. (2001). *Zeitliche Variationen des Gravitationsfeldes der Erde.* ISBN-10 3-934205-11-9, ISBN-13 978-3-934205-11-6.

No. 13: Egger D. (2001). *Astronomie und Java – Objekte der Astronomie.* ISBN-10 3-934205-12-7, ISBN-13 978-3-934205-12-3.

No. 14: Steigenberger P. (2002). MATLAB-*Toolbox zur TOPEX/POSEIDON Altimeterdatenverarbeitung.* ISBN-10 3-934205-13-5, ISBN-13 978-3-934205-13-0.

No. 15: Schneider M. (2002). *Zur Methodik der Gravitationsfeldbestimmung mit Erdsatelliten.* ISBN-10 3-934205-14-3, ISBN-13 978-3-934205-14-7.

No. 16: Dorobantu R., Gerlach C. (2004). *Investigation of a Navigation–Grade RLG SIMU type iNAV–RQH.* ISBN-10 3-934205-15-1, ISBN-13 978-3-934205-15-4.

No. 17: Schneider M. (2004). *Beiträge zur Bahnbestimmung und Gravitationsfeldbestimmung mit Erdsatelliten sowie zur Orientierung von Rotationssensoren.* ISBN-10 3-934205-16-X, ISBN-13 978-3-934205-16-1.

No. 18: Egger D. (2004). *Astro-Toolbox, Theorie.* ISBN-10 3-934205-17-8, ISBN-13 978-3-934205-17-8.

No. 19: Egger D. (2004). *Astro-Toolbox, Praxis.* ISBN-10 3-934205-18-6, ISBN-13 978-3-934205-18-5.

No. 20: Fackler U. (2005). *GRACE - Analyse von Beschleunigungsmessungen.* ISBN-10 3-934205-19-4, ISBN-13 978-3-934205-19-2.

No. 21: Schneider M. (2005). *Beiträge zur Gravitationsfeldbestimmung mit Erdsatelliten.* ISBN-10 3-934205-20-8, ISBN-13 978-3-934205-20-8.

No. 22: Egger D. (2006). *Sinus-Netzwerk.* ISBN-10 3-934205-21-6, ISBN-13 978-3-934205-21-5.

No. 23: Schneider M. (2006). *Gravitationsfeldbestimmung unter Verwendung von Bilanzgleichungen für beliebige Observablen .* ISBN-10 3-934205-22-4, ISBN-13 978-3-934205-22-2.

No. 24: Mladek F. (2006). *Hydrostatische Isostasie.* ISBN-10 3-934205-23-2, ISBN-13 978-3-934205-23-9.

No. 25: Stummer C. (2006). *Analyse der Gradiometergleichungen der GOCE Satellitenmission zur Schwerefeldbestimmung.* ISBN-10 3-934205-24-0, ISBN-13 978-3-934205-24-6.

No. 26: Fecher T. (2008). *Methodische Grundlagen von kombinierten Schwerefeldmodellen.* ISBN-13 978-3-934205-25-3.

No. 27: Albertella A., Savcenko R., Bosch W., Rummel R. (2008). *Dynamic Ocean Topography - The Geodetic Approach.* ISBN-13 978-3-934205-26-0.

No. 28: Svehla D. (2009). *ACES and FUTURE GNSS-Based EARTH OBSERVATION and NAVIGATION.* ISBN-13 978-3-934205-27-7.

No. 29: Egger D. (2009). *Numerische Integration von Satellitenbahnen.* ISBN-13 978-3-934205-28-4.

No. 30: Murböck M. (2011). *Genauigkeitssimulation von Schwerefeld-Satellitenmissionen.* ISBN-13 978-3-934205-29-1.

No. 31: Tuttas S. (2011). *Joint gravimetric and geometric survey of geophysical signals - Feasibility study for the TERENO alpine and prealpine Ammer observatory.* ISBN-13 978-3-934205-30-7.

Weitere Exemplare können bezogen werden unter / Copies are available from:
Institut für Astronomische und Physikalische Geodäsie
Technische Universität München
Arcisstrasse 21, D-80290 München, Germany
Telefon: +49-89-289-23190, Telefax: +49-89-289-23178, Email: rechel@bv.tum.de

Oder im Internet / Or via Internet:
http://www.iapg.bv.tum.de/Schriftenreihe/

ISSN 1437-8280, ISBN-13 978-3-934205-30-7